HENRY
Hydraulic Engineering Repository

Ein Service der Bundesanstalt für Wasserbau

Doctoral Thesis, Published Version

Mucha, Philipp

On Simulation-based Ship Maneuvering Prediction in Deep and Shallow Water

---

Verfügbar unter/Available at: https://hdl.handle.net/20.500.11970/105067

Vorgeschlagene Zitierweise/Suggested citation:
Mucha, Philipp (2017): On Simulation-based Ship Maneuvering Prediction in Deep and Shallow Water.

Standardnutzungsbedingungen/Terms of Use:

Die Dokumente in HENRY stehen unter der Creative Commons Lizenz CC BY 4.0, sofern keine abweichenden Nutzungsbedingungen getroffen wurden. Damit ist sowohl die kommerzielle Nutzung als auch das Teilen, die Weiterbearbeitung und Speicherung erlaubt. Das Verwenden und das Bearbeiten stehen unter der Bedingung der Namensnennung. Im Einzelfall kann eine restriktivere Lizenz gelten; dann gelten abweichend von den obigen Nutzungsbedingungen die in der dort genannten Lizenz gewährten Nutzungsrechte.

Documents in HENRY are made available under the Creative Commons License CC BY 4.0, if no other license is applicable. Under CC BY 4.0 commercial use and sharing, remixing, transforming, and building upon the material of the work is permitted. In some cases a different, more restrictive license may apply; if applicable the terms of the restrictive license will be binding.

BY NC ND

On Simulation-based Ship Maneuvering Prediction in Deep and Shallow Water

Von der Fakultät für Ingenieurwissenschaften, Abteilung Maschinenbau
und Verfahrenstechnik
der
Universität Duisburg-Essen
zur Erlangung des akademischen Grades
eines
Doktors der Ingenieurwissenschaften
Dr.-Ing.
genehmigte Dissertation

von

Philipp Mucha
aus
Duisburg

Gutachter: Univ.-Prof. Dr.-Ing. Bettar Ould el Moctar
Univ.-Prof. Ph.D. Paul D. Sclavounos
Tag der mündlichen Prüfung: 09.01.2017

Abstract

A simulation-based framework for the prediction of ship maneuvering in deep and shallow water is presented. A mathematical model for maneuvering represented by coupled nonlinear differential equations stemming from Newtonian mechanics is derived. Hydrodynamic forces are modeled by multivariat polynomials, and therein included are coefficients representing ship-specific hydrodynamic properties which are determined by way of captive maneuvering tests using Computational Fluid Dynamics (CFD). The development and evaluation of efficacy of the proposed framework encompasses verification and validation studies on numerical methods for maneuvering and flows around ships in shallow water. The flow field information available from numerical simulations are used to discuss hydrodynamic phenomena related to viscous and free surface effects, as well as squat.

Kurzfassung

Ein Verfahren zur simulationsbasierten Vorhersage der Bewegungen von Schiffen beim Manövrieren in tiefem und flachem Wasser wird vorgestellt. Für diesen Zweck wird ein mathematisches Modell formuliert, das unter Anwendung Newton'scher Mechanik durch gekoppelte nichtlineare Differentialgleichungen repräsentiert wird. Hydrodynamische Kräfte werden durch multivariate Polynome beschrieben, deren schiffspezifische Koeffizienten hydrodynamische Eigenschaften darstellen, die auf Basis der numerischen Lösung der Navier-Stokes Gleichungen bestimmt werden. Die Grundlage des vorgestellten Verfahrens zur Parameteridentifikation bilden gefesselte Manövrierversuche auf idealisierten Bahnverläufen. Gegenstand der Entwicklung des simulationsbasierten Verfahrens sind Untersuchungen zur Verifikation und Validierung der numerischen Methode, sowie die Diskussion der Hydrodynamik von Schiffsumströmungen bei geringer Kielfreiheit. Dazu zählen der Einfluss von Viskosität, schiffsinduzierte Änderungen der Wasseroberfläche und Änderungen der Schwimmlage infolge von Squat.

Acknowledgments

I am grateful of the support associated with this work from Professor Bettar el Moctar. I acknowledge his guidance, collaboration and critical reflection on my work, which have been of great help in conducting the presented research. Besides, I am thankful for the funding and support of research activities associated with this thesis from the Federal Waterways Engineering and Research Institute (Bundesanstalt für Wasserbau, BAW) and Thorsten Dettmann of BAW. Special acknowledgments are referred to Professor Paul D. Sclavounos of MIT, with whom I discussed dedicated problems centered on ship hydrodynamics during my graduate studies, which have benefited my work and which became a valuable asset for my research. I acknowledge the provision of experimental data by organizations referenced in the thesis. I benefited from a number of discussions along the way. I express particular appreciation for the collaboration with Thomas Schellin, Olav Rognebakke and Alexander von Graefe of DNV GL, Ganbo Deng of École Centrale de Nantes and Tim Gourlay of Curtin University. I appreciate discussions about - and beyond - engineering with my fellow student Max Montenbruck. First and foremost, I thank my family for their great support.

Contents

List of Figures

List of Tables

Notation

α	Inflow angle
α_i	Volume fraction, $i = 1, 2, ...N$
β	Drift angle
$\boldsymbol{\Omega}$	Vector of rotational velocities
$\boldsymbol{\tau}$	Viscous shear stress tensor
δ	Rudder angle
ϵ_P	Propeller advance angle
γ	Yaw reference angle
Γ_t	Diffusion coefficient
κ	Von Kármán's constant
Λ	Geometric rudder aspect ratio
λ	Scale factor
$\mathbf{b}$	Vector of body forces per unit mass
$\mathbf{H}$	Moment of momentum
$\mathbf{I}$	Unit matrix
$\mathbf{M}$	Vector of hydrodynamic forces
$\mathbf{M}$	Vector of hydrodynamic moments
$\mathbf{n}$	Face normal vector
$\mathbf{r}_g$	Vector of distances to the center of gravity
$\mathbf{T}$	Stress tensor
$\mathbf{T}_i$	Transformation matrices, $i = 1, 2$
$\mathbf{V}$	Vector of translational velocities
μ	Dynamic viscosity
ν	Kinematic viscosity
ω	Frequency
ϕ	Roll angle
Ψ	Course angle
ψ	Yaw angle
ρ	Fluid density
σ_ϕ	Turbulent Schmidt number
τ_w	Wall shear stress
θ_p	Circumferential propeller orientation angle
ϑ	Pitch angle
ζ	Free surface elevation
a_{ij}	Component of added mass tensor, $i, j = 1, 2, ...6$
A_R	Rudder area
A_W	Waterline area

B	Ship breadth
c_B	Block coefficient
c_D	Drag coefficient
C_{fl}	Courant number
c_F	Friction resistance coefficient
c_i	Hull lift coefficient, $i = 1, 2$
c_L	Lift coefficient
c_P	Pressure coefficient
c_Q	Induced-drag coefficient
c_{TH}	Propeller load coefficient
c_T	Total resistance coefficient
c_W	Wave resistance coefficient
d_i	Hull lift coefficient, $i = 1, 2$
D_P	Propeller diameter
e_i	Hull lift coefficient, $i = 1, 2$
F	Generalized force component
$F_{n,h}$	Froude depth number
F_n	Froude number
G	Rankine source
g	Gravitational acceleration constant
h	Water depth
I_{xwl}	Waterline second moment of area
I_x	Moment of inertia with respect to x-axis
I_y	Moment of inertia with respect to y-axis
I_z	Moment of inertia with respect to z-axis
J	Advance number
K	Hydrodynamic roll moment
k	Form factor
K_Q	Propeller torque coefficient
K_T	Propeller thrust coefficient
L	Ship length between perpendiculars
l_r	Lever arm of the hydrodynamic yaw damping force
l_v	Lever arm of the hydrodynamic sway damping force
M	Hydrodynamic pitch moment
m	Ship mass
N	Hydrodynamic yaw moment
n	Propeller rate of revolution
p	Roll velocity
$P_{0.7}$	Propeller pitch at $0.7r_p$
Q	Torque
q	Pitch velocity
R	Resistance
r	Yaw velocity
R^2	Coefficient of determination
r_h	Propeller hub radius
r_p	Propeller radius

R_q^k	Normalized residual
Re	Reynolds number
S	Control volume surface area
S_W	Wetted surface area
T	Thrust
t	time
T_m	Ship mean draft
U	Ship speed
u	Longitudinal velocity
U_P	Propeller inflow speed
V	Volume
v	Transverse velocity
W	Local cross-flow
w	Vertical velocity
X	Longitudinal hydrodynamic force
x	Longitudinal coordinate
X_{xwl}	Center of waterline area
Y	Transverse hydrodynamic force
y	Transverse coordinate
y^+	Nondimensional wall distance
Z	Vertical hydrodynamic force
z	Vertical coordinate

1. Introduction

The prediction of maneuverability is a classic problem in ship hydrodynamics. Likewise, ship motions in restricted waters have been studied for a long time. In the open sea, where the major part of ship journeys takes place, the focus lies on the prediction of propulsion characteristics and wave-induced motions in stochastic environments. Ship maneuvering, however, is relevant in coastal areas and harbor approaches, where space is limited, traffic heavier, and where hydrodynamic interaction effects are present, increasing hazards. The renewed attention referred to maneuvering prediction in general, and its extension to restricted waters in particular, is attributable to three trends. First, ships are becoming bigger in size while existing waterways are not growing at the same pace. Consequently, waterway administrations are strongly interested in ship motion predictions in the context of the entering of ports and channel systems. Further incentives emerge from the application of ship handling simulators, which widely come into operation for training of nautical staff, but which are increasingly being used for navigability analyses too. Such investigations require accurate modeling of ship motions and validation of simulations. Second, a novel regulatory framework following the call for green shipping brings attention to minimum power requirement estimation to ensure safe and economic ship operation in adverse conditions. In light of an expected trend towards an overall decrease in power installation, predictions of wave and shallow water impacts on maneuvering performance are needed for the design of efficient and safely operable ships. Third, numerical methods and computational resources have advanced to turn simulation-based analyses of ship flows into a competitive alternative to experiments. While models for ship maneuvering in shallow water have been proposed and investigated based on experimental fluid dynamics, little is known about the performance and reliability of entirely simulation-based methods. The complexity of the task rests with the modeling of turbulence, free surface effects and rigid body motions. Among the latter particular attention is directed to ship squat. Computational Fluid Dynamics (CFD) is meanwhile applicable to a host of problems in ship hydrodynamics, including maneuvering. The solution of the Reynolds-averaged Navier-Stokes (RANS) equations is the predominate choice for CFD applications in ship hydrodynamics. Yet, the need exists for further assessment of reliability, especially for shallow water problems. Notwithstanding the advance of CFD, potential flow methods still embody a valuable and cost-efficient tool for hydrodynamic analyses. Against the background of an anticipated increasing relevance of viscous effects in restricted water it is desirable to explore performance, prospects and limitations of such numerical methods.

1.1 State of the art in ship maneuvering prediction

The study of ship maneuverability started with the invention and use of surface vessels, because ship pilots and designers were interested in the response characteristics to commanded changes of the direction of ship motions, which ties in with the fundamental definition of maneuvering given in the Principles of Naval Architecture (PNA), Mandel (1965) and Crane et al. (1989). Over millennia the role of ships in trade, transport, warfare and leisure has continuously become more important; and so did the interest in performance estimation and improvement increase. A compact summary of the scientific dedication to the problem of maneuverability analysis up to the mid-1960s is given in Newman (1966). A more comprehensive treatment of the recent history of related research can be found in Sutulo and Guedes Soares (2011). Practical aspects of ship maneuverability are abundantly covered by Brix (1993). A notable work towards the formulation of mathematical models for maneuvering prediction is presented in Davidson and Schiff (1946), who derived a linear framework of ship maneuvering equations of motion in the horizontal plane. Nomoto et al. (1957) discussed a model for dynamics in yaw, which has widely been applied to heading control problems. Successive investigations and developments towards nonlinear extensions are related to Norrbin (1960) or Wagner-Smith (1971). An important contribution to the mathematical modeling of maneuvering is referred to Abkowitz (1964), who formulated maneuvering equations in six degree-of-freedom (DoF) based on modified Taylor-series expansions of functionals of hydrodynamic forces. Such models use multivariat algebraic polynomials to account for dependencies of forces on rigid body motions and control surface variables and involve a host of coefficients describing hydrodynamic properties. Above introduced ideas of Abkowitz (1964) received great attention in the hydrodynamic community with the introduction of mechanic oscillators at experimental facilities, which started at David Taylor Model Basin (DTMB), Gertler (1959), Goodman (1966). Such devices, which came to be called Planar Motion Mechanisms (PMM), enabled prescribed and captive motions of ship models in towing tanks, which could be used to study motions relevant for maneuvering, e.g. pure sway or pure yaw oscillations. Evaluation of such tests with respect to identification of maneuvering coefficients is covered in Strøm-Tejsen and Chislett (1966). A facility for planar motion testing of ship models arose in Hamburg, Germany, in the context of the joint research pool for shipbuilding, designated Sonderforschungsbereich Schiffbau 98 (SFB 98), Grim et al. (1976). The particular device installed was a Computerized Planar Motion Carriage (CPMC), which enabled large amplitude motions with high precision in trajectory prescription and measurement. Main contributions to mathematical modeling of maneuvering within SFB 98 relate to Oltmann and Sharma (1984) and Wolff (1981). Oltmann (1978), Oltmann and Wolff (1979) and Wolff (1981) discussed the operation of the CPMC for captive and free-running maneuvering tests and synchronization of results for system identification of maneuvering models. Fedajevski and Sobolev (1964) discussed the modeling of hydrodynamic damping forces by second-order modulus functions based on the hydrodynamic drag concept, which was later extended by Hooft (1994). Widely referenced contributions refer to the Japanese Maneuvering Modeling Group (JMMG, Ogawa, 1977), e.g. Inoue (1981), Yasukawa and Yoshimura (2014). Models proposed by JMMG draw upon decomposed formulations of force effects and application of experiments, theory and empirics to identify emerging maneuvering coefficients. The use of slender-body theory in the ship maneuvering context is covered by Newman (1978) and Söding (1982c). Important theoretical contributions on consideration of time-dependent modeling of ship motions accounting for fluid memory effects were made by Cummins (1962) and Ogilvie (1964). A broad overview of established maneuvering models tailored to different application domains is given in Fossen (2011). Full-scale maneuvering sea trials have been the method of choice to analyze maneuvering performance in absence of computational methods and experiments and are practically relevant for maneuvering criteria by the International Maritime Organisation (IMO), MSC 137(76) (2002). Published reports including results for validation purposes for the Mariner standard ship and a tanker relate to Morse and Price (1961) and Ogawa (1971). The advance of computational methods and the increase in computational power enabled numerical studies into ship flows around maneuvering ships using CFD. While initially valuable insight into steady drift and yaw motions, as well as rudder forces was gained, Sato (1998) and el Moctar (2001a, 2001b), such methods were soon able to replicate captive model tests, and it became feasible to derive maneuvering coefficients with CFD, Cura-Hochbaum (2006). Applications to maneuvering prediction in deep water were verified and validated in the SIMMAN workshop, Stern et al. (2011). Primary investigations were confined to double-body flows. More complex cases involving the modeling of the free surface and ship motions were dealt with preliminary only in deep water conditions. Recently, direct CFD simulations of rudder maneuvers were performed, which model the appended hull geometry and resolve ship motions transiently, using available numerical techniques for consideration of propeller and rudder motions. These simulations are time-consuming and rendered infeasible for parametric investigations. Only few publications are available, Carrica et al. (2013), Mofidi and Carrica (2014), el Moctar et al. (2014). A general evaluation of capabilities and prospects of CFD can be found in Larsson and Bertram (2003) and Larsson et al. (2013). A regular survey of related research activities is done by the Maneuvering Committee of the International Towing Tank Conference (ITTC, 2014).

1.2 State of the art in ship hydrodynamics in restricted waters

Weinblum (1934), Brard (1951), Schuster (1952) and Silverstein (1957) addressed the issue of ship motions in shallow water relatively early compared to the treatise of maneuvering in deep water. Prediction of shallow water effects on forward motion, involving the change in ship resistance and consideration of squat, was notably dealt with by Kreitner (1934), Havelock (1939) and Thews and Landweber (1935). The summary of Tuck (1978) is a comprehensive dedication to ship hydrodynamic problems encountered in restricted waters. The attention in research was mainly drawn to the prediction of ship-induced shallow water waves, the formulation of forces on the hull in presence of vertical and lateral restrictions and consequences for ship motions. Shallow water ship waves were studied by Chen (1999), Chen and Sharma (1995), Sharma and Chen (2000) and Jiang (2003) using depth-averaged flow equations of Boussinesq-type. Notable contributions in conjunction with ship-induced shallow water waves also relate to Li and Sclavounos (2002) and Alam and Mei (2008). In response to parallel developments and better understanding of slender-body theory for the formulation of ship motions in deep water, Tuck (1963, 1966, 1967) and Tuck and Taylor (1970) studied the extension of the mathematical framework to finite water depth. Newman (1969), Beck et al. (1975), Beck (1977), Breslin (1972) and Norrbin (1971) studied forces on ships in channels using slender-body theory. Zhao (1986) presented related applications to ship maneuvering in shallow water and included comparisons to experimental studies by Fujino (1968, 1972, 1984). Interaction effects with banks and ships are addressed in Tuck and Newman (1978), who developed formulations of the sway force and yaw moment for two bodies moving on a parallel path for the shallow and deep water case, and Yeung (1978). Söding (2005) presented the study of overtaking maneuvers with panel methods, which are extended in von Graefe (2015). Straight line stability and control related problems in restricted waters leaning on hydrodynamic analysis with a Rankine panel method were discussed in Thomas and Sclavounos (2006). Norrbin (1971) discussed consequences of finite water depth for mathematical models for maneuvering. Inoue (1969) studied linear and nonlinear lifting theory applied to flows around ships in shallow water on the basis of the ideas presented in Bollay (1936). Systematic experimental investigations on the influence of water depth and consequences for various mathematical maneuvering models were performed by Fujino (1968) and Gronarz (1993, 1997). Experimental studies on ship-ship interaction and bank-effects were performed by Vantorre et al. (2002), Eloot and Vantorre (2009) and Lataire and Vantorre (2008). Eloot et al. (2015) and Tonelli and Quadvlieg (2015) reported on efforts of validation of shallow water maneuvering simulations through free-running experiments. The prediction of squat is of paramount importance in under-keel clearance (UKC) management for ships and has been receiving great attention in the hydrodynamic community. Definition of terminology is provided by Tuck (1978). Gourlay (2000, 2001, 2006, 2008, 2011) applied Tuck's theories to a host of squat problems. Millward (1992) summarized theoretical and empirical squat prediction methods. Graff et al. (1964) discussed a detailed study on squat prediction through model experiments. Early application of CFD to lifting flows in shallow water was confined to inviscid or double-body simulations, neglecting both free surface disturbances and squat, e.g. Gronarz (1997). Deng et al. (2014) represents a relevant contribution with respect to the reliability of CFD for application to squat and resistance predictions. Comparing investigations of different numerical methods are found in Mucha and el Moctar (2014) and Mucha et al. (2014, 2016). A review of activities in the field is found in regular reports of the Manoeuvring Committee of ITTC and the proceedings of the International Conference on Ship Manouevring in Shallow and Confined Waters (MASHCON), e.g. Eloot and Vantorre (2009). Applications of CFD to flows around ships in shallow water have recently been addressed at MASHCON, Uliczka et al. (2016).

1.3 Objectives and organization of the thesis

The thesis at hand aims to assess the capabilities of a simulation-based framework for the prediction of rudder maneuvers in deep and shallow water. It is organized according to three objectives. In a first step, a review of relevant established approaches to the modeling of hydrodynamic forces in the maneuvering equations of motion was conducted. Particular attention was referred to coefficient-based mathematical models, which are represented mathematically by a set of coupled nonlinear differential equations in the framework of Newtonian mechanics, and which draw upon the formulation of hydrodynamic forces in maneuvering through multivariat polynomials. The specific formulation of the model structure for the purposes of this thesis included the discussion and formulation of suitable parameter identification procedures for the emerging hydrodynamic coefficients. The parameter identification method leaned on the performance of captive maneuvering tests on idealized trajectories. Taking the perspective of the early stage of ship design, when generally no experimental data is available, such motivated simulation methods allow systematic variations of water depth and synchronization with underlying mathematical models and require only a three-dimensional virtual, geometric representation of the ship. In a second step, the performance and reliability of a RANS-based CFD method for parameter identification was assessed through comparison with experiments. Special emphasis was laid on ship-induced free surface disturbances and the prediction of the decrease of UKC through dynamic sinkage and trim (squat), which was expected to be important for the computation of forces and moments on maneuvering ships in shallow water. Comparison was drawn to other numerical methods for hydrodynamic analyses. In a third step, above framework was applied to maneuvering prediction on shallow water for a candidate ship and compared to available time responses of free-running maneuvering experiments with scale models.

2. Theory of Ship Maneuvering and Mathematical Modeling

This chapter introduces ship maneuverability and maneuvering theory constituting the basis for the development of the simulation-based maneuvering prediction framework. The discussion of maneuverability includes a general definition, presentation of maneuvering requirements and established methodology for evaluation purposes. Equations of motion of maneuvering ships are formulated through application of classic Newtonian mechanics for rigid bodies. The problem of modeling hydrodynamic forces in maneuvering is introduced. The discussion starts with deep water conditions and related established concepts. Following a general treatise of hydrodynamic effects on maneuvering in shallow water, these concepts are scrutinized in terms of their capabilities to take mathematical account of these effects. Special attention is given to multivariat polynomial models. Suitable parameter identification procedures are addressed.

2.1 Definitions and frames of reference

An earth-fixed inertial reference frame $Ox_Oy_Oz_O$, defined by origin O and right-handed Cartesian axes x_O, y_O, z_O, is introduced. Origin O is located at the calm water level. Axes x_O and y_O are mutually perpendicular in the horizontal plane and z_O points downwards.

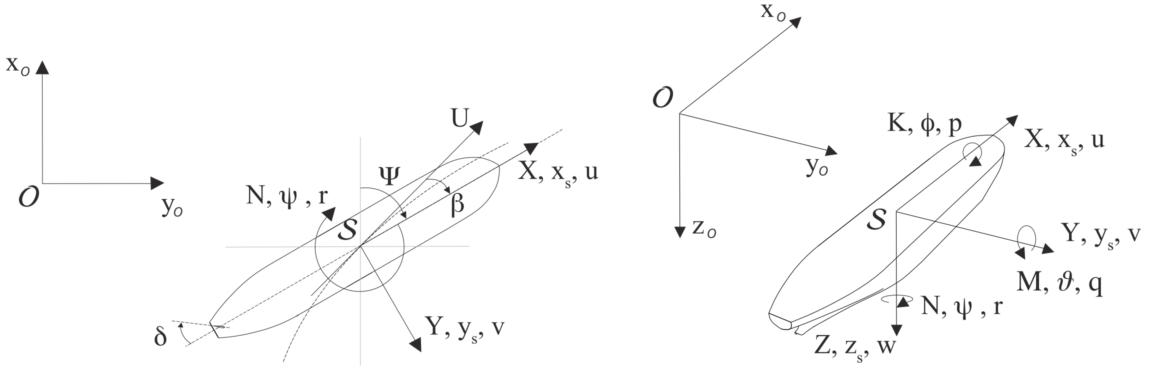

Figure 2.1: Coordinate systems for ship maneuvering in the horizontal plane (l.h.s.) and general conventions for kinematics, forces and moments in six-DoF (r.h.s.).

Additionally, a body-fixed reference frame $\mathcal{S}xyz$, defined by origin $\mathcal{S}$ and right-handed Cartesian axes x, y, z, is used. Axis x points into the ship's forward direction, lays in the xy-plane of symmetry and coincides with the calm waterline. Axis y points positively to starboard and axis z positively downward. Generalized coordinates of the ship are Cartesian coordinates x_O, y_O, z_O in the earth-fixed frame, with generalized velocities $\mathbf{V}_O = [\dot{x_O}, \dot{y_O}, \dot{z_O}]^T$, and with Eulerian angle[a] orientation ϕ (around x-axis), θ (around y-axis) and ψ (around z-axis). Angular velocities are part of vector $\mathbf{\Omega}_O = \left[\dot{\phi}, \dot{\theta}, \dot{\psi}\right]^T$. In maneuvering theory, it is common practice to use the projections of instantaneous ground velocity vector $\mathbf{V} = [u, v, w]^T$ and angular velocity vector $\mathbf{\Omega} = [p, q, r]^T$ onto the ship-fixed reference frame $\mathcal{S}xyz$. The transformation between the reference systems consequently follows as per

$$\begin{bmatrix} \mathbf{V_O} \\ \mathbf{\Omega_O} \end{bmatrix} = \begin{bmatrix} \mathbf{T_1} & 0 \\ 0 & \mathbf{T_2} \end{bmatrix} \begin{bmatrix} \mathbf{V} \\ \mathbf{\Omega} \end{bmatrix} \tag{2.1}$$

where

$$\mathbf{T_1} = \begin{bmatrix} c_\psi c_\theta & c_\psi s_\theta s_\phi - s_\psi c_\phi & c_\psi s_\theta c_\phi + s_\psi s_\phi \\ s_\psi c_\theta & s_\psi s_\theta s_\phi + c_\psi c_\phi & s_\psi s_\theta c_\phi - c_\psi s_\phi \\ -s_\theta & c_\theta s_\phi & c_\theta c_\phi \end{bmatrix} \tag{2.2}$$

$$\mathbf{T_2} = \begin{bmatrix} 1 & s_\phi \tan\theta & c_\phi \tan\theta \\ 0 & c_\phi & -s_\phi \\ 0 & \frac{s_\phi}{c_\theta} & \frac{c_\phi}{c_\theta} \end{bmatrix} \tag{2.3}$$

and $c_\phi = \cos\phi$, $c_\theta = \cos\theta$, $c_\psi = \cos\psi$ and $s_\phi = \sin\phi$, $s_\theta = \sin\theta$, $s_\psi = \sin\psi$. Consistent with Fig. 2.1, instantaneous ship speed U in the xy-plane (w=0) is defined as

$$U = \sqrt{u^2 + v^2} \tag{2.4}$$

and ship heading Ψ is related to the horizontal orientation of the ship with respect to $O x_O y_O$. Drift angle β is given by

$$\beta = \arcsin\left(v / - u\right) \tag{2.5}$$

Rudder deflection angle is δ. UKC is the distance from the ship keel at draft T to the vertical flow restriction at water depth h, Fig. 2.2. Ship squat is defined as the decrease

---

[a] The well-known Gimbal lock associated with the inability of the Euler angles to describe arbitrary rotations due to topological constraints does not affect the present problem, because of the physically confined range of values the Euler angles take for maneuvering surface ships.

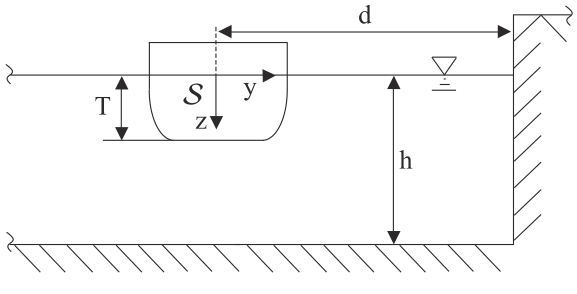

Figure 2.2: Definition of ship dimensions and associated notation in restricted water.

of UKC in response to pressure variations along the ship hull underway, which cause the ship to adjust her dynamic floating position in terms of a vertical translation (sinkage) and a rotational displacement in pitch mode of motion (trim), accompanied by a change of the ambient free water surface level. The six-DoF hydrodynamic forces and moments are denoted by X, Y, Z, K, M, N, Fig. 2.1. In straight ahead motion, ship resistance R_T equals the negative longitudinal hydrodynamic force X. Following common practice in ship hydrodynamic analysis, results are presented in nondimensional form, where appropriate. Nondimensional quantities are furnished with a prime, e.g. u'. Basic quantities for nondimensionalization, if not stated otherwise, are water density ρ, ship speed U, and ship length between perpendiculars L. For a generalized force component F it follows

$$F' = \frac{F}{0.5\rho U^2 L^2} \tag{2.6}$$

and for a generalized moment M with L as the characteristic length

$$M' = \frac{M}{0.5\rho U^2 L^3} \tag{2.7}$$

Rigid body velocities are made nondimensional as per

$$u' = \frac{u}{U}; \qquad v' = \frac{v}{U}; \qquad r' = \frac{rL}{U} \tag{2.8}$$

Further, propeller advance number J is introduced as per

$$J = \frac{U_p}{nD_p} \tag{2.9}$$

where U_p is propeller inflow velocity, see Eq. (2.49) , n propeller rate of revolution and D_p propeller diameter. For ease of comparison with relevant references, therein established notation for particular expressions is adopted. This tangibly affects the notation for hydrodynamic forces, moments and rigid body velocities, i.e.

$$F_2 \equiv Y, M_3 \equiv N, V_1 \equiv u, V_2 \equiv v, \Omega_3 \equiv r$$

The established notation of Imlay (1961) denotes entries of the added mass tensor a_{ij} as given in Newman (1978), see Eq. (2.25), by variables of hydrodynamic forces carrying indices of respective rigid body accelerations or velocities, e.g. $a_{11} \equiv X_{\dot{u}}$, $a_{22} \equiv Y_{\dot{v}}$.

2.2 Maneuverability assessment

Ship maneuverability concerns dynamic response characteristics of ships to commanded changes in direction of travel or speed through theur control surfaces, Newman (1966). Conventional control surfaces are rudders, propellers and fins. Bow and stern thrusters, as well as azimuthal pod-driven thrusters represent unconventional maneuvering devices. Maneuverability requirements refer to course, lane, or speed changing and keeping, as well as to positioning. Maneuverability is rated based on the costs employed to meet these requirements, e.g. the time to complete a maneuver, applied control effort or change of forward speed in response to maneuvering. Conventionally, these properties are checked in sea trials with appropriate standard maneuvers. Associated guidelines and recommendations are issued by IMO (2002) and the maneuvering trial code of ITTC (1975). IMO's criteria are non-binding, but the display of a poster on-board ships informing about general maneuvering properties is mandatory, IMO (1987). Sea trials represent the real system behavior free of scale effects or model assumptions, which are encountered in model experiments and simulation-based predictions. On other hand, environmental conditions like winds, waves or currents impair the assessment of calm water maneuverability. Sea trials are also infeasible in the early stage of new ship designs in absence of sister ships, which emphasizes the need for alternative prediction methods. A host of standard maneuvers is available to study maneuverability. For the particular purpose of validation studies for benchmarking of different prediction methods turning and zig-zag maneuvers have been established in the hydrodynamic community. Hard-rudder turning maneuvers involve large-amplitude motions in sway and yaw, including excitations of nonlinear effects , while zig-zag maneuvers offer valuable insight into the flow when control surfaces are dynamically varied in sign. The experimental analysis of maneuverability in shallow water through maneuvering trials is impaired, because it is hard to find a test region with the desired uniform water depth. According to the Permanent International Association of Navigation Congresses (PIANC, 1992) extreme shallow water condition is present for water depth to draft ratio $h/T \leq 1.2$, Fig. 2.2. If UKC is in the order of anticipated squat for practically relevant forward speeds, ship operation has inevitably to be adapted to prevent grounding. In laterally restricted waters, ship-induced wave loads on banks influence the choice of appropriate forward speeds. Apart from these special problems, in any restricted water, increasing hydrodynamic forces in all modes of motion are causative to the increased response time to commanded changes in horizontal motion, as will be addressed further down the line. Typical forward speeds of sea-going vessels with drafts in the order of 7 m (e.g. Feeders) to 20 m (e.g. Very Large Crude Carriers) lay between 6 and 10 kts in presence of UKC of 20% of ship draft. These operational facts will be shown to affect the mathematical modeling of maneuvering in confined waters, too.

2.2.1 Zig-zag maneuver

Zig-zag maneuvers start from straight ahead approach at constant speed. The rudder is deflected to a desired angle. Typical values are 10°, 20° or 35°. Upon the desired change of heading $\Delta\Psi_e$ counter-rudder is applied until the same course change $\Delta\Psi_e$ with respect to the initial course is reached in the opposite direction, Fig. 2.3. Typical values are 10° or 20°. This procedure is repeated for an appropriate number of runs. The test gives initial turning time t_{as}, yaw checking time t_s, overshoot angles to starboard α_s and port side α_p. Upon initiation of the maneuver through deflection of the rudder, the ship enters a turning motion with increasing rate of turn and transverse velocity, attaining a drift angle in the direction of turning. Forward speed decreases in response to increased resistance through the deflection of the rudder and damping effects associated with the attained lifting flow. Upon application of counter-rudder, the rate of turn reaches its maximum and is decreased thereafter, still turning the ship into the same direction, until the rate of turn becomes zero and the change in actual heading reaches its maximum. The difference to prescribed change of heading $\Delta\Psi_e$ is the overshoot angle. The gradual decrease in rate of

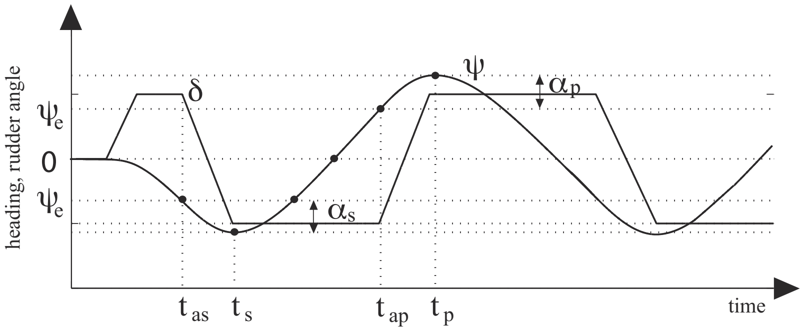

Figure 2.3: Schematic of a zig-zag maneuver and definition of relevant information.

turn is attributable to inertia, whereas hydrodynamic damping dominates the speed of its decay. Above procedure will take place repeatably into the other heading direction, not necessarily in symmetric fashion due to possible constant disturbances present at forward motion in sway and yaw.

2.2.2 Turning maneuver

Turning maneuvers start from straight ahead approach at constant speed. The rudder is deflected to either port or starboard to a desired angle and kept constant until a prescribed number of turning circles is completed and until the yaw rate has settled to a constant value. Usually, turning maneuvers are terminated with a pull-out, i.e. applying zero rudder angle. The test provides the longitudinal distance traveled at 90° course change $x_O(\Delta\psi = 90°)$, called advance, the lateral distance traveled at 90° course change $y_O(\Delta\psi = 90°)$, called transfer, and the lateral distance traveled at 180° course change $y_O(\Delta\psi = 180°)$, which is the tactical diameter, Fig. 2.4. Upon initiation of the turning maneuver through deflection of the rudder, the ship enters a turning motion with increasing rate of turn and transverse velocity, attaining a drift angle in the direction of turning. Forward speed decreases in response to increased resistance through the deflection of the rudder and damping effects associated with the attained lifting flow. Depending on damping characteristics of the hull the rate of turn can experience an overshoot before settling to a constant value in the attained steady turning motion.

2.2.3 Spiral test

Important insight into maneuvering behavior is revealed in spiral tests, where the application of a range of rudder angles is investigated in terms of the steady state turning rate response. Spiral tests enable a broad evaluation of turning performance and yaw stability. In particular, they provide characteristic plots of steady turning rate r over rudder angle δ, which reveal the associated input passivity behavior of the ship, Fig. 2.5. Input passivity refers to the property of a dynamic system to yield only a single output for each given input. A non-input passive system thus shows a hysteresis loop in the input-output plot.

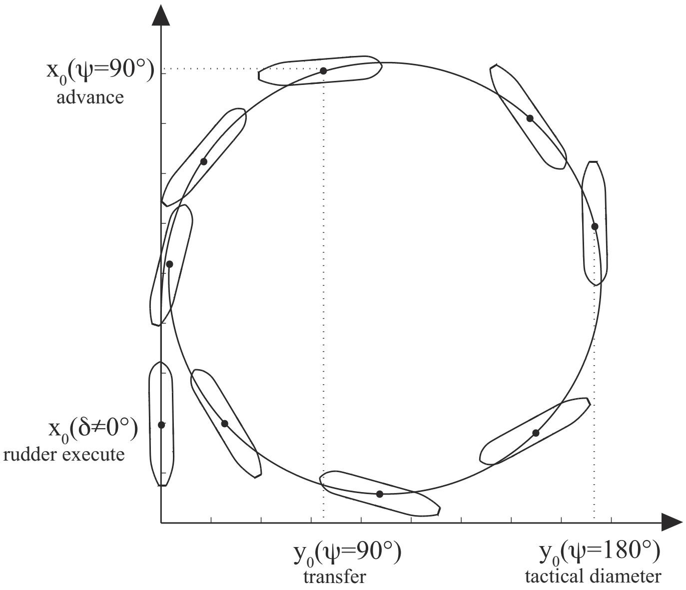

Figure 2.4: Schematic of a turning maneuver and definition of relevant information.

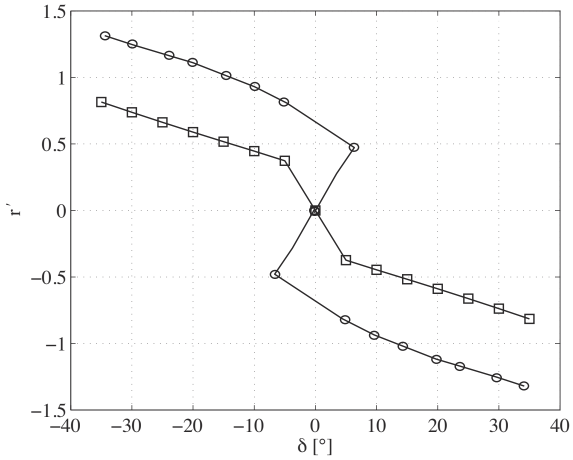

Figure 2.5: Spiral test results showing *r* against *δ* for a ship with input passivity (squares) and a ship without input passivity (circles).

2.3 Maneuvering prediction

For simulation-based predictions and analyses of maneuvering a mathematical system description is required. In developing a mathematical framework for maneuvering prediction it is assumed that ship shape, mass and mass distribution do not change in time. Consistent with this notion classic rigid body dynamics apply. The inertial response characteristics of ships are available from mechanics, while the sum of external forces and moments is unknown. Formulations of hydrodynamic forces embracing all known flow phenomena, amenable to solution within short time, are not available. Difficulties in modeling hydrodynamic forces for maneuvering ships are related to the influence of viscosity and ship-induced free surface disturbances. The constitution of a model structure depends on the application domain. Compared to the simulation of arbitrary ship motions involving different engine settings, reduction in complexity and parameter identification effort are possible for the prediction of rudder maneuvers for a given engine operational condition. A mathematical description for inertial response characteristics is obtained from Newtonian mechanics. The conservation of momentum is postulated by Newton's Second Law:

$$\mathbf{F} = m\frac{d}{dt}\left(\mathbf{V}_O + \mathbf{\Omega}_O \times \mathbf{r_g}\right) \tag{2.10}$$

where $\mathbf{F} = [X, Y, Z]^T$ is external force vector and t is time. Distances to the center of gravity (CoG) in the ship-fixed system are given by $\mathbf{r_g} = \left[x_g, y_g, z_g\right]^T$. Eq. (2.10) is valid, if Coriolis and centripetal effects due to the rotation of the earth are neglected. Conservation of moment of momentum $\mathbf{H}$ satisfies

$$\mathbf{M} = \frac{d}{dt}\mathbf{H} + \mathbf{r_g} \times m\frac{d}{dt}\left(\mathbf{V}_O + \mathbf{\Omega}_O \times \mathbf{r_g}\right) \tag{2.11}$$

where $\mathbf{M} = [K, M, N]^T$ is external moment vector. Following vector algebraic analysis and rearrangement of terms it follows in component notation for the six-DoF rigid body ship maneuvering equations of motion

$$\begin{aligned}
m[\dot{u} - vr + wq - x_g(q^2 + r^2) + y_g(pq - \dot{r}) + z_g(pr + \dot{q})] &= X && (2.12)\\
m[\dot{v} - wp + ur - y_g(r^2 + p^2) + z_g(qr - \dot{p}) + x_g(qp + \dot{r})] &= Y && (2.13)\\
m[\dot{w} - uq + vp - z_g(p^2 + q^2) + x_g(rp - \dot{q}) + y_g(rq + \dot{p})] &= Z && (2.14)\\
I_x\dot{p} + (I_z - I_y)qr - (\dot{r} + pq)I_{xz} + (r^2 - q^2)I_{yz} + (pr - \dot{q})I_{xy} & && \\
+m[y_g(\dot{w} - uq + vp) - z_g(\dot{v} - wp + ur)] &= K && (2.15)\\
I_y\dot{q} + (I_x - I_z)rp - (\dot{p} + qr)I_{xy} + (p^2 - r^2)I_{zx} + (qp - \dot{r})I_{yz} & && \\
+m[z_g(\dot{u} - vr + wq) - x_g(\dot{w} - uq + vp)] &= M && (2.16)\\
I_z\dot{r} + (I_y - I_x)pq - (\dot{q} + rp)I_{yz} + (q^2 - p^2)I_{xy} + (rq - \dot{p})I_{zx} & && \\
+m[x_g(\dot{v} - wp + ur) - y_g(\dot{u} - vr + wq)] &= N && (2.17)
\end{aligned}$$

where moments of inertia about axes in $\mathcal{S}xyz$ are

$$I_x = \sum_i \left(y_i^2 + z_i^2\right)m_i; \qquad I_y = \sum_i \left(x_i^2 + z_i^2\right)m_i; \qquad I_z = \sum_i \left(x_i^2 + y_i^2\right)m_i \tag{2.18}$$

In Eq. (2.18), x_i, y_i, z_i are Cartesian coordinates of discrete mass points m_i Products of inertia follow as per

$$I_{xy} = I_{yx} = \sum_i x_i y_i m_i; \qquad I_{xz} = I_{zx} = \sum_i x_i z_i m_i; \qquad I_{yz} = I_{zy} = \sum_i y_i z_i m_i \tag{2.19}$$

If axis through $\mathcal{S}$ are principal axes of inertia, terms involving products of inertia vanish. For a host of maneuvering prediction purposes, motions in heave, pitch and roll can be neglected, because they do not affect motions in the horizontal plane. Roll becomes relevant in maneuvering for ships with flared lines traveling at high forward speeds, e.g. containerships entering hard-rudder maneuvers. Yasukawa and Yoshimura (2014) present a detailed investigation into the effect of roll motions on maneuvering. Operational conditions in shallow water do usually not excite significant roll motions. However, in drift motions at low UKC low-pressure fields can be generated on the leeward side in the bilge region. The particular role of heave and pitch in the modeling of maneuvering in shallow water is central to Chapter 2.5. The transverse CoG for port-starboard symmetric ships lays on the centerline, hence $y_g = 0$. Under these assumptions, the equations of motion for conventional surface ships can be studied in the horizontal plane comprising surge, sway and yaw

$$m\left(\dot{u} - vr - x_g r^2\right) = X \tag{2.20}$$

$$m\left(\dot{v} + ur + x_g \dot{r}\right) = Y \tag{2.21}$$

$$I_z \dot{r} + m x_g \left(\dot{v} + ur\right) = N \tag{2.22}$$

2.4 Hydrodynamic forces and moments

Having obtained a mathematical formulation of the inertial response characteristics of maneuvering surface vessels, the solution of the maneuvering equations requires knowledge of hydrodynamic forces on the r.h.s. of Eq. (2.20-2.22). Discussions of modeling hydrodynamic forces start with the unrestricted flow condition. Ship maneuvering involves large-amplitude motions in sway and yaw, which give rise to free surface disturbances and vorticity shed from the ship hull. These effects impair the formulation of a holistic theory, which would enable for a solution in practically reasonable time. There are theoretical and experimental grounds to assume that in a given fluid, hydrodynamic forces on maneuvering ships depend on the shape of the hull, rigid body kinematics, control surface input and external disturbances. Following the principle of *divide and conquer*, a pragmatic modeling approach emerged in the hydrodynamic community to express the forces following a decomposition of force effects. Decompositions have been established based on fundamental concepts of fluid dynamics. Predominately, this resulted in mathematical formulations for hydrodynamic forces in terms of coefficients, which represent ship-specific hydrodynamic properties, acting on state and control surface variables within the framework of coupled nonlinear differential equations of motion. The efforts associated with the formulation and parameter identification of such motivated models are circumvented by transient numerical computations with field methods, which offer fine resolution of the flow around maneuvering ships in space and time by solving the Navier-Stokes equations. Hydrodynamic forces are available from the numerical solution itself, demonstrated by el Moctar et al. (2014) and Carrica et al. (2013) for standard rudder maneuvers in deep water. Transient numerical computations were shown to be very expensive and required the presence of High Performance Computing (HPC) environments. The time required to obtain the prediction of a standard rudder maneuver at a given operational condition is in the order of several days to weeks, el Moctar et al. (2014), and rendered impractical for parametric investigations. When attempting to arrive at simplified models, the problem emerges of identifying above introduced ship-specific hydrodynamic coefficients. On one hand, so-called modular models have been established. Force effects are formulated for the ship hull and control surfaces separately; and these modules may include decompositions themselves. Modular models are advocated by the possibility to study variations in single system components in an economic way, as terms unaffected by variations remain constant. On other hand, so-called global models seek to find hydrodynamic properties by integral evaluation of forces on the ship including all system contributions of the fully equipped ship. Often, they are established to cover only a limited perturbation range from a given approach condition to a maneuver. Within the notion of global models interactions between the hull and control surfaces are included in the coefficients without additional modeling or identification effort. Global models thus appeal to investigations of standard rudder maneuvers at a given approach speed. Parameter identification of global models is a pure exercise of model experiments and regression analysis. Disadvantages associated with modular models are the need for further modeling assumptions with regard to interactions of system components. Prior to the formulation of a model for the present purpose of demonstrating simulation-based maneuvering predictions in deep and shallow water, a summary is given of the concept of the decomposition of forces, which facilitates the comprehension of force effects in maneuvering.

2.4.1 Decomposition of force effects

Hydrodynamic forces are seen as a superposition of various force effects. A typical decomposition for a generalized force and moment component F was discussed by Sharma (1982) and takes the form

$$F = F_I + F_L + F_{CF} + F_R + F_P \tag{2.23}$$

where index $_I$ stands for ideal flow, $_L$ for lift, $_{CF}$ for cross-flow, $_R$ is referred rudders, and $_P$ to propellers. Forces F_I relate to inertial forces as present in inviscid and vorticity-free flow. Lift forces F_L emerge from the introduction of vorticity and associated effects from the general theory of wings including lift and induced drag in oblique flows. Cross-flow forces F_{CF} include pressure and friction resistance to the ship hull in drift and yaw and combined drift-yaw motion. Inertial force contributions are significant in acceleration phases, and usually an order of magnitude less than the dominating lift and cross-flow forces. Forces induced by propeller action mainly concern the longitudinal mode of motion, as propeller thrust seeks to cancel ship resistance to forward motion. However, in maneuvering propeller blades in oblique flow can generate lateral forces which typically are an order of magnitude less than thrust, but affect the sway and yaw modes of motion. Above decomposition motivated the formulation of a modular mathematical model for arbitrary rudder-engine maneuvers within the four-quadrants of ship operation, whereupon the different force contributions are expressed as functions only to the four angles addressing the states of engine operation (forward/reverse) and direction of motion (forward/backward), Oltmann and Sharma (1979):

$$\beta; \qquad \gamma = \arctan\left(\frac{rL}{2u}\right); \qquad \delta_e = \delta + \beta_R; \qquad \epsilon_p = \arctan\left(\frac{C_p}{U_p}\right) \tag{2.24}$$

In Eq. (2.24) γ is yaw angle , δ_e is effective rudder angle taking into account the rudder drift angle β_R, see Eq. (2.42), ϵ_p propeller advance angle, $C_p = 0.7\pi n D_p$, with n propeller revolutions and D_p propeller diameter.

Ideal flow effects

A quintessential finding from potential flow theory is that forces acting on arbitrarily shaped bodies moving arbitrarily in an unbounded, ideal fluid are related to entries of the hydrodynamic added mass tensor, Newman (1978)

$$a_{ij} \;=\; \rho \int_S \phi_i \frac{\partial \phi_j}{\partial \mathbf{n}} \, \mathrm{d}S. \tag{2.25}$$

where S is body surface and $\mathbf{n}$ its normal vector. Dependencies between the added mass tensor and rigid body kinematics are established through Kirchoff's (1869) equations for fluid kinetic energy. Upon the introduction of symmetry properties of the ship hull with respect to the waterline and midship plane, Sharma (1982) formulated the ideal flow force effects in component notation as per

$$X_I \;=\; X_{\dot{u}}\dot{u} - Y_{\dot{v}} r v - Y_{\dot{r}} r^2 \tag{2.26}$$

$$Y_I \;=\; Y_{\dot{v}}\dot{v} - X_{\dot{u}} r u - Y_{\dot{r}} \dot{r} \tag{2.27}$$

$$N_I \;=\; N_{\dot{r}}\dot{r} + \left(Y_{\dot{v}} - X_{\dot{u}}\right) u v + N_{\dot{v}} \left(\dot{v} + u r\right) \tag{2.28}$$

Eq. (2.28) includes the well-known broaching moment term $\left(Y_{\dot{v}} - X_{\dot{u}}\right) uv$, which came to be called Munk moment, Munk (1924).

Lifting flow effects

Lifting flow effects are seen as potential flow effects under consideration of vortices of a body in oblique flow. In this concept, a ship is considered as a wing of aspect ratio $2T/L$. Classic wing theories of Prandtl and Tietjens (1957) were applied to a ship by Sharma (1982). Lifting forces are formulated as functions of aspect ratio, drift angle, stagnation pressure and effective inflow at the transom of the ship, and moments are found from multiplication with appropriate lever arms. The respective forms of X_L, Y_L and N_L read

$$X_L = \frac{\rho}{2} L T \left[\frac{u\left(-\sqrt{c_1} v + \sqrt{c_2} r 0.5 L \operatorname{sgn} u\right)^2}{\sqrt{u^2 + v^2 + 0.5 L^2}} \right] \left[1 - \frac{d_1 v^2 + d_2 r^2 0.5 L^2}{u^2 + v^2 + r^2 + 0.5 L^2} \right] \tag{2.29}$$

$$Y_L = \frac{\rho}{2} L T \left[\frac{-c_1 u^2 v}{\sqrt{u^2 + v^2}} \left(1 + \frac{d_1 v^2}{u^2 + v^2}\right) + \frac{c_2 u \left|u\right| r 0.5 L}{\sqrt{u^2 + v^2 + 0.5 L^2}} \left(1 + \frac{d_2 r^2 0.5 L^2}{u^2 + v^2 + 0.5 L^2}\right) \right] \tag{2.30}$$

$$N_L = \frac{\rho}{2} L^2 T \left[\frac{e_1 u \left|u\right| v}{\sqrt{u^2 + v^2}} \left(1 + \frac{d_1 v^2}{u^2 + v^2}\right) - \frac{e_2 u^2 r 0.5 L}{\sqrt{u^2 + v^2 + 0.5 L^2}} \left(1 + \frac{d_2 r^2 0.5 L^2}{u^2 + v^2 + 0.5 L^2}\right) \right] \tag{2.31}$$

where c_1 is drift coefficient, c_2 is yaw coefficient, d_i, $i = 1, 2$, are combined drift and yaw coefficients and e_i, $i = 1, 2$, are lever arm coefficients for drift and yaw, respectively. Coefficients are found from drift, yaw and combined drift and yaw experiments, Sharma (1982). Bollay (1936) studied the flow past wings of low-aspect ratio in the nonlinear lifting theory of rectangular plates. A fundamental conclusion was that bound vortices were assumed to be constant along the wing span, elliptically distributed along the chord and leave the tip of the chord as a horse-shoe vortex trailing at an angle half of the angle of attack. Inoue (1969) presents an application to ship flows.

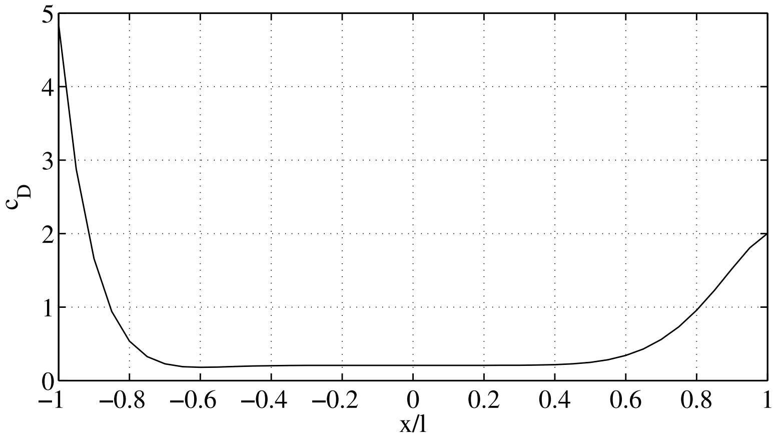

Figure 2.6: Exemplary trend of the cross-flow drag coefficient of a tanker over the ship length, Sharma (1982).

Cross-flow drag effects

Cross-flow drag effects relate to nonlinear force contributions attributable to pressure, friction and flow separation in oblique flow. The sectional side force on element dx at longitudinal ship position x is assumed to be a function of stagnation pressure of local cross-flow $W(x)$, local draft $T(x)$ and drag coefficient $c_D(x)$

$$Y_{CF} = -\frac{\rho}{2}\int_{-l_a}^{l_f} T(x)\, c_D(x)\, W(x)\, |W(x)|\, \mathrm{d}x \tag{2.32}$$

$$N_{CF} = -\frac{\rho}{2}\int_{-l_a}^{l_f} xT(x)\, c_D(x)\, W(x)\, |W(x)|\, \mathrm{d}x \tag{2.33}$$

where local cross-flow $W(x)$ is given by

$$W(x) = v + rx \tag{2.34}$$

Conventionally, $l_a = l_f = 0.5L$ and $T(x) = T_m$ are assumed constant. Sharma (1982) proposed a polynomial of the form

$$c_D(x) = a_0 + a_7 (x/L)^7 + a_8 (x/L)^8 + a_9 (x/L)^9 \tag{2.35}$$

to obtain the distribution of the ship-specific cross-flow drag coefficient over the length of the ship. Unknown coefficients a_i are to be determined from experiments. Fig. 2.6 shows a respective numerical example, Sharma (1982), valid for a tanker with

$$a_0 = 0.207; \qquad a_7 = 5.310; \qquad a_8 = 3.218; \qquad a_9 = 6.732; \tag{2.36}$$

The longitudinal force at straight ahead motion is taken as

$$X = -\frac{\rho}{2} c_T u^2 S_w \tag{2.37}$$

where S_w is wetted surface area, and relies on conventional drag coefficients from the ITTC 1978 method, ITTC (1999)

$$c_T = (1 + k)\, c_F (R_e) + c_W (F_n) \tag{2.38}$$

where c_F is determined from the plate friction correlation line, c_W is wave resistance coefficient and k form factor, found from experiments. Reynolds number is R_e and Froude number F_n, see Chapter 4. Hooft (1994) covers theoretical considerations on the cross-flow drag concept.

Rudder forces

Rudder forces are commonly approximated based on classic wing theory for symmetric profiles with practically motivated corrections to take into account interactions with the ship hull and propeller. Söding (1982a) provided a model representative of this class, which has in similar form been used by Sharma (1982). A mere geometric decomposition of rudder forces in the ship-fixed coordinate system gives

$$X_R = F_{R,L} \sin(\beta_R) - F_{R,D} \cos(\beta_R) \tag{2.39}$$

$$Y_R = F_{R,L} \cos(\beta_R) + F_{R,D} \sin(\beta_R) \tag{2.40}$$

$$N_R = Y_R (x_R + \Delta x_L) \tag{2.41}$$

where $F_{R,L}$ is rudder lift force, perpendicular to inflow V_R, and $F_{R,D}$ is rudder drag force, parallel to the inflow. Local effective drift angle is given by β_R

$$\beta_R = \arctan\left(\frac{v + x_R r}{u}\right); \qquad \beta_R = \alpha + \delta \tag{2.42}$$

It is equivalent to the angle enclosed by V_R and longitudinal axis of the ship. Angle α is enclosed by V_R and the longitudinal axis of the rudder, Fig. 2.7. The position of point of attack is x_R and Δx_L is a factor of length scale which takes into account the shift of effective lateral force due to rudder-induced changes in the pressure field in the aft ship. In homogeneous flow a deflected wing induces disturbances to the flow already ahead of the

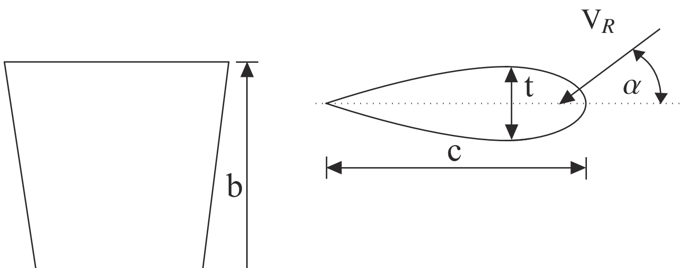

Figure 2.7: Definition of rudder dimensions and kinematics of rudder flows.

tip upstream. This effect is intensified through the presence of the hull, which impedes the balance of the mentioned disturbances as encountered in free inflow. A pressure difference between port and starboard results, increasing the total rudder-induced force on the hull and rudder and shifting its effective point of attack in positive x-direction. At the same time, the presence of the hull affects the effective inflow to the rudder. Consistent with classic wing theory, $F_{R,L}$ and $F_{R,D}$ are found from

$$F_{R,L} = 0.5\rho c_{R,L} V_R^2 A_R; \qquad F_{R,D} = 0.5\rho c_{R,D} V_R^2 A_R \tag{2.43}$$

where A_R is rudder surface area, $c_{R,L}$ is rudder lift coefficient and $c_{R,D}$ is rudder drag coefficient, approximated by

$$c_{R,L} = \frac{2\pi\Lambda\,(\Lambda + 1)}{(\Lambda + 2)^2} \sin\alpha + c_Q \sin\alpha\,|\sin\alpha| \cos\alpha \tag{2.44}$$

where $\Lambda = b^2/A_R$ is geometric rudder aspect ratio and c_Q induced-drag coefficient in lateral rudder inflow. For drag coefficient $c_{R,D}$ it follows

$$c_{R,D} = \frac{1}{\pi\Lambda}\left(\frac{2\pi\Lambda\,(\Lambda + 1)}{(\Lambda + 2)^2} \sin\alpha\right)^2 + c_Q\left|\sin^3\alpha\right| + 2c_F \tag{2.45}$$

Usually, $c_{R,L}$, c_Q, and $c_{R,D}$ are found from model tests and are available in tables of different profiles and Reynolds numbers, Abbott and Doenhoff (1959), Whicker and Fehlner (1958), Thieme (1992). The propeller slipstream affects the rudder inflow as propeller racing increases the effective wash on the rudder surface. Söding (1982a) suggests to take the local velocity of a location far behind the propeller as

$$V_R = u\,(1 - w)\,\sqrt{1 + c_{TH}} \tag{2.46}$$

where $c_{TH} = 8K_T/(J^2\pi)$ is thrust load coefficient and w is nominal wake fraction number and thrust coefficient K_T defined in Eq. (2.47). Similar approximations for finite positions behind the propeller are found in Sharma (1982) and Gutsche (1952). In Söding (1982a, 1982b) the particular arrangement of the rudder in the aft ship, including the clearance to the hull or the free surface, factor into the formulations of rudder forces in terms of coefficients, which in the reference are suggested to be available from BEM computations using lifting line theory. Theoretical treatise of lifting line theory is given in Newman (1978). Oltmann and Sharma (1979) demonstrate the application of such rudder force models to a maneuvering model for simulation of arbitrary engine-rudder maneuvers. A representative example for the use of semi-empirical hull-propeller-rudder interaction coefficients in maneuvering models is given in Yasukawa and Yoshimura (2015). The flow around rudders in homogeneous flow, and in the case of fully-appended ships involving hull-propeller-rudder interactions were shown to be accurately predictable with CFD, el Moctar (2001b).

Propeller forces

Propeller forces for maneuvering models can be obtained from open-water propeller performance curves derived for different operational settings, and wake and thrust deduction

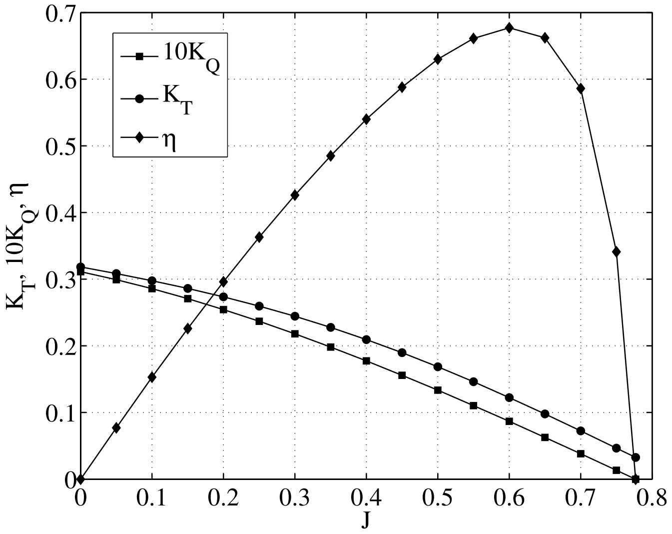

Figure 2.8: Open water propeller performance diagramme.

factors found from propulsion tests, Sharma (1982). The results of such tests are thrust coefficient K_T and torque coefficient K_Q, Fig. 2.8

$$K_T = \frac{T}{\rho n^2 D_p^4} \tag{2.47}$$

$$K_Q = \frac{Q}{\rho n^2 D_p^5} \tag{2.48}$$

which are functions of J, using by local inflow speed

$$U_p = u\,(1 - w) \tag{2.49}$$

In the longitudinal mode of motion, the propeller force contribution would enter the r.h.s. of the maneuvering equations as

$$X_p = T\,(1 - t) \tag{2.50}$$

where t is thrust deduction factor. Thrust and torque affect maneuvering in terms of the effective wash on the rudder surface. In oblique flows the propeller generates lateral forces which can significantly contribute to the balance of forces and moments. Then, the effective angle of attack α_e varies as a function of the blade's circumferential position θ. This gives rise to transverse forces on the propeller shaft, a transverse shift of the center of thrust and reversing loads on the propeller blades. Fig. 2.9 depicts the kinematics of oblique inflow for a sectional representation of a blade profile, el Moctar (2001a). Here, α_g is the geometric angle of attack, Φ the local nose-tail pitch angle, β_α the angle of advance, v_i the propeller induced velocity, v_r the resulting velocity. The Cartesian coordinate system is located at $r_p = 0.7R_p$, where R_p is propeller radius.

$$v(r,\theta) \quad = \quad v\sqrt{(\cos\alpha)^2 + \left(\frac{2\pi n r}{v} + \sin\alpha\cos\theta\right)^2 + (\sin\alpha\sin\theta)^2} \tag{2.51}$$

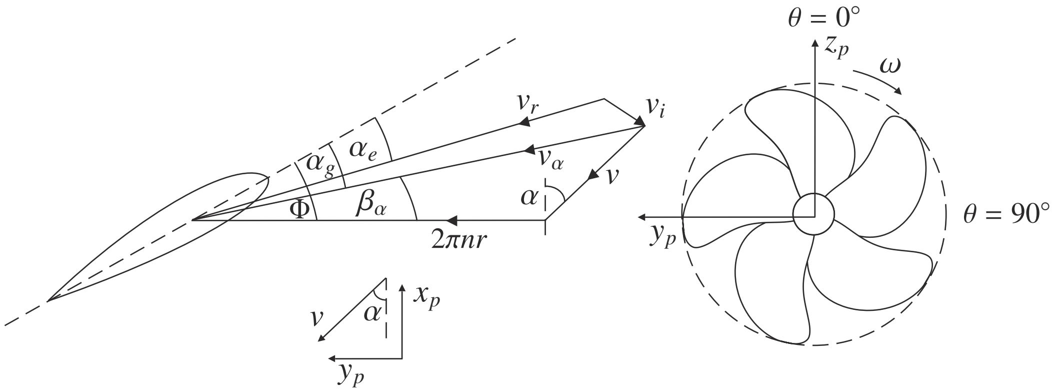

Figure 2.9: Kinematics of oblique propeller inflow, reproduced from el Moctar and Bertram (2000).

$$\beta_\alpha = \tan^{-1}\left(\frac{v\cos\alpha}{\pi nr + v\sin\alpha\cos\theta}\right) \tag{2.52}$$

The x-axis points into the ship's forward direction, the y-axis points to portside and the z-axis points upwards. The sign of the angle of inflow α is positive in Fig. 2.9. In a cylindrical coordinate system fixed to the propeller axis, Eq. (2.51) follows for the inflow velocity v_α. If the blades runs against the oblique flow, propeller forces increase with the increase of angle of attack and velocity. If the blade runs with the oblique flow in the other half of the rotation, the opposite effect takes place, but forces decrease by a smaller magnitude. The resulting mean thrust and torque are larger than in homogeneous inflow and functions of J and α; and a transverse force perpendicular to the propeller axis arises. The point of attack of mean thrust moves towards the side the blade runs against, which induces a moment about the vertical axis in $\mathcal{S}xyz$. The distance of this shift also increases with J and α. El Moctar and Bertram (2000) showed from numerical analysis that the mean lateral force generated by horizontal oblique inflow can be 18% of propeller thrust, and the shift of the thrust point of attack can be 10% of the propeller radius for $J = 0.7$. In the numerical example the drift angle of the investigated tanker was $\beta = 12°$. The presence of the hull diminishes this effect due to its flow-directing function to the propeller. Maneuvering model tests or CFD computations which include the propeller consider these effects in measuring or computing integral forces and moments on the hull.

Influence of engine dynamics

Hull forces are increased in maneuvering. Propeller torque increases to an upper threshold in response, determined by the engine characteristics, and decreases correspondingly the propeller rate of revolution. The so-emerging interaction between hull, propeller and engine affects rudder forces. Engine dynamics are usually excluded in ordinary maneuvering simulations which seek to compute general maneuvering properties from standard maneuvers, but are an essential requirement for ship handling simulations. Related discussions on the impact on maneuvering is provided in el Moctar and Cura-Hochbaum (2005) and el Moctar et al. (2014).

2.4.2 Multivariat polynomial models

The first consequent formulation of a global maneuvering model using multivariat algebraic polynomials for an integral evaluation of forces and moments for the fully-equipped ship in a given fluid is related to Abkowitz (1964). The starting point are Taylor-series expansions in powers of the variables of a functional like

$$\mathbf{F} = f\left(x_0, y_0, \psi, u, v, r, \dot{u}, \dot{v}, \dot{r}, \delta, \dot{\delta}, \ddot{\delta}\right) \tag{2.53}$$

The functional may be extended by propeller revolution n, or any other parameter considered to affect $\mathbf{F}$. This notion presumes continuous functions and derivatives for the considered range of operation. It follows

$$X(\mathbf{x}) \approx X(\mathbf{x}_0) + \sum_{i=1}^{n}\left(\left.\frac{\partial X(\mathbf{x})}{\partial x_i}\right|_{\mathbf{x}_0} \Delta x_i + \frac{1}{2}\left.\frac{\partial^2 X(\mathbf{x})}{\partial x_i^2}\right|_{\mathbf{x}_0} \Delta x_i^2 + \frac{1}{6}\left.\frac{\partial^3 X(\mathbf{x})}{\partial x_i^3}\right|_{\mathbf{x}_0} \Delta x_i^3 + ...\right) \tag{2.54}$$

$$Y(\mathbf{x}) \approx Y(\mathbf{x}_0) + \sum_{i=1}^{n}\left(\left.\frac{\partial Y(\mathbf{x})}{\partial x_i}\right|_{\mathbf{x}_0} \Delta x_i + \frac{1}{2}\left.\frac{\partial^2 Y(\mathbf{x})}{\partial x_i^2}\right|_{\mathbf{x}_0} \Delta x_i^2 + \frac{1}{6}\left.\frac{\partial^3 Y(\mathbf{x})}{\partial x_i^3}\right|_{\mathbf{x}_0} \Delta x_i^3 + ...\right) \tag{2.55}$$

$$N(\mathbf{x}) \approx N(\mathbf{x}_0) + \sum_{i=1}^{n}\left(\left.\frac{\partial N(\mathbf{x})}{\partial x_i}\right|_{\mathbf{x}_0} \Delta x_i + \frac{1}{2}\left.\frac{\partial^2 N(\mathbf{x})}{\partial x_i^2}\right|_{\mathbf{x}_0} \Delta x_i^2 + \frac{1}{6}\left.\frac{\partial^3 N(\mathbf{x})}{\partial x_i^3}\right|_{\mathbf{x}_0} \Delta x_i^3 + ...\right) \tag{2.56}$$

where

$$\mathbf{x} = \left[x_0, y_0, \psi, u, v, r, \dot{u}, \dot{v}, \dot{r}, \delta, \dot{\delta}, \ddot{\delta}\right]^T \tag{2.57}$$

and the perturbation from the equilibrium state is $\Delta\mathbf{x} = \mathbf{x} - \mathbf{x}_0 = [\Delta x_1, \Delta x_2, \Delta x_3, ..., \Delta x_n]^T$. The established notation (Imlay, 1961) for the emerging partial derivatives is

$$Y_v = \left.\frac{\partial Y}{\partial v}\right|_{\mathbf{x}=\mathbf{x}_0}, Y_{vv} = \left.\frac{1}{2}\frac{\partial^2 Y}{\partial v^2}\right|_{\mathbf{x}=\mathbf{x}_0}, \cdots \tag{2.58}$$

as an example for the derivative in Y with respect to v. For higher-order terms the index is powers of v. The so-defined coefficients are called hydrodynamic derivatives. From a formal point of view, the emerging unknown coefficients do not represent derivatives, but the terminology has widely been adopted in the ship hydrodynamic community, (Sutulo and Guedes Soares, 2011). In the remainder, they will be called hydrodynamic coefficients. Above approach is valid for an equilibrium point from which the motion of interest departs. Often this is the straight ahead condition at a certain approach speed U_0, with v, r and δ being zero. Assuming that the longitudinal hull force cancels the propeller thrust T, no net force acts on the ship hull in this condition, $X_0 = T$. The expansion results in a large number of unknown hydrodynamic coefficients. Initial assumptions to reduce the number of parameters are that force and moment contributions related to rudder action solely depend on rudder deflection δ, rather than its temporal derivatives. Forces are also assumed to be independent of initial position x_0, y_0, and orientation ψ_0. Further, if acceleration forces exclusively result from inertia properties not interacting with viscous effects, as dictated by potential flow theory, only linear terms have to be retained. In ship maneuvers exhibiting large departures from the equilibrium state, nonlinearities are dominant raising the questions of which powers in the expansion are relevant. Following Abkowitz (1964) it was sufficient to include the nonlinearity up to third order. A detailed discussion of relevant powers in the expansion is governed by geometric properties in conjunction with physical considerations treated separately for surge, sway and yaw. Hence, port-starboard symmetry of ships suggests only to keep even powers of v, r and δ in X. Considering that these force contributions depend on angle of attack, itself influenced by forward velocity u, it follows that these forces vary with u. With these considerations, the nonlinear form of X reads

$$\begin{aligned} X &\approx X_{\dot{u}}\dot{u} + X_u\Delta u + X_{uu}\Delta u^2 + X_{uuu}\Delta u^3 + X_{vv}v^2 + X_{rr}r^2 + X_{\delta\delta}\delta^2 + X_{vr}vr \\ &+ X_{v\delta}v\delta + X_{r\delta}r\delta + X_{vvu}v^2\Delta u + X_{rru}r^2\Delta u + X_{\delta\delta u}\delta^2\Delta u + X_{rvu}rv\Delta u \\ &+ X_{v\delta u}v\delta\Delta u + X_{r\delta u}r\delta\Delta u \end{aligned} \tag{2.59}$$

where $\Delta u = u - U_0$ is the perturbation from the approach speed. In deriving formulations for Y and N, the same arguments are invoked, considering that along with symmetry considerations, terms for v, r and δ are now odd functions. Additionally, if for zero rudder deflection the ship has a turning moment N_0 and a side force Y_0, these terms are considered as well as combinations with Δu to account for their change with forward speed. Analogous forms of Y and N, correspondingly, under these assumptions read

$$\begin{aligned} Y &\approx Y_{\dot{v}}\dot{v} + Y_{\dot{r}}\dot{r} + Y_0 + Y_{0u}\Delta u + Y_{0uu}\Delta u^2 + Y_v v + Y_{vvv}v^3 + Y_\delta\delta + Y_{\delta\delta\delta}\delta^3 + Y_r r \\ &+ Y_{rrr}r^3 + Y_{vrr}vr^2 + Y_{rvv}rv^2 + Y_{r\delta\delta}r\delta^2 + Y_{\delta rr}\delta r^2 + Y_{v\delta\delta}v\delta^2 + Y_{\delta vv}\delta v^2 + Y_{rv\delta}rv\delta \\ &+ Y_{\delta u}\delta\Delta u + Y_{vu}v\Delta u + Y_{vuu}v\Delta u^2 + Y_{ru}r\Delta u + Y_{ruu}r\Delta u^2 + Y_{\delta uu}\delta\Delta u^2 \end{aligned} \tag{2.60}$$

Hydrodynamic coefficients are usually determined through model experiments. Here, two kinds of parameter identification methods are available. In direct parameter identification coefficients are found from systematic captive model tests and regression analysis of resulting force records. In indirect parameter identification, time histories of state variables and inputs of free-running tests are processed with appropriate identification algorithms. For various coefficients, empirical formulas exist (Clarke et al., 1983), stemming from model tests and having limited use for ships and operational conditions outside of the framework of this investigation.

General objections

Fundamental objections associated with the presented approach were communicated initially in conjunction with the advance of PMM experiments, which had their birth in naval hydrodynamics at David Taylor Model Basin (DTMB), Gertler (1959) and Goodman (1966). The summary mainly refers to Newman (1966) and SFB 98, Oltmann (1978). Abkowitz's model assumes that hydrodynamic forces and moments are analytic functions only of instantaneous accelerations, velocities and displacements, i.e. that they remain independent of the history of the hull-water interaction. A more exact model would consider also the dependence of **F** on past motions by means of a convolution integral, as presented by Cummins (1962). Physical phenomena giving rise to memory effects primarily depend on free surface disturbances and vorticity. The use of slow motion hydrodynamic coefficients is referred to the relatively long time, during which the dynamic response of a ship to a commanded change in the direction of motion takes place. Identification of hydrodynamic coefficients was predominately done via captive oscillatory model tests, and frequency effects were also of concerns in model tests themselves. ITTC recommended guidelines and procedures (2014) and reference therein treat this particular problem, see also a study by Renilson (1986). The guidelines can generally not be transferred straightforwardly to the shallow water case, because both free surface disturbances and vorticity change, and it is anticipated that they are functions of oscillation frequency. Fundamental objections associated with the presented approach were communicated initially in conjunction with the advance of PMM experiments, which had their birth in naval hydrodynamics at David Taylor Model Basin (DTMB), Gertler (1959) and Goodman (1966). The summary mainly refers to Newman (1966) and SFB 98, Oltmann (1978). Abkowitz's model assumes that hydrodynamic forces and moments are analytic functions only of instantaneous accelerations, velocities and displacements, i.e. that they remain independent of the history of the hull-water interaction. A more exact model would consider also the dependence of **F** on past motions by means of a convolution integral, as presented by Cummins (1962). Physical phenomena giving rise to memory effects primarily depend on free surface disturbances and vorticity. The use of slow motion hydrodynamic coefficients is referred to the relatively long time, during which the dynamic response of a ship to a commanded change in the direction of motion takes place. Identification of hydrodynamic coefficients was predominately done via captive oscillatory model tests, and frequency effects were also of concerns in model tests themselves. ITTC recommended guidelines and procedures (2014) and reference therein treat this particular problem, see also a study by Renilson (1986). The guidelines can generally not be transferred straightforwardly to the shallow water case, because both free surface disturbances and vorticity change, and it is anticipated that they are functions of oscillation frequency.

Model specific objections

The second major objection in Newman (1966) relates to the proposed Taylor-series expansion wherein the side force is expressed as an odd function in cubic power of v, attributable to port-starboard symmetry. However, Newman (1966) remarks that both in theory and experiment for slender bodies with transverse symmetry in steady drift motion the side force contribution associated with flow separation drag is of second-order of drift angle β:

$$\begin{aligned} Y &\approx A\sin 2\beta + B\sin\beta\,|\sin\beta| \\ &\approx 2A\beta + B\beta\,|\beta| + O\left(\beta^3\right) \end{aligned} \tag{2.61}$$

In Eq. (2.61) A and B are constant unknown coefficients. Emphasizing that force contributions associated with lifting-surface theory in an ideal fluid can be expressed with the Taylor-series approach, Newman (1966) concludes that both second- and third-order terms should appear in the side force and yaw moment of a nonlinear model. In this context, special attention is drawn to extrapolation since separation drag is amenable to Reynolds scaling rather than Froude similarity. However, the validity of these assumptions remains questionable for bluff ships which exceed beam to length ratios of 0.15. For single-screw ships model assumptions from symmetry considerations are controversial. Oltmann and Wolff (1979) argue that the mere introduction of constant side force and yaw moment terms Y_0, N_0 is too simple and consequent modifications to the model extend to the consideration of odd powers in the expansion for X and even powers in Y and N, respectively. Moreover, they also call for a modification of rudder coefficients towards higher-order terms than $O\left(\delta^4\right)$, to more accurately capture flow separation at large rudder deflections. The argumentation is challenged by scale effects involved in the extrapolation of the results from regression analysis performed at model scale to the dimensions of the ship, since stall conditions are dependent on Reynolds number. Stall occurs at greater angles with increasing Reynolds number. Oltmann and Wolff (1979) also plea for considering cross-couplings between acceleration and velocities, and the nonlinear dependence on accelerations, which is neglected in Abkowitz's model. Other experimental investigations back the simplification, Strøm-Tejsen and Chislett (1966). Of additional concern is if the identified significance of the contributions in idealized captive model tests is encountered in simulated free-running maneuvers and full-scale ship flows. Viallon et al. (2012) argue that neither polynomials of order higher than three, nor terms considering acceleration-velocity coupling must be used in ship maneuvering. Sutulo and Guedes Soares (2011) address the issue of multicollinearity and over-parametrization in conjunction with the use of both second-order modulus functions and third-order polynomials to express damping forces. Experimental evidence contributing to the discussion is presented in Kose (1982), who concluded with the recommendation for the use of algebraic polynomials of order three. Multivariat polynomial models are readily applicable to the formulation of hull forces in a modular maneuvering model, too. A popular approach is to substitute the separate treatment of ideal, lifting and cross-flow effects by introducing mulitivariat polynomials of the rigid body kinematic variables. For consideration of a wide operational range of rigid body kinematic variables, models have been proposed using Fourier series in terms of drift and yaw angle instead of polynomials of v and r, e.g. Gronarz (1997).

2.5 Shallow water effects on maneuvering

Ship motions in shallow water involve hydrodynamic interactions with vertical flow restrictions, affecting the dynamic floating position of ships underway and hydrodynamic properties relating to inertia, lift and cross-flow forces. A detailed treatise of maneuvering forces in shallow water is given in the following, based on the extension of the decomposition of forces for the deep water case. Prior to this discussion, main hydrodynamic interactions in shallow and confined water are discussed. Hydrodynamic interaction effects in shallow water mean water-depth dependent changes in the pressure field ambient to the ship. These effects can be related to the principle of conservation of energy along a streamline in ideal flow, postulated by Bernoulli's equation. According to the Bernoulli equation a decrease in the flow cross-section results in a concurrent increase of the flow velocity and decrease of pressure. Consequences of Bernoulli's effect for floating bodies are dynamic adjustments of the floating position and orientation. Ships in forward motion experience a vertical displacement in the heave mode (sinkage) and a rotational displacement in the pitch mode (trim), accompanied by a decrease of the mean ambient water level, decreasing UKC, Fig. 2.10. Such decrease in UKC is called squat. From a ship hydrodynamic point of view, the classification of shallow water flows has to take into account a suitable quantity of dimension of velocity. For analysis of forward motion the Froude depth number $F_{nh} = u/\sqrt{gh}$ has been established. In the sub-critical flow regime of $F_{nh} < 1$ squat is dominated by the pressure field between the shoulders of the ship, resulting in the midship sinkage. The difference in sinkage at the fore and aft perpendicular, determining trim, is about an order of magnitude less than midship sinkage. When sailing at small UKC, the pressure on the ship hull shows a distinct decrease between the forward and aft shoulders. The centroid of this low pressure region determines the position of attack of the resulting vertical forces. Dynamic trim is therefore driven by the difference between large quantities. Squat is expected to influence hull forces in maneuvering as dynamic trim changes the point of attack of the lateral sway and yaw damping forces, thereby affecting stability properties. This phenomenon can take either a stabilizing or destabilizing effect, depending on the inherent stability properties of the ship and the sign of trim. A strong bow-down trim would shift the pressure centroid in lifting flows bow-wards. In general, the overall larger hydrodynamic forces in response to steering and control actions lead to an increase of turning and yaw checking in shallow water. Analogous interactions occur in horizontal modes of motion in laterally confined water. Forces and moments arising from pressure variations on the ship hull, when traveling at close separation distance to a wall or bank, came to be denoted by the term bank effects. The decreased flow cross-section results in a decrease of pressure on the side of the restriction, inducing a suction force towards the wall and a moment, which for most conventional ship hulls tends to turn the ship bow-out off the wall. A change in ambient water level accompanies the suction effects, and at high speeds, the difference between the water levels on the open water side and the side facing the restriction dominates the suction forces proportional to the difference in water level. Fig. 2.11 is a schematic of a typical ship-bank interaction scenario. The suction force and bow-out moment cause the ship to move closer to the wall and induce a Munk moment. Typically, applying rudder in the direction of the wall while still maintaining a small bow-out drift mitigates the bank effects. In shallow water, the presence of the bank increases squat.

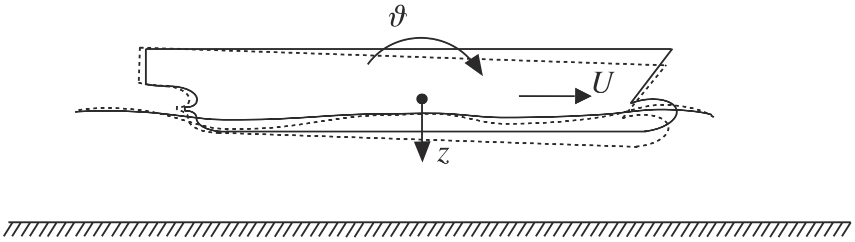

Figure 2.10: Schematic of squat.

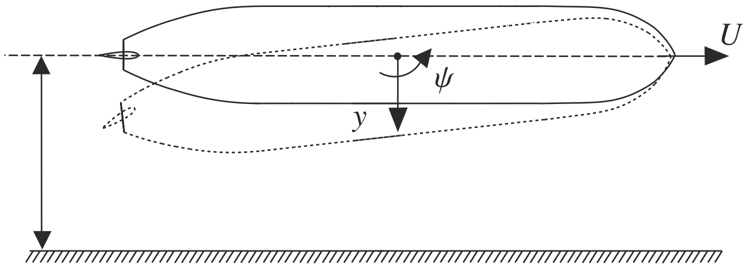

Figure 2.11: Schematic of bank effects.

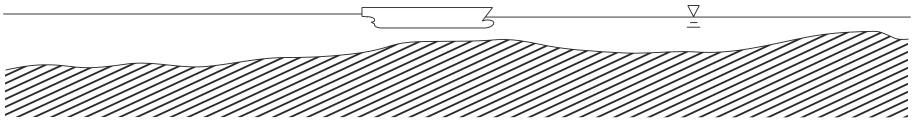

Figure 2.12: Schematic of varying water depth.

Further hydrodynamic interactions are related to a change in ship-induced wave dynamics and an increase in friction resistance in response to increased local flow velocities on one hand, and interactions between the ship hull boundary layer and the bottom on other hand. Before discussing the account for the shallow water effect in the framework of the aforementioned mathematical models, preliminary considerations on the intended degree of resolution of these effects appear necessary. In coastal harbor approach areas or rivers the sea and river beds are usually uneven. If UKC becomes a function of both space and time, Fig. 2.12, relative motions between ships and varying bathymetry give rise to unsteady free surface disturbances and pressure variations on the hull. Such transient hydrodynamic phenomena cannot be modeled using quasi-steady hydrodynamic models, but call for application of field methods which are capable of providing the appropriate level of resolution. The transient resolution of varying bottom topology in the framework of multivariat polynomial models is additionally impaired by emergence of coefficients acting on gradients of water depth with respect to time, describing the effect of the temporal rate of change in UKC. Parameter identification of such terms in the general identification procedure is infeasible. However, if the changes in h take place gradually and moderately, these terms could be neglected. In the majority of practical navigability analyses a constant or reasonable mean water depth can be defined and above discussion becomes obsolete, e.g. in canals.

2.5.1 Considerations on the shallow water effect and the decomposition of forces

From a theoretical point of view, each of the presented force effects is subject to characteristic changes in response to decreasing UKC. Above discussion is thus carried through to the shallow water effect on single force contributions.

Inertial forces

Added masses increase in shallow water owing to the increased flow blockage, which impairs the acceleration of fluid particles in the vicinity of accelerating ships. Fig. 2.13 shows the trends of hydrodynamic coefficients related to accelerations in sway and yaw over h/T for the Series-60 ship found from experiments, Yasukawa (1988). A quintessential observation is that the change in magnitude is characteristic to each component. Special attention shall be brought to the Munk moment. While the added mass in longitudinal direction a_{11}, or coefficient $X_{\dot{u}}$, is generally an order of magnitude smaller than ship mass, a_{22}, or $Y_{\dot{v}}$, is in the order of ship mass and doubles in magnitude in the numerical example from deep water to a UKC of 20% of ship draft. For constant ship speed in drift motion ($v \neq 0$) the Munk moment will consequently increase almost proportionally to the increase in $Y_{\dot{v}}$. Given appropriate numerical methods based on potential flow theory the added mass tensor can efficiently be computed at various water depths. The three-dimensional Rankine panel code GLRankine (see Chapter 3.5.2) was applied within the scope of the present investigation to derive added masses relevant for the sway and yaw modes of motion for KVLCC2 (Tab. 5.1) at various shallow water depths, Fig. 2.14. Strip theory approximations for added masses tend to over-prediction as they introduce additional blockage by neglecting the longitudinal direction of flow. Thomas and Sclavounos (2006) give a numerical example for the Series-60 standard ship in laterally confined water, where strip theory predictions were around 10% higher than results from a three-dimensional method.

Lifting forces

Lifting forces increase in shallow water through a virtual increase of the effective wing aspect ratio, which impairs the pressure balancing between the pressure and suction side of the wing, resulting in a greater pressure gradient and consequently greater lift. Söding (1982c) examined the limiting case of zero UKC, for which the aspect ratio of the ship hull changes from the deep water value of $2T/L$ to infinity. Based on an approximation for the lift coefficient using Eq. (2.44), the resulting lift is estimated to be 40 times greater. Numerical examples of Eq. (2.29-2.31) for various water depths are discussed in Gronarz (1997).

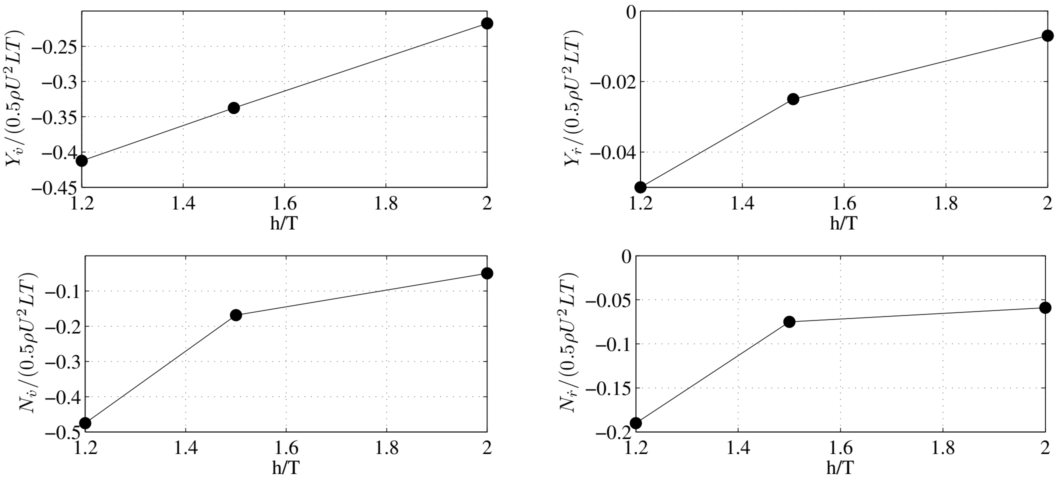

Figure 2.13: Trends of hydrodynamic acceleration coefficients of the Series-60 standard ship over nondimensional water depth, Yasukawa (1988).

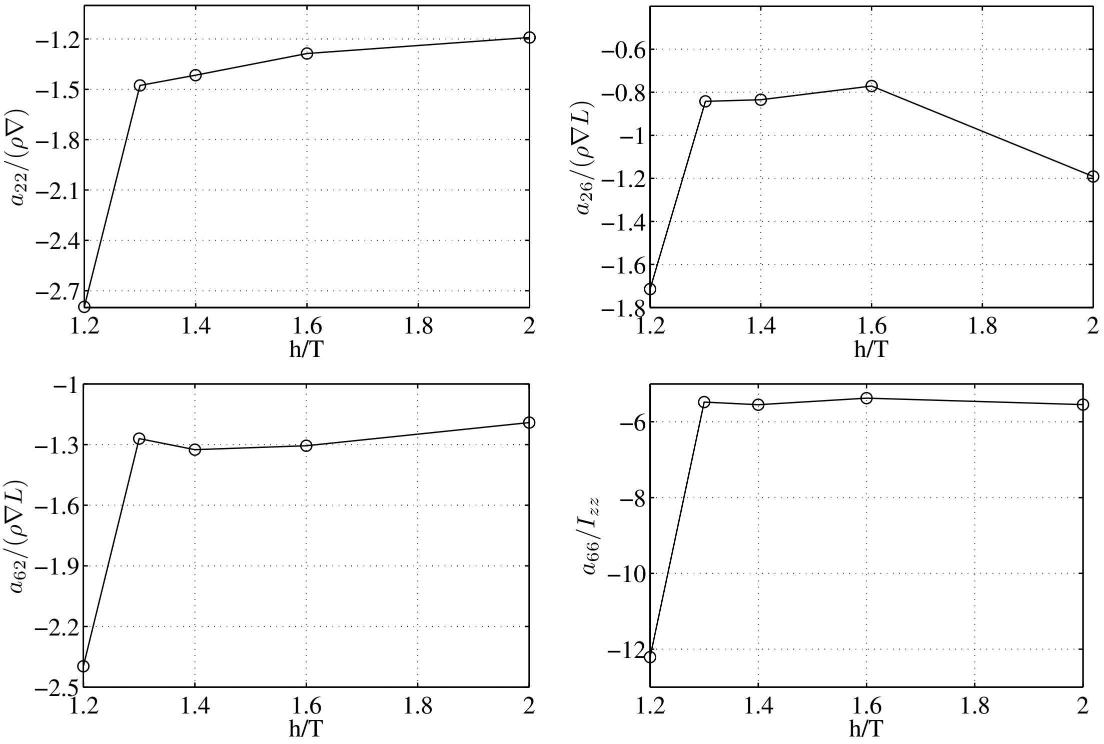

Figure 2.14: Trends of added mass coefficients of KVLCC2 over nondimensional water depth.

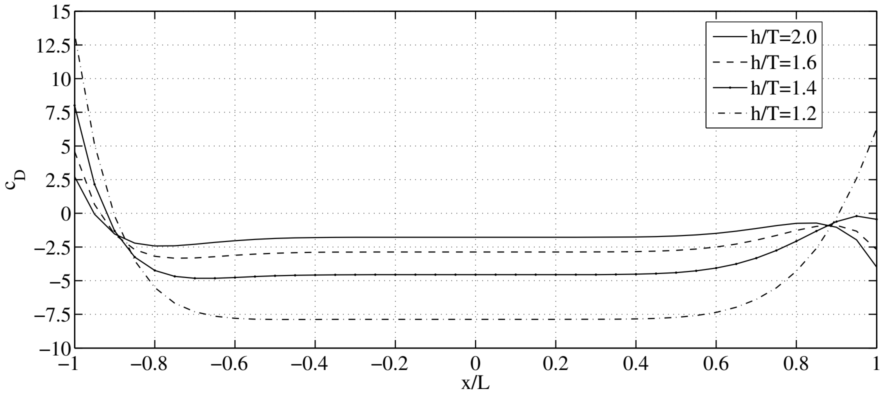

Figure 2.15: Trend of cross-flow drag coefficients of KCS over ship length and water depth, Gronarz (1997).

Cross-flow forces

Cross-flow drag is increased in shallow water due to an increase of local flow velocities emerging from Bernoulli's effect. Moreover, aforementioned interactions between the ship hull boundary layer and the bottom change the cross-flow characteristics. Application of cross-flow drag coefficients $c_D(x)$ from the deep water case is not admissible, since the change of the distribution of c_D over the ship length with decreasing UKC is unknown. Gronarz (1997) investigated the effect of shallow water on cross-flow forces for the Panmax-class Kriso Containership (KCS, Tab. 4.3 and 5.1), Fig. 2.15.

Rudder and propeller forces

Due to their position in the ship wake and propeller slipstream the effect of shallow water on rudder forces is multi-faceted, with effects leading to an increase of lift and drag, and effects leading to a decrease. Discussions of the change of hull-propeller-rudder interactions with decreasing UKC is governed by the change in ship wake and propeller inflow. Due to a more dominant role of viscosity in shallow water condition, the ship wake increases in magnitude and spatial distribution, becoming evident in a broadening of isolines of u_x/u_0. Higher wake results in higher propeller loading. Propeller-rudder interactions are governed by the propeller slipstream and its effective wash on the rudder surface. Experimental studies on the influence of shallow water on the propeller slipstream showed small to moderate influence, Isay (1962). Analogous to the estimation of hull lift forces for the limiting case of zero UKC given in Söding (1982c), rudder lift was estimated to multiply by a factor 2.5 compared to a rudder with aspect ratio two, which is an order of magnitude less than the increase of hull lift forces. In the investigation of the shallow water effect in modular mathematical models Gronarz (1997) concluded that rudder and propeller forces were only weakly affected by decreasing UKC and, for simplicity, the use of the deep water rudder and propeller force coefficients was suggested, Fig. 2.16. From a formal standpoint, empirical coefficients aiming at the account for hull-propeller-rudder interactions have to be adapted for the shallow water case.

2.5.2 Shallow water effect in multivariat polynomial models

When extending multivariat polynomials to consider finite water depth h, the question arises whether to retain a constituted deep water model structure with coefficients identified for the desired water depth, taking the mathematical form

$$\mathbf{F} = f\left(u, v, r, \dot{u}, \dot{v}, \dot{r}, \delta\right)\Big|_{h} \tag{2.62}$$

or, to formulate a novel model structure with explicit h-terms involved in the functional

$$\mathbf{F} = f\left(u, v, r, \dot{u}, \dot{v}, \dot{r}, \delta, h\right) \tag{2.63}$$

Theoretical considerations on this extension start with the reduction of the six-DoF equations of motion to arrive at the three-DoF model, since aforementioned hydrodynamic interactions with the vertical restriction affect heave and pitch modes of motion in terms of squat. Consistent with the Taylor-series expansion, coefficients will arise from z, $\dot{z}$, ϑ, $\dot{\vartheta}$ and cross-couplings with other state variables. Consequences are extended regression problems with huge identification effort. The number of factors can be reduced by retaining the reduced three-DoF model, but performing the identification procedure in unconstrained mode for heave and pitch, so that their effect is implicitly included in the derivation of hydrodynamic coefficients in surge, sway and yaw. There are theoretical and experimental grounds to assume that within the framework of multivariat polynomial models each coefficient undergoes characteristic changes over h. Gronarz (1997) conducted a systematic investigation into the extension of different mathematical models to shallow water. Hydrodynamic coefficients were obtained for KCS by way of captive model tests on various water depths. Sets of maneuvering coefficients for various shallow water depths are plotted in Fig. 2.17. The assumption of characteristic changes of each coefficient over water depth was confirmed. Most coefficients change in nonlinear fashion and undergo significant amplification. Coefficients related to rigid body velocities represent damping terms, including lift and cross-flow effects, which also increase with decreasing UKC. An additional observation is that with increasing UKC the trend of the coefficients appears to strive asymptotically towards an anticipated deep water value. For maneuverability analysis at a desired shallow water depth using multivariat polynomial models hydrodynamic coefficients should thus be determined at just this desired water depth. In presence of multiple water depth-specific sets of coefficients it is possible to apply regression analysis to approximate a set of coefficients for a water depth which was not investigated explicitly, but lays within the range of available data. Gronarz (1997) addressed suitable interpolation schemes, e.g. using cubic splines, but concluded that least-squares curve fitting using power functions specific to each coefficient was more appropriate. This approach takes the form

$$F = \underbrace{f\left(u, v, r, \dot{u}, \dot{v}, \dot{r}, \delta\right)}_{f_0} + f_n \left(T/h\right)^n \tag{2.64}$$

where f_0 refers to the basic deep water functional and $f_n\left(T/h\right)$ is the shallow water extension in yet to be determined power of T/h. The power functions were shown to provide smooth trends of each coefficient over the water depth and to be suitable to model the asymptotic trend approaching the deep water case. The dependence of hydrodynamic forces on squat on one hand, and the dependence of squat on forward speed on other hand, brings to the attention the relevance of terms which arise from the expansion of Δu and consider the effect of forward speed changes on F. A concluding remark on the suitability of multivariat polynomials to model hydrodynamic forces in maneuvering relates to the theoretical notion of the frequency-invariance of hydrodynamic coefficients and the change in inertial response characteristics anticipated for ship maneuvering in shallow water. Ships in confined water are operated at low speeds and experience increased hydrodynamic forces acting upon the hull in response to commanded changes in direction. The increase in both inertia and damping forces on the hull increases the time span during which the state variables in a maneuver vary, or settle to a steady state, which caters to the notion of quasi-steady models. In this context, the discussion of forward speed perturbation terms deserves a review, because of the generally low forward speeds and anticipated low forward speed losses in shallow water. Challenges arise for the identification of multivariat polynomial models in conjunction with the flow restriction and hydrodynamic interactions (squat) in captive maneuvering tests. In experimental shallow water towing tank setups finite tank dimensions add to the flow blockage, and the setup is prone to be affected by wave reflection initiated in the acceleration phase of the model. These effects are to be seen as a constraining factor for the choice of prescribed motion parameters in surge, sway and yaw. Particularities and challenges of identification and regression analysis will be addressed later.

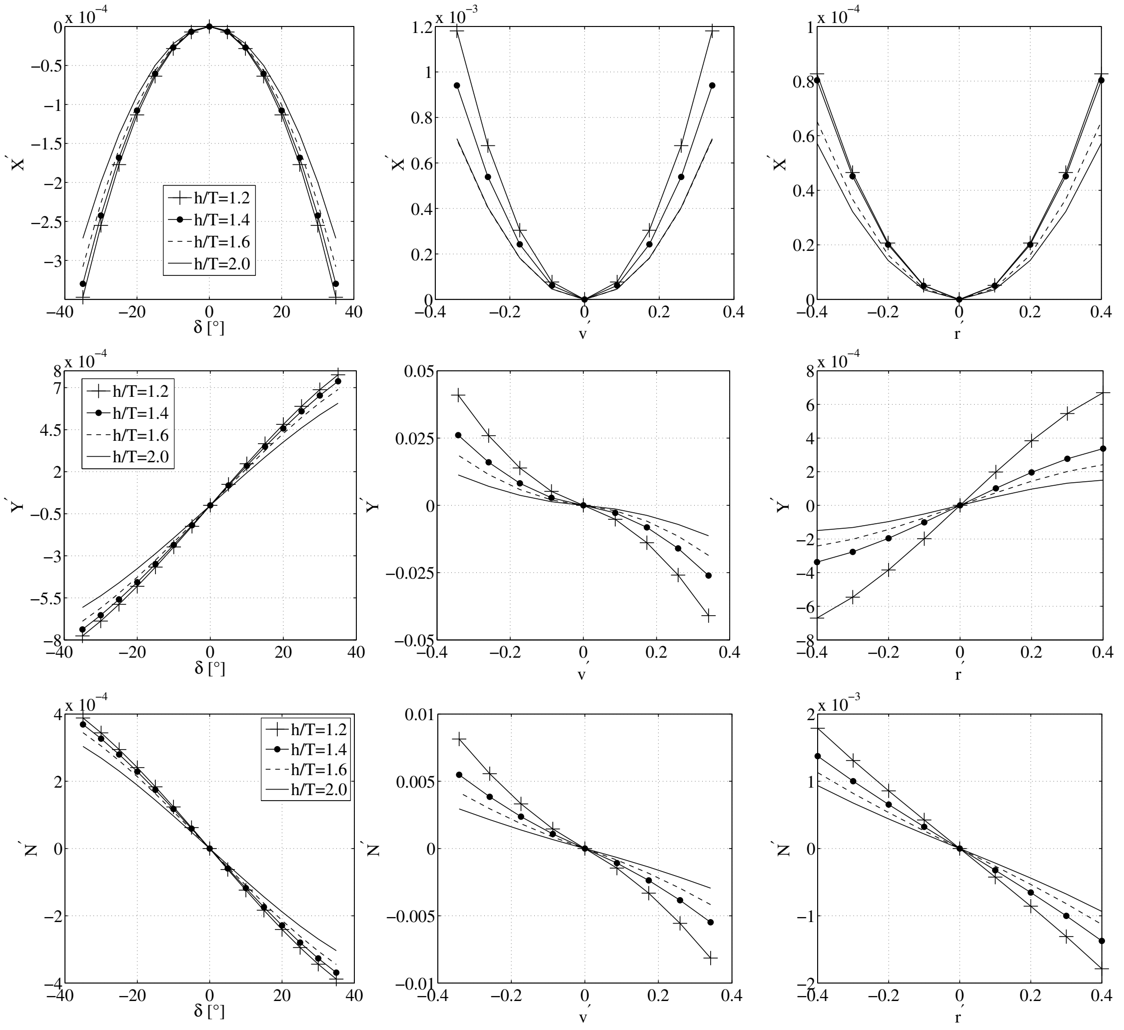

Figure 2.16: Hydrodynamic forces of KCS as a function to rudder angle, sway velocity and yaw rate for various water depths, Tab. 8.2, Gronarz (1997).

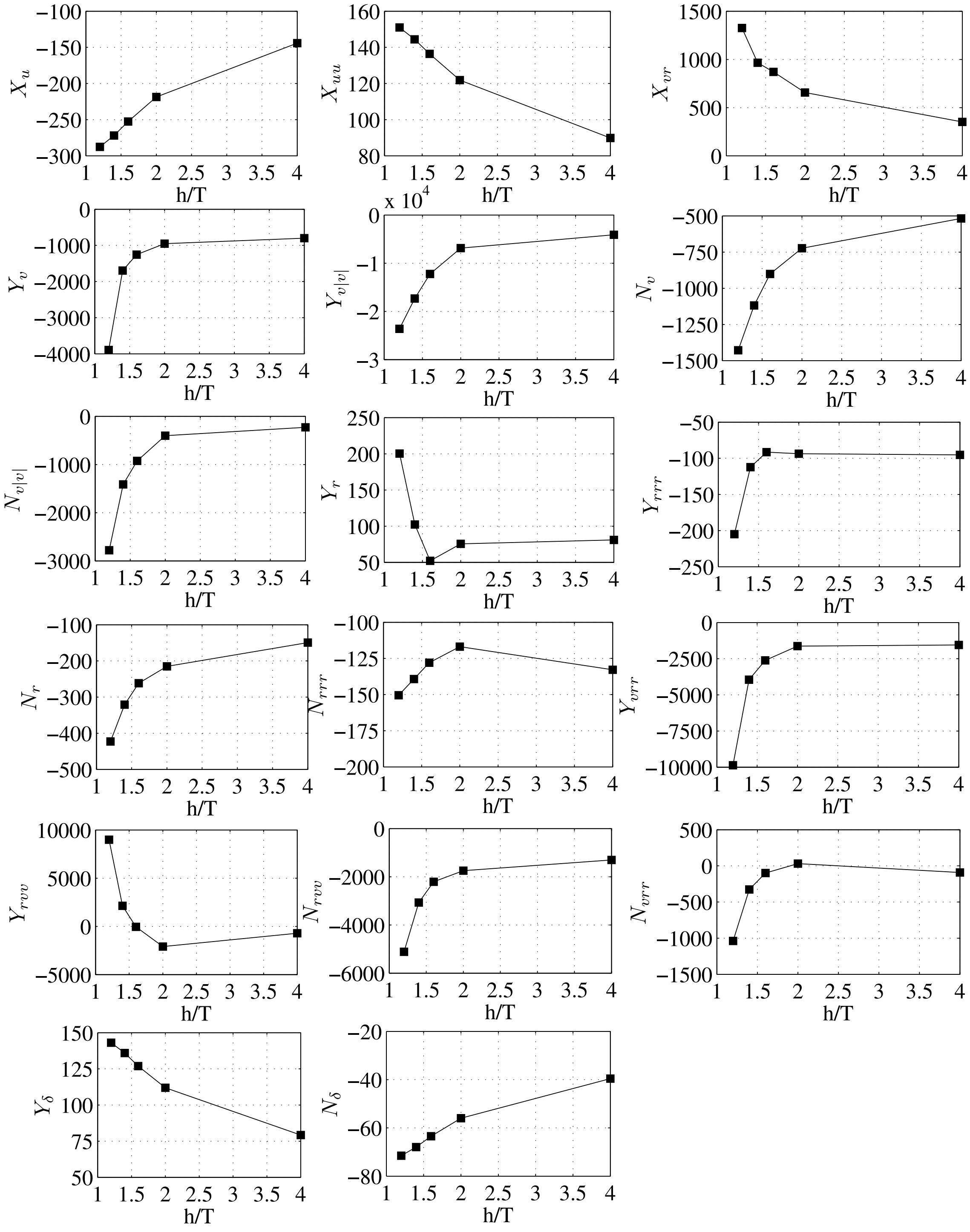

Figure 2.17: Hydrodynamic maneuvering coefficients of KCS over nondimensional water depth multiplied by 1000, Gronarz (1997).

2.6 Linear equations of motion and straight line stability analysis

For maneuvering problems involving small deviations in sway and yaw from a mean ship trajectory constant cruise speed ($U \approx U_0$) can be assumed and a sway-yaw-subsystem model can be established. The linear time-invariant framework of maneuvering dynamics enables classic investigation of inherent system stability properties, which are useful for general maneuvering performance evaluation, e.g. straight line motion stability. If only linear terms are retained, the maneuvering equations of motion can be rewritten as

$$\mathbf{M}\dot{\mathbf{x}} + \mathbf{N}\mathbf{x} = \mathbf{F}_R\delta \tag{2.65}$$

$$\mathbf{M} = \begin{bmatrix} -Y_{\dot{v}} + m & -Y_{\dot{r}} + mx_g \\ -N_{\dot{v}} + mx_g & -N_{\dot{r}} + I_z \end{bmatrix}$$

$$\mathbf{N} = \begin{bmatrix} -Y_v & -Y_r + mU_0 \\ -N_v & -N_r + mx_gU_0 \end{bmatrix}$$

$$\mathbf{x} = [v\ r]^T$$

$$\mathbf{F}_R = [Y_\delta\ N_\delta]^T$$

with state vector $\mathbf{x}(t)$, mass and inertia matrix $\mathbf{M}$, hydrodynamic damping matrix $\mathbf{N}$, and rudder force vector $\mathbf{F}_R$, constituting a classic mass-damper system. The latter can readily be arranged in state-space representation for time-invariant linear systems with system matrix $\mathbf{A} = -\mathbf{M}^{-1}\mathbf{N}$, input vector $\mathbf{B} = \mathbf{M}^{-1}\mathbf{F}$ and input $u(t) = \delta$

$$\dot{\mathbf{x}}(t) = \mathbf{A}\mathbf{x}(t) + \mathbf{B}u(t) \tag{2.66}$$

with general solution

$$\mathbf{x}(t) = e^{\mathbf{A}t}\mathbf{x}(0) + \int_0^t e^{\mathbf{A}(t-\tau)}\mathbf{B}u(\tau)\,\mathrm{d}\tau \tag{2.67}$$

In absence of controls Eq. (2.67) reduces to

$$\mathbf{x}(t) = e^{\mathbf{A}t}\mathbf{x}_0 \tag{2.68}$$

and the inherent stability behavior of the dynamic system can be studied by turning to the eigenvalues λ of $\mathbf{A}$, where eigenvalues with positive real part, $\Re(\lambda) > 0$, give way to unbounded amplification in response to arbitrary external excitations. It can be shown from evaluation of the characteristic polynomial

$$|\mathbf{A} - \lambda\mathbf{I}| = 0 \tag{2.69}$$

$$|\mathbf{M}|\,\lambda^2 - (A_{11} + A_{22})\,\lambda + \frac{|\mathbf{N}|}{|\mathbf{M}|^2} = 0 \tag{2.70}$$

and by application of Vieta's rule that stability is guaranteed for

$$-\frac{(A_{11} + A_{22})}{|\mathbf{M}|} > 0 \qquad \wedge \qquad \frac{|\mathbf{N}|}{|\mathbf{M}|^3} > 0 \tag{2.71}$$

where

$$A_{11} = -\frac{1}{|\mathbf{M}|}\begin{vmatrix} M_{22} & M_{12} \\ N_{21} & N_{11} \end{vmatrix}; \quad A_{22} = -\frac{1}{|\mathbf{M}|}\begin{vmatrix} M_{11} & M_{21} \\ N_{12} & N_{22} \end{vmatrix} \tag{2.72}$$

The l.h.s. criterion is always met, because both $-(A_{11} + A_{22})$ and $|\mathbf{M}|$ are always positive for ships, which leaves the stability criterion rest with the sign of the determinant of the damping matrix, which after rearrangement of terms yields

$$|\mathbf{N}| = Y_v\,(Y_r - mU_0)\left(\frac{N_r - mx_gU_0}{Y_r - mU_0} - \frac{N_v}{Y_v}\right) > 0 \tag{2.73}$$

The analysis of hydrodynamic coefficients related to damping

$$Y_v < 0; \qquad N_r < 0; \qquad N_v < 0; \qquad Y_r > 0 \tag{2.74}$$

reveals that $Y_v\,(Y_r - mU_0)$ is always positive. In general, the sign of N_v is ambiguous, as it can indeed be a (albeit small) positive value. The nature of the arrangement of terms in the damping matrix enables an illustrative discussion from a physical standpoint, Abkowitz (1964), Söding (1982c). Rearrangement of terms in Eq. (2.73) allows the expression in terms of the point of attack of the lateral yaw damping force with respect to the longitudinal axis x as

$$l_r = \frac{N_r - mx_gU_0}{Y_r - mU_0} \tag{2.75}$$

and the point of attack of the lateral sway damping force with respect to axis x as

$$l_v = \frac{N_v}{Y_v} \tag{2.76}$$

which furnishes the discussion of straight line stability with the general conclusion that a ship is stable, if the lateral yaw damping force attacks ahead of the lateral sway damping force

$$l_r > l_v \tag{2.77}$$

Available water depth-dependent hydrodynamic coefficients (Fig. 2.17) for KCS were used to study the shallow water effect on straight line stability. Results are organized in a plot showing the ratio l_r/l_v over h/T, Fig. 2.18. A value of one indicates the above defined stability threshold.

2.7 Parameter identification

The presented mathematical models include unknown ship-specific parameters, which in absence of analytic methods for determination require experiments for identification. Parameter identification procedures encompass the design of experiments in accordance with the mathematical model, the conduction of the experimental programme and a suitable mathematical method to synchronize experimental results with the mathematical model. This section deals with identification procedures for multivariat polynomial models relying on captive maneuvering tests on idealized trajectories, albeit large parts of the presented methodology are also applicable to other maneuvering models. In the ship hydrodynamic community a differentiation has been established between so-called indirect and direct parameter identification, which will be defined in the remainder.

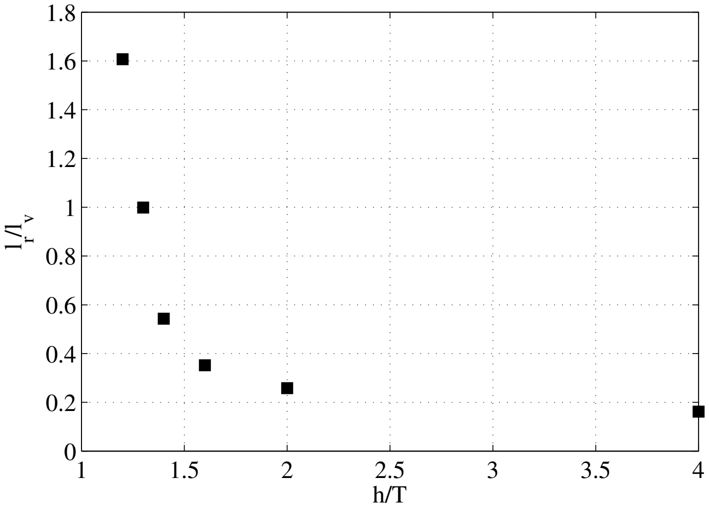

Figure 2.18: Straight line stability analysis for KCS over nondimensional water depth.

2.7.1 Indirect parameter identification in ship maneuvering

Indirect parameter identification draws upon measurements from free-running maneuvering tests available from either sea trials or scale model experiments. In free-running maneuvering tests, the transient position of the ship or ship model (and deducible derivatives) are tracked, and the histories of inputs to the dynamic system (rudder angle, propeller rate of revolution, etc.) are recorded. Different algorithms are in place to adjust the unknown model parameters as to fit the experimental data in optimal fashion, e.g. the method proposed by Kudva and Narendra (1974). Such algorithms predominately seek to minimize errors of the simulated prediction compared to the source test data, but require a fairly good estimate of the entire set of coefficients as a starting point for the iterative procedure. Oltmann (1978) provides examples for applications to ship maneuvering.

2.7.2 Direct parameter identification in ship maneuvering

Direct parameter identification follows a regression analysis of forces and moments from a host of captive maneuvering test on idealized trajectories. The model of the ship is towed on either straight path with prescribed rudder or drift angle, or in steady turning motion. Additionally, pure sway, pure yaw, combined sway-yaw or yaw oscillations with steady drift angle are run. The experimental setup allows for a prescribed constraining of particular modes of motion. Fig. 2.19 is a schematic of a typical CPMC device, Grim et al. (1976). The figure shows a longitudinal section of the towing tank and the alignment of the CPMC.

2.7.3 Remarks on scale effects

While the experimental direct parameter identification approach is confined to model scale ship flows, CFD-based replications can handle both model and full scale investigations. However, such simulations are still performed for model scale only to ensure a common basis for validation of force computations through comparison with model experiments.

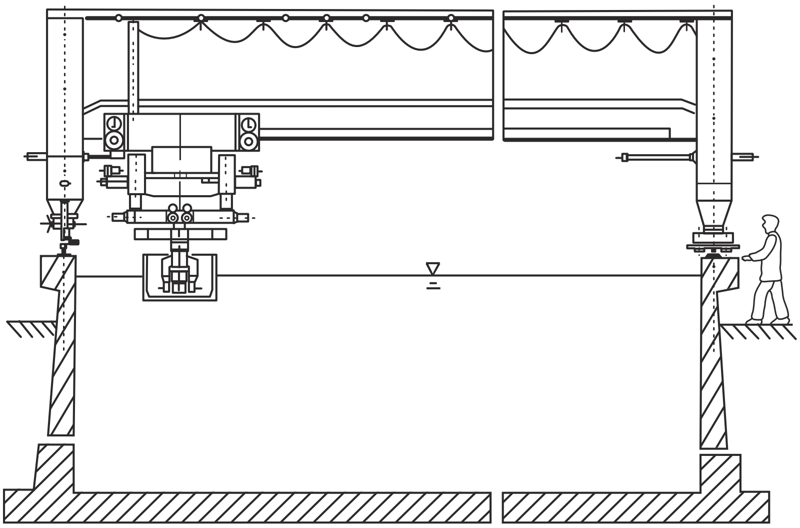

Figure 2.19: Schematic of a CPMC device, Grim et al. (1976).

Extrapolation to full-scale maneuvering predictions relies on Froude similarity. Notwithstanding the fact that the majority of force effects in maneuvering are expected to be pressure-dominated, a discussion of scale effects appears necessary for the framework of the present investigation. CFD is increasingly being used to gain more insights into scale effects involved in maneuvering. El Moctar et al. (2014) give a summary on anticipated influences on maneuvering due to different Reynolds number flows. Main scale effects are associated with different wake numbers, the lack of a friction deduction force in maneuvering experiments and different engine characteristics. These effects will differ between single-screw and twin-screw ships. For a single-screw ship, the higher wake number and propeller loading have opposite effects on rudder forces. Ideally, the errors cancel completely. For a twin-screw ship, the wake effect is weak as the propellers operate in more homogeneous flow. The propeller loading effect remains for twin-screw ships. Hence, twin-screw ships are assumed to have stronger scale effects. Recent studies in deep water conditions reveal experimental evidence that scale effects involved in ship maneuvering in deep water remain moderate, Lantermann et al. (2015).

2.7.4 Analysis of captive steady motion tests

Linear curve fitting based on least-squares minimization is the predominate choice to analyze captive steady motion tests. The classic linear regression problem of generalized form is stated as

$$\mathbf{\Phi}_i = \mathbf{f}\,(\mathbf{x_i})\mathbf{a} + \epsilon_i \qquad i = 1, 2, ...N \tag{2.78}$$

where Φ_i is response of experiment i, $\mathbf{f}\,(\mathbf{x}_i)$ vector of regressors, $\mathbf{x}$ vector of factors, $\mathbf{a}$ vector of regression parameters and ϵ_i random measurement error. Captive static maneuvering tests comprise a host of steady motion runs in which one or more parameters are varied over a desired number of factors

$$\mathbf{x} = [x_1, x_2, ..., x_m]^T \tag{2.79}$$

In experiments time histories of forces and moments of each run are averaged to give steady state results. Repeatability studies involve statistical evaluation. In steady CFD simulations results are used after satisfaction of a defined convergence criterion of a single simulation, not involving random scatter. These results populate response vector $\mathbf{\Phi}$

$$\mathbf{\Phi} = [\Phi_1, \Phi_2, ..., \Phi_N]^T \tag{2.80}$$

Usually, the number of responses m is greater than the number of unknown parameters n, but at least has to be equal. In least-squares approaches, unknown regression parameters

$$\mathbf{a} = [a_0, a_1, ..., a_n]^T \tag{2.81}$$

are found by minimizing the residual vector using the Euclidean norm

$$\min \left\| \mathbf{A}\mathbf{a}^T - \mathbf{\Phi} \right\|_2^2 \tag{2.82}$$

to give the system of linear equations

$$\mathbf{A}^T\mathbf{A}\mathbf{a} = \mathbf{A}^T\mathbf{\Phi} \tag{2.83}$$

where $\mathbf{A}$ is called design matrix and composed according to

$$\mathbf{A} = \begin{bmatrix} f_1(x_1) & f_2(x_1) & \cdots & f_n(x_1) \\ f_1(x_2) & f_2(x_2) & \cdots & f_n(x_2) \\ \vdots & \vdots & \vdots & \vdots \\ f_1(x_m) & f_2(x_m) & \cdots & f_n(x_m) \end{bmatrix} \tag{2.84}$$

The least-squares estimate for $\mathbf{a}$ is

$$\mathbf{a} = \left(\mathbf{A}^T\mathbf{A}\right)^{-1}\mathbf{A}^T\mathbf{\Phi} \tag{2.85}$$

$\mathbf{A}^T\mathbf{A}$ is known as Fisher's information matrix, $\left(\mathbf{A}^T\mathbf{A}\right)^{-1}$ as variance matrix and $\left(\mathbf{A}^T\mathbf{A}\right)^{-1}\mathbf{A}^T$ as Moore-Penrose inverse of $\mathbf{A}$. The goodness of the fit is checked by coefficient of determination R^2

$$R^2 = \frac{\sum_{i=1}^{N}(f(\mathbf{x}_i, \mathbf{a}) - \overline{\Phi})^2}{\sum_{i=1}^{N}(\Phi_i - \overline{\Phi})^2} \tag{2.86}$$

and

$$\overline{\Phi} = \frac{1}{N}\sum_{i=1}^{N}\Phi_i \tag{2.87}$$

R^2 of 1 means all data points actually lay on the curve fit. Upper and lower bounds of confidence p_{cb} for computed factors within above framwork can be obtained by

$$p_{cb} = a \pm t\sqrt{S} \tag{2.88}$$

where a is the fitted coefficient, t is a factor based on Student's distribution function and the anticipated confidence level - a common choice is 95% - and S stems from the product of the diagonal elements of the variance matrix and mean-square error. The difference between the lower and upper confidence bounds indicate the level of uncertainty involved in the curve fitting.

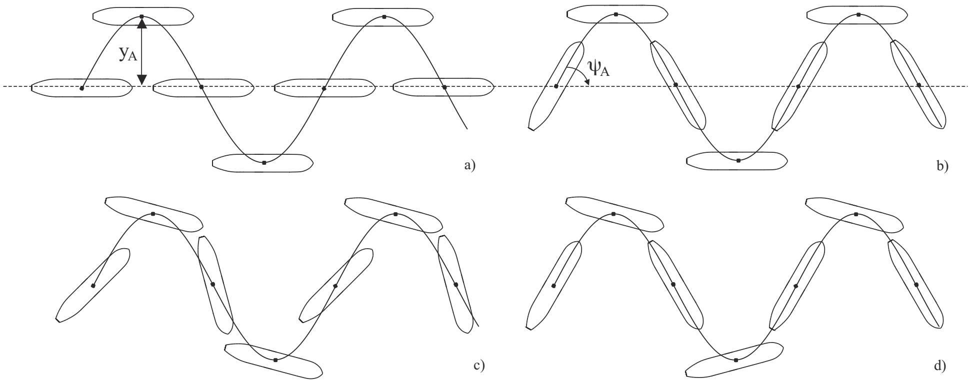

Figure 2.20: Schematic of captive maneuvering tests: *a*) Pure sway, *b*) Pure yaw, *c*) Yaw with drift, *d*) Sway-yaw (asynchronous)

2.7.5 Analysis of captive dynamic motion tests

Captive dynamic maneuvering tests are prescribed harmonic motions in sway, yaw, or a combination of sway-yaw superposed to steady forward motion. Fig. 2.20 illustrates the trajectories and orientation of the model in pure sway, pure yaw, sway-yaw (here asynchronous) or yaw oscillation with fixed drift angle. Above motions are characterized by parameters:

$$\omega' = \frac{\omega L}{U_c} \tag{2.89}$$

$$v' = y_A \omega' \tag{2.90}$$

$$r' = \psi_A \omega' \tag{2.91}$$

where ω' is nondimensional frequency of oscillation stemming from $\omega = 2\pi/T$, where T is oscillation period. Steady forward speed of the carriage device is U_c, y_A is the maximum transverse displacement of the prescribed harmonic trajectory and ψ_A is the maximum yaw angular displacement. ITTC (2014) provides recommendations for the choice of nondimensional frequency ω'. For dynamic tests the periodic time series of measured or computed forces are subjected to Fourier analysis to give force contributions in-phase and out-of-phase with the trajectory. The underlying assumption is that the force record is 2π-periodic and can be approximated by the Fourier series

$$f(t) = a_0 + \sum_{k=1}^{\infty} (a_k \cos kt + b_k \sin kt) \tag{2.92}$$

with coefficients

$$a_0 = \frac{1}{T} \int_0^T f(t)\, \mathrm{d}t \tag{2.93}$$

$$a_k = \frac{2}{T} \int_0^T f(t) \cos kt\, \mathrm{d}t \tag{2.94}$$

$$b_k = \frac{2}{T} \int_0^T f(t) \sin kt\, \mathrm{d}t \tag{2.95}$$

Two methods can be employed for the tests, i.e. the so-called multiple-run and the single-run method. Following the multiple-run method coefficients are found from processing data from a series of tests over a range of frequencies. Coefficients for the mathematical model are then found by extrapolation to zero-frequency. Fig. 2.21 illustrates results for first-order hydrodynamic coefficients related to inertia and damping from a series of pure sway motion tests with a spheroid of typical ship dimensions, Mucha and el Moctar (2013). The l.h.s. plot shows $Y_{\dot{v}}$ as a function of ω^2 and for two amplitudes y_A. $Y_{\dot{v}}$ takes higher norm values the smaller the frequency gets, this trend approaches the reference value of $a_{22}/(\rho\nabla)$ from potential flow theory, Newman (1978). The lowest frequency corresponds to the smallest ITTC recommendation $\omega' = 0.25$ and the highest frequency is equivalent to $\omega' = 4$. Results scatter around the reference value by maximum 5%. The r.h.s. plots show the Fourier decomposed force contributions without normalization as a function of sway velocity $y_A\omega$ and acceleration $y_A\omega^2$. By varying the frequency memory effects and nonlinearities involved in the test procedure can be identified, Renilson (1986). The difference between the amplitude curves indicates memory effects. The deviation of these curves from a straight line reveals nonlinearities. In the single-run method data from a single run are evaluated. Both motion amplitude and oscillation frequency are subject to constraints, e.g. finite tank dimensions. In general, frequencies must be chosen in accordance with the underlying mathematical model, which by virtue of the concept of slow-motion hydrodynamic coefficients prohibits the use of high frequencies. To circumvent non-stationary lift and memory effects a maximum ω' of typically 1-2 for sway and 2-3 for yaw tests is recommended. Comparable values result from considerations on lateral wake patterns. Considerations on errors in the accuracy of the trajectory yield compromise values for ω' in the range of 2-4 for yaw tests, and 0.25-2 for pure sway tests. Additionally, the circular frequency must not be selected in the vicinity of the eigenfrequency of the carriage and measurement system. The same applies to possible resonance with the water in the tank to avoid standing waves. The number of oscillations per test run is again limited by tank dimensions, but should at least be three. In the practical parameter identification setup this guideline almost exclusively prevailed over inference of more sophisticated established identification procedures stemming from system theory, which ensure mathematically that input signals were suitable for the excitation of the dynamics of the system and ensure convergence of the parameter identification procedure, Kudva and Narendra (1974) and Yuan and Wonham (1977). In general, for common ship model sizes between 5-7 m in length, satisfactory practical experience was gained with motion periods around $T = 20$ s, Wolff (1981), Cura (2008). First-order force contributions might be determined from low-amplitude tests, e.g. $v' \leq 0.1$, $r' \leq 0.4$. For higher-order contributions large-amplitude tests must be performed to excite nonlinearities in the responses to prescribed motions, e.g. $v' \geq 0.25$, $r' \geq 0.5$. Special attention is referred to application of captive tests in shallow water, where flow blockage gives rise to dynamic sinkage and trim of ship models, which limits the range of motion amplitudes. Also, the different nature of free surface disturbances brings to the attention the questions of memory effects, and the expected change of flow characteristics with respect to viscosity raises concerns about the validity of Froude scaling.

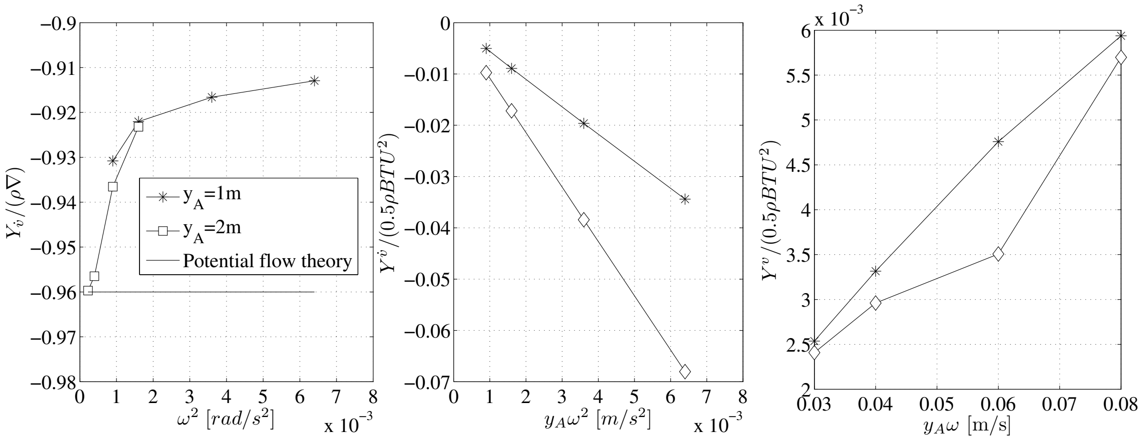

Figure 2.21: Frequency dependence study on hydrodynamic coefficients of a spheroid.

Table 2.1: Required number of test runs in different experimental designs, Sutulo and Guedes Soares (2002).

Number of factors k	1	2	3	4	5	6	7
Classic 3-level	3	9	27	81	243	729	2187
Classic 5-level	5	25	125	625	3125	15625	78125
Classic 7 level	7	49	343	2401	16807	117649	823543
Saturated 3-polynomial	4	10	20	35	56	84	122

2.7.6 Efficient design of maneuvering tests

Efficient setups of maneuvering tests can be achieved through application of the theory of the experimental design and optimization, Hahn (1984) and Steinberg and Hunter (1984). Sutulo and Guedes Soares (2002) provide a discussion on this theory and extend it to the application of optimized designs for ship maneuvering experiments. The present treatise is based on these references. In light of the need for a database of responses to perform the presented linear regression analysis, the problem emerges of rapidly increasing experimental costs with increasing number of independent variables (factors), if the intuitive concept of *one-factor-at-a-time* variation is applied using a certain number of test runs (levels) for each factor. Such designs are called full-factorial designs. If only a few factors are involved, e.g. transverse velocity v, yaw rate r and rudder angle δ (i.e. three factors), the additional experimental cost of full-factorial designs will be moderate. However, if more factors are involved, e.g. forward speed u and water depth h (i.e. five factors) full-factorial designs become uneconomic. A first step to economic designs is the exploration of mathematical properties of the particular regression problem, e.g. a third-order polynomial requires the least-squares evaluation of (just) four responses. However, generating more responses would serve as redundancy and feedback on the validity of the underlying model assumptions. Such designs are called saturated designs. Tab. 2.1 is taken from Sutulo and Guedes Soares (2002) to illustrate the problem in terms of required number of test runs for various design concepts and factors. The number of responses

N to be generated by an experimental programme is linked to the number of regression coefficients n by

$$N = \nu n \tag{2.96}$$

where ν is called redundancy factor. Consistent with introductory discussions $\nu = 1$ is the saturated design and hence, $\nu \geq 1$ always. The concept of the optimized experimental design is to find the optimal distribution of test parameter combinations (factor points) in the design domain. Among the various optimization criteria available, the so-called D-optimality has received special attention, Sutulo and Guedes Soares (2002). The reference leans on the pioneering contributions of the general theory of experimental design and optimization algorithms, e.g. Mitchell (1974) and Welch (1984). The D-criterion seeks to minimize the average variance of the regression parameter estimates, i.e. minimizing the magnitude of the determinant of the variance matrix

$$\min \mathbf{D} = \min \left(\mathbf{A}^T \mathbf{A}\right)^{-1} \tag{2.97}$$

Particular challenges in the optimization are the performance of the actual iterative search algorithm and the selection of initial conditions required to solve the optimization problem . Sutulo and Guedes Soares (2002) demonstrated the efficacy of D-optimized experimental designs for a typical maneuvering model with 20 unknown coefficients relating to three factors β, r and δ, which achieved an eight- to nine-fold saving in the number of test runs compared to a full-factorial design without significantly trading accuracy of the regression.

3. Numerical Fluid Dynamics for Ship Flows

The analysis of fluid motions stems from the mass, momentum and energy conservation equations based on principles of classic continuum mechanics and the generalized transport theorem. It is represented mathematically by a set of partial differential equations. Variations of flow variables transported through a given control domain are seen to be driven by convection, diffusion and sources or sinks within the control domain. For flows around ship the formulation of these equations is relevant for either water only, or for multi-phase flows including air. Upon determination of the flow variables velocity and pressure, integral quantities like forces and moments on ships can be deduced, which enable the computation of rigid body motions in fluids. This chapter presents the fundamental concepts of modeling fluid dynamics for flows around ships, encompassing the discussion of the mathematical framework and techniques for numerical solution with CFD and a Rankine panel Boundary Element Method (BEM). Fundamentals of fluid dynamics and numerical methods are mainly summarized from Fox et al. (2010), Ferziger and Perić (2002) and Newman (1978).

3.1 Definitions and frames of reference

Fluid dynamics are formulated for an earth-fixed inertial reference frame in a Cartesian coordinate system. The x-axis points upstream, the y-axis leftward and the z-axis is directed upwards. The longitudinal fluid particle velocity is denoted by u, transverse velocity v and vertical velocity w. Cartesian positions are included in vector $\mathbf{x}$. The fluid velocity vector is denoted $\mathbf{v}$. Conservation equations are formulated in Eulerian sense for an arbitrary control volume (CV) enclosed by surface S and fixed in space. Face normals $\mathbf{n}$ point out of CVs. When appropriate, index notation is used, where x_i refers to Cartesian coordinates x, y, z and v_i to the Cartesian components of velocity vector $\mathbf{v}$, where $i = 1, 2, 3$.

3.2 Classification of fluid flows for ship hydrodynamics

Prior to formulating flow equations a basic classification of fluids based on their properties is made to find simplified mathematical descriptions tractable for solution within reasonable time in an engineering context. Flows around ships can be assumed incompressible, which states that the ratio of a characteristic fluid velocity u and speed of sound u_s, called Mach number and denoted by $M = u/u_s$, is not greater than 0.3. In incompressible flows fluid density is constant. For gas phases common speed ranges of ships also yield incompressible flows, and it is a reasonable assumption to take air as an ideal gas. Real fluid flows are viscous. The presence of shear stresses between two fluid particles requires steadiness of the tangential velocity between them. At solid boundaries this results in equal velocities of the boundary and the fluid on the boundary surface. Viscous flow is formulated for Newtonian fluids, assuming that shear stresses are a linear function of the wall tangential fluid velocity. Another feature of flows around ships is turbulence. Turbulent flows exhibit random velocity fluctuations in space and time. Both the influence of viscosity and turbulence can be related to the ratio of kinetic to viscous energy, called Reynolds number and denoted by $R_e = uL/\nu$, where L is characteristic length and ν kinematic fluid viscosity. However, for a host of problems in ship hydrodynamics the viscous wall boundary layer is relatively thin and it is a reasonable approach to assume inviscid flow, reducing the computational cost of numerical solutions considerably. Finally, ship flows include waves, the prediction of which requires a formulation for the water surface elevation in space and time, too. Ship waves are gravity surface waves, which are related to the ratio of kinetic to gravitational energy, called Froude number and denoted by $F_n = u/\sqrt{gL}$.

3.3 Formulation of fluid motions

The starting point is the formulation of conservation of mass and momentum. In integral vector notation the mass conservation equation reads

$$\rho \frac{\partial}{\partial t} \int_V \mathrm{d}V + \rho \int_S \mathbf{v} \cdot \mathbf{n} \, \mathrm{d}S = 0 \tag{3.1}$$

In incompressible flows the first term in Eq. (3.1) is zero. However, it is retained here, because it becomes non-zero for moving grid problems which will be discussed later. Eq. (3.1) is called the continuity equation. The conservation of momentum is given by

$$\rho \frac{\partial}{\partial t} \int_V \mathbf{v} \, \mathrm{d}V + \rho \int_S (\mathbf{v}\mathbf{v}) \cdot \mathbf{n} \, \mathrm{d}S = \int_S \mathbf{T} \cdot \mathbf{n} \, \mathrm{d}S + \rho \int_V \mathbf{b} \, \mathrm{d}V \tag{3.2}$$

In Eq. (3.2), $\mathbf{b}$ is a vector describing a force per unit mass and $\mathbf{T}$ denotes the stress tensor

$$\mathbf{T} = p\mathbf{I} + \boldsymbol{\tau} \tag{3.3}$$

where p is pressure and τ the shear stress tensor, which in Cartesian component and index notation reads

$$\tau_{ij} = \mu \left(\frac{\partial v_i}{\partial x_j} + \frac{\partial v_j}{\partial x_i} \right) \tag{3.4}$$

where μ is dynamic viscosity. Eq. (3.1-3.2) form the Navier-Stokes equations.

3.3.1 Turbulence

Turbulent flows are characterized by fluctuations in space and time over a wide range of scales. A dominant property is the mix of transported flow quantities, called turbulent diffusion, because it is responsible for the reduction of kinetic energy. An accurate numerical prediction of turbulent transport of momentum has to encompass the resolution of turbulence-induced eddies of all scales, which can be achieved by solving the Navier-Stokes equations free of any approximations, other than those needed for numerical solution, called Direct Numerical Simulation (DNS). DNS requires a fine discretization of computational domains and is computationally expensive. To reduce this cost approximations for small-scale turbulent structures can be introduced, while large-scale fluctuations are still resolved within the exact framework of flow equations. This approach is known as Large Eddy Simulation (LES). Further trading accuracy against cost, a general averaging of flow equations with respect to time, space or a set of flow realizations can be done. This method refers to Reynolds-averaged Navier Stokes (RANS) equations and has become the choice over DNS and LES for the majority of analyses of flows around ships. Assuming a statistically steady flow the velocity and pressure field can be expressed as the sum of a mean value and its fluctuation, here given symbolically by ϕ

$$\phi\left(\mathbf{x},t\right)=\overline{\phi\left(\mathbf{x},t\right)}+\phi'\left(\mathbf{x},t\right) \tag{3.5}$$

where

$$\overline{\phi\left(\mathbf{x},t\right)}=\frac{1}{T}\int_0^T\phi\left(\mathbf{x},t\right)\,\mathrm{d}t \tag{3.6}$$

and

$$\overline{\phi\left(\mathbf{x},t\right)'}=0 \tag{3.7}$$

The time intervall T ideally runs to infinity but must be sufficiently large compared to the fluctuation time scale. In unsteady flows, the mean value is found from ensemble averaging

$$\overline{\phi\left(\mathbf{x},t\right)}=\frac{1}{N}\sum_{n=1}^{N}\phi_n\left(\mathbf{x},t\right) \tag{3.8}$$

where the number of ensembles N ideally runs to infinity but must be sufficiently large to compensate fluctuation effects. Upon introduction to the Navier-Stokes equations, it follows

$$\rho\frac{\partial}{\partial t}\int_V \mathrm{d}V+\rho\int_S\overline{\mathbf{v}}\cdot\mathbf{n}\,\mathrm{d}S\;=0 \tag{3.9}$$

$$\frac{\partial}{\partial t}\int_V\rho\overline{\mathbf{v}}\,\mathrm{d}V+\int_S\rho\left(\overline{\mathbf{v}}\,\overline{\mathbf{v}}+\overline{\mathbf{v}'\mathbf{v}'}\right)\cdot\mathbf{n}\,\mathrm{d}S\;=\int_S\overline{\mathbf{T}}\cdot\mathbf{n}\,\mathrm{d}S\;+\int_V\rho\mathbf{b}\,\mathrm{d}V \tag{3.10}$$

The emerging $\rho\overline{v_i'v_j'}$ terms are known as the Reynolds stresses. The averaging of the product of these fluctuations does not cancel them out because their correlation function can take a non-zero value. The presence of these terms leads to the so-called closure problem. For practical applications approximations have been formulated. These predominately draw upon semi-empirical approaches like the concept of eddy viscosity. Eddy viscosity models base on the assumption that turbulent effects can be considered as to act like increased viscosity, which in mathematical sense leads to equations of equivalent form as the viscous stresses

$$\rho\overline{v_i'v_j'} = -\mu_t\left(\frac{\partial\overline{v_i}}{\partial x_j} + \frac{\partial\overline{v_j}}{\partial x_i}\right) + \frac{2}{3}\delta_{ij}\rho k \tag{3.11}$$

and

$$\overline{v_i'\phi'} = -\Gamma_t\frac{\partial\overline{\phi}}{\partial x_i} \tag{3.12}$$

where μ_t is turbulent eddy viscosity, k is turbulent kinetic energy, Γ_t is turbulent diffusion coefficient and δ_{ij} is Kronecker delta. Turbulent viscosity and diffusivity are defined as:

$$\mu_t = C_\mu\rho\frac{k^2}{\epsilon} \tag{3.13}$$

and

$$\Gamma_t = \frac{\mu_t}{\sigma_\phi} \tag{3.14}$$

where σ_ϕ is the turbulent Schmidt number which is determined empirically. Two transport equations need to be solved to obtain k and ϵ:

$$\frac{\partial(\rho k)}{\partial t} + \frac{\partial\left(\rho\overline{v_j}k\right)}{\partial x_j} = \frac{\partial}{\partial x_j}\left(\left(\mu + \frac{\mu_t}{\sigma_k}\right)\frac{\partial k}{\partial x_j}\right) + P_k - \rho\epsilon \tag{3.15}$$

$$\frac{\partial(\rho\epsilon)}{\partial t} + \frac{\partial\left(\rho v_j\epsilon\right)}{\partial x_j} = C_{\epsilon1}P_k\frac{\epsilon}{k} - \rho C_{\epsilon2}\frac{\epsilon^2}{k} + \frac{\partial}{\partial x_j}\left(\frac{\mu_t\partial\epsilon}{\sigma_\epsilon\partial x_j}\right) \tag{3.16}$$

where P_k is turbulent production rate, σ_ϵ is turbulent dissipation number and $C_{\epsilon1}$ and $C_{\epsilon2}$ are nondimensional coefficients quantified in Launder and Spalding (1974). This model is known as the $k\epsilon$-model. Another widespread turbulence model which involves two additional transport equations is the $k\omega$-model. Here, ω is specific turbulent dissipation. The two transport equations for k and ω read

$$\frac{\partial(\rho k)}{\partial t} + \frac{\partial\left(\rho\overline{v_j}k\right)}{\partial x_j} = P_k - \rho\beta^*k\omega + \frac{\partial}{\partial x_j}\left[\left(\mu + \frac{\mu_t}{\sigma_k^*}\right)\frac{\partial\omega}{\partial x_j}\right] \tag{3.17}$$

$$\frac{\partial(\rho\omega)}{\partial t} + \frac{\partial\left(\rho v_j\omega\right)}{\partial x_j} = \alpha P_k\frac{\omega}{k} - \rho\beta\omega^2 + \frac{\partial}{\partial x_j}\left[\left(\mu + \frac{\mu_t}{\sigma_\omega^*}\right)\frac{\partial\omega}{\partial x_j}\right] \tag{3.18}$$

with turbulent Prandtl number σ_k and coefficients β, β^* and α, quantified in Wilcox (1988). Within this concept turbulent eddy viscosity is proportional to the ratio of turbulent kinetic energy and specific dissipation:

$$\mu_t \propto \frac{k}{\omega} \tag{3.19}$$

Menter (1994) developed the shear stress transport (SST) $k\omega$-model which seeks to combine the benefits of the $k\omega$- and $k\epsilon$-models by switching between them in the free-stream and near-wall region. Special attention is brought to the near-wall treatment of flow equations, and associated discretization and solution procedures. In light of high and anisotropic fluctuations of turbulent flow variables in the vicinity of walls, a very fine grid resolution normal to the boundary becomes necessary when pursuing to integrate the RANS-equations down to the wall. For high Reynolds number flows with a thin viscous sub-layer fine near-wall grid resolution and the resulting increase in computational effort is unfavorable. In near-wall turbulence modeling, wall functions are alternatively used to circumvent this problem. Wall functions base on the assumption of a logarithmic velocity profile normal to the wall:

$$u^+ = \frac{u_m}{\sqrt{|\tau_w| / \rho}} = \frac{1}{\kappa} ln\left(y^+\right) + B \tag{3.20}$$

where u_m is mean wall-parallel velocity, τ_w wall shear stress, κ von Kármán's constant, y^+ nondimensional wall distance, defined as

$$y^+ = \frac{\rho y \sqrt{|\tau_w| / \rho}}{\mu} \tag{3.21}$$

with y the distance from the wall to the first cell computation point and B a roughness coefficient. Wall-functions are referred to high y^+, or high Reynolds number models. Linear eddy viscosity models have been shown to yield deviations in predicting local and integral flow quantities in presence of vorticity generation from turbulence anisotropy which is pronounced for hulls with distinct streamline curvature, Deng and Visonneau (1999, 2005). Reynolds stress models (RSM) abandon the eddy viscosity concept and seek to compute the stress tensor directly, Launder et al. (1975). Application of RSM is often impaired by numerical stability problems. Rodi (1976) proposed an algebraic stress model (ASM) stemming from the so-called weak equilibrium condition and including a nonlinear treatment of the production-to-dissipation rate ratio. Issues regarding robustness have been circumvented by an explicit solution scheme, Gatski and Speziale (1993). Deng and Visonneau (2005) discuss the application of explicit algebraic stress models (EASM) to flows around ship. Discussions of turbulent flows are presented in detail in Pope (2000).

3.3.2 Pressure coupling

The momentum conservation equations contain the pressure gradient ∇p, but a separate equation to be solved for the pressure is missing. A solution to the problem can be found from the application of projection methods, Chorin (1967). Projection methods decouple the computation of the velocity and pressure field making use of Helmholtz decomposition. The fundamental idea behind Helmholtz decomposition is to look upon a given vector field as the sum of a divergence-free and an irrotational vector field. Following this notion an intermediate velocity field is determined, which at this point does not satisfy the continuity equation, but can be used to map the pressure onto the divergence-free velocity field and correct the velocity and pressure thereafter. The divergence of the momentum conservation equation in conjunction with the continuity equation can be used to derive a Poisson type equation for pressure of the form

$$\frac{\partial}{\partial x_i}\left(\frac{\partial p}{\partial x_i}\right) = -\frac{\partial}{\partial x_i}\left[\frac{\partial\left(\rho v_i v_j\right)}{\partial x_j}\right] \tag{3.22}$$

Instead of this equation the solution method implemented in the solver described in Section 3.5.1 uses a pressure-correction equation which is derived from the discretized continuity and momentum equations following the Semi-Implicit Method for Pressure-linked Equations (SIMPLE) algorithm proposed by Caretto et al. (1972). A compact summary of the iterative solution procedure for incompressible flows is as follows:

1. Solve the linearized momentum equations with a pressure estimate from the previous iteration or time step
2. Find the intermediate velocity field and the emerging mass-imbalance due to violation of the continuity equation
3. Use this mass-imbalance to correct the pressure field and find the velocity field which finally satisfies the continuity equation
4. Repeat 1-3 until both mass and and momentum conservation equations are satisfied

Upon solution for the pressure forces and moments on a ship hull and appendages are finally found from integration of the pressure over the wetted ship and appendages surfaces

$$\mathbf{F} = \int_S (p + \tau_w) \cdot \mathbf{n} \, \mathrm{d}S \tag{3.23}$$

$$\mathbf{M} = \int_S (p + \tau_w) \cdot (\mathbf{r} \times \mathbf{n}) \, \mathrm{d}S \tag{3.24}$$

where **r** denotes the vector comprising the distances of boundary face centroids to the coordinate system's origin.

3.4 Potential flow

The computation of water-depth dependent added mass tensors described in Section 2.5.1 was performed with a panel code in potential flow regime. Besides, the performance of such methods of squat computations was investigated. If viscous effects are assumed negligible the stress tensor in the Navier-Stokes equation can be discarded. This invokes a simplified expression of the momentum conservation equations

$$\frac{\partial}{\partial t} \int_V \rho \mathbf{v} \, \mathrm{d}V + \int_S \rho \, (\mathbf{v}\mathbf{v}) \cdot \mathbf{n} \, \mathrm{d}S = \int_S p\mathbf{I} \cdot \mathbf{n} \, \mathrm{d}S + \int_V \rho \mathbf{b} \, \mathrm{d}V \tag{3.25}$$

which are known as Euler's equations. A further simplifying assumption is irrotational flow. Mathematically, vanishing vorticity of the flow reads

$$\nabla \times \mathbf{v} = 0 \tag{3.26}$$

The conservation of circulation H states that for any given closed body shape moving with an ideal fluid, acted upon only by conservative forces, H is constant, which is known as Kelvin's theorem. It can be shown that, under these assumptions, a velocity potential $\phi(\mathbf{x}, t)$ exists, relating to the velocity vector by

$$\mathbf{v} = \nabla \phi \tag{3.27}$$

Plugged into the continuity equation a Laplace equation for the velocity potential results

$$\Delta\phi = 0 \tag{3.28}$$

where Δ is the Laplace operator. For flows around ships with given constant velocity $\mathbf{U}$ the velocity field within a moving Cartesian coordinate system (z points upwards and is located at the undisturbed free water surface) is expressed by

$$\mathbf{v} = \nabla\phi + [-U, 0, 0]^T\, x \tag{3.29}$$

An equation for the pressure in the inviscid flow regime can be derived from Euler's equations. If the external force term is assumed only to consider gravitational force per unit volume, i.e. $\mathbf{F}_b = [0, 0, \rho g z]$ it follows

$$\frac{\partial\phi}{\partial t} + \frac{1}{2}\left|\nabla\phi\right|^2 = -\frac{1}{\rho}\left(p + \rho g z\right) + C\left(t\right) \tag{3.30}$$

which is known as Bernoulli's equation. The arbitrary constant $C = C(t)$ does not affect the gradient of ϕ and is omitted in the remainder of the summary.

3.4.1 Boundary value problem

Above framework of equations in conjunction with appropriate formulations of flow conditions on the boundaries of the fluid domain constitutes a boundary value problem. The Laplace equation is valid for ϕ in the entire fluid domain. Boundary conditions anticipating expressions for the fluid velocity are set on boundary surfaces, where no fluid is allowed to flow through. The moving ship hull surface is impermeable and it holds

$$(\mathbf{U} + \nabla\phi) \cdot \mathbf{n} = 0 \tag{3.31}$$

For non-moving walls it follows

$$\nabla\phi \cdot \mathbf{n} = 0 \tag{3.32}$$

On the free water surface with vertical displacement $\zeta = \zeta\left(x, y, t\right)$ the total pressure p is equal to atmospheric pressure p_a. With Bernoulli's equation it follows

$$g\zeta + \frac{\partial\phi}{\partial t} + \mathbf{U} \cdot \nabla\phi + \frac{1}{2}\left|\nabla\phi\right|^2 = 0 \tag{3.33}$$

which is known as the dynamic boundary condition. The velocity field is coupled to free surface dynamics by

$$\frac{\partial\zeta}{\partial t} + (\mathbf{U} + \nabla\phi) \cdot \mathbf{n} = 0 \tag{3.34}$$

which is known as the kinematic boundary condition. In unrestricted flow $\nabla\phi$ must go to zero as z goes to infinity. Appropriate radiation conditions have to be fulfilled on the free surface to ensure that ship-induced waves propagate downstream. Examples are given in Jensen (1986).

3.5 Numerical solution of flow equations

Continuous formulations of fluid dynamics have to be brought into discrete representation to allow for numerical solution. The categorization of viscous and inviscid flows leads to the separate treatise of a field and a boundary value problem.

3.5.1 Field method for viscous flows

The commercial CFD application STAR-CCM+ and its Finite Volume (FV) method were applied in this investigation, CD-adapco (2016). Tying in with the main reference, Ferziger and Perić (2002), formulations of the discretized equations are given in generic representation. FV methods compose solution domains of a finite number of CVs which can be arbitrarily shaped. For each CV the conservation equations of the respective flow model are formulated. The solution to a generic transport equation of the form

$$\frac{\partial}{\partial t}\int_V \rho\phi \,\mathrm{d}V + \int_S \rho\phi\mathbf{v}\cdot\mathbf{n}\,\mathrm{d}S = \int_S \Gamma_\phi \nabla\phi\cdot\mathbf{n}\,\mathrm{d}S + \int_V q_\phi\,\mathrm{d}V \tag{3.35}$$

involves approximation of convective and diffusive fluxes which are represented by surface and volume integrals. The discussion and choice of appropriate discretization schemes is driven by the trade of discretization order of accuracy against computational effort. A straightforward application is the midpoint rule, expressing the integral as the product of the mean value, index m, of the integrand over S. For convective terms this reads

$$\int_S \rho\phi\mathbf{v}\cdot\mathbf{n}\,\mathrm{d}S \approx (\rho\phi\mathbf{v})_m S \tag{3.36}$$

Variable values at face centroids are taken to represent the mean value over area S, which represents a second-order approximation of the integrals. Since unknown variables are computed at CV centroids, interpolation has to be used to obtain values at cell faces. In STAR-CCM+ upwind-biased approximations of first and second order are available, based on variable values and their gradients at CV centers upstream of cell faces. The midpoint rule can also be applied to diffusive fluxes

$$\int_S \Gamma_\phi\nabla\phi\cdot\mathbf{n}\,\mathrm{d}S \approx \left(\Gamma_\phi\nabla\phi\right)_m S \tag{3.37}$$

Gradients of ϕ at CV centers are approximated using midpoint rule:

$$\left(\frac{\partial\phi}{\partial x_i}\right)_{P_0} \approx \frac{\int_V \frac{\partial\phi}{\partial x_i}\,\mathrm{d}V}{\Delta V} \tag{3.38}$$

Gauss' theorem is used to convert volume integrals in above equation into surface integrals over all faces of CVs:

$$\frac{\int_V \frac{\partial\phi}{\partial x_i}\,\mathrm{d}V}{\Delta V} = \int_S \phi\mathbf{i}_i\cdot\mathbf{n}\,\mathrm{d}S \tag{3.39}$$

The r.h.s is approximated as in Eq. (3.36). An alternative approach is to express the difference between variable values at CV center P_0 and centers of neighbor CVs P_j as:

$$\phi_{P_j} - \phi_{P_0} = (\nabla\boldsymbol{\phi})_{P_0}\cdot\left(\mathbf{x}_{P_j} - \mathbf{x}_{P_0}\right) \tag{3.40}$$

where $\nabla\boldsymbol{\phi}$ represents gradient vector and $\mathbf{x}$ position vector. Since in 3D the number of neighbors is larger than three, least-square methods are used to explicitly compute three components of the gradient vector (derivatives of $\boldsymbol{\phi}$ w.r.t. x, y, z) from an over-determined system of equations. The gradient at face centroids is computed by linear interpolation from cell centers on either side, Ferziger and Perić (2002).

Boundary conditions

Domain boundaries require assignment of appropriate flow conditions on and beyond boundaries. In the conventional numerical towing tank setup upstream boundaries specify flow velocity, volume fraction and pressure in multi-phase flows, turbulent kinetic energy and dissipation rate. Outlet boundaries are usually positioned far downstream, where zero-gradient conditions can be applied. Velocities are thus obtained by extrapolation from cells next to boundaries and a uniform (for internal flows) or hydrostatic (for free-surface flows) pressure distribution is specified. They can be formulated to take into account inflow in terms of the normal component of boundary recirculation. Conventional remaining domain boundary types are planes of symmetry and so-called slip walls, stating zero normal-face velocity. Walls with zero-tangential face velocity, attributable to friction, are called no-slip walls.

Multiphase flows

The introduced FV method leans on the Volume of Fluid (VoF) method for the modeling of multi-phase flows. The free surface displacement is found from an additional transport equation for volume fraction $\alpha_i = V_i/V$ of fluid phase i and appropriate boundary conditions, Muzaferija and Perić (1999), which reads

$$\frac{\partial}{\partial t}\int_V \alpha_i \,\mathrm{d}V + \int_S \alpha_i \mathbf{v}\cdot\mathbf{n}\,\mathrm{d}S = 0 \tag{3.41}$$

The application of the VoF method imposes fine grid resolution requirements on the phase boundary interface region. High-Resolution Interface Capturing (HRIC) is used to achieve tracking of sharp interfaces between phases. Simpler convection schemes were shown to be highly diffusive in resolving phase volume fraction propagation, Ferziger and Perić (2002). Alternative free surface treatment in CFD is described in the introduced literature.

Unsteady flows

For time-varying flows an implicit time integration scheme at three time levels n is used

$$\frac{d}{dt}\int_V \rho\phi \,\mathrm{d}V \approx \frac{3(\rho\phi)^{n+1} - 4(\rho\phi)^{n} + (\rho\phi)^{n-1}}{2\Delta t} V \tag{3.42}$$

where Δt is time step. The Courant number C_{fl} is introduced as

$$C_{fl} = \frac{u\Delta t}{\Delta x} \tag{3.43}$$

where Δx is grid spacing. Unlike in explicit integration schemes a stability criterion w.r.t. C_{fl} does not exists for implicit schemes. However, consistent with aforementioned properties of HRIC schemes there are restrictions for C_{fl} for flows involving the free surface.

Solution of the algebraic system of equations

Having found approximations for all terms of the conservation equations enables for solving a resulting algebraic equation of the form

$$C_{P_0}\phi_{P_0} + \sum_{j=1}^{N} C_{P_j}\phi_{P_j} = b_{P_0} \tag{3.44}$$

where ϕ_{P_0} are unknown variables in centers of CVs and ϕ_{P_j} are unknown variables in neighboring CVs j. Coefficients C_{P_0}, C_{P_j}, b_{P_0} stem from approximations involved in Eq. (3.35). The so-constituted system of nonlinear coupled equations is solved by an iterative algorithm, which successively solves for one dependent variable and came to be called segregated solution scheme. Upon linearization of Eq. (3.44) using Picard iterations a system of equations is obtained with a sparse, diagonally dominant system matrix, which can be handled efficiently with appropriate solvers. In light of the anticipated great dimensions of the resulting matrices, direct solvers based on Gauss elimination or LU decomposition are not suitable. The present method uses algebraic multi-grid methods and conjugate gradient type solvers, CD-adapco (2016). This particular solution procedure is referred to so-called inner iterations. The update of coefficients based on the solution of Eq. (3.44) is repeated in so-called outer iterations until a prescribed convergence criterion is met. The present method checks for the decrease of the absolute normalized residual R_ϕ^k

$$R_\phi^k = \frac{\sum\limits_{i=1}^{N} \left| b_{P_0} - C_{P_0}\phi_{P_0} + \sum\limits_{j=1}^{N_j} C_{P_j}\phi_{P_j} \right|}{\sum\limits_{i=1}^{N_j} \left| C_{P_0}\phi_{P_0} \right|} \leq \epsilon \tag{3.45}$$

where k is running index of iterations and ϵ a prescribed fraction of the initial value of the absolute normalized residual R_ϕ^0. When using unstructured grids, special modifications have to be applied in the overall solution procedure to account for arising irregularities in the relations between neighboring CVs, Ferziger and Perić (2002).

Rigid body motions

Various hydrodynamic studies of ship maneuverability require modeling of rigid body motions. For direct consideration of rigid body motions in response to fluid forces the evaluation of Eq. (3.23-3.24) is coupled to rigid body Eq. (2.10-2.11) and solved using appropriate integration schemes. Often it is desirable to constrain motions, if their influence on trajectories is assumed negligible. In this case rigid body equations of motion are modified in terms of zero-displacement conditions in the respective modes of motion. Details on practical realization are given in Hadžić et al. (2002) and Brunswig and el Moctar (2004).

Global motion of solution domains

Motions in absence of flow restrictions can be considered by relative velocities and reformulation in moving reference frames. Then, the form of equations is no longer in

Eulerian, but coupled Arbitrary Lagrangian-Eulerian (ALE) sense. This approach is not per se conserving mass, and to guarantee the satisfaction of the continuity equation an additional condition demanding the conservation of space is set

$$\frac{\partial}{\partial t}\int_V \mathrm{d}V - \rho\int_S \mathbf{v}_S \,\mathrm{d}S = 0 \tag{3.46}$$

where $\mathbf{v}_S$ is surface velocity. A rigorous derivation of so-defined flow equations is given in Ferziger and Perić (2002).

Rotating body motions

Moving reference frames can be taken advantage of in a host of rotating body motion problems which are assumed steady or weakly unsteady. Classic applications refer to rotor-stator problems, as encountered in the replication of open water propeller performance tests. The solution domain is composed of an axially symmetric inner sub-domain, within which the rotation of the flow is defined and which is matched to the outer flow field at interfaces. A more complex approach uses sliding grid interfaces. Here, the inner sub-domain performs prescribed rotations and outer and inner flow fields are matched by means of the generalized grid interface (GGI) technique. The least expensive and most simplified method to consider the effect of propellers in ship flows stems from introduction of body forces to the momentum equations in the propeller region, circumventing both the modeling of the propeller geometry and realization of rotation. Rudimentary body force propellers take into account only radially distributed source terms based on interpolation from apriori determined rotor performance curves using a mean inflow velocity ahead of the propeller region. More elaborate techniques consider the angle of attack and change in radial distribution of the aft-body flow, which in turn requires generation of appropriate look-up tables. The latter approach allows for efficient synergies with BEM, e.g. based on lifting line theory or Vortex-Lattice methods, which are able to give thrust and torque coefficients in a time-efficient manner. The capabilities and performance of CFD methods to generate propeller performance curves were addressed in previous chapters. The particular method applied in the present investigation defines the body force propeller region in terms of its position, thickness t_p, hub ratio r_h and operational point (here prescription of rate of revolutions). A small distance upstream of the propeller region a polar plane is discretized in accordance with the dimensions of the propeller region and used to compute radially distributed mean inflow velocities to determine advance number J, which in turn feeds the interpolation for K_T and K_Q, as per Eq. (2.47-2.48). The radial distribution of body forces stems from the vortex theory of Goldstein (1929), whereupon

$$F_{b,x} = A_x r^s \sqrt{1-r^s} \tag{3.47}$$

$$F_{b,\theta} = A_\theta \frac{r^s\sqrt{1-r^s}}{r^s(1-r_h)+r_h} \tag{3.48}$$

and

$$r^s = \frac{(\frac{r}{r_p} - r_h)}{(1-r_h)} \tag{3.49}$$

where r is radial position and r_p radial position of the propeller tip. Longitudinal body force is $F_{b,x}$ and tangential body force is $F_{b,\theta}$. Coefficients A_x and A_θ are quantified in CD-adapco (2016).

Grid deformation

Relative motions between bodies and boundaries can be modeled by deformation of the computational grid in response to rigid body displacements, known as mesh morphing. The deformation imposed on the numerical grid uses multi-quadratic interpolation, Hardy (1990), moving vertices of CVs, but retaining the overall grid topology. The actual motion of vertices follows

$$\mathbf{d}\left(\mathbf{x}\right) = \sum_{j=1}^{N} r_{ij}\boldsymbol{\lambda}_j + \boldsymbol{\alpha} \tag{3.50}$$

where $\mathbf{d}$ is known displacement vector, $\mathbf{x}$ vertex position vector, r_{ij} radial basis function acting on respective entries i, j of expansion vector $\boldsymbol{\lambda}$ and $\boldsymbol{\alpha}$ is a vector to bind excessive expansion for large $\mathbf{x}$. Appropriate conditions have to be set at domain boundaries. The method of the present study allows for definition of a thinned vertex field to be taken into account for the morphing procedure, which spares out a prescribed number of control points in the evaluation of Eq. (3.50). Challenges refer to computational expense, because matrices involved in the morphing process can become dense, and grid resolution requirements are imposed in conjunction with motion amplitudes. CVs which are being stretched to the point of taking unfavorable aspect ratios or zero volume, lead to the disintegration of simulations. The algorithm implemented in the overall solution method involves application of the Fast Multi-pole Method (FMM, Beatson et. al, 2006) and a conjugate gradient method, which is preconditioned with Krylov subspace algorithms, Faul et al. (2005), Gumerov and Duraiswami (2007).

Overset grids

Overset grid methods allow multiple grids within one computational background domain to overlap arbitrarily, thus enabling relative body motion simulations. The method was proposed, developed and discussed by Atta (1981), Benek et al. (1983), Dougherty (1985), Heshaw (1985), Chesshire and Heshaw (1990) and Hadžić (2005). Overlapping grids are interconnected by classification into discretization, interpolation and inactive (hole) cells in overlapping regions. Discretization cells are involved in the approximation of governing flow equations and take the role of a donor, interpolation cells take up the information on the state of the flow from the donor cells and represent the receptor, while inactive cells are separated from the computational domain by virtual boundaries in the background mesh. The interpolation is based on the general form

$$\phi_{P_i} = \sum_{j=1}^{N_D} \alpha_{w_k}\phi_{D_k} \tag{3.51}$$

where ϕ_{P_i} is the interpolated function value at node P_i, ϕ_{D_k} is the donor function value and α_{w_k} a weighting factor stemming from the employed interpolation scheme, which are usually of linear type. The method is not per se mass conservative, because mass fluxes are not balanced explicitly in the framework of the interpolation schemes. Methods to ensure conservative inter-grid interpolation are discussed in Chesshire and Heshaw (1994). In the present method mass conservation can be enforced at overset interfaces by balancing mass in the pressure-correction equation or by balancing fluxes at interface boundaries, CD-adapco (2016). Special techniques are available for close proximity configurations or intersection of overset and background meshes.

3.5.2 Boundary Element Method for potential flows

The method GLRankine was applied in this investigation for the computation of water-depth dependent added mass tensors and squat in steady forward motion. The following descriptions stem from Söding (1993, 2012), von Graefe (2015) and references therein. In boundary element methods, only the boundaries of the solution domain are discretized. GLRankine relies on unstructured first-order triangular panels on the submerged ship surface and block-structured quadrilateral panels are employed on the free surface. Rankine sources are distributed following the desingularization method. The Laplacian is satisfied by the formulation of the induced potential

$$G\left(\mathbf{x}, \xi_j\right) = \frac{4\pi}{\left|\mathbf{x} - \xi_j\right|} \tag{3.52}$$

where ξ_j denotes source location points, and the linear combination

$$\phi = \phi\left(\mathbf{x}\right) = \sum_{j=1}^{n} q_j G\left(\mathbf{x}, \xi_j\right) \tag{3.53}$$

with unknown strengths q_j, consistent with the method of fundamental solutions, Fairweather and Karageorghis (1998). Following the desingularization method the location of sources ξ is at small distances from each panel outside of the fluid domain, and boundary conditions are fulfilled in average over each panel. Source strengths q_j are chosen to enforce the body boundary conditions, introduced by Eq. (3.31-3.34). The detailed solution algorithm is presented in von Graefe (2015).

Pressure computation

Knowledge of ϕ enables computation of pressure p at each panel τ with Bernoulli's equation for steady flow

$$p = \frac{1}{2}\rho\left(|\mathbf{U}|^2 - |\mathbf{U} + \nabla\phi|^2\right) - \rho g z \tag{3.54}$$

Hydrostatic pressure is evaluated exactly through knowledge of the vertical component z at each panel's center. According to Söding (1993) the dynamic pressure is obtained with average velocity $\overline{\nabla\phi}$, which is available through evaluation of the tangential velocity at each panel found from linear approximation of potentials at each corner of the panel.

Free surface conditions

In order to fulfill boundary conditions on the free surface, the residuum r_i for panel τ_i is formulated, equivalent to the flux through a panel

$$r_i = \sum_{j=1}^{n} q_j \int_{\tau_i} G\left(\mathbf{x}, \xi_j\right) \cdot \mathbf{n}\, \mathrm{d}S - U \int_{\tau_i} \mathbf{n}\, \mathrm{d}S = 0 \tag{3.55}$$

An iterative solution algorithm of Newton-type is used

$$\sum_{j=1}^{n} \frac{dr_i}{dq_j} \Delta q_j \nu + r_i^{\nu} = 0 \tag{3.56}$$

where source strengths are updated within each iteration ν. To account for dependence of $\zeta = \zeta\,(x, y)$ on potential ϕ, being a function of q_j, the derivative of the residuum on the free surface is introduced

$$\frac{dr_i}{dq_j} = \frac{\partial r_i}{\partial q_j} + \frac{\partial r_i}{\partial \zeta} \frac{\partial \zeta}{\partial q_j} \tag{3.57}$$

Details on the numerical treatment are given in von Graefe (2015). After each iteration ζ is updated.

Radiation condition

Radiation conditions ensure physically consistent solutions of the boundary value problem by enforcing downstream propagating ship waves. The present method draws upon the technique of shifting sources downstream, which is free of numerical damping, Jensen (1986). Associated challenges for numerical solution due to reconditioning of the equation system are covered by von Graefe (2015).

Other boundary conditions

For low Froude numbers ship waves become shorter, which results in finer discretization requirements for the free surface. Consistent with the double-body approach a symmetry plane condition of Neumann-type can be employed at the height of the free surface

$$\frac{\partial \phi}{\partial z} = 0 \tag{3.58}$$

using the method of images, Newman (1978). In this approach, no panels are needed on the free surface level, and boundary conditions are fulfilled automatically using images of Rankine sources. This approach can be used to model any plane boundary parallel to the direction of inflow. Alternatively, for channel walls or flat bottoms, triangular panels with Neumann-type conditions might be used. For high Froude numbers the free surface is assumed to be attached to the lower edge of the ship transom and the atmospheric pressure assumption is valid. In the present method free surface panels are adapted to the transom lower edge, Raven (1996). Breaking waves are suppressed by artificial wave damping, von Graefe (2015).

Computation of trim and sinkage

Trim and sinkage are found upon determination of forces and moments from hydrostatic balancing. The equilibrium floating position is found if the following iteration converges and the vertical force Z and the pitch moment M become zero

$$\begin{bmatrix} Z^\nu \\ M^\nu \end{bmatrix} + \begin{bmatrix} \Delta Z^\nu \\ \Delta M^\nu \end{bmatrix} = 0 \tag{3.59}$$

where ΔZ^ν and ΔM^ν are the change of force and moment due to the change in midship sinkage Δz^ν and trim angle $\Delta\theta^\nu$ in iteration step ν. The iteration scheme follows the linear equations system constituted by

$$\begin{bmatrix} \Delta Z^\nu \\ \Delta M^\nu \end{bmatrix} = \begin{bmatrix} \frac{\Delta Z}{\Delta z} & \frac{\Delta Z}{\Delta\theta} \\ \frac{\Delta M}{\Delta z} & \frac{\Delta M}{\Delta\theta} \end{bmatrix} \begin{bmatrix} \Delta z^\nu \\ \Delta\theta^\nu \end{bmatrix} \tag{3.60}$$

Assuming dominance of hydrostatic terms ΔZ and ΔM are approximated accordingly to yield

$$\begin{bmatrix} Z^\nu \\ M^\nu \end{bmatrix} = \rho g \begin{bmatrix} A_W & A_W x_{cwl} \\ A_W x_{cwl} & I_{xwl} \end{bmatrix} \begin{bmatrix} \Delta z^\nu \\ \Delta\theta^\nu \end{bmatrix} \tag{3.61}$$

where A_W is waterline area, x_{cwl} waterline area centroid and I_{xwl} waterline second moment of area. The total change of trim and sinkage is finally found from integration over all iteration steps. Upon determination of the new ship position and orientation, the dynamic boundary condition is used to find the new free surface elevation, waterline and grid positions. The convergence criterion is a decrease of the maximum residuum to 2% of maximum residuum of the first two iterations, and a variation of the wave resistance of less than 1% between two successive iterations.

3.6 Verification and validation

Verification and validation exercises refer to the analysis of numerical simulation results in terms of their uncertainties and comparison to benchmark experimental data. The objective is to obtain quantification of the fidelity of a numerical simulation result. Verification describes the assessment of uncertainties involved in the numerical simulation. Main sources of error and uncertainty are iterations, spatial and temporal discretization. Other parameters might be added in special cases. Validation describes the comparison of numerical simulation results to experimental benchmark data involving estimated experimental uncertainties.

3.6.1 Recommended procedures and guidelines

ITCC (2002) provides recommended procedures and guidelines on verification and validation in the context of uncertainty analysis in CFD. Further reading refers to Roache (1998) and references within ITTC (2002). The recommended approach is to assess numerical errors in regard to iterations, grid spacing, time steps and other parameters considered a source of error to arrive at an aggregated numerical solution error δ^*_{SN}, which is used to correct a given simulation result S

$$S_C = S - \delta^*_{SN} \tag{3.62}$$

where S_C is the resulting numerical benchmark result. Numerical errors are to be obtained from parameter refinement studies, varying one parameter at a time. Refinement ratio r_k is defined as

$$r_k = \frac{\Delta x_{k,m}}{\Delta x_{k,m-1}} \tag{3.63}$$

where $m \geq 2$ is the refinement stage index of k^{th} input parameter Δx. At least three stages are required to obtain convergence ratio

$$R_k = \frac{S_{k_2} - S_{k_1}}{S_{k_3} - S_{k_2}} \tag{3.64}$$

which yields either monotonic convergence ($0 < R_k < 1$), oscillatory behavior ($R_k < 0$) or divergence ($R_k > 1$). In case of monotonic convergence generalized Richardson extrapolation is used to estimate the leading order term of the power series expansion of δ^*_k. Estimated numerical error and order of accuracy follow as per

$$p_k = \frac{\ln R_k^{-1}}{\ln r_k} \tag{3.65}$$

and

$$\delta^*_{k_1} = \frac{S_{k_2} - S_{k_1}}{r_k^{p_k} - 1} \tag{3.66}$$

Formulations change with number of available solution and resulting change in the order of the power expansion. Uncertainties and correction factors are derived on the basis of Eq. (3.65-3.66), ITTC (2002). Validation is based on the comparison error E

$$E = D - S \tag{3.67}$$

between experimental data D and simulation result S taking into account determined errors and uncertainties.

3.6.2 Alternative procedure

Problems of the method recommended by ITTC (2002) concerning application to transient flow computations were addressed by Oberhagemann (2016). Given the discretization of both space and time, it would be reasonable to pursue refinement strategies with constant C_{fl} number in order to uniformly consider both grid spacing and time integration step. Oberhagemann (2016) showed that non-uniform refinement was shown to conflict with bounds of solution validity in the asymptotic approach region. The references provides an altered formulation of discretization error estimation.

4. Formulation of Mathematical Models for Maneuvering

The general review of established concepts for the mathematical modeling of maneuvering is concluded with the derivation of a model using multivariat polynomials for the prediction of arbitrary rudder maneuvers in deep and shallow water. Available sets of coefficients from captive maneuvering experiments were used to perform system dynamic and sensitivity analyses to establish model structures which are relevant for the CFD-based parameter identification procedure of the general simulation-based maneuvering prediction framework.

4.1 Maneuvering model for deep water conditions

In light of the abundance of published and validated maneuvering models using multivariat polynomials, it appeared advisable to draw the development upon an appropriate candidate model. The model presented in Wolff (1981) was chosen to be the baseline of this investigation. The generalized modified form of hydrodynamic forces in the maneuvering equations is presented in Eq. (4.1), where F stands for either X, Y, N and is leveled with appropriate powers of u. The model of Eq. (4.1) includes previously discussed modifications and extensions to Abkowitz's (1964) model as a result of extensive experimental studies into the effect of nonlinearities and frequency dependencies in the course of SFB 98. Wolff (1981) determined maneuvering properties of five representative ship models based on captive model tests. Wolff's work has been validated using both free-running model and full-scale measurements to verify the reconstruction of the time responses of the real systems. The purpose was to provide a benchmark for such model tests and the maneuvering performance of a tanker, a bulker, a Mariner ship, a containership and a ferry. Based on the evaluation of captive maneuvering tests through stepwise and multiple least-squares regression analysis a formal decision was made on which terms in Eq. (4.1) were retained or discarded for each particular ship type. The method provided the reduction of variance with respect to force contributions as a measure of goodness of curve fitting. Details of the particular procedure are given in Wolff (1981) and Oltmann (1978). Parts of the present investigation were discussed in Mucha and el Moctar (2015).

$$
\begin{aligned}
F &= f\left(u, v, r, \dot{u}, \dot{v}, \dot{r}, \delta\right) \\
&= F_0 u^2 + F_u u \Delta u + F_{uu} \Delta u^2 + F_{uuu} \frac{\Delta u^3}{u} \\
&+ F_{\dot{u}} \dot{u} + F_{\dot{u}\dot{u}} \frac{\dot{u}^2}{u^2} + F_{\dot{u}\dot{u}\dot{u}} \frac{\dot{u}^3}{u^4} + F_{\dot{u}u} \frac{\dot{u}\Delta u}{u} + F_{\dot{u}uu} \frac{\dot{u}\Delta u^2}{u^2} \\
&+ F_v uv + F_{vv} v^2 + F_{vvv} \frac{v^3}{u} + F_{vvvv} \frac{v^4}{u^2} + F_{vvvvv} \frac{v^5}{u^3} \\
&+ F_{v|v|} v \left|v\right| \\
&+ F_{\dot{v}} \dot{v} + F_{\dot{v}\dot{v}} \frac{\dot{v}^2}{u^2} + F_{\dot{v}\dot{v}\dot{v}} \frac{\dot{v}^3}{u^4} + F_{\dot{v}v} \frac{\dot{v}v}{u} + F_{\dot{v}vv} \frac{\dot{v}v^2}{u^2} \\
&+ F_r ur + F_{rr} r^2 + F_{rrr} \frac{r^3}{u} + F_{rrrr} \frac{r^4}{u^2} + F_{rrrrr} \frac{r^5}{u^3} \\
&+ F_{r|r|} r \left|r\right| \\
&+ F_{\dot{r}} \dot{r} + F_{\dot{r}\dot{r}} \frac{\dot{r}^2}{u^2} + F_{\dot{r}\dot{r}\dot{r}} \frac{\dot{r}^3}{u^4} + F_{\dot{r}r} \frac{\dot{r}r}{u} + F_{\dot{r}rr} \frac{\dot{r}r^2}{u^2} \\
&+ F_\delta u^2 \delta + F_{\delta\delta} u^2 \delta^2 + F_{\delta\delta\delta} u^2 \delta^3 + F_{\delta\delta\delta\delta} u^2 \delta^4 + F_{\delta\delta\delta\delta\delta} u^2 \delta^5 \\
&+ F_{\delta|\delta|} u^2 \delta \left|\delta\right| \\
&+ F_{vu} v \Delta u + F_{vuu} \frac{v \Delta u^2}{u} + F_{vvu} \frac{v^2 \Delta u}{u} + F_{vvvu} \frac{v^3 \Delta u}{u^2} + F_{v|v|u} v \left|v\right| \frac{\Delta u}{u} \\
&+ F_{ru} r \Delta u + F_{ruu} \frac{r \Delta u^2}{u} + F_{rru} \frac{r^2 \Delta u}{u} + F_{rrru} \frac{r^3 \Delta u}{u^2} + F_{r|r|u} r \left|r\right| \frac{\Delta u}{u} \\
&+ F_{\delta u} u \delta \Delta u + F_{\delta uu} \delta \Delta u^2 + F_{\delta\delta u} u \delta^2 \Delta u + F_{\delta\delta\delta u} u \delta^3 \Delta u + F_{\delta|\delta|u} u \delta \left|\delta\right| \Delta u \\
&+ F_{vr} vr + F_{vrr} \frac{vr^2}{u} + F_{vrrr} \frac{vr^3}{u^2} + F_{vvr} \frac{v^2 r}{u} + F_{vvrr} \frac{v^2 r^2}{u^2} \\
&+ F_{vvvr} \frac{v^3 r}{u^2} + F_{v|r|} v \left|r\right| + F_{|v|r} \left|v\right| r \\
&+ F_{v\delta} uv\delta + F_{v\delta\delta} uv\delta^2 + F_{vv\delta} v^2 \delta + F_{|v|\delta} u \left|v\right| \delta + F_{v|\delta|} uv \left|\delta\right| \\
&+ F_{r\delta} ur\delta + F_{r\delta\delta} ur\delta^2 + F_{rr\delta} r^2 \delta + F_{|r|\delta} u \left|r\right| \delta + F_{r|\delta|} ur \left|\delta\right| \\
&+ F_{vru} \frac{vr\Delta u}{u} + F_{v\delta u} v\delta\Delta u + F_{r\delta u} r\delta\Delta u + F_{vr\delta} vr\delta
\end{aligned}
\tag{4.1}
$$

In arriving at a model structure for the purposes of the present work above model was explored in terms of performance and sensitivities, and additional criteria were formulated. The minimum complexity principle was pursued, which seeks to involve as few regressors as possible without forfeiting accuracy, and to avoid excessive higher-order terms to enhance robustness, Sutulo and Kim (1998). Further incentives to arrive at models with such characteristics emerged from considerations on parameter identification procedures in the context of the model extension to various shallow water depths, which involve an additional factor in the regression problem and increased costs. A framework for simulation of arbitrary rudder maneuvers was developed. Maneuvering Eq. (2.20-2.22) were rearranged for rigid body accelerations and integrated in time using Euler's difference method. The solution was performed in nondimensional representation. The entire range of published turning and zig-zag maneuvers was simulated to verify trajectories and temporal evolution of state variables.

4.1.1 Model test setup and conditions

The models were free to heave and pitch, but otherwise constrained and fixed to the CPMC. The propeller rates for the investigated test speeds were chosen for self-propulsion of the ship models. The tanker, the Mariner ship and the twin-screw ferry were investigated. The tanker represented a bluff single-screw ship, the Mariner ship a more slender and widely studied ship. The twin-screw ferry was of interest because the presence of two propellers and associated symmetry properties affect the mathematical model. Their main particulars are given in Tab. 4.1 and their lines plans shown in Fig. 4.1. Hydrodynamic coefficients are presented in Tab. 8.1. The tanker was fitted with a simplex rudder, the Mariner ship with a semi-spade rudder and the ferry with a semi-spade rudder with fixed fin.

4.1.2 Validation of time responses

Simulations for all ships using coefficients of Tab. 8.1 were validated using free-running zig-zag maneuvers available in Wolff (1981). Besides, for the Mariner ship a host of results from model tests (Oltmann, 1979) and sea trial measurement campaigns (Morse and Price, 1961) was available. A detailed evaluation of the comparison is given in Oltmann (1979). Agreement with free-running model tests was altogether good. Maneuvering performance of the full-scale tanker was investigated by Ogawa (1971) and shows fair agreement to predictions based on Wolff's simulations. Exemplary, Fig. 4.2 shows the simulated zig-zag maneuver for the model of the Mariner ship compared to Wolff's measurements. Fig. 4.3 illustrates results from the full-scale turning maneuver simulation.

Table 4.1: Main particulars: length between perpendiculars L, beam at waterline B_{wl}, draft T_m, block coefficient C_B, longitudinal position of centre of gravity x_g measured from amidships, approach speed U_0, scale factor λ, propeller diameter D_P, disc ratio A_e/A_0, pitch ratio $P_{0.7}/D_P$

	L [m]	B_{wl} [m]	T_m [m]	C_B [-]	x_g [m]	U_0 [kn]	λ [-]
Tanker	290.00	47.50	16.00	0.81	5.18	15	35
Mariner	160.93	23.18	7.45	0.60	-3.48	15	25
Ferry	139.60	16.77	5.90	0.64	-2.38	20	16
	No. of Propellers	D_P [m]	A_e/A_0 [-]	$P_{0.7}/D_P$ [-]			
Tanker	1	7.91	0.60	0.75			
Mariner	1	6.70	0.66	0.96			
Ferry	2	3.44	0.52	1.14			

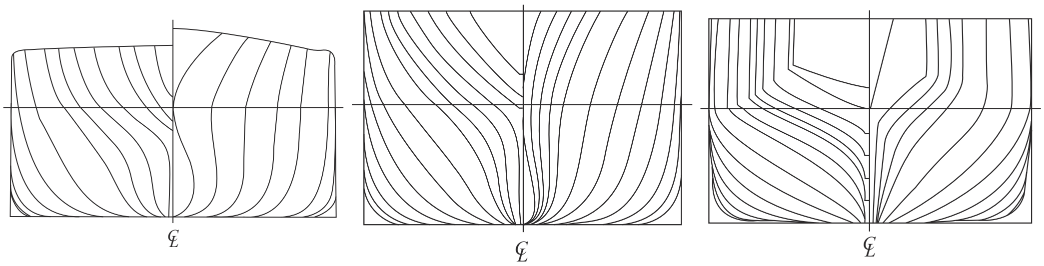

Figure 4.1: Body plans of the tanker, Mariner ship and ferry (from left to right).

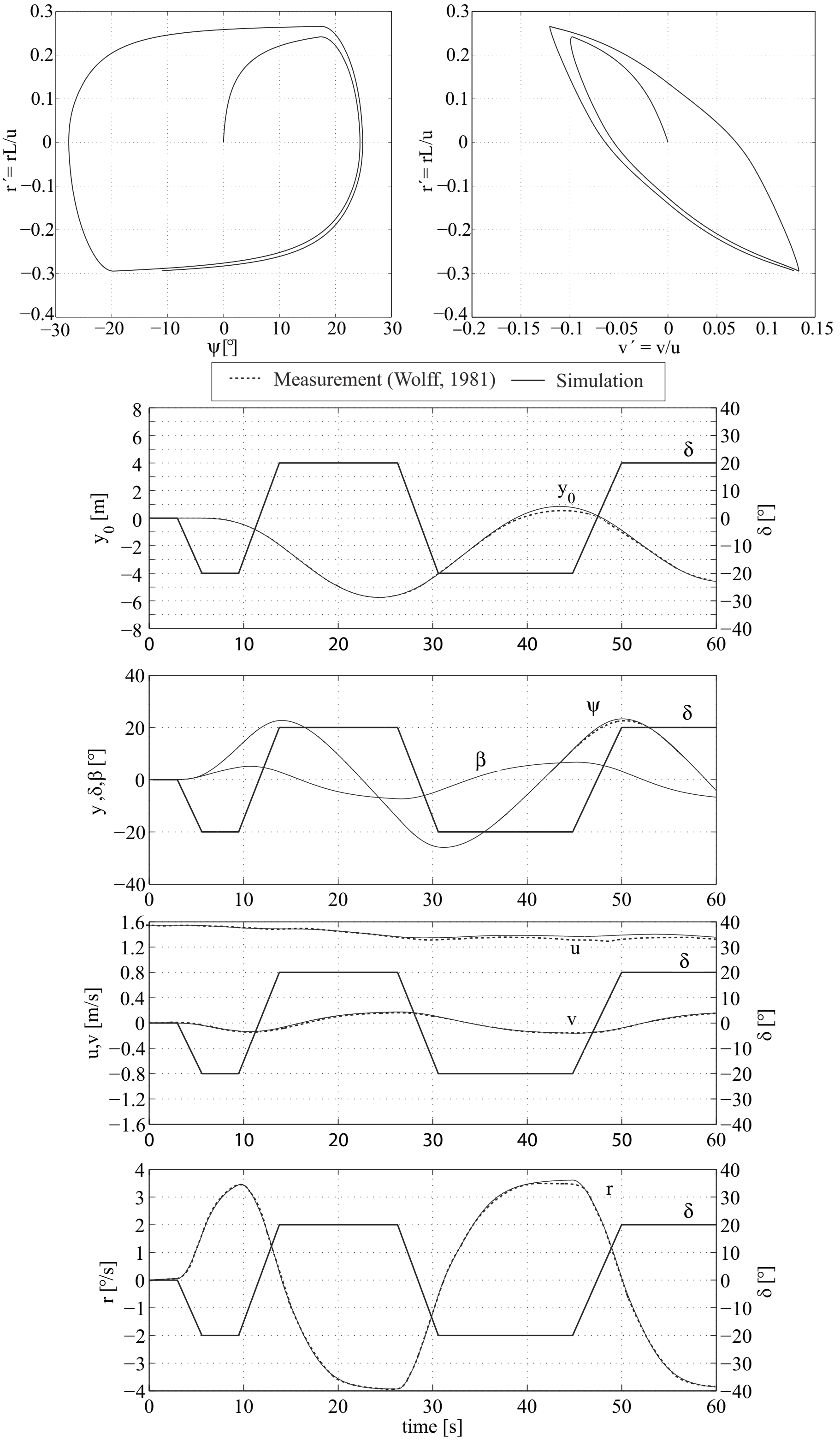

Figure 4.2: Simulation of the 20/10 zig-zag maneuver for the Mariner ship at model scale. Phase plans (top) and time histories of state variables and rudder angle (bottom).

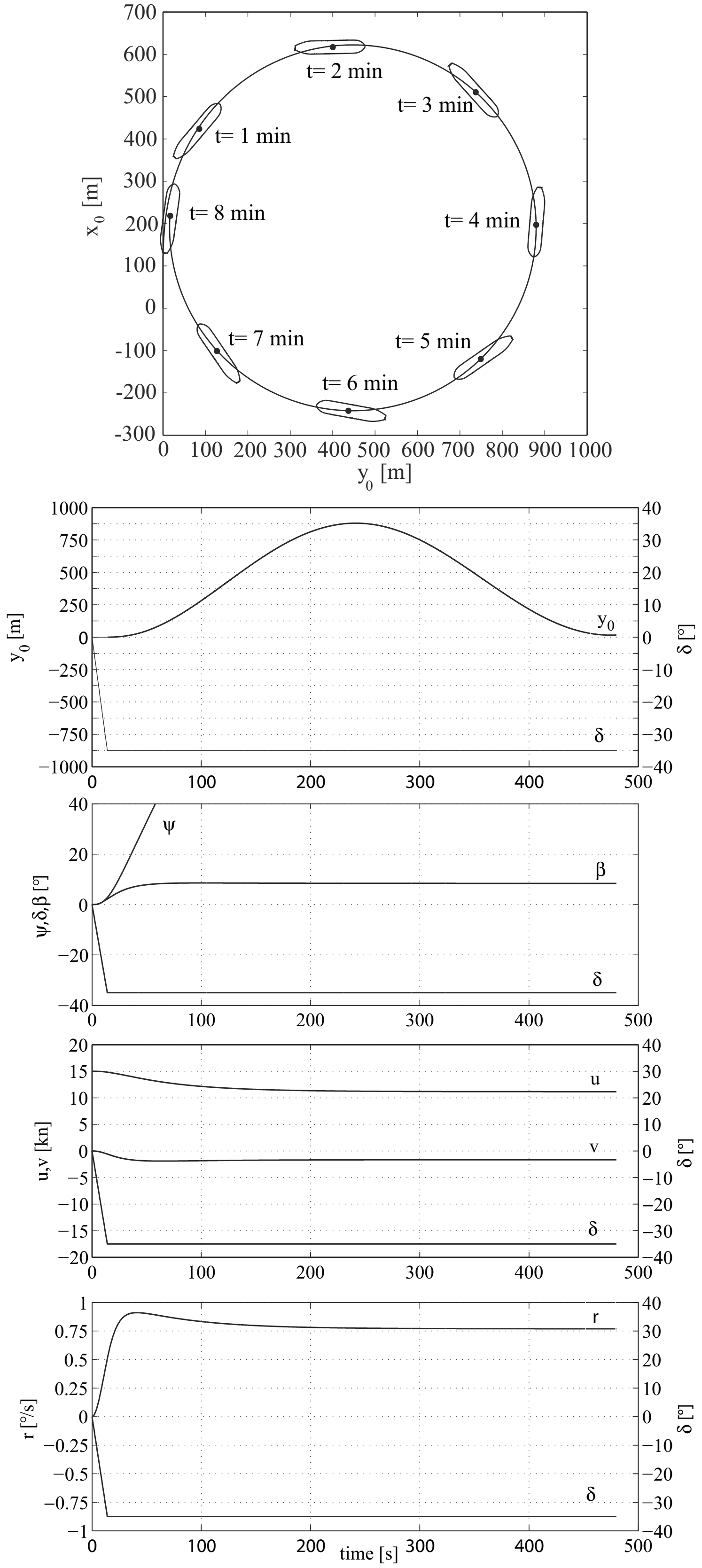

Figure 4.3: Simulation of the -35° turning maneuver for the Mariner ship at full-scale. Turning trajectory (top) and time histories of state variables and rudder angle (bottom).

The presented model was considered validated to reproduce the behavior of the real system, and the investigation was aimed at identifying the importance of single functional dependencies. A fundamental selection of terms and reduction of the model was already done via regression analysis and could be seen as an objective, yet formal judgment, since it relates only to the goodness of curve-fitting. The next step was to focus on the actual maneuvering prediction and quantify selected output parameters as coefficients were either varied in magnitude or sub-functionals were neglected completely. Additionally, instantaneous forces were compared to monitor their magnitude and significance during maneuvering. The investigation of dynamics of hard-rudder turning maneuvers was of special interest with regard to anticipated nonlinearities in forces arising from the rudder deflection and rigid body velocities.

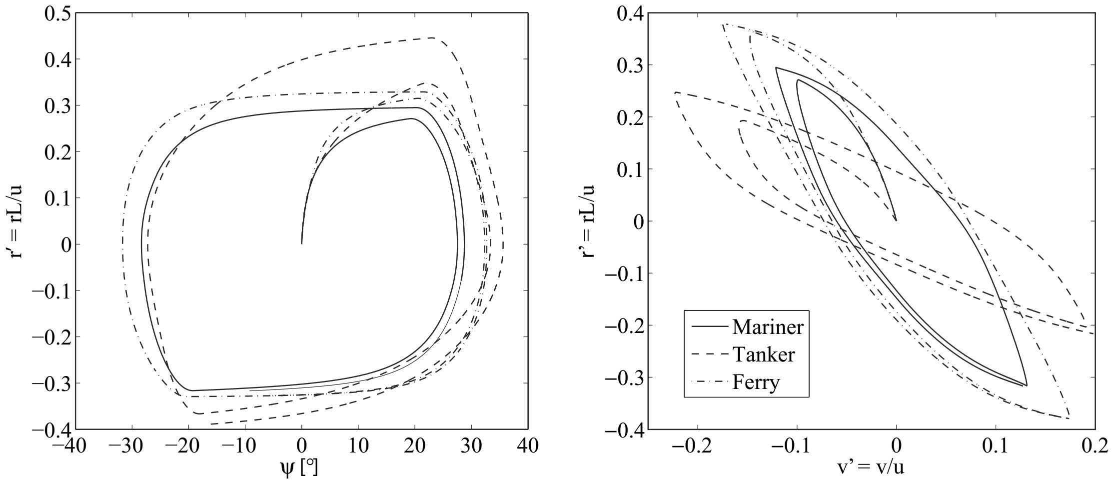

Figure 4.4: Phase plans of 20/20 zig-zag maneuver for all ships at full-scale.

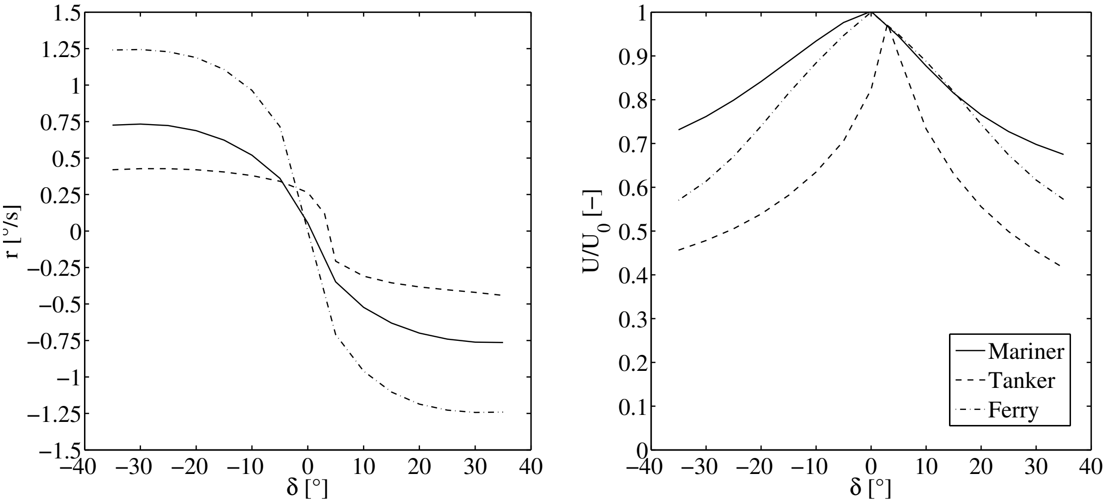

Figure 4.5: Spiral curve r against δ and trends of U/U_0 for all ships at full-scale.

However, since the rudder deflection is fixed after the initiation of the turn, this maneuver is more amenable to gaining insight into steady response characteristics in turning. The study of zig-zag maneuvers, in contrast, offers valuable information on the system behavior as the input is varied in sign. A global picture of this motion, comparing the sample ships, is given by the phase plans of Fig. 4.4., and Fig. 4.5 shows the trends of r and U/U_0 against rudder angle δ.

4.1.3 Sensitivity studies

To investigate the sensitivity of important maneuvering parameters to perturbations of hydrodynamic coefficients a stepwise variation of parameters was performed. The magnitude of a single coefficient was increased by 20%, while other parameters remained undisturbed. For turning maneuvers the output parameter of choice was the tactical diameter. For zig-zag maneuvers the maximum positive overshoot angle was chosen. For each ship all simulations were run using the time history of the rudder angle from the undisturbed simulation. The relative deviation of the output parameter was expressed by ζ, defined as

$$\zeta_i = \frac{\alpha_i - \alpha_0}{\alpha_0} \tag{4.2}$$

where α is output parameter, indices i relate to the i^{th} variation run, and index 0 refers to the value of the output parameter from the prediction of the undisturbed simulation. For both kinds of maneuvers and all three ships the majority of outputs took deviations of less than 5%. Thus, only those coefficients in the bar plots of Fig. 4.7 and 4.9, which had a larger impact on output parameters are presented. Fig. 4.6 and 4.8 compare undisturbed simulation results with the results from simulations which yielded the largest deviations. For turning maneuver simulations only terms in N were identified as particularly important. The ships altogether showed similar magnitudes for ζ of not more than 0.12 throughout the range of significant coefficients. An anticipated and general conclusion for all ships was drawn with regard to the importance of the linear contributions of N in sway and yaw, and the linear term in the rudder efficacy.

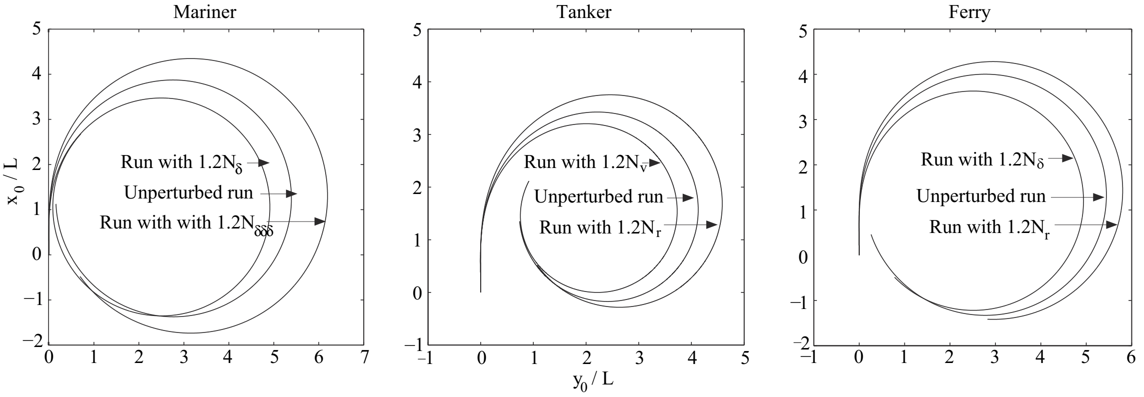

Figure 4.6: Comparison of turning maneuver predictions for the sample ships from the sensitivity study.

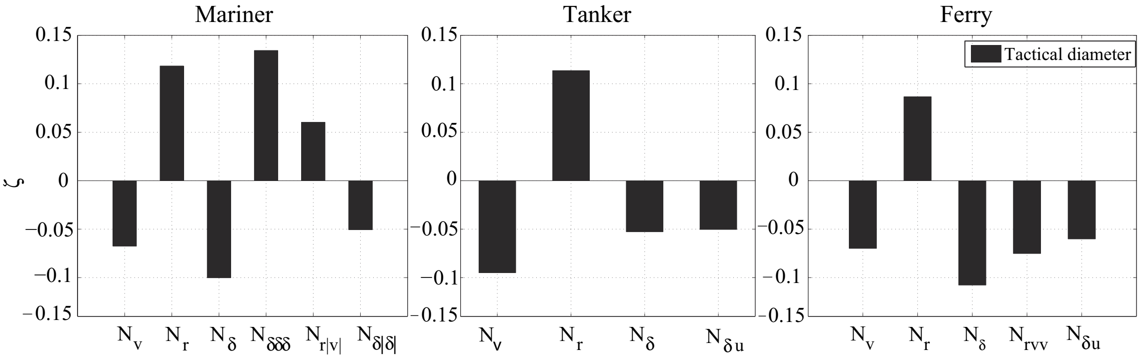

Figure 4.7: Relative deviations of tactical diameter with ζ >0.05 for turning maneuver simulations.

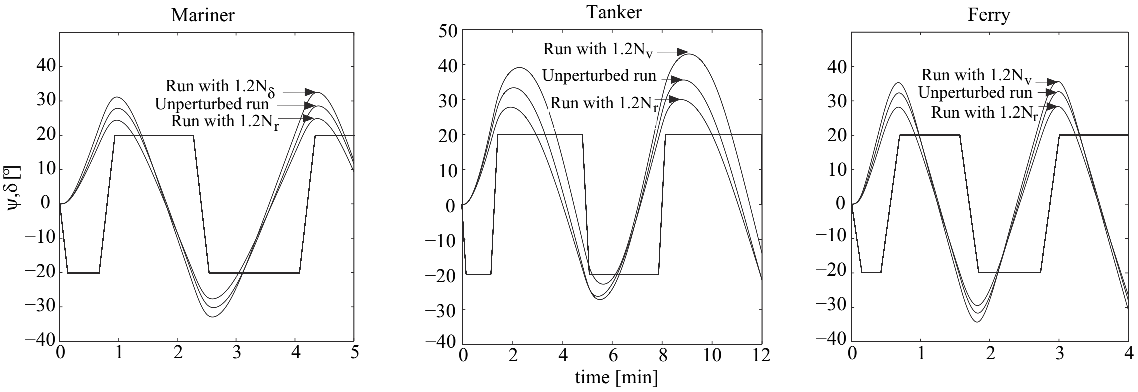

Figure 4.8: Comparison of zig-zag maneuver predictions for the sample ships from the sensitivity study.

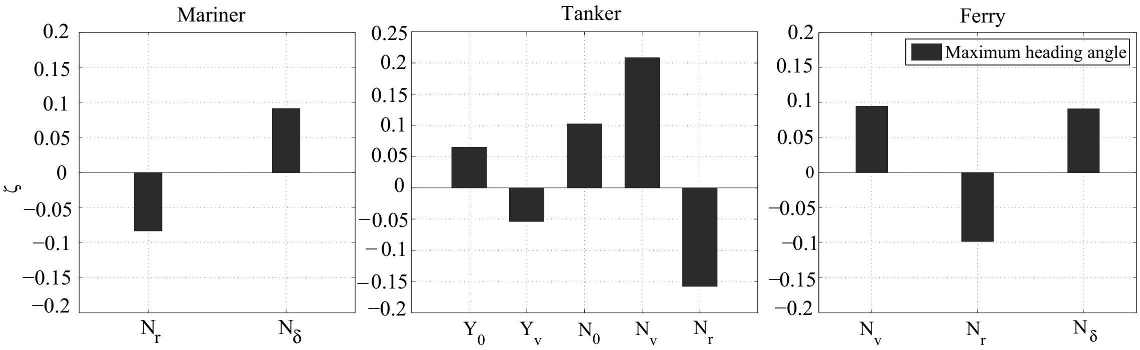

Figure 4.9: Relative deviations of positive maximum heading angle with ζ >0.05 for zig-zag maneuver simulations.

Additionally, for the Mariner ship the tactical diameter was sensitive to higher-order rudder terms, which can be referred to the higher geometric rudder aspect ratio ($\Lambda = 2.1$) compared to the tanker ($\Lambda = 1.5$) and the ferry ($\Lambda = 1.6$). Static rudder test results in Wolff (1981) show that the nonlinearity in $Y'(\delta)$ and $N'(\delta)$ curves occurred around 30° for the Mariner ship, but not before 40° for the tanker and around 35° for the ferry. Next to the linear motion and rudder coefficients the terms Y_0 and N_0 additionally appeared to be important for the tanker. The tanker, in contrast to other ships, showed a large sensitivity to N_v and N_r, but N_δ was not shown to be particularly important.

4.1.4 Analysis of instantaneous forces in maneuvering

Hydrodynamic forces and moments arising during a hard-rudder turning maneuver ($\delta = 35°$are plotted against time in Fig. 4.10 to 4.12. The plots of force contributions are organized in such a way, that groups of coefficients which belong to the same functional dependence are summarized and denoted by $F'\left(x_i x_j\right)$, where arguments relate to u, v, r or δ or combinations of these. The tables of coefficients Tab. 8.1 can be used to determine the actual sum of contributions. These plots are split into significant force contributions (l.h.s., Fig. 4.11 and Fig. 4.12), those with an order of magnitude less (center), and those relating to acceleration (r.h.s.). Plots for X' show these in the l.h.s. figures, too. Time histories of force contributions followed similar trends for all ship kinds. Cross-coupling terms between rigid body acceleration and velocities appeared to be of minor impact in general. Contributions with less than an order of magnitude than the dominating forces relate to coupled terms in rigid body velocities and rudder deflection, being valid for all ships. In X' these are $X'(\delta u)$, $X'(v\delta)$, $X'(r\delta)$ and if present in the ship specific model, $X'(vu)$ and $X'(ru)$. Single-variable terms relating to damping and rudder action governed the sum of external forces and moments, while in X' and Y' couplings between v and r and for Y' and N' between δ and Δu are dominant. These findings were already encountered in captive model tests since combined sway-yaw runs gave larger forces than observed in separate pure sway and pure yaw tests with the same motion parameters. For ships subject to large drift angles during turning these terms become even more important. These hypotheses were confirmed in the present investigation since these terms were more dominant for the tanker ($\beta = 17.85°$, $r = 0.42°/\mathrm{s}$) and the ferry ($\beta = 13.4°$, $r = 0.99°/\mathrm{s}$) compared to the Mariner ship ($\beta = 8.4°$, $r = 0.78°/\mathrm{s}$). A physical explanation for the importance of the $\delta\Delta u$ terms is the change in rudder efficacy in conjunction with the loss of forward speed U during turning, the effect of which was drastic for the tanker ($U/U_0 = 0.46$), significant for the ferry ($U/U_0 = 0.62$), and only moderate for the Mariner ship ($U/U_0 = 0.75$).

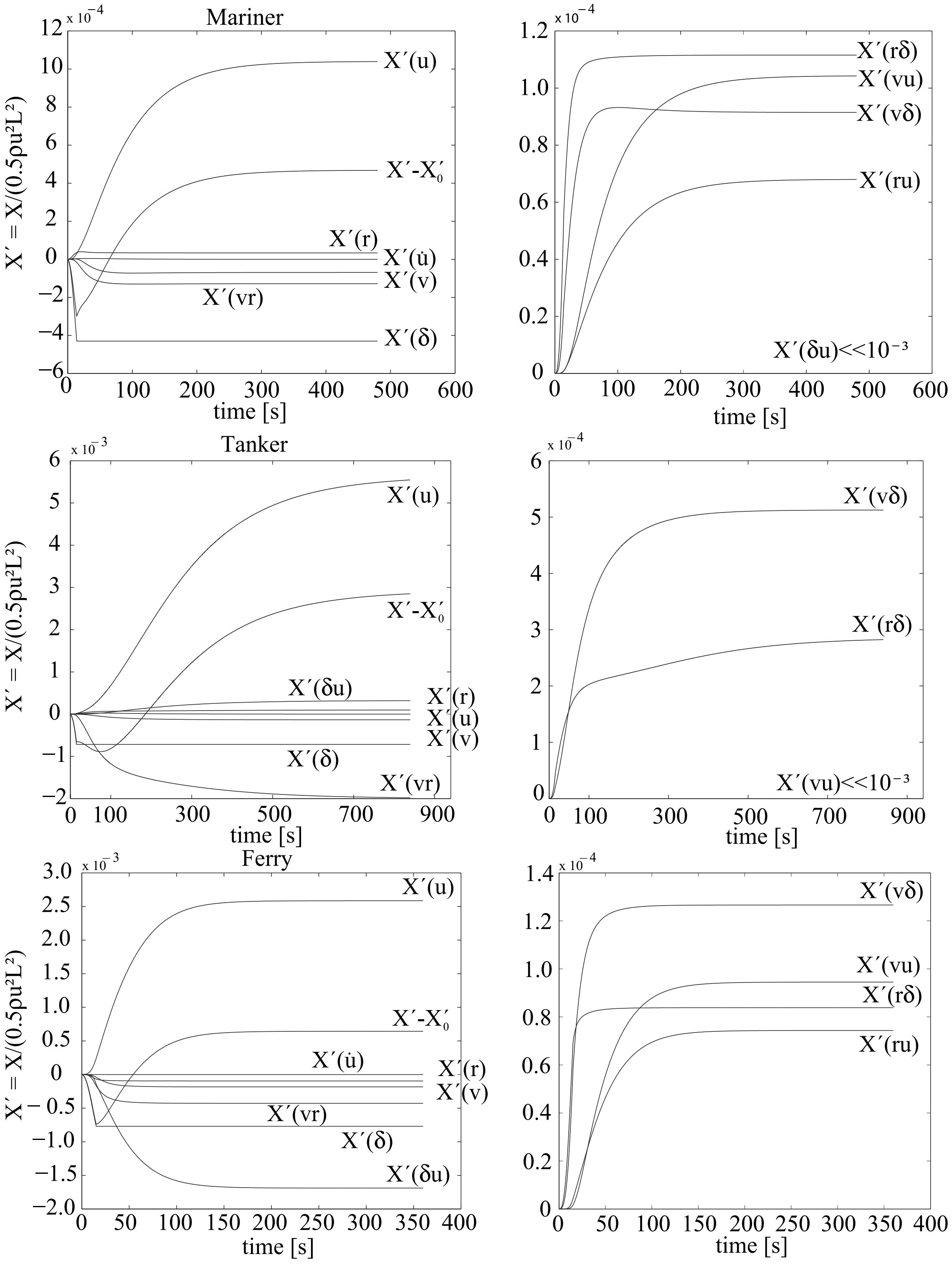

Figure 4.10: Time histories of X'-force contributions during a -35° turning maneuver.

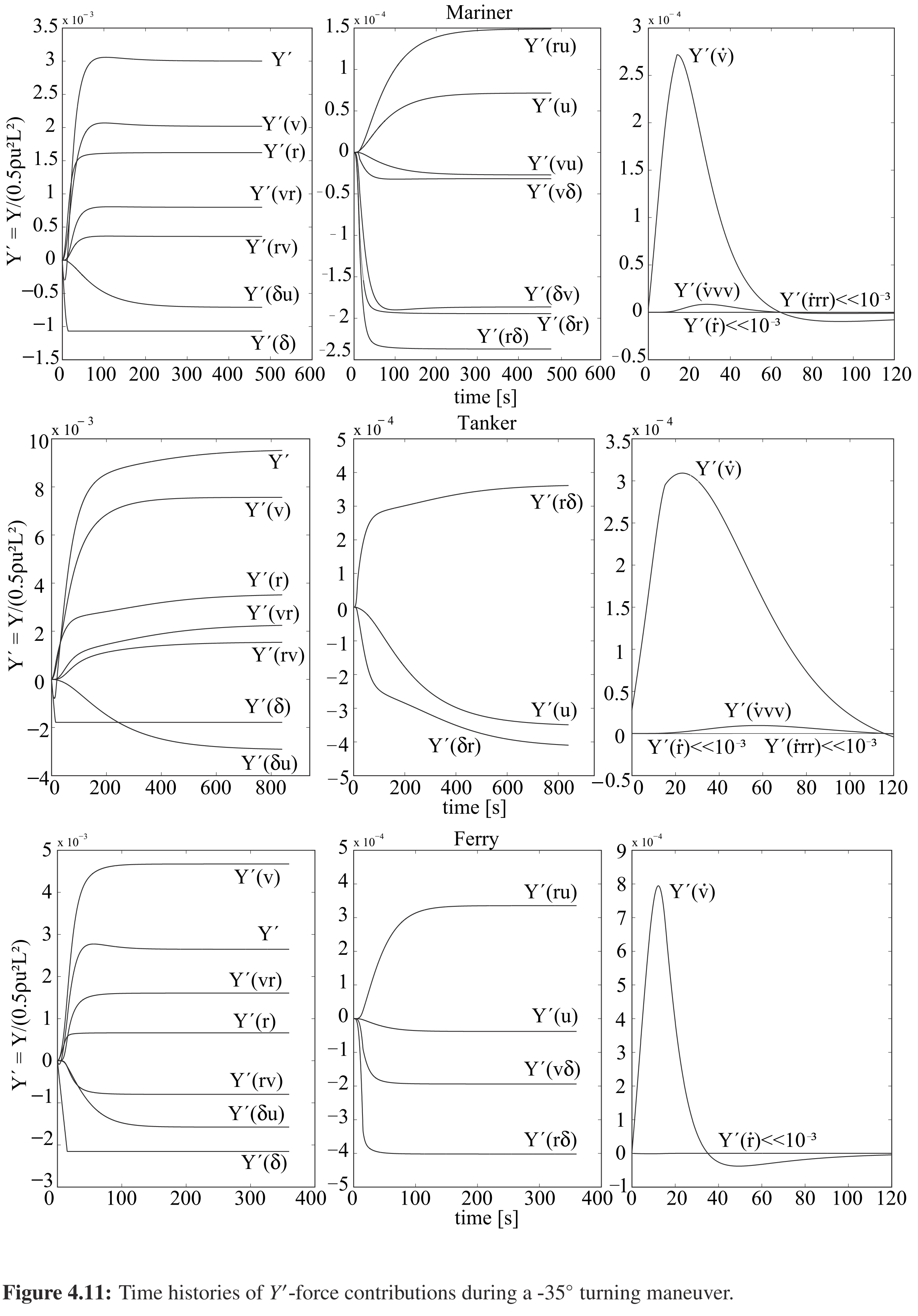

Figure 4.11: Time histories of Y'-force contributions during a -35° turning maneuver.

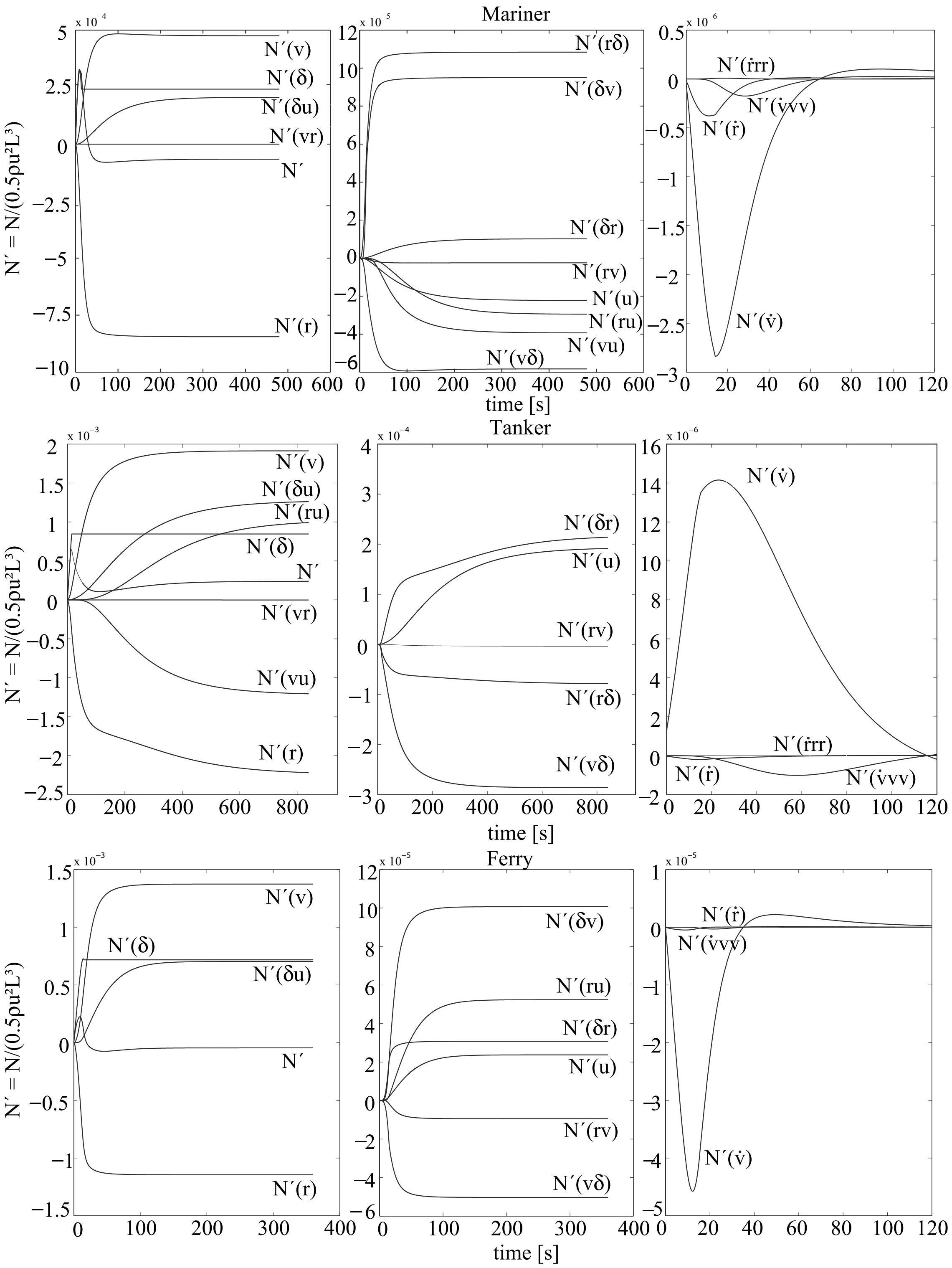

Figure 4.12: Time histories of N'-moment contributions during a -35° turning maneuver.

4.1.5 Model reduction

The role of particular coefficients should in general be debated carefully under consideration of the simplifications and assumptions of multivariat polynomial models themselves, in light of the complexity of ship flows in maneuvering. From a strictly formal point of view a mathematical model with estimated coefficients from regression analysis must not be changed in terms of discarding, blending or introducing novel contributions. However, once coefficients are estimated, checking responses of the system can serve as a feedback to change the model structure and re-estimate the coefficients in a new regression, Sutulo and Guedes Soares (2011). The instantaneous force analysis helped to decide upon terms with minor influence in the balance of forces, which might be dropped without trading accuracy in simulations. A direct parameter identification approach benefits if terms were neglected which necessitate separate test runs, and if this neglection was valid for all considered modes of motion. In cases where these conditions were not entirely met reducing these terms would just reduce the number of coefficients. To arrive at a final model structure, which is consistent with the concept of minimum complexity, the time response and sensitivity study is extended in terms of discarding functionals meeting above criteria, i.e. $F'(r\delta)$, $F'(v\delta)$, $F'(ru)$ and $F'(vu)$. Tab. 4.2 shows the results of this investigation, listing both turning and zig-zag maneuver parameters. Tactical diameter, advance, and steady state values of turning rate, drift angle and forward speed were chosen for the turning motion and the two largest overshoot angles from zig-zag tests. The first column lists coefficients of minor impact during turning, and associated lines present the relative deviation from the full-set of coefficients in turning maneuver simulation. If these deviations were be less than 5%, an additional zig-zag maneuver simulation was run. If the magnitude of deviation was confirmed therein, the coefficient was considered irrelevant and discarded in the specific model. The setting of the threshold for the decision was influenced by the objective of the maneuvering investigation in general. If the ship was in either way far from violating the performance criteria of IMO, the tolerance for acceptable deviations could reasonably have been less strict. The presented approach is conservative since re-estimation of reduced models through a new regression is expected to decrease deviations in Tab. 4.2. Following the discussion on the order of polynomials and the trading of identification effort against inclusion of less significant terms the basic model structure is chosen as per

$$
\begin{array}{rcll}
X & = & X_{\dot{u}}\dot{u} + X_u\Delta u + X_{uu}\Delta u^2 + X_{\delta\delta}\delta^2 + X_{vv}v^2 + X_{rr}r^2 + X_{vr}vr & (4.3) \\
Y & = & Y_{\dot{v}}\dot{v} + Y_{\dot{r}}\dot{r} + Y_0 + Y_v v + Y_{vvv}v^3 + Y_r r + Y_{rrr}r^3 + Y_\delta\delta + Y_{\delta\delta\delta}\delta^3 & (4.4) \\
 & + & +Y_{vrr}vr^2 + Y_{rvv}rv^2 + Y_{\delta u}\delta\Delta u & \\
N & = & N_{\dot{v}}\dot{v} + N_{\dot{r}}\dot{r} + N_0 + N_v v + N_{vvv}v^3 + N_r r + N_{rrr}r^3 + N_\delta\delta + N_{\delta\delta\delta}\delta^3 & (4.5) \\
 & + & +N_{vrr}vr^2 + N_{rvv}rv^2 + N_{\delta u}\delta\Delta u &
\end{array}
$$

The model of Eq. (4.3-4.5) is full in terms of the assumed nonlinearity in v, r and δ in all modes of motion. Important couplings between sway velocity and yaw rate is included by terms consistent with the assumed polynomial order. Finally, the change in rudder efficacy in response to forward speed variation is considered through the $\delta\Delta u$ terms. Models of similar structure are discussed by Cura-Hochbaum (2008). In presence of experimental

Table 4.2: Relative deviations of selected turning maneuver (columns 2-6) and zig-zag maneuver (columns 7 and 8) output parameters in response to perturbations.

	Tactical diameter	Advance	β	r	U	ψ_{min}	ψ_{max}
Mariner							
$r\delta$	-0.150	0.114	-0.109	-0.123	0.006	...	...
$v\delta$	-0.022	0.015	-0.034	-0.040	-0.020	0.051	-0.01
ru	-0.009	0.006	0.048	-0.037	-0.026	0.010	0.002
vu	0.023	-0.006	-0.009	0.006	-0.027	-0.011	-0.005
$r\delta v\delta$	-0.175	0.129	-0.143	-0.158	-0.013	...	...
$ruvu$	0.020	-0.004	0.044	-0.030	-0.059	-0.001	-0.003
Tanker							
$r\delta$	-0.015	0.010	0.004	-0.039	-0.018	0.1	0.001
$v\delta$	0.092	-0.055	0.016	0.084	-0.095	...	...
ru	-0.066	0.007	-0.031	-0.150	0.083	...	...
vu	0.135	-0.021	-0.086	0.510	-0.176	...	...
$r\delta v\delta$	0.076	-0.045	0.017	0.035	-0.104	...	...
$ruvu$	0.071	-0.014	0.013	0.017	-0.053	...	...
Ferry							
$r\delta$	-0.014	0.001	-0.047	-0.008	-0.005	0.011	0.017
$v\delta$	-0.011	-0.004	-0.017	-0.021	-0.016	0.016	0.006
ru	-0.031	0.008	0.045	-0.040	-0.012	0.014	0.007
vu	0.178	-0.075	0.003	0.212	-0.057	...	...
$r\delta v\delta$	-0.019	0.006	-0.064	-0.031	-0.021	0.026	0.022
$ruvu$	0.152	-0.056	0.071	0.137	-0.078	...	...

time responses the search for a suitable model structure can be improved. A formal approach from regression analysis is the method of stepwise forward regression, which starts from the basic linear model and suggests to successively add the one regressor among all candidates within one iteration step which brings the maximum reduction in mean square error compared to the experiment, Draper and Smith (1998). It applied to regression models for maneuvering by Viallon et al. (2012). It is also possible to feed indirect parameter identification algorithms with initial values of coefficients found from above procedure for tuning in mathematical optimization sense.

4.2 Maneuvering model for shallow water conditions

The investigations into the model structure for the deep water case are synchronized with the theoretical treatise of shallow water effects in multivariat polynomial models. The extended investigation relied on available sets of coefficients for KCS (Gronarz, 1997) found from captive maneuvering tests on different water water depths, tailored to an apriori defined model structure, see Tab. 8.2. For the purpose of the present investigation these coefficients populated the maneuvering equations of motions, which were solved to generate time responses of turning and zig-zag maneuvers, which helped to clarify whether

Table 4.3: Main particulars of KCS in addition to Tab. 5.1. T_f is draft at fore perpendicular and T_a draft at aft perpendicular.

T_f [m]	T_a [m]	x_G [m]	λ [-]
9.60	10.50	-2.18	40

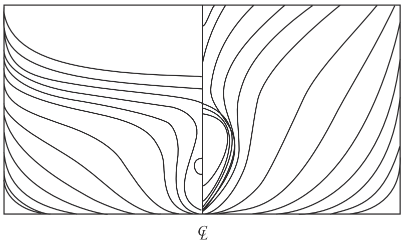

Figure 4.13: Lines plan of KCS.

such models were generally capable of reproducing the effect of decreasing UKC on maneuverability. However, no comparison to free-running maneuvering tests was available, and henceforth, only qualitative conclusions could be drawn. Geometries and conditions of KCS are summarized in Tab. 4.3, Tab. 5.1 and Fig. 4.13. Investigated water depths for the scope of this work corresponded to h/T values of 1.2, 1.4, 1.6 and 2.0.

4.2.1 Time responses

Hard-rudder turning maneuvers with rudder deflection of $\delta = 35°$ were simulated at an approach speed of 16 kts, which was the reference speed in the underlying parameter identification and valid for all water depths, Gronarz (1997). The trajectories reveal that advance, transfer and tactical diameter increase with decreasing UKC, attributable to increased inertia and damping, which was already reflected in the plots of hydrodynamic coefficients over h/T, Fig. 2.17. The increase in damping in the sway and yaw mode of motion is apparent in the time histories of yaw rate and drift angle, Fig. 4.14. The increased resistance to turning and lateral motion was also reflected in the evolution of ship speed, which took a longer time to settle to a constant value. The loss of forward speed from the approach condition decreased with decreasing UKC. The overriding role of hydrodynamic damping with decreasing UKC is emphasized in the study of zig-zag maneuvers. Here, a -35°/5° maneuver was studied. Overshoot angles show a nonlinear increase with increasing UKC, Fig. 4.15. The phase plots 4.16 and 4.17 provide further insight into hydrodynamic damping characteristics, as phase trajectories expand with increasing UKC. The steady-state time responses of r over different inputs δ represent additional evidence for the drastic change of damping characteristics in shallow water. The smaller the water depth, the smaller the magnitude of steady-state yaw rate and its gradient in terms of the rudder angle. Input passivity was observed for all water depths, while the curves for greater UKC tend to take the shape of a hysteresis loop, Fig. 4.18.

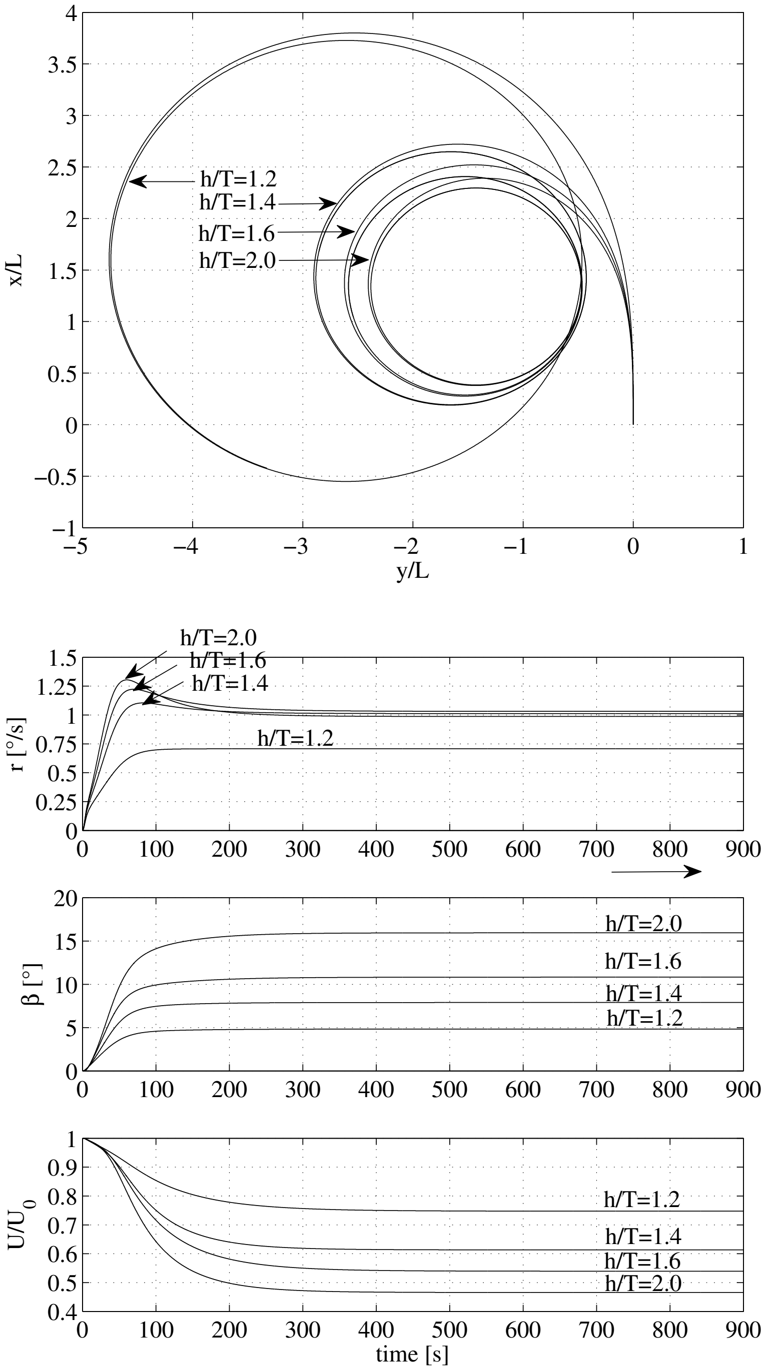

Figure 4.14: Turning maneuver trajectories and time histories of state variables of 35° turning maneuver at various water depths.

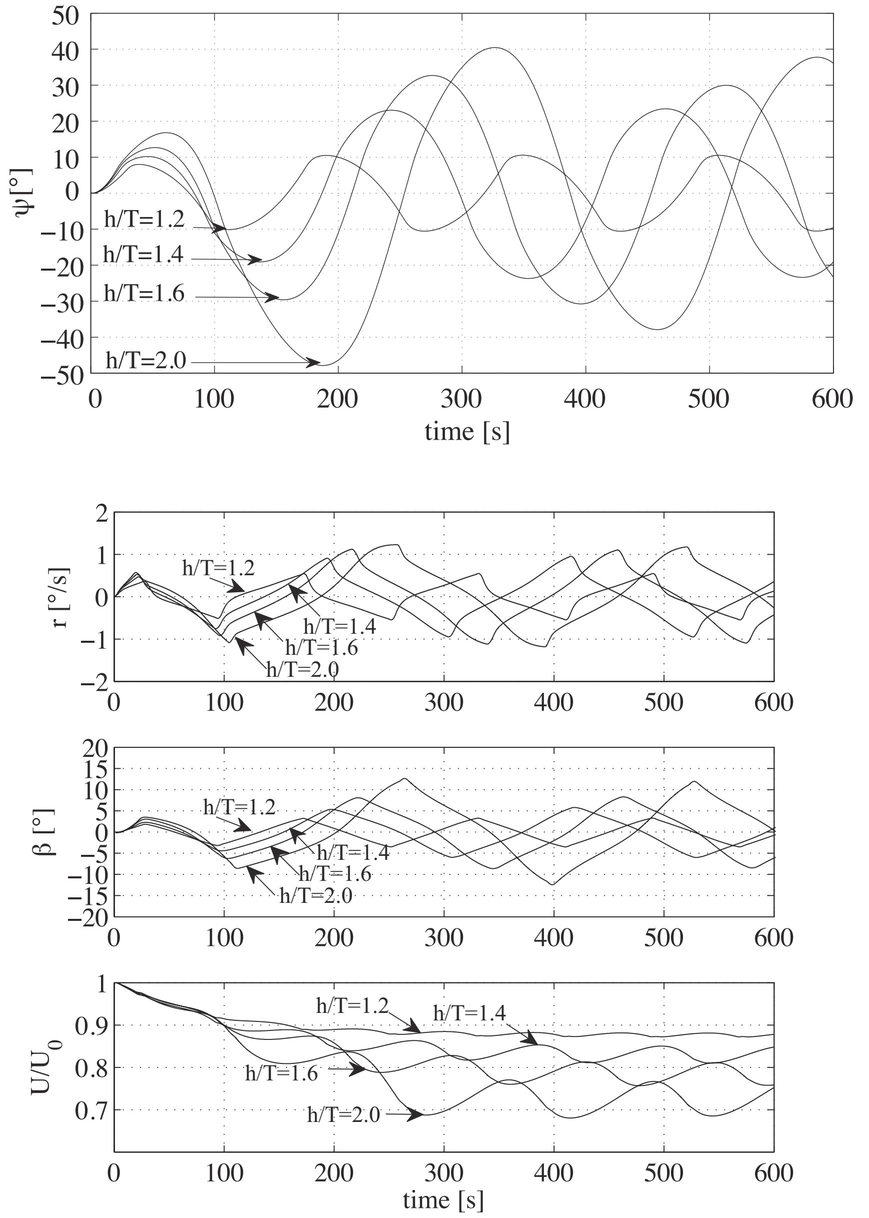

Figure 4.15: Time histories of heading angle and state variables of 35°/5° zig-zag maneuver at various water depths.

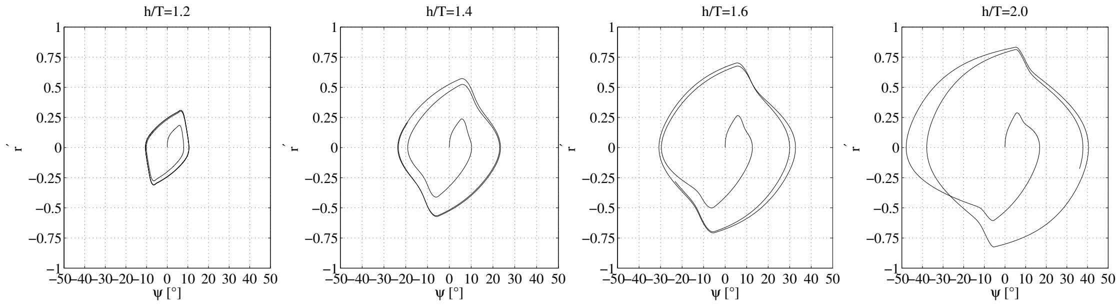

Figure 4.16: Phase diagrams r over ψ of 35°/5° zig-zag maneuver at various water depths.

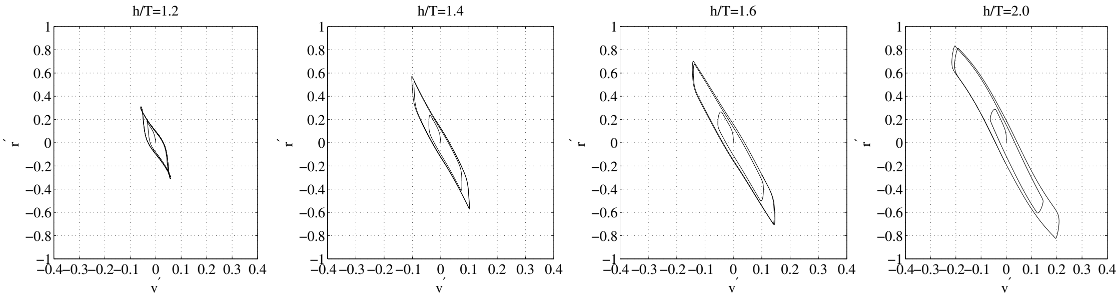

Figure 4.17: Phase diagrams r over v of 35°/5° zig-zag maneuver at various water depths.

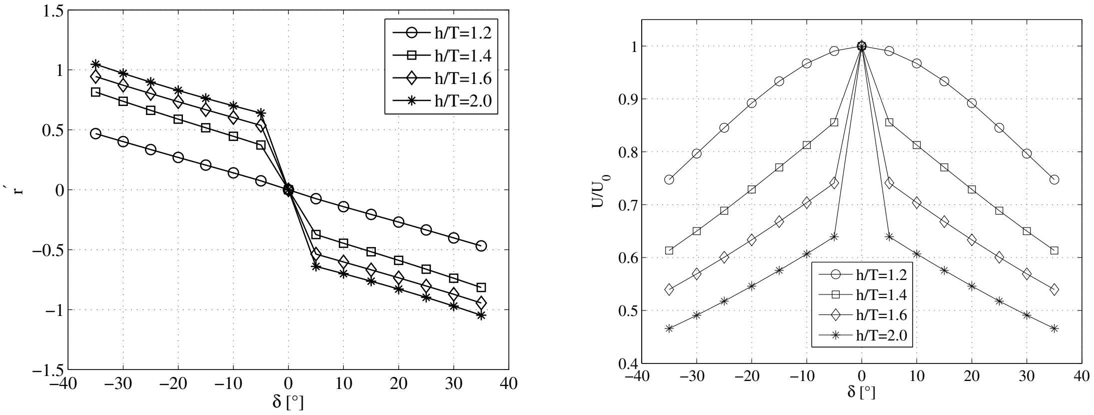

Figure 4.18: Spiral test results at various water depths.

4.2.2 Sensitivity analysis

For both kinds of maneuvers hydrodynamic coefficients were successively perturbed by an increase of 20% and time responses were compared to the results of the unperturbed model simulation. Fig. 4.19 presents those perturbed coefficients which led to a relative deviation ζ greater than 5%. For the turning maneuver the same coefficients were identified sensitive for all water depths, albeit with different magnitude. Sensitivity was higher the smaller UKC. The paramount importance of linear damping terms in sway and yaw, as well as linear term of rudder action was confirmed. A different behavior was observed for the zig-zag maneuver, Fig. 4.20. Coefficients N_v and N_r were identified sensitive at all water depths, and their perturbation yielded the largest deviations in tactical diameter. The significance of other linear terms as Y_v, Y_δ and N_δ was confirmed, whereas some coefficients proved sensitive only at distinct water depths, albeit at the lower threshold of the 5% criterion, e.g. X_u and $Y_{\delta vv}$. It was concluded that within the presented framework of multivariat polynomial models the shallow water effect on maneuverability can be modeled. Validation to time responses is still to be conducted. This was done for the entire simulation-based method and is presented in Chapter 6.

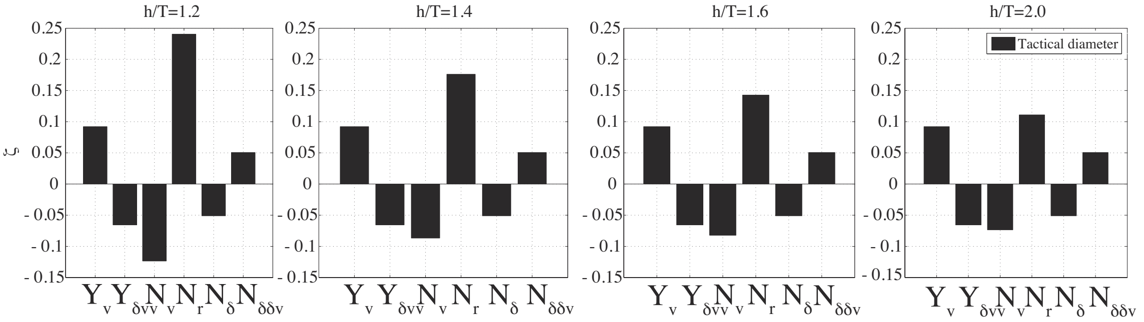

Figure 4.19: Sensitivity studies for -35° turning maneuver at various water depths.

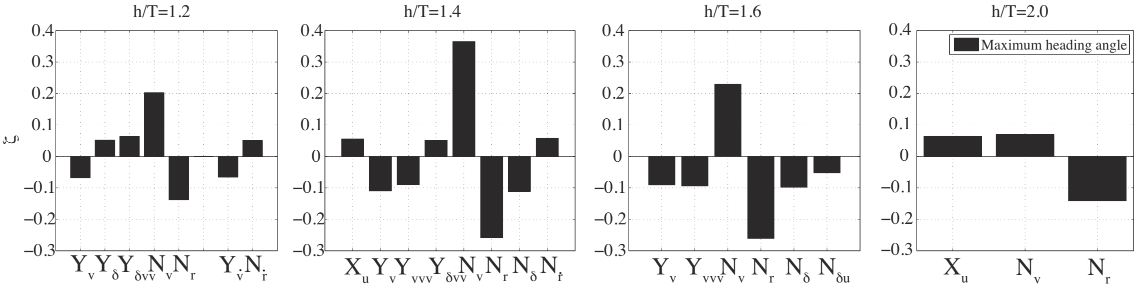

Figure 4.20: Sensitivity studies for 35°/5° zig-zag maneuver at various water depths.

5. Numerical Analysis of Captive Maneuvering Tests

This chapter encompasses validation exercises on numerical methods for hydrodynamic analyses related to maneuvering in deep and shallow water. It presents the results of the CFD-based parameter identification procedure. Comparison to experimental data serves as the reference for the assessment of the reliability of simulations. Following the introduction of candidate ships and experimental setups, the general strategy for captive maneuvering tests in deep water with CFD is presented. Aforegoing to the extension of simulations to shallow water was a numerical study on the prediction of squat in straight ahead and lifting flow conditions. Given the flow field information available from CFD simulations, special hydrodynamic issues of flows around ships in shallow water are addressed. Problems under scrutiny concern viscous and free surface effects.

5.1 Candidate ships

Three ship test cases are investigated. Kriso Very Large Crude Carrier (KVLCC) 2 is a modern tanker design. KVLCC2 was abundantly investigated in CFD benchmarking workshops for resistance, maneuvering and seakeeping, Larsson et al. (2003). Measurements from free-running maneuvering tests with KVLCC2 in deep and shallow water were available through SIMMAN (2014), Quadvlieg and Brouwer (2011), Tonelli and Quadvlieg (2015), Eloot et al. (2015). The parameter identification procedure was applied to KVLCC2 to derive maneuvering coefficients and perform a comparing investigations of maneuvering simulations to measurements in Chapter 6. Duisburg Test Case (DTC) and KCS represent containership designs of the Post-Panmax and Panmax generation, respectively. Measurements from experimental investigations with KCS in shallow water were available from Gronarz et al. (2009). Geometries are publicly available, SIMMAN (2014), el Moctar et al. (2012). No full-scale representations exist. Main particulars and information on rudders and propellers valid for this chapter are given in Tab. 5.1 and Fig. 5.1.

Table 5.1: Main particulars of KVLCC2, KCS and DTC. Notation as per Tab. 4.1, S_W is wetted surface area.

	L [m]	B_{wl} [m]	T [m]	c_B [-]	x_G [m]	λ [-]	S_W [m^2]
KVLCC2	320.00	58.00	20.80	0.81	11.136	46.426	27194
KCS	229.20	32.20	10.00	0.64	-2.18	40	8992.00
DTC	360.00	51.00	14.00	0.66	-0.56	40	21560
	Propeller	D_P [m]	A_e/A_0 [-]	$P_{0.7}/D_P$ [-]	Z [-]	Hub ratio [-]	Orientation
KVLCC2	1	9.86	0.72	0.43	4	0.16	clockwise
KCS	1	7.9	0.8	0.99	5	0.18	clockwise
DTC	1	8.91	0.8	0.96	5	0.18	clockwise
	Rudder	A [m^2]	Turn rate [°/s]				
KVLCC2	Horn	273.3	2.34				
KCS	Horn	115	2.32				
DTC	Full-spade	255	n.A.				

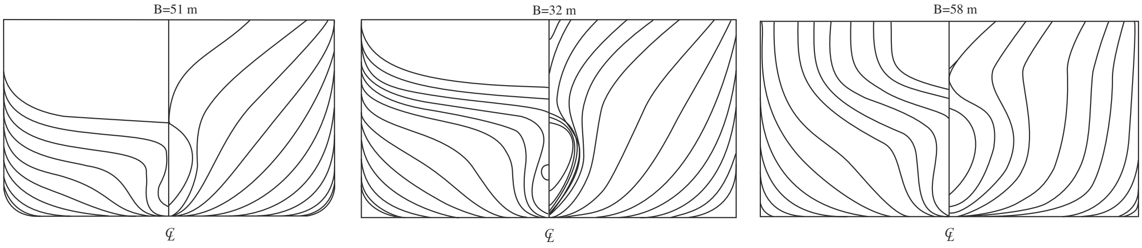

Figure 5.1: Lines plans of DTC, KCS and KVLCC2 (not drawn to scale).

5.2 Numerical analysis of flows around maneuvering ships in deep water

The validation of the virtual captive maneuvering test procedure is performed for the basic deep water model Eq. (4.3-4.5). A summary of the submodels and associated test runs is given in Tab. 5.2. The order of the listed test runs reflects the order of the stepwise regression problem. Evaluation of dynamic test results is appended in Chapter 8.1.

5.2.1 Experimental setups

Captive maneuvering tests with KVLCC2 were conducted at the Hyundai Maritime Research Institute (HMRI), SIMMAN (2014). The model was equipped with appendages and was tested in deep water condition. The tank at HMRI is 210 m in length, 14 m wide and 6 m deep. Drift tests, rudder tests and combined drift and rudder tests were carried out at Froude number $F_n = 0.142$, corresponding to $U = 15.5$ kts at full scale. Propeller revolutions were set to the model self propulsion point (MSPP) and kept constant. Dynamic runs comprised pure sway and yaw oscillations. The model was free to heave and trim, but otherwise constrained. Longitudinal forces were measured by a gauge located

Table 5.2: Overview of the captive maneuvering test programme and relevant functionals of hydrodynamic forces.

Test	Model	Parameters
Resistance	$X' = X'_u \Delta u' + X'_{uu} \Delta u'^2$ $Y' = Y'_0 (U_0)$ $N' = N'_0 (U_0)$	U/U_0=0.1:0.1:1.2
Rudder	$X' = X'_{\delta\delta} \delta^2$ $Y' = Y'_\delta \delta + Y'_{\delta\delta\delta} \delta^3$ $N' = N'_\delta \delta + N'_{\delta\delta\delta} \delta^3$	δ=-10:5:35° U/U_0=1;0.4
Drift	$X' = X'_{vv} v'^2$ $Y' = Y'_v v' + Y'_{vvv} v'^3$ $N' = N'_v v' + N'_{vvv} v'^3$	β=-20:5:20°
Turn	$X' = X'_{rr} r'^2$ $Y' = Y'_r r' + Y_{rrr} r'^3$ $N' = N'_r v' + N'_{rrr} r'^3$	r'=-0.5:0.1:0.5
Pure sway	$Y' = Y'_{\dot{v}} \dot{v}' + Y'_v v' + Y'_{vvv} v'^3$ $N' = N'_{\dot{v}} \dot{v}' + N'_v v' + N'_{vvv} v'^3$	v'=0.085 ω'=0.59
Pure yaw	$Y' = Y'_{\dot{r}} \dot{r}' + Y'_r r' + Y'_{rrr} r'^3$ $N' = N'_{\dot{r}} \dot{r}' + N'_r v' + N'_{rrr} r'^3$	r'=0.2 ω'=1.18
Drift and yaw	$X' = X'_{\dot{r}} + X'_{rr} r'^2 + X'_{vv} v'^2 + X'_{vr} v' r'$ $Y' = Y'_{\dot{r}} \dot{r}' + Y'_r r' + Y'_{rrr} r'^3 +$ $Y'_{vrr} v' r'^2 + Y'_{rvv} r' v'^2 + Y'_v v' + Y'_{vvv} v'^3$ $N' = N'_{\dot{r}} \dot{r}' + N'_r r' + N'_{rrr} r'^3 +$ $N'_{vrr} v' r'^2 + N'_{rvv} r' v'^2 + N'_v v' + N'_{vvv} v'^3$	r'=0.26 β=0:4:16° ω'=1.85

at LCG and transverse forces were measured by two gauges 1 m boward and aftward of amidships, respectively. No repeatability studies were available.

5.2.2 Numerical setups

The commercial solver STARCCM+ (CD-adapco, 2016) was applied. The method follows the formulation of the FV-method presented in Chapter 3. The solution domain was discretized using unstructured hexahedral CVs. On the surface of the ship prismatic cells were used to achieve better resolution of the near-wall flow and boundary layer. These layers were aligned in accordance with the targeted nondimensional wall distance $y^+ \approx 60$ of the wall function used in the framework of the applied turbulence model kω-SST, Menter (1994). One ship length upstream of the fore perpendicular a velocity inlet boundary condition was set. Two ship lengths downstream a pressure outlet condition held. The width of the numerical tank equaled the width of the tank from the model test facility. Free slip conditions were applied to the tank walls and the bottom. In light of the low Froude number a double-body flow was realized, employing a symmetry condition at the height of the draft. The propeller was modeled through body forces using the method described

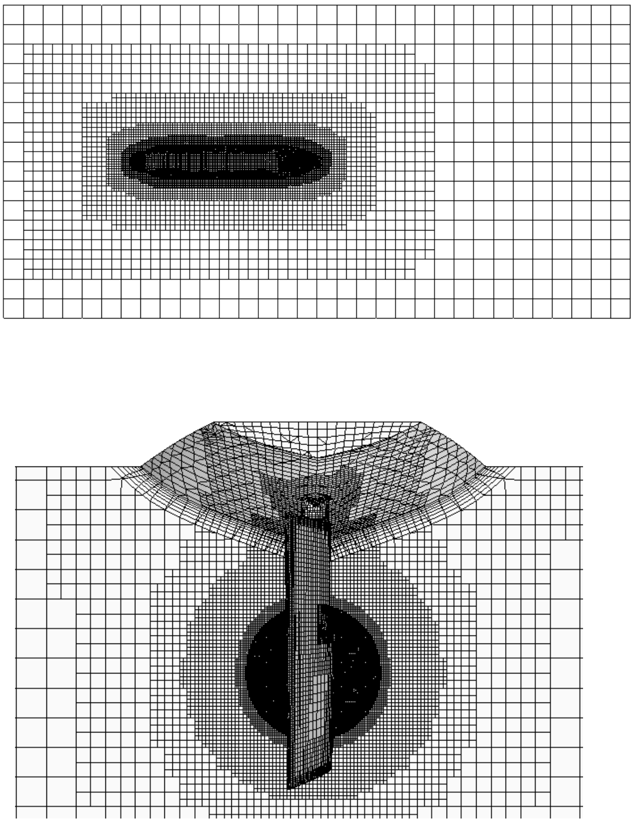

Figure 5.2: Detail view of grid setups for deep water simulations with KVLCC2 (double-body setup).

in Chapter 3.5.1. At low forward speeds and moderate propeller loading the wash of the propeller slipstream over the rudder surface and its effect on rudder forces was assumed small, justifying the application of the body force propeller. The numerical grid was locally refined in regions where larger gradients of the flow quantities were expected. Fig. 5.2 shows sections of the mesh and refinement areas, including the body force propeller region. Face values for convective and diffusive fluxes were evaluated through a second-order upwind discretization scheme. In steady simulations solutions were considered converged if the absolute normalized residuals of momentum, continuity and the turbulence quantities had decreased by four orders of magnitude, and if the iteration history of forces showed converged behavior. In unsteady simulations an implicit second-order time integration scheme was applied and each dynamic run covered four periods of oscillation to check on the repeatability of oscillations of forces. The time step was chosen based on sensitivity studies. All simulations were performed on a HPC system using the Message Passing Interface (MPI) technique to parallelize jobs, where appropriate. Numerical experiments yielded an optimal load balancing for job parallelization using a distribution of $5{\cdot}10^4$ CVs per core. Jobs were run on the respective number of Intel(R) Sandy Bridge nodes (16 cores per node). Variation of rudder and drift angles required remeshing, which was incorporated into the job batching routines. Hydrodynamic forces and moments were determined on four different grids of various resolution to investigate the sensitivity of the solution to spatial discretization. Near-wall grid composition remained unchanged.

Table 5.3: Grid sensitivity study: hydrodynamic forces on KVLCC2 in steady drift motion at $\beta = 12°$.

$n_{CV}/10^6$	X'	Y'	N'
0.7	-0.0189	0.0744	0.0225
1.3	-0.0184	0.0730	0.0227
2.5	-0.0186	0.0745	0.0232
4.0	-0.0183	0.0723	0.0229
Experiment	-	0.0776	0.0231
E%	-	6.80	0.83

Table 5.4: Grid sensitivity study: hydrodynamic forces on KVLCC2 from a static rudder test at $\delta = 10°$. The sign convention for the rudder angle from the experiments was adopted (positive rudder angle to starboard).

$n_{CV}/10^6$	X'	Y'	N'
0.7	-0.0198	-0.00815	0.00388
1.3	-0.0196	-0.00823	0.00392
2.5	-0.0195	-0.00817	0.00390
4.0	-0.0196	-0.00790	0.00378
Experiment	-	-0.00821	0.00411
E%	-	3.78	8.03

Where possible, the order of the discretization error was assessed following ITTC (2002). Tab. 5.3 and Tab. 5.4 list the results of this study for a drift test at $\beta = 12°$ and a rudder test at $\delta = 10°$. Therein, $E\%$ is the error ratio $E\% = 100(D - S)/D$ between experimental data D and simulation result S. Except for simulations obtained on the coarsest grid the sensitivity to spatial discretization was weak. Deviations between results obtained on the finest and the second coarsest grid were less than 5%. Monotonic convergence was not observed and no extrapolation could be made. The application of the ITTC procedure for error estimation was therefore omitted. The test programme was run on the medium resolution grid with $1.3 \cdot 10^6$ CVs. For steady flow problems convergence was observed after 400 iterations and 15 minutes computing time.

5.2.3 RANS-based captive maneuvering tests in deep water

Forward speed coefficients relevant to X' were obtained from resistance tests. In the experimental tank the model was towed with zero drift and rudder angle at constant speed until a steady state was reached. Forward speed was varied in successive runs. Experimental data only covered a range with small perturbations from the approach speed chosen for maneuvering simulations.

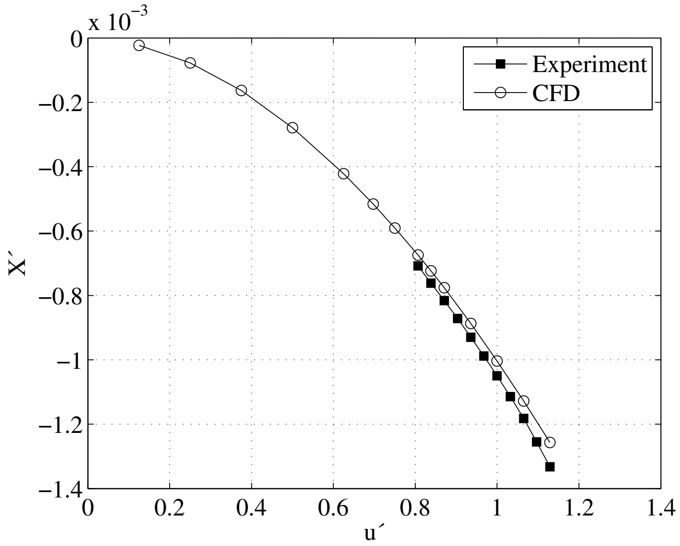

Figure 5.3: Comparison of the predictions of the nondimensional longitudinal force X' against forward speed u by simulation (double-body) and experiment.

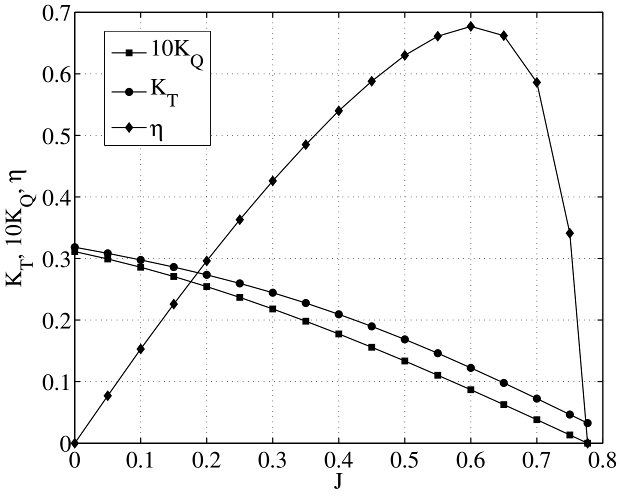

Figure 5.4: Open-water propeller performance curves for KVLCC2 determined by experiments, SIMMAN (2014).

Fig. 5.3 shows that the agreement between experimental and simulation results is favorable. At approach speed corresponding to $F_n = 0.142$ the deviation is 5%. Deviations grow with increasing forward speed, which is attributable to the double-body flow setup, as wave resistance becomes more important for $F_n > 0.15$. However, differences remain moderate even for the highest considered speed. Results were transformed to give the functional $X'(\Delta u')$ required for parameter identification. Fig. 5.4 shows the open water propeller performance curves available from experiments, which fed the body force propeller model. Open water propeller tests can also efficiently be computed with CFD making use of moving reference frames, e.g. demonstrated for DTC in Mucha and el Moctar (2011). Thrust coefficient K_T, torque coefficient K_Q and propeller efficiency η are plotted over advance number J. Results are valid for homogeneous inflow of constant speed in a circulating tank. Propeller revolutions were altered in successive runs. Fig. 5.5 presents the comparison of measured and computed side force Y' and yaw moment N' for various fixed rudder angles. While the agreement is generally favorable for side forces between $\delta = -15°$ and $10°$, deviations are observed at greater rudder angles, and for yaw moments in the negative rudder angle range. Yaw moment predictions show a distinct asymmetry with respect to to the origin at $\delta = 0°$, where greater absolute yaw moments result if the rudder was turned to starboard. This asymmetry is more pronounced in measurements compared to CFD predictions. While integral side forces on the ship in response to rudder deflection are dominated by pressure-dominated side forces on the rudder, the yaw moment on the ship is affected by the pressure field in the aft ship, which is altered by the propeller and deflected rudder. The application of the body force propeller affects the modeling of hull-propeller-rudder interactions and might be associated with above observations. Uncertainty analysis of measurements and simulations involving the actual propeller geometry and rotation would provide more insight into observed deviations. Fig. 5.6 shows the distribution of pressure coefficient $c_p = p/\left(0.5\rho U^2\right)$ over the suction side of the rudder blade in comparison of rudder deflection angles of $\delta = 5°$ and $\delta = 20°$. Consistent with the theory of wings, the relative low pressure field on the blade at rudder angle of $\delta = 20°$ is more distinct than for $\delta = 5°$, generating lift. Additional tests were simulated at a forward speed corresponding to $U/U_0 = 0.4$, which served as input to the identification of coefficients related to the functional $F'(\delta\Delta u')$.

Experiments and simulations agree well in the comparison of Y' and N' in steady drift motion, Fig. 5.7. Deviations for $v' = 0.5$, corresponding to a drift angle of $\beta = 30°$ amount to 7%, which is assumed to rest with turbulence modeling and free surface effects. Fig. 5.9 shows the distribution of c_p over the windward side of the wetted hull surface comparing drift angles of $\beta = 4°$, $\beta = 9°$ and $\beta = 20°$. Consistent with the notion of lifting flows, the stagnation pressure field increases in magnitude and extent the higher the drift angle. The pressure differences between the wind- and leeward side increase. The numerical solution was used to plot the distribution of ΔY over the ship length by integrating the pressure and shear stress over segments of the ship hull. In line with the analysis of the distribution of c_p, $\Delta Y'$ increases towards the bow Fig. 5.8.

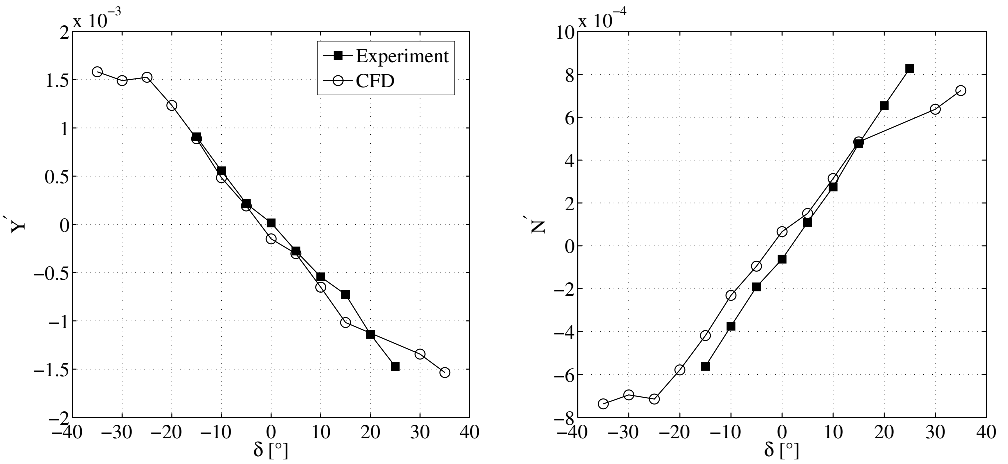

Figure 5.5: Comparison of the predictions of the nondimensional lateral force Y' and yaw moment N' against rudder deflection angle δ by simulation and experiment. The sign convention for the rudder angle from the experiments was adopted (positive rudder angle to starboard).

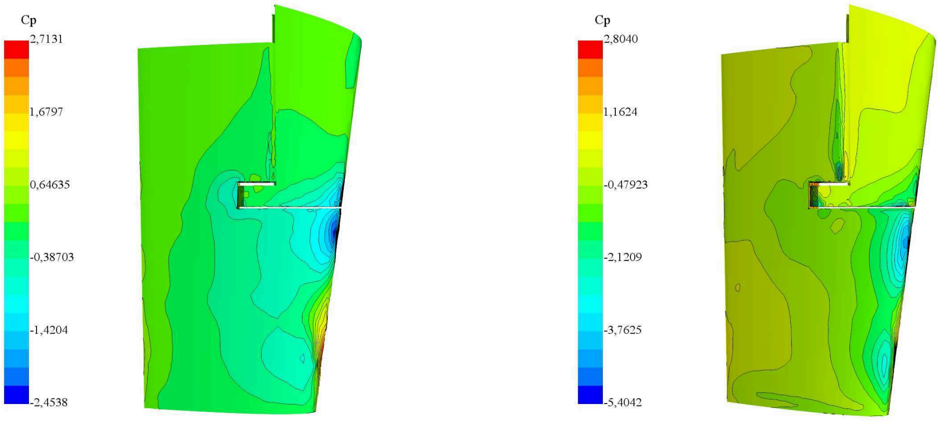

Figure 5.6: Distribution of pressure coefficient c_p on the suction side of the rudder at 5° and 20° deflection (from top to bottom).

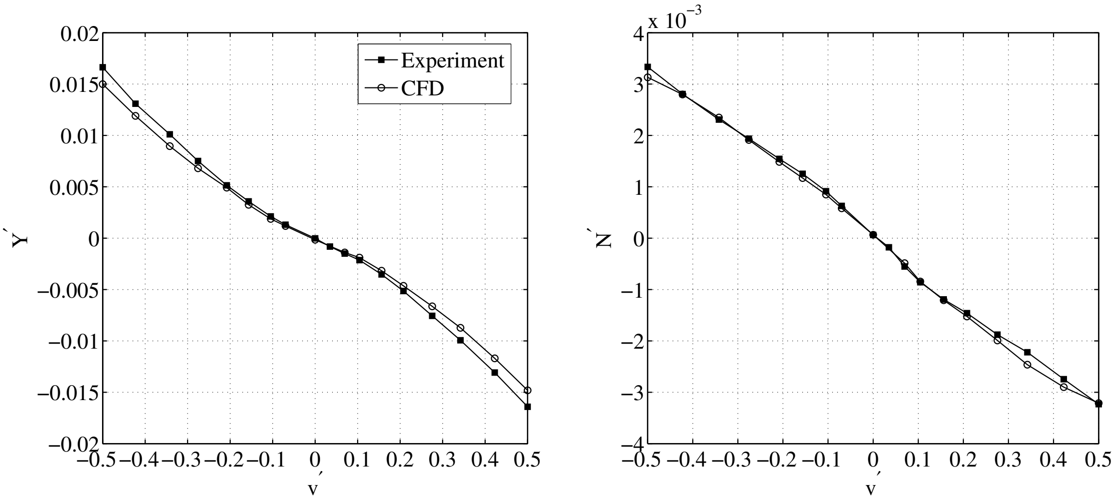

Figure 5.7: Comparison of the predictions of the nondimensional lateral force Y' and yaw moment N' against nondimensional sway velocity v' by simulation and experiment.

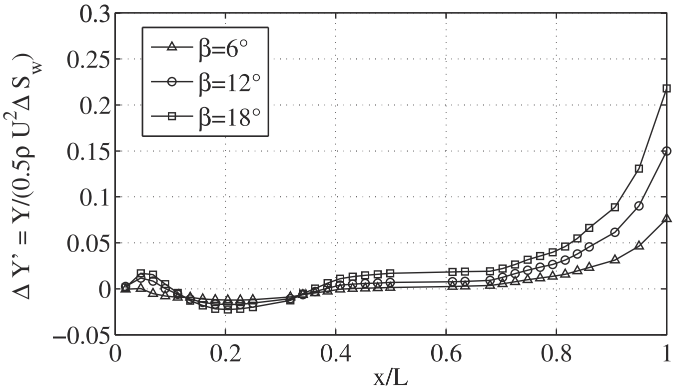

Figure 5.8: Lateral forces in steady drift motion over the ship length. Sectional wetted surface area is denoted by S_W.

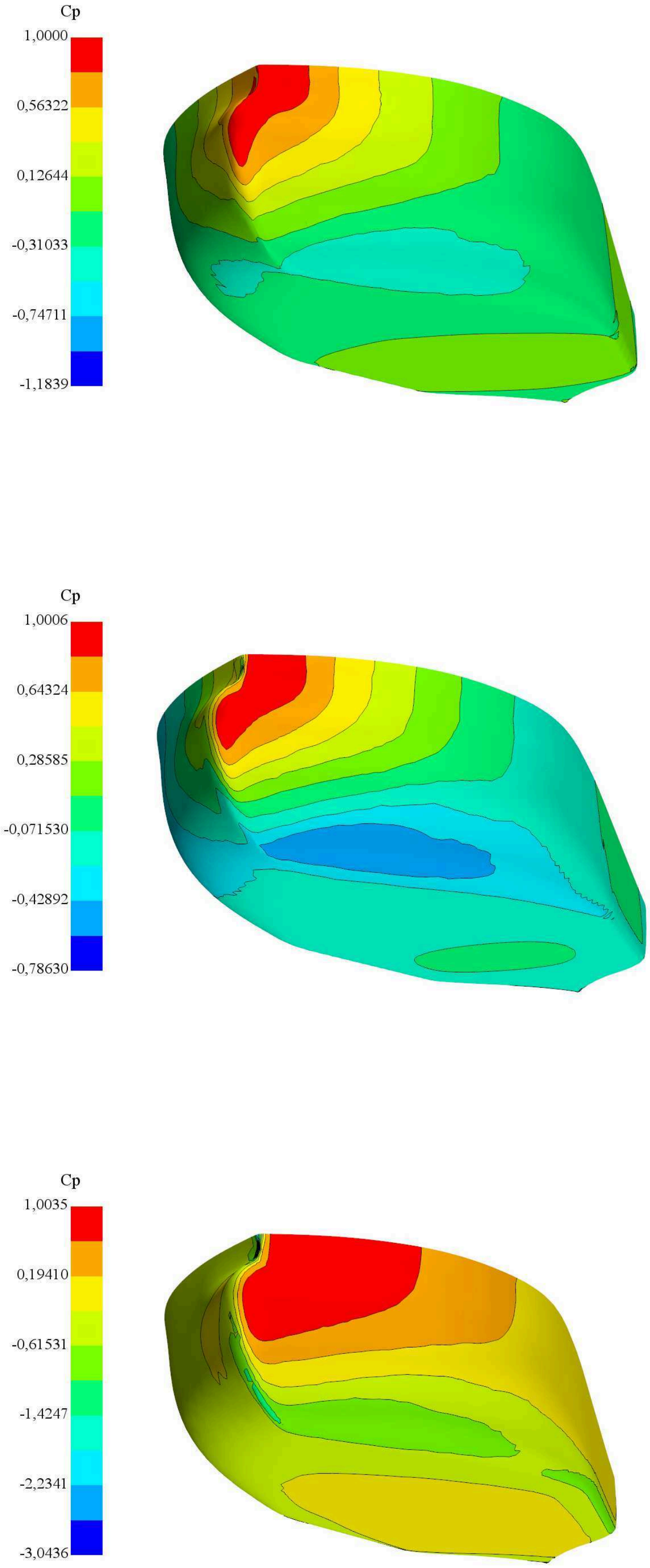

Figure 5.9: Distribution of pressure coefficient c_p in 4°, 9° and 20° steady drift motion (from top to bottom).

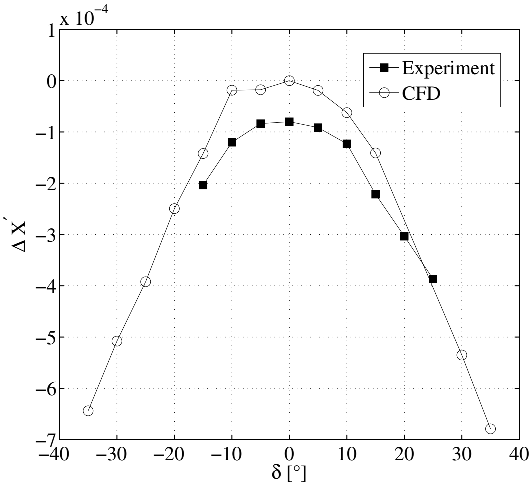

Figure 5.10: Comparison of the predictions of the nondimensional lateral force Y' and yaw moment N' against nondimensional sway velocity v' by simulation and experiment.

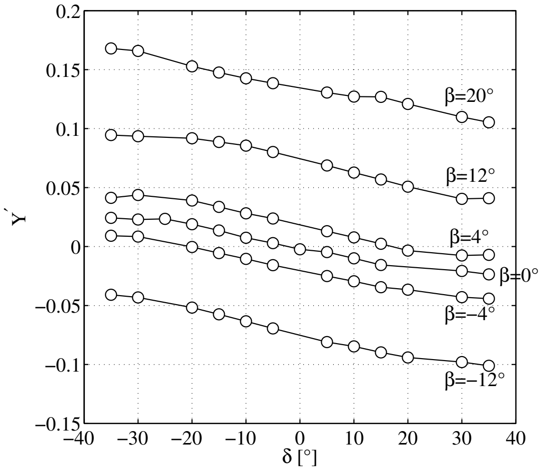

Figure 5.11: Comparison of the predictions of the nondimensional lateral force Y' and yaw moment N' against rudder angle δ by simulations for different β. The sign convention for the rudder angle from the experiments was adopted (positive rudder angle to starboard).

Fig. 5.10 shows the trends of $\Delta X'$ over δ and over v', where the straight ahead resistance was subtracted from the CFD solution to establish a common basis for the comparison with EFD, i.e. for computation it holds $\Delta X' = X' - X'_0$. While the CFD solution refers to the computed longitudinal force on the hull, measurements include both the longitudinal force and propeller thrust, i.e for experiments it holds $\Delta X' = X' - T'$. The residual non-zero value for $\Delta X'$ from measurements results from the subtraction of two measured forces of similar magnitude, and is small compared to the magnitude of the forces. Large deviations in the relative comparison error were between experiments and CFD were observed for small rudder angles. In the ship-fixed coordinate system $\Delta X'$ increases with increasing rudder deflection, as the lifting surface induces an additional resistance to the forward motion of the ship. In drift motion $\Delta X'$ decreases with increasing v' until the net longitudinal hull force at $\beta = 90°$ becomes zero and the system force equals just the propeller thrust. To gain insight into the dependency of interacting effects of δ and v' on Y' and N', rudder tests were performed at different drift angles. Fig. 5.11 reveals that rudder efficiency was virtually constant over v'. Resembling steady turning motions in unrestricted water condition can be realized through employment of moving reference frames, which base upon prescription of ship forward speed and yaw rate, or through boundary conditions in terms of the fluid velocity vector

$$\mathbf{v} = [-u - ry, v - rx, 0]^T \tag{5.1}$$

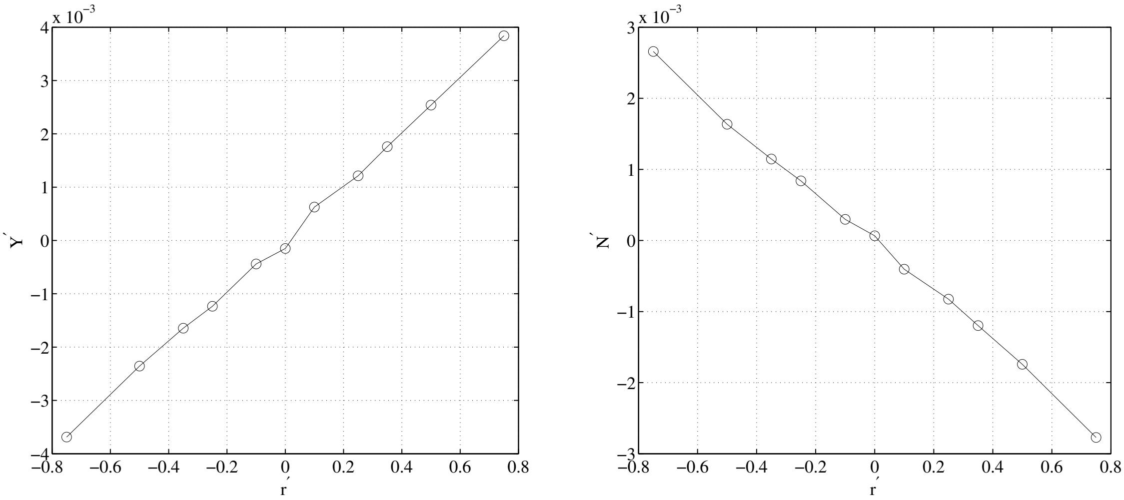

Figure 5.12: Predictions of the nondimensional lateral force Y' and yaw moment N' against nondimensional yaw rate r' by simulations.

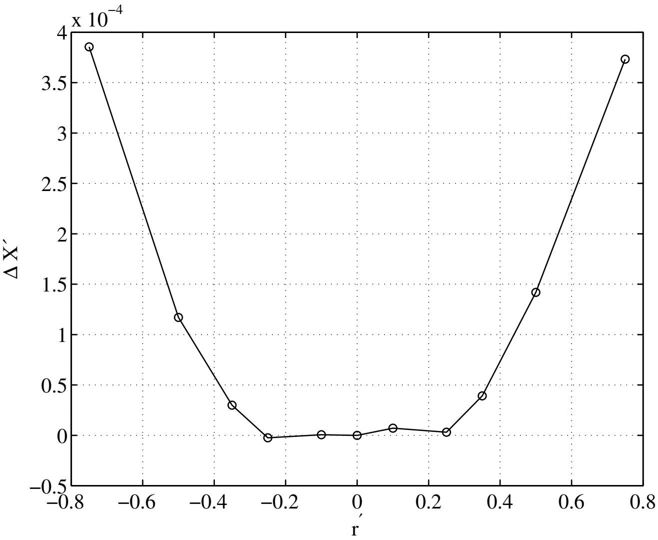

Figure 5.13: Predictions of the nondimensional longitudinal force X' against nondimensional yaw rate r' by simulations.

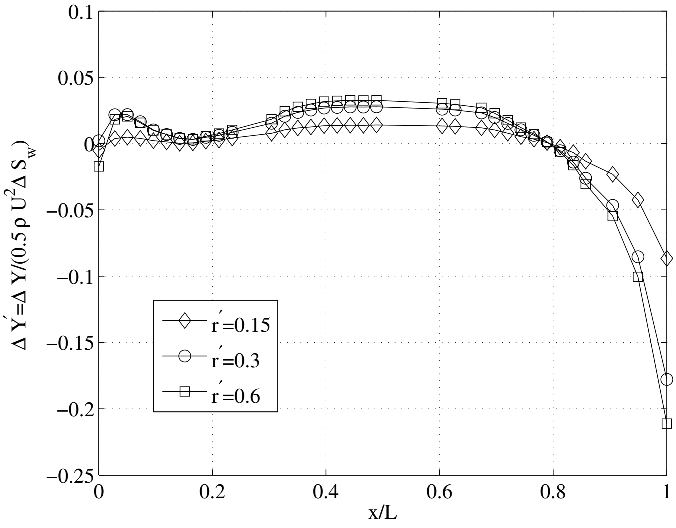

Figure 5.14: Lateral forces in steady yaw motion over the ship length. Sectional wetted surface area is denoted by S_W.

The dependency of $Y'$and N' on yaw rate is virtually linear in the investigated range of r', Fig. 5.12. The lateral force in steady turning was shown to point towards the center of the turning circle. No experimental data was available for comparison. The resemblance of steady turning tests in deep water condition with CFD has been shown to yield similar accuracy like steady drift motion tests, Cura-Hochbaum (2006), el Moctar et al. (2014). The effect of yaw rate on the longitudinal force is qualitatively the same as the effect of the drift angle, albeit with smaller magnitude at maximum relevant motion amplitudes. In steady turning forces on midship sections dominate the integral lateral force, Fig. 5.14. Local forces in the bow area of great magnitude acting into the eccentric direction are surmounted by steady forces between the fore and aft shoulder.

The replication of captive pure sway and yaw oscillations on idealized trajectories with CFD required changes in the numerical setup to account for the unsteady flow character. A host of numerical techniques within the framework of the presented FV-method is available to replicate prescribed motions. Among these are the prescribed motion of the entire domain, prescribed moving reference frames, the deformation of CVs (mesh morphing) and overset grids. Mesh morphing and overset grids become mandatory in presence of relative motions of ships to boundaries like tank walls. These represent the most complex and expensive methods. In unrestricted waters advantage can be taken of methods not involving challenging deformation of CVs or interpolation between background and overset meshes. Small motion amplitudes of the test cases and the broad tank of the model test facility suggested to impose motions on the entire solution domain. Lateral boundaries of the numerical tank were extended by $0.5L$ and changed from slip walls to a combined pressure outlet and velocity inlet boundary condition. Prescribed motions were defined in the ship-fixed coordinate system, which participated in motions. The trajectory and prescribed motion parameters are plotted over simulation time in Fig. 5.16 and 5.17. Additional sensitivity studies with respect to the time step were required in unsteady simulations. The time step was varied corresponding to 200, 400 and 800 steps per period of oscillation, for which C_{fl} was well below 1, albeit a limiting stability criterion does not exist for the employed implicit time-integration scheme. Varying the time step from 400 to 800 steps hardly affected the trends of Y' and N'. Computational time increased proportionally to the time step. It was concluded to run all remaining tests with 400 time steps per period of oscillation. Computing time for one period of oscillation was 30 minutes. The second and third period of oscillation gave equal periodic time histories of forces and moments, so that the solution was considered converged and the third period of oscillation was used for Fourier analysis. The comparison between CFD and EFD in Fig. 5.16 and 5.17 shows overall good agreement in Y' and N', while a small phase lag was observed in terms of the lateral force in pure sway oscillations. The maximum value of the yaw moment occurring at $t/T = 0.5$ is under-predicted by the simulation, if the EFD results was seen as the benchmark. Deviations observed in the trends of X' stood in the context of the overall small span within which X' varies over t/T and the aforementioned discussion on the balance of thrust and the longitudinal hydrodynamic force. The comparison of pure yaw tests between EFD and CFD predictions for X' follows the evaluation of the pure sway oscillation, i.e. quantities of small magnitude having emerged from the subtraction of two quantities with an order of magnitude greater are compared and show greater relative errors. Compared to the experimental results, CFD results showed a symmetric trend of Y' over one period of oscillation, and the so-introduced deviation in terms of the amplitude of Y' amounts to 30%. No experimental repeatability studies were available.

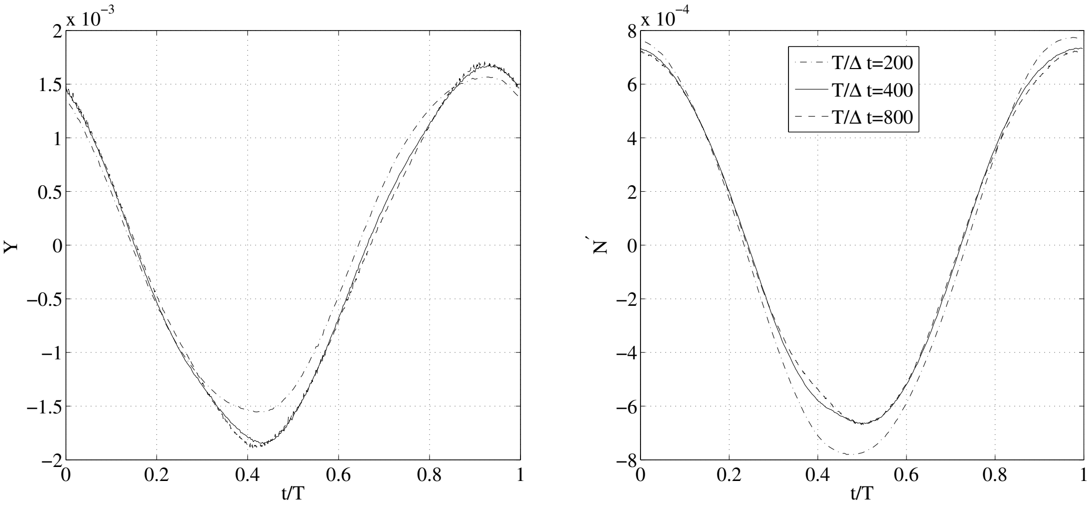

Figure 5.15: Comparison of the predictions of the nondimensional lateral force Y' and yaw moment N' during a pure sway motion simulation using various time steps.

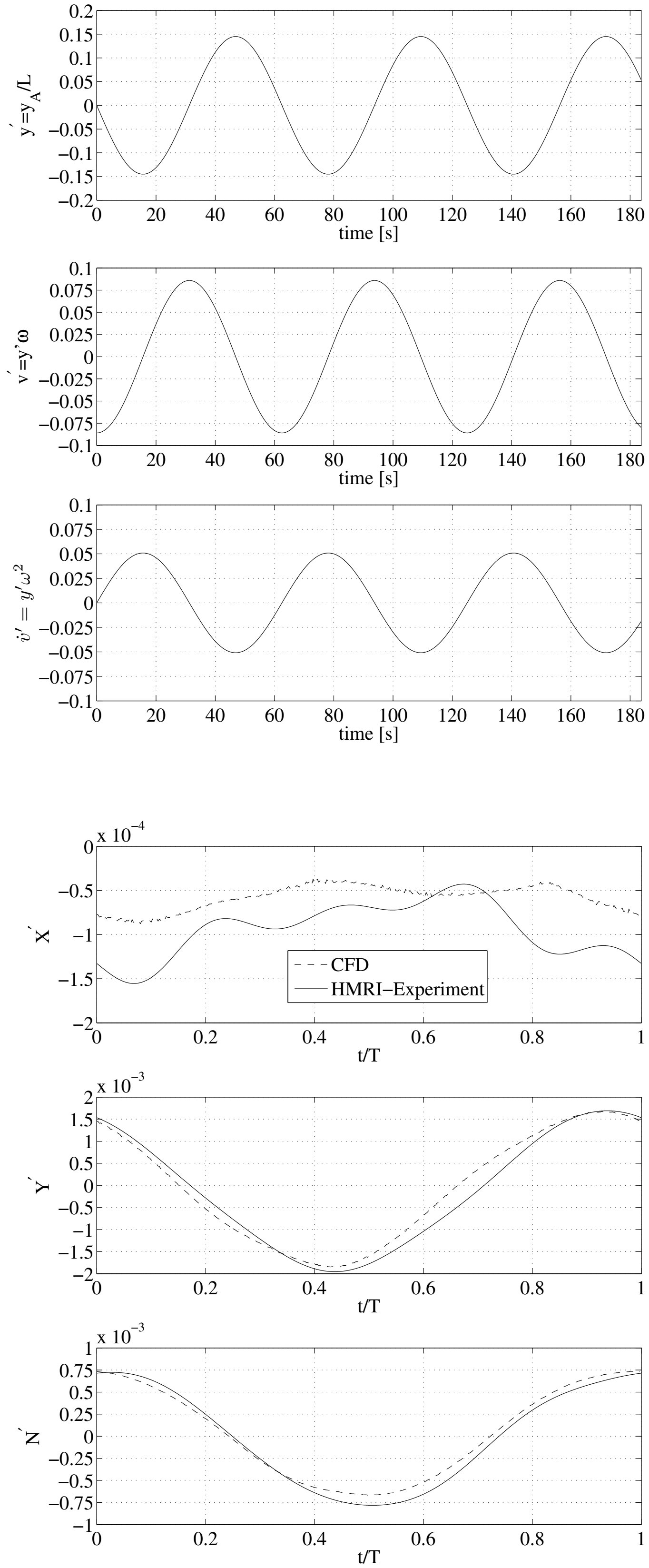

Figure 5.16: Time histories of prescribed motion parameters (top) and comparison of the predictions of the nondimensional hydrodynamic forces X', Y' and yaw moment N' during a pure sway motion simulation compared to experimental results (bottom).

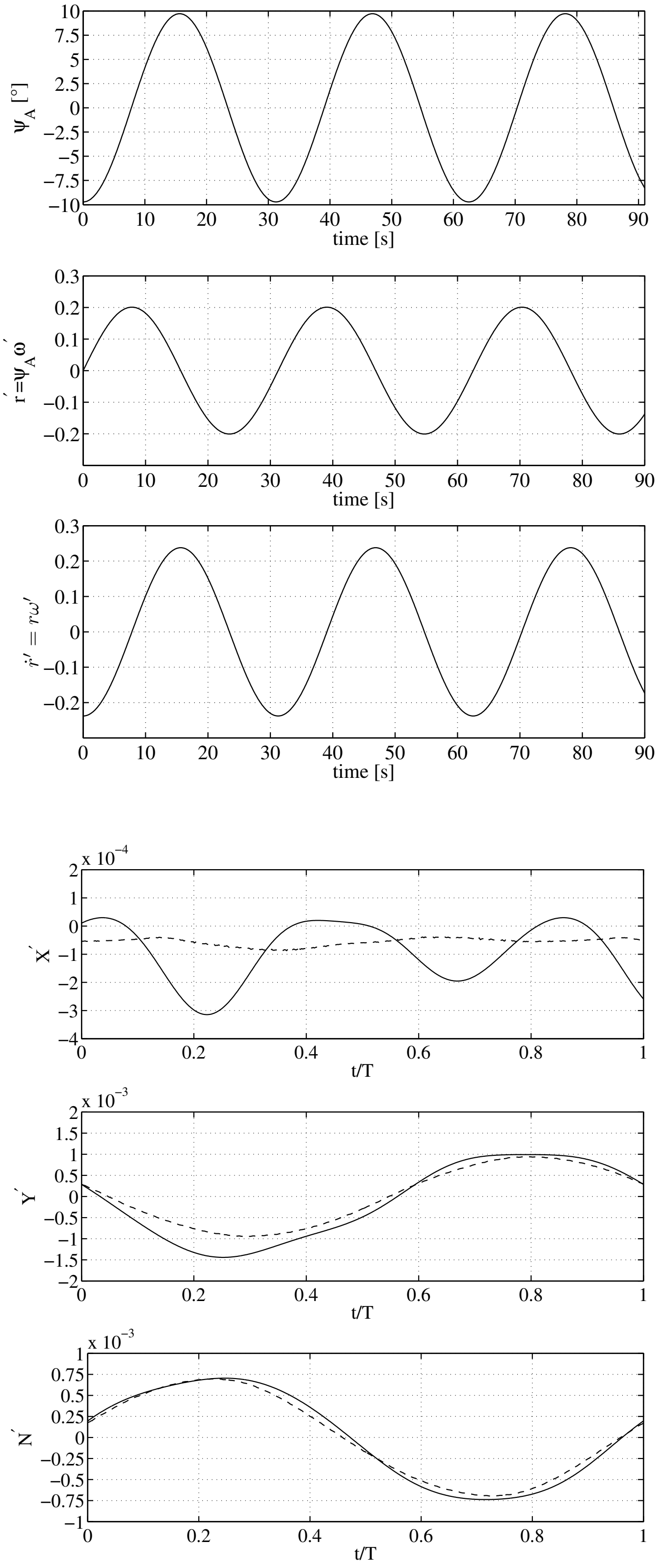

Figure 5.17: Time histories of prescribed motion parameters (top) and comparison of the predictions of the nondimensional hydrodynamic forces X', Y' and yaw moment N' during a pure yaw motion simulation compared to experimental results (bottom).

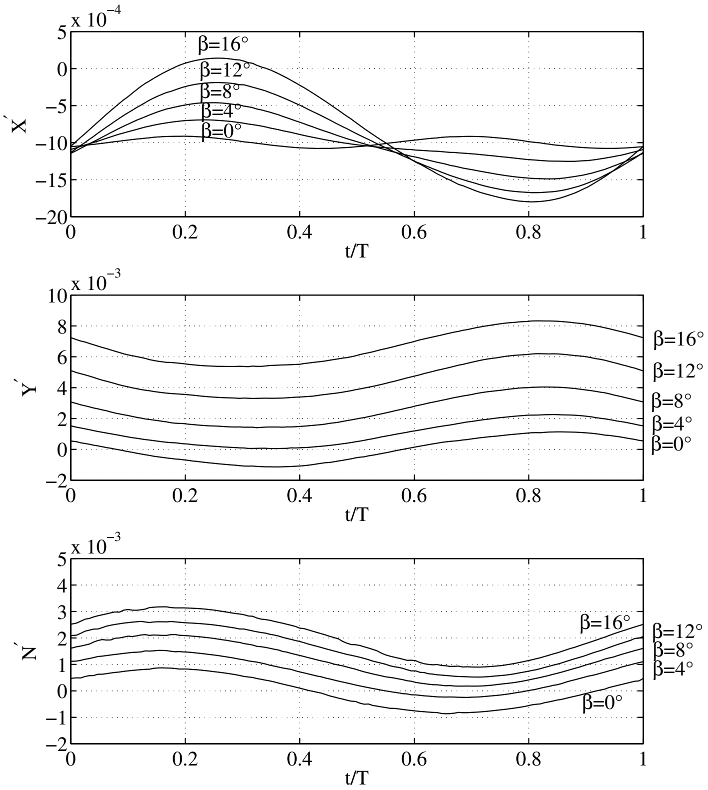

Figure 5.18: Comparison of the predictions of the nondimensional hydrodynamic forces during yaw oscillation simulations with fixed drift angles.

Fig. 5.18 shows results from harmonic yaw tests with fixed drift angle, which were used to derive the combined sway-yaw coefficients. The constant drift angle in yaw oscillations induced a constant lateral force and yaw moment, which shifts the periodic time histories of forces and moments along the ordinate according to the orientation of the ship. The periodic trend of longitudinal force X' underwent amplitude amplifications in response to induced drag arising from drifting.

5.3 Numerical analysis of flows around maneuvering ships in shallow water

The extension of simulations to shallow water conditions brings attention to several employed simplifications for deep water conditions. This discussion is driven by concerns regarding the reliability of turbulence models and the validity of the wall function approach, as well as the modeling and significance of free surface effects and squat. In light of the anticipated increase in complexity of simulations, the extension of simulations started with straight ahead conditions, laying emphasis on resistance and squat predictions, before transferring to steady lifting flows and finally, to dynamic captive motion tests in shallow water. There are theoretical and experimental grounds to anticipate that effects of turbulence and viscosity are more dominant in shallow water than in deep water flow regimes. This conflict is aggravated by the predominate investigation of ship flows at model scale to establish a common basis for validation through comparison with experiments, because viscous effects are overbooked in lower Reynolds number regimes. For the particular problem of squat prediction these hypotheses were confirmed in the PreSquat workshop (Mucha et al., 2014) and related studies, Deng et al. (2014), Mucha et al. (2016). A quintessential finding referred to appropriate treatment of near-wall ship flows. Wall functions are commonly applied in routine computations in industrial contexts to economize on computational resources. They have been shown to yield good results for resistance prediction of conventional displacement ships in unrestricted waters, and pressure-dominated flows around propellers and rudders, Larsson et al. (2003), Larrson et al. (2013). Their application to ship flows in shallow water remained questionable. While the neglection of modeling the free water surface for unconfined flows of small to moderate Froude number has widely been shown to be admissible, the physics of flows around ships in shallow water make the extension to two-phase modeling mandatory. Pressure variations in response to the blockage of the flow translate into variations of the free surface ambient to ships which in turn govern the dynamic floating position. These effects are a function of Froude depth number. Given the general capabilities to model both free surface dynamics and rigid body motions the objective was to assess the functionality and reliability of CFD, extending previous numerical studies on idealized flows around maneuvering ships, which drew upon fixed floating position and rigid free surface condition.

5.3.1 Experimental Setups

Model experiments were performed in the shallow water tanks of the Development Centre for Ship Technology and Transport Systems (DST) in Duisburg, Germany, Gronarz et al. (2009). The tank is operated at actual desired water depths up to approximately 1.1 m, rather than using so-called false bottoms in actual deep water tanks. Captive maneuvering tests in shallow water were carried out with a bare hull model of KCS at scale 40 at various water depths and forward speeds corresponding to Froude depth numbers between $F_{nh} = 0.27$ and $F_{nh} = 0.68$. Measurements of forces were performed using a PMM carriage, which differs from the conventional towing carriage for resistance predictions. The setup of the PMM device was adjusted as to allow heave and pitch motions, but constrain all other modes of motion. Sinkage was measured by means of laser plates at positions 1.44 m and -1.33 m with respect to amidships. Static trim was zero. Conditions are summarized in Tab. 5.1. The towing tank at DST is 200 m long and 10 m wide. The following discussion on resistance and squat prediction includes investigations with a model of DTC, which were carried out at DST for the aforementioned PreSquat workshop. While validation exercises involve the replication of experimental setups in the numerical towing tank, in practice the interest in ship motions often centers on open water predictions. Thus, it was desirable to check for the influence of tank walls on hydrodynamic forces and squat. The width of conventional towing tanks is in the order of one and a half to two times the length of the model ship. Wave reflections and flow blockage might affect measurements. Flow blockage was anticipated to increase squat and lateral forces in lifting flows. These aspects were taken up in sensitivity studies.

5.3.2 Numerical Setups

The account for the two-phase flow required the extension of the solution domain into the air phase. The domain extended about $0.5L$ above the ship. The grid was locally refined around the free water surface level in accordance with requirements of the HRIC scheme of the introduced VoF method. Near the outlet boundary the grid was coarsened in horizontal directions to allow introduction of numerical damping of the downstream propagating ship waves. Additional grid refinement was allocated to the UKC and stern region. Near-wall grid resolution depended on the wall treatment approach and targeted y^+. In case of applying a Low-Reynolds number turbulence model it was $y^+ \leq 1$. Fig. 5.19 and 5.20 represent detail views of sections of the grid in the yz- and xz-plane amidships for KCS valid for the Low-Reynolds number setup. Tab. 5.5 introduces abbreviations used in the discussion of numerical analyses. In the remainder, particular near-wall treatments at the hull and tank bottom are described using these abbreviations. LRN-WF refers to Low-Reynolds number treatment on the hull and wall function on the tank bottom, e.g. The number of CVs for the LRN-WF setup is usually 50 to 100 % higher than for WF-SLIP, and six to seven times higher than for double-body computations in deep water. A slip wall condition is usually applied to the tank bottom. However, in ship flows with small UKC a boundary layer may develop, and inflicting zero face-tangential velocity (no-slip wall) yields the physically consistent boundary condition. Wall functions were applied at the tank bottom. Bottom cells are assigned the velocity of the undisturbed flow to resemble relative motions between the ship and the bottom (moving no-slip). Two methods are distinguished in the computation of squat, which require coupling of the flow and rigid body equations of motion. The first method is the one of actual transient resolution, hereafter called free motion approach. The second method uses quasi-hydrostatic balancing, where the actual coupling is circumvented by stepwise release of the rigid body based on prescribed increments for sinkage and trim on one hand, and convergence criteria within the iterations of the stepwise release on other hand. The application of this approach is only admissible in steady or weakly unsteady flows. Stepwise hydrostatic balancing mitigates the well-known shock effect - i.e. divergence of the numerical solution due to severe rigid body motions in the initialization of the numerical solution, during which the pressure field around the ship is physically inconsistent. Due to port-starboard symmetry of conventional ship hulls, the question arose whether only half of the fluid domain could be modeled in straight ahead condition and a Neumann-type boundary condition in the plane of symmetry could map the solution onto the domain image. From a theoretical standpoint possible occurrence of flow separation, vortex shedding and associated asymmetry in the flow around the ship in shallow water make modeling of the entire domain mandatory.

Table 5.5: Abbreviations used in hydrodynamic analyses.

LRN	WF	SLIP	DB
Low-Reynolds number	Wall function	Slip wall	Double-body

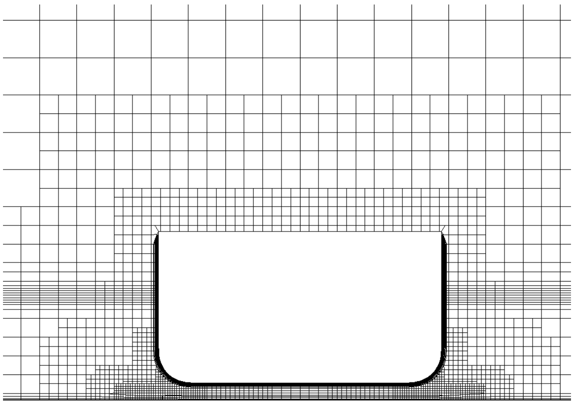

Figure 5.19: Grid setup in shallow water: midship section of KCS in the *yz*-plane.

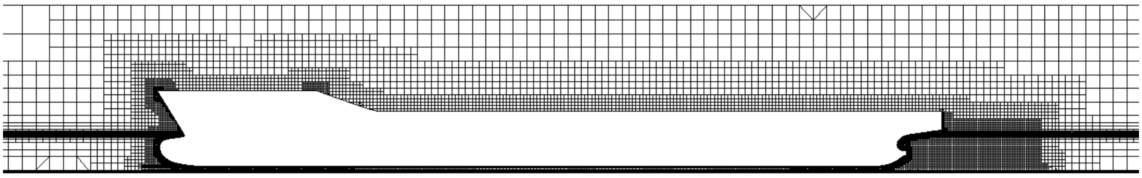

Figure 5.20: Grid setup in shallow water: midship section of KCS in the *xz*-plane.

5.3.3 Preliminary remarks on resistance and squat prediction

A summary is given of the quintessential findings of the state of the art in resistance and squat prediction, based on the investigation discussed in Deng et al. (2014) and Mucha et al. (2014). Fig. 5.21 shows the comparison of different resistance predictions for the DTC containership in shallow water condition ($h/T = 1.14$). Results referenced with ISIS-CFD relate to Yahfoufi and Deng (2014) and application of the ISIS CFD-code, Queutey and Visonneau (2007). The given reference includes estimation of discretization errors. It was found that applying wall functions instead of a slip boundary condition at the bottom wall yielded an increase in resistance prediction in the order of 1-2%. The predicted resistance with EASM was about 3-5% higher than with the kω-SST model and in better agreement with experimental results. The effect was more dominant in the lower speed regime. The maximum difference between the limiting cases of applying the kω-SST model in the WF-SLIP setup and the EASM in the LRN-WF setup was 8.3%, valid for $U = 0.632$ m/s. At the highest speed the LRN-WF setup and the computation with the EASM still yielded more than 5% difference to the experimental result. Sensitivity to turbulence modeling and tendency for underprediction of resistance was considered to rest with occurrence of flow separation in the aft ship. Shortcomings of RANS-based field methods in resolving such flow phenomena with required accuracy have been addressed, Deng and Visonneau (2005). Investigations at the highest forward speeds are particularly suitable to study the effect of turbulence, but are furnished with a strong academic character, since forward speeds beyond 10 kts are practically irrelevant for containerships of Post-Panmax class at $h/T = 1.14$. However, the better performance of EASM compared to kω-SST was assumed to emerge from the account for nonlinearities in the production-to-dissipation rate ratio and consideration of turbulence anisotropy in EASM, which leads to an associated reinforcement of drag. This effect is routed mathematically in the conservation of vorticity equation. A detailed treatise is presented by Deng and Visonneau (2005). The discussion of results of midship sinkage and trim predictions by experiments and numerical simulations is governed by the reliability of the experimental method and the general capabilities of the employed numerical methods. Besides above discussed RANS-methods, applications of GLRankine (von Graefe, 2015) and ShallowFlow (Gourlay, 2014) were presented, a method based on slender-body shallow water theory, Tuck (1967). ShallowFlow uses linearized boundary conditions for the hull and free surface.

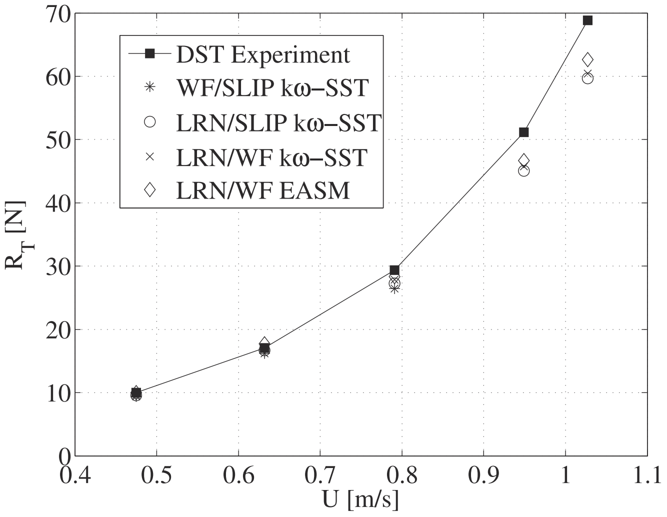

Figure 5.21: Comparison of resistance predictions by ISIS-CFD for the DTC containership at $h/T = 1.14$, 0.24< F_{nh} <0.52, Yahfoufi and Deng (2014).

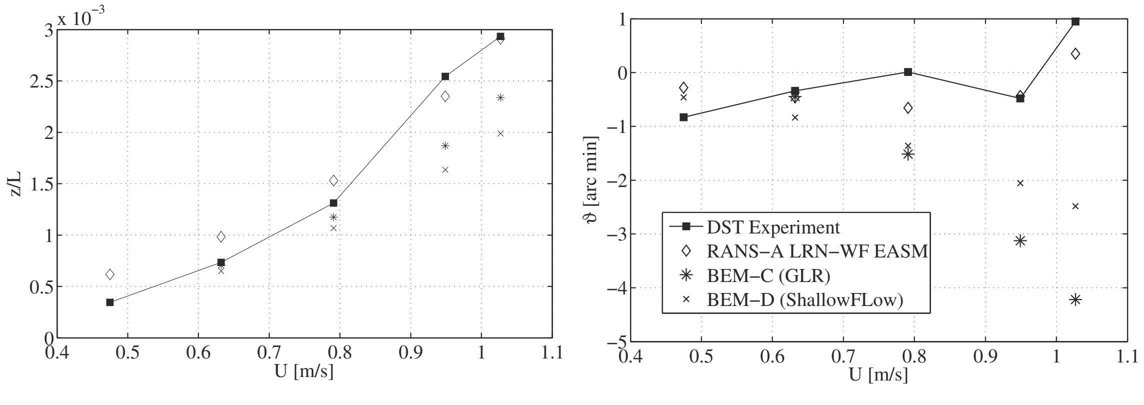

Figure 5.22: Comparison of squat predictions for the DTC containership at $h/T = 1.14$, $0.24 < F_{nh} < 0.52$, Mucha et al. (2015), Yahfoufi and Deng (2014).

It was concluded that in low Froude depth number regimes all methods provided similar results of pressure-dominated midship sinkage, while larger deviations were observed for higher forward speeds, especially in predicting trim. Agreement with experimental results was best with the RANS-method. Repeatability studies in experiments were considered desirable. Due to the overall very small trim angles measured, relative comparison errors were higher compared to those for midship sinkage. All in all, it was found that further validation studies were required to judge on the reliability of prediction methods involved.

5.3.4 Resistance and squat

In continuation of available validation studies on resistance and squat prediction with DTC, the introduced RANS-method (Chapter 3) was applied to KCS at four shallow water depths. Emphasis laid on flows around KCS at nondimensional water depth $h/T = 1.2$, for which sensitivity studies on spatial discretization and the influence of finite tank dimensions were conducted. All cases were set up in the LRN-WF configuration. For the method of hydrostatic balancing choices for sinkage and trim increments should be based on the Froude depth number. Numerical experiments yielded a range of 0.5 to 1 mm for sinkage and 0.5 to 1 arc minutes for trim. A computation using hydrostatic balancing took between six and eight hours until a converged trend of resistance, trim and sinkage was observed, using the introduced HPC environment. This represented a speed-up of factor in computing time of two to four compared to the free motion approach, depending on Froude depth number and resulting displacements in heave and pitch. Results differed by less than 2%. When using the free motion approach solutions for squat and resistance take a long time to settle to constant value. When applying the method of stepwise release trim and sinkage converge faster, which causes the solution for hydrodynamic forces to approach a constant value faster, too (Fig. 5.23). A grid sensitivity study for KCS is presented in Tab. 5.6. For resistance and sinkage the difference between computed results from different grids is small (max. 2.7%), but did not show monotonic convergence. No attempt was made to perform Richardson extrapolation. Remaining computations were performed using the medium sized grid. The relative comparison error to the experimental result is large for the longitudinal force (18.36%) and trim (16%), but moderate for midship sinkage (6%). While the differences in the prediction of the longitudinal force are consistent with previously addressed account for turbulence anisotropy and nonlinearities in the production-to-dissipation rate ratio, the comparison error for trim stands in light of the generally small magnitude ($\vartheta < 2$ arc min). For the validation case at $h/T = 1.2$, additional CFD predictions with ISIS-CFD were available for comparison (Mucha et al., 2016). Consistent with previous findings, application of EASM yielded better results compared to the $k\omega$-SST model. At the highest speed, deviations between EFD and CFD predictions are between 17% (ISIS-CFD, EASM) and 25% (STARCCM+, $k\omega$-SST), Fig. 5.24. Fig. 5.25 presents results of squat predictions. CFD predictions showed good agreement with model experiments for both midship sinkage and trim predictions. The two lowest forward speeds lay slightly outside this trend. Above simulations were resembled for KVLCC2 at $h/T = 1.2$ using equivalent grid setups and solution strategies, Mucha et al. (2016). The investigation was performed in an overall lower Froude depth number range and showed better agreement in predicting resistance between CFD and EFD on one hand, and the two different CFD codes on other hand. The performance of BEM is discussed in a dedicated section. Fig. 8.1 and 8.2 extend the validation study to greater UKC. Agreement between CFD simulation and experiments generally improved with regard to all computed quantities as UKC increased. The hydrostatic balancing routine was seen to converge faster the deeper the water depth was.

Table 5.6: Grid sensitivity study on hydrodynamic forces and squat $h/T = 1.2$, $U = 0.82$ m/s.

$n_{CV}/10^6$	X [N]	z [mm]	ϑ [arcmin]
4.4	-10.22	10.38	-1.175
6.9	-10.13	10.10	-1.488
12.5	-10.23	10.30	-1.19
Experiment	-12.53	10.96	-1.429
E%	18.36	6.00	16.00

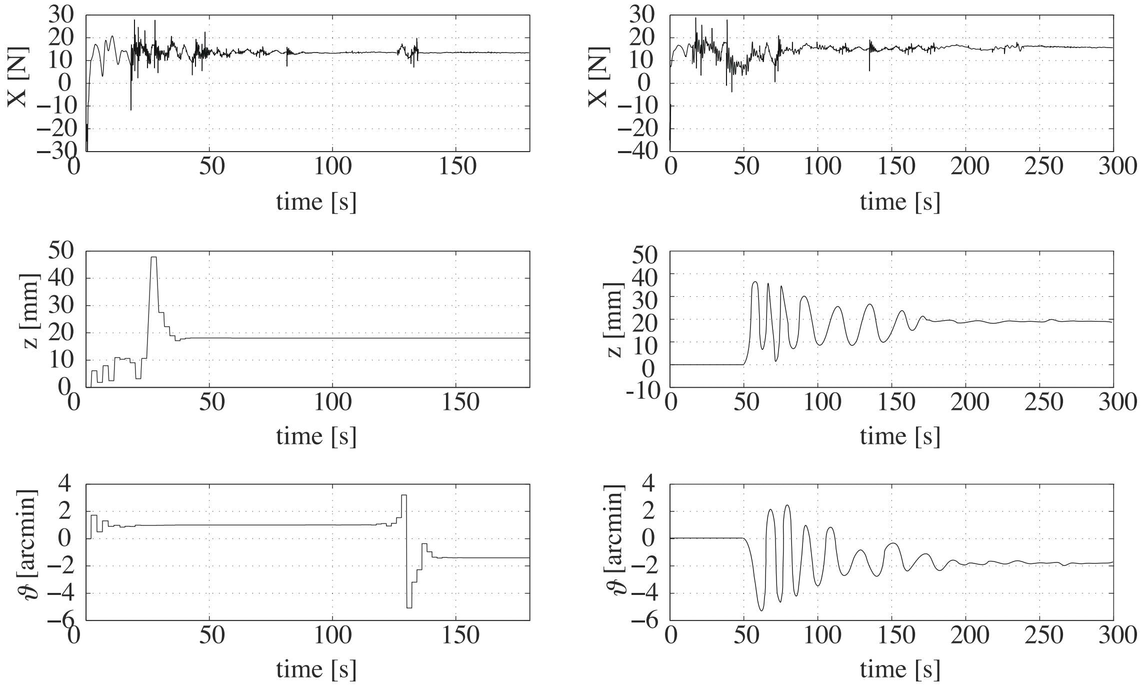

Figure 5.23: Time histories of resistance and squat predictions for KCS at $F_{nh} < 0.48$ using hydrostatic balancing (l.h.s.) and free motion (r.h.s.) simulation.

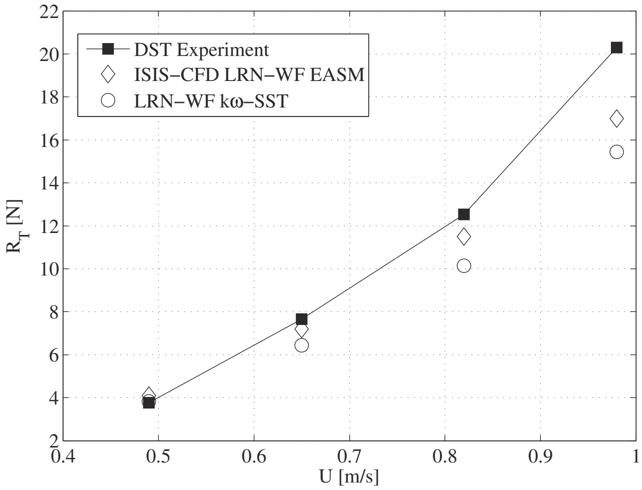

Figure 5.24: Comparison between EFD and CFD resistance predictions for KCS at $h/T = 1.2$, $0.29 < F_{nh} < 0.57$. Results were generated for Mucha et al. (2016): ISIS-CFD (Deng), BEM-ShallowFlow (Gourlay).

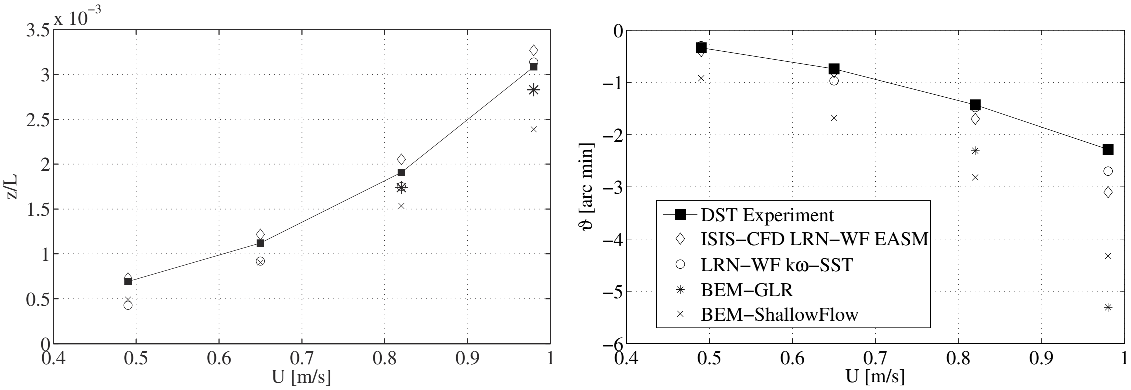

Figure 5.25: Comparison between EFD and CFD squat predictions for KCS at $h/T = 1.2$, $0.29 < F_{nh} < 0.57$. Results were generated for Mucha et al. (2016): ISIS-CFD (Deng), BEM-ShallowFlow (Gourlay).

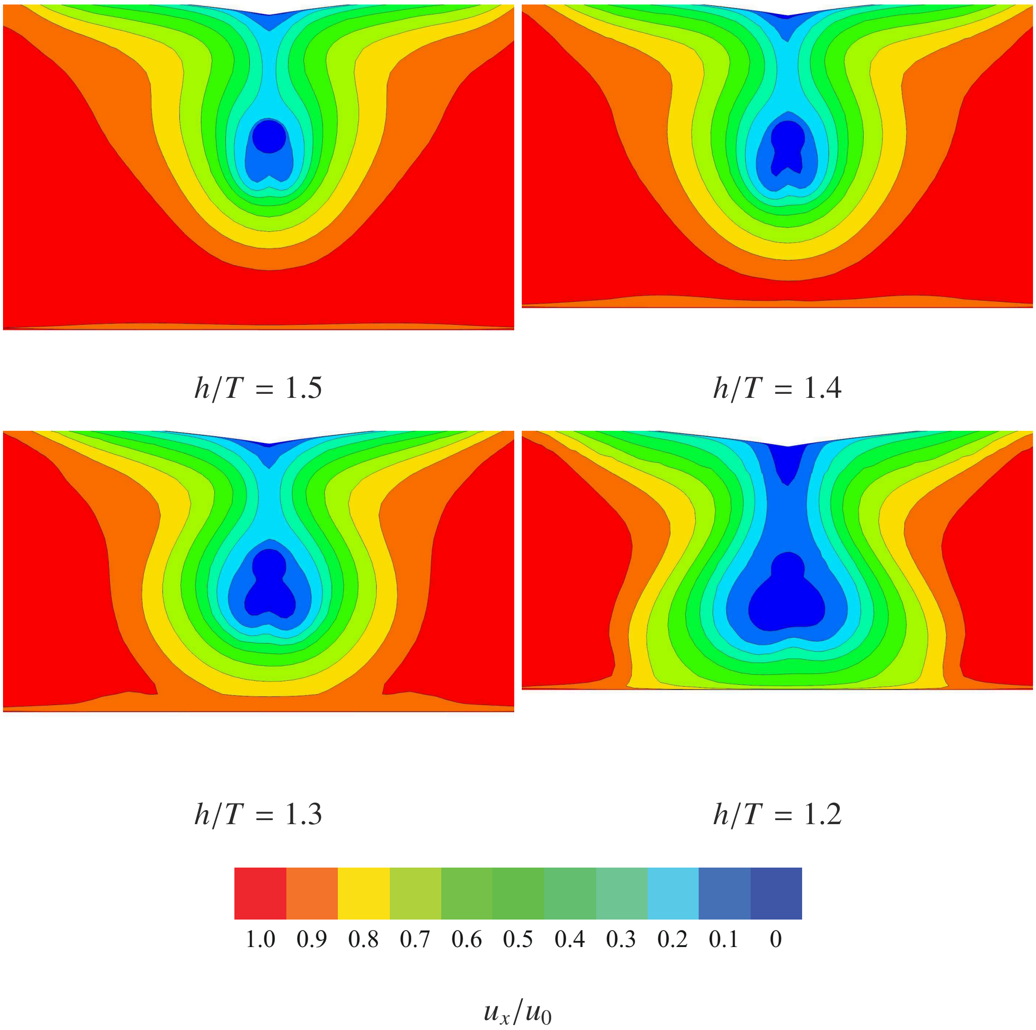

Figure 5.26: Scalar plots of u_x/u_0 in the propeller plane of KCS for $h/T = 1.2$, 1.3, 1.4 and 1.5..

Nondimensional axial velocity fields u_x/u_0 in a section through the propeller region provide insight into ship-bottom interactions over h/T. The decrease in UKC affects the shape of the ship wake in terms of a general widening of the isolines of equal u_x/u_0 towards the bottom and an expansion of regions of zero-axial velocities. These observations relate to the introduced discussion on turbulence modeling in RANS-based methods, but raise additional questions of general character on their capabilities to account for possible occurrence of flow recirculation in such flow regimes and the associated unsteady nature of the flow.

Squat predictions with BEM

The Rankine panel code GLRankine (GLR) was applied to test cases at $h/T = 1.2$ for the present investigation. Results generated with ShallowFlow (Gourlay, 2014) were available from Mucha et al. (2016) and are included in the discussion. A typical computational setup of GLRankine comprised between 1000 and 1800 panels. Fig. 5.27 shows the distribution of quadrilateral panels on the free surface in the vicinity of the ship hull, and the triangular panel grid on the ship hull. The domain extended three ship lengths downstream and three ship lengths upstream, according to recommendations from numerical experiments, von Graefe (2015). Computations were performed on an ordinary desktop PC (2.4GHz, 4GB RAM) and took between one and four hours, depending on the Froude depth number and convergence criteria. Since the objective of the computations was to determine sinkage and trim, the default convergence criterion related to wave resistance could be relaxed, decreasing computational costs. ShallowFlow provided results readily within minutes. The case with the lowest speed was not run with GLRankine due to divergence in the overall computational setup. Low forward speeds give small ship wave lengths, which require small panel sizes and high computational effort. These challenges could be circumvented with double-body simulations, demonstrated with GLRankine in von Graefe (2015). For DTC (Fig. 5.22) and KCS (Fig. 5.24) both BEMs showed increasing deviations to experimental results with increasing speed. In the lower speed regime ShallowFlow yielded good agreement with experiments and GLRankine. As F_{nh} increased above 0.6 ShallowFlow significantly under-predicted sinkage. This was referred to the increasing importance of nonlinear effects at all speeds in narrow canals, or at high speed in wide canals. Experimentally predicted trim angles were generally small, which has to be taken into account in the discussion of relative comparison errors. These observations were consistent with the established notion that sinkage is dominating in the subcritical speed regime, i.e. midship sinkage is an order of magnitude greater than the difference between sinkage at the fore and aft perpendicular. Both BEMs predicted a strong bow-down trim increasing with increasing forward speed. BEMs under-predicted sinkage and over-predicted trim in the higher forward speed regime. The Rankine panel method was again seen to be closer to model test results at $F_{nh} > 0.6$. The overall more bow-down trim predictions of BEMs encountered in investigations with DTC and KCS were referred to the neglect of the viscous boundary layer and its thickening towards the stern. Squat is governed by a low-pressure region between the fore and aft shoulders and the position of the longitudinal center of buoyancy. While midship sinkage depends on the magnitude of the resulting pressure field, dynamic trim is driven by the difference between downward forces of large magnitude at the fore and aft shoulder, and thus, particularly sensitive with regard to numerical prediction. Small changes in submerged volume change the balance of forces, which is discussed for squat of various containership shapes in Gourlay et al. (2015). In light of higher Reynolds numbers in full-scale ship flows BEMs are expected to show improved agreement when compared to full scale measurements. The same conclusion is drawn with respect to flows in moderate shallow water. For model scale ship flows systematic experimental studies might be translated into empirical corrections for sinkage and trim, as demonstrated in Gourlay et al. (2015).

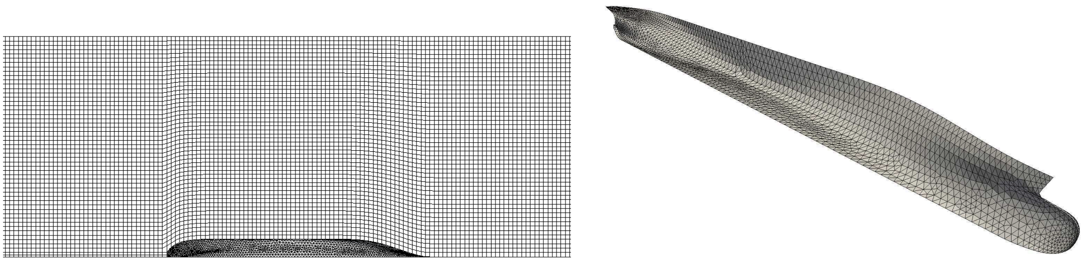

Figure 5.27: Detail view of free surface panels and triangular panels on the hull of KCS.

Influence of squat on resistance

To gain insight into the influence of squat on resistance simulations for KCS at $h/T = 1.2$ were run by constraining heave and pitch motions. Fig. 5.28 shows that in low and moderate forward speed regime differences remain small to moderate, while the case with highest Froude depth number $F_{nh} = 0.57$ shows a deviation of 17%. Previous investigations confirmed the increasing importance of trim contributions to resistance. The mean sinkage of the midship region leads to a mean decrease of the free water surface level between the fore and aft shoulders, which affects the primary wave system of the ship. Different vertical positions of the fore and aft shoulder, as well as the bulbous bow, which are caused by trim, alter the secondary wave system, which governs wave resistance.

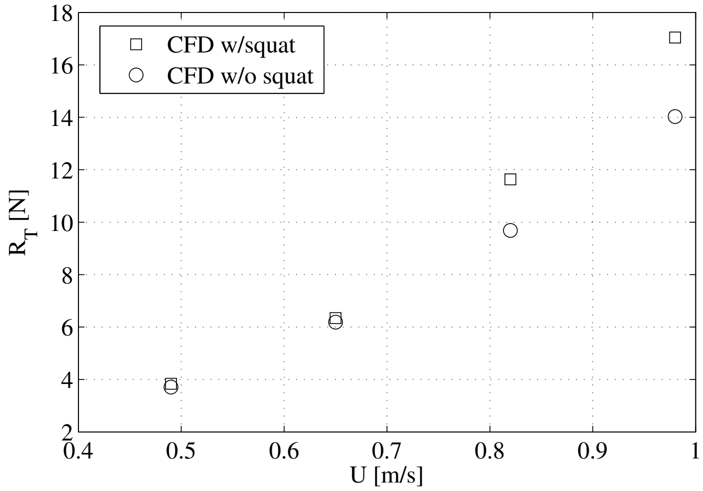

Figure 5.28: Comparison of CFD resistance predictions with and without taking into account squat for KCS at $h/T = 1.2$, $0.29 < F_{nh} < 0.57$.

Analysis of friction resistance

RANS simulations offer separate analysis of friction resistance R_F. Fig. 5.29 presents the change of R_F over h/T from the KCS investigation and the plate friction correlation line used in the ITTC 78 formula, where

$$R_F = 0.5 \rho c_F U^2 S_w \tag{5.2}$$

and

$$c_F = \frac{0.075}{(\log R_e - 2)^2} \tag{5.3}$$

Eq. (5.3) does not take into account the Froude depth number and is therefore only valid for the deep water case. CFD results refer to forces obtained from the integration of shear stresses over the wetted hull surface. The evaluation of the change of friction resistance with decreasing UKC shows that in low and moderate forward speed regime differences remain small to moderate, while the case for highest Froude depth number

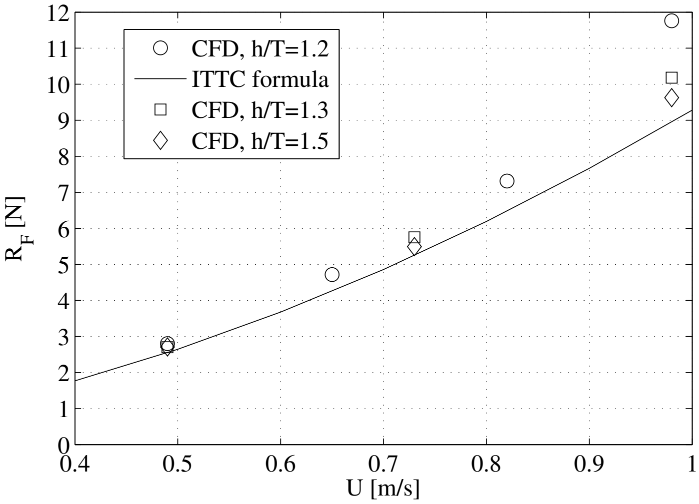

Figure 5.29: Analysis of friction resistance in various shallow water conditions.

shows a deviation of 33% compared to the friction correlation line. The increase in shear stresses with decreasing UKC is considered to preliminarily stem from the increase in local flow velocities in response to increased flow blockage.

5.3.5 Lifting flows

The investigation of lifting flows around the candidate ships in shallow water encompassed the simulation of idealized maneuvering motions, i.e. drift and turning motions. The focal point of interests laid on the prediction of lateral forces and yaw moments, as well the dependency of squat on drift angle and yaw rate. While steady drift motions are inherent part of experimental studies, model experiments with ships in steady turning motion in shallow water condition are seldom, because they require space which conventional rectangular shallow water towing tanks do not have. The analysis of idealized maneuvering motions in shallow water with respect to turning thus usually relies on captive oscillatory motion tests in the yaw mode of motion. Measurements of forces on the bare hull model of KCS from steady drift motion tests were available for various water depths and forward speeds, Gronarz et al. (2009). CFD analyses focused on the investigation water depth of $h/T = 1.2$ and an approach speed corresponding to 8 kts in full scale. Ship models in drift motion increase the effective blockage[a] in towing tanks significantly. Therefore, simulations considering finite tank width were compared to simulations in open water condition. To gain insight into the sensitivity of hydrodynamic forces to squat in steady drift motion, additional simulations were run with fixed floating position. Fig. 5.30 to 5.32 present the results of the analysis. The under-prediction of longitudinal forces in shallow water condition with the employed numerical method was addressed in previous sections and is causative to the deviations observed in the drift tests, too. Experimental uncertainty was not assessed, but was expected to be greater than in deep water conditions. The observed trend of X' over drift angle shows distinct deviations from the theoretically assumed quadratic dependency.

[a] By effective blockage the ratio between the projected frontal area of the ship and the tank cross-section in the yz-plane is meant.

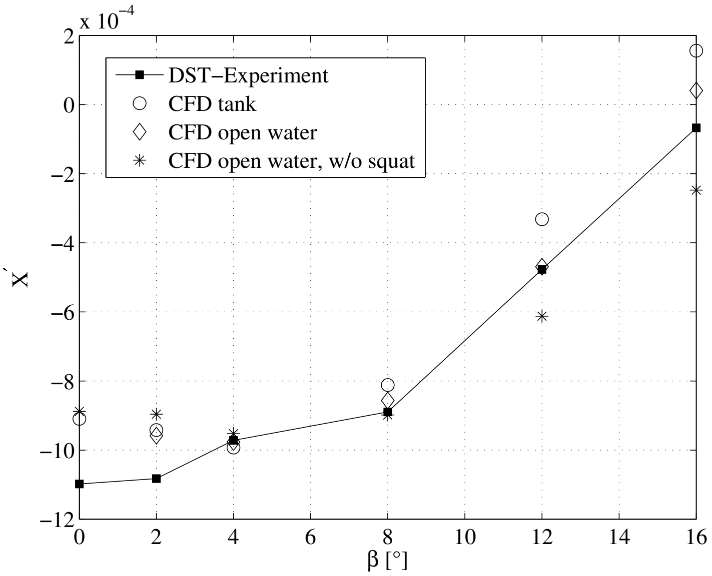

Figure 5.30: Comparison of EFD and CFD predictions of longitudinal forces in drift motion for KCS at $h/T = 1.2$, $F_{nh} = 0.38$.

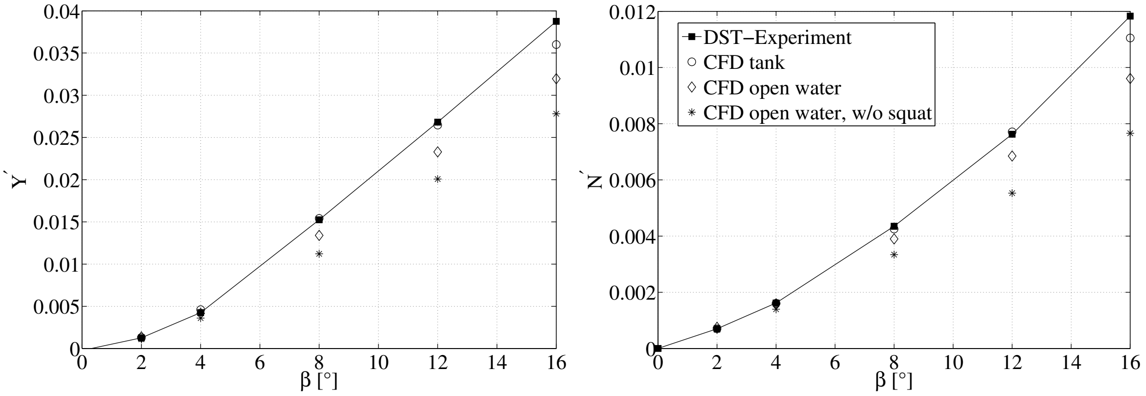

Figure 5.31: Comparison of EFD and CFD predictions of lateral forces and yaw moments in drift motion for KCS at $h/T = 1.2$, $F_{nh} = 0.38$.

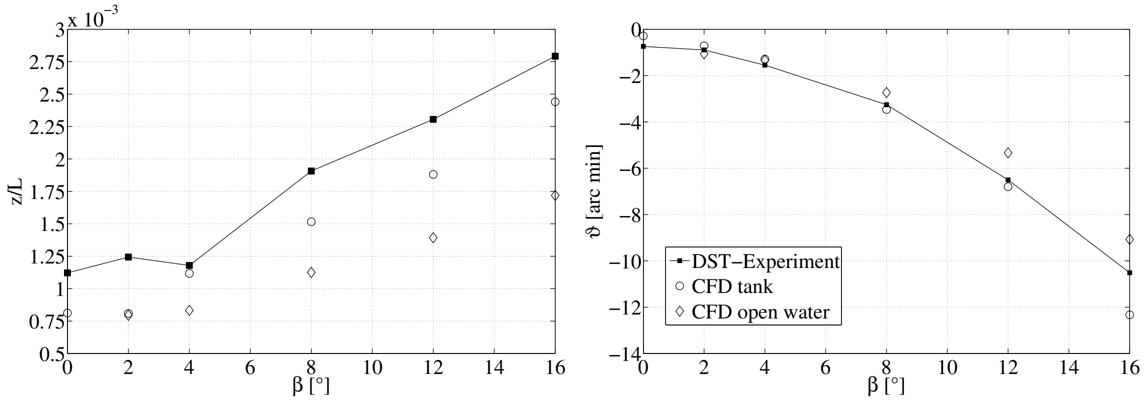

Figure 5.32: Comparison of EFD and CFD predictions of midship sinkage and trim in drift motion for KCS at $h/T = 1.2$, $F_{nh} = 0.38$

Agreement of predictions of Y' between simulations which resembled the towing tank dimensions are best, with a maximum deviation of 5%. Beyond $\beta = 8°$ simulations modeling laterally unrestricted flow, and simulations with fixed floating position in laterally unrestricted flow showed increasing deviations. At $\beta = 16°$ the deviation of the open water case was 11% and the deviation of the open water and fixed floating position case was 24% compared to the numerical towing tank case. The evaluation of the comparison of N' follows in analogy. Squat was shown to amplify significantly with increasing drift angle. This observation complies with the notion of a strong dependency of squat on the effective blockage. With the ship drifting at an angle of $\beta = 16°$, sinkage almost doubled, while the bow-down trim became almost four times greater than in straight ahead condition. Sinkage in laterally unrestricted water was between 20% and 30% less than computed in the towing tank setup. Experimental results for midship sinkage show aforementioned irregularities with respect to anticipated trend over the drift angle, too. The bow-down trim resulted in increased differences in the water level in the bow area between the wind- and leeward sides. Fig. 5.33 compares the free surface elevation around KCS in a drift motion of $\beta = 12°$ including squat and with fixed floating position. The decrease in local UKC is visible. Significant differences extend from the bow position to the fore shoulder, visible through the altered wave pattern.

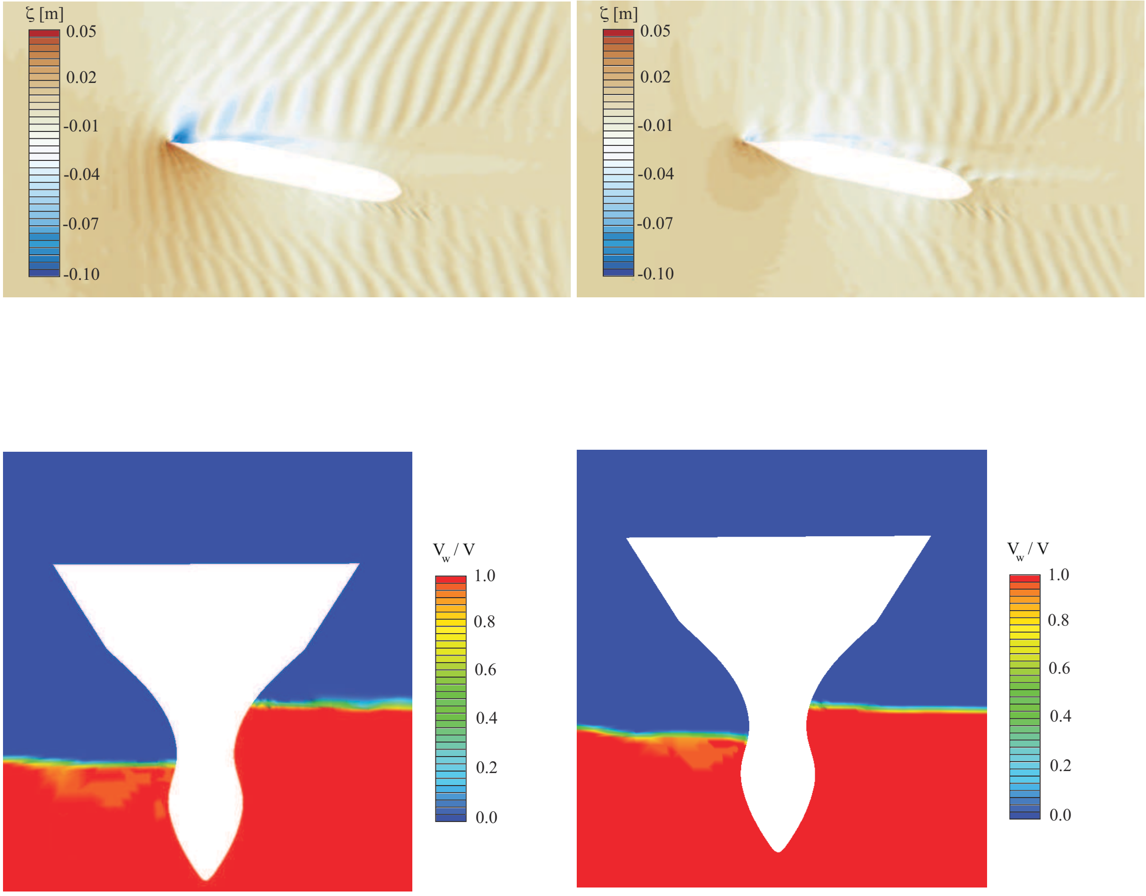

Figure 5.33: Detail view of the computed free surface elevation around KCS at 12° drift angle with free (l.h.s.) and fixed floating position (neglection of dynamic squat, r.h.s.). Bottom figures show computed volume fractions of water (red) and air (blue) at a section in the bow area.

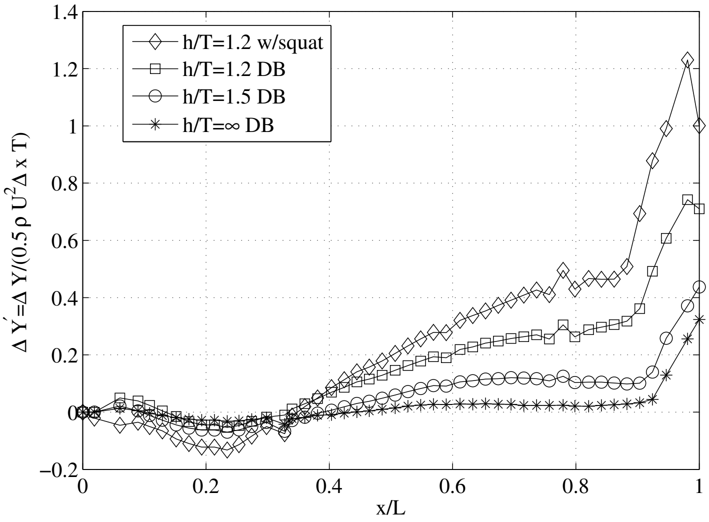

Figure 5.34: Lateral forces over segmented ship length of KCS.

The different water levels induced an increase of Y' and yaw moment N'. Such force contributions are anticipated to be proportional to $\rho g \Delta\zeta$, integrated over the ship length, where $\Delta\zeta$ is the local water level difference. The effect is a function of F_{nh}. The study of the distribution of lateral forces over the ship length from the validation studies in deep water is taken up to investigate the dependency on h/T. A practically relevant moderate drift angle of $\beta = 6°$ and forward speed corresponding to 7 kts in full scale is chosen. Fig. 5.34 shows the side forces on the segmented ship hull from double-body simulations in deep water, $h/T = 1.5$ and $h/T = 1.2$. Additionally, for the very shallow water case a simulation was run including the effects of the free surface and squat. The lower the UKC, the higher the magnitude of the forces in the fore ship. Besides, the point from where side forces increase towards the bow-area, shifts from a point near the fore shoulder towards amidships $x/L = 0.5$.

Since no experimental data was available for the numerical analysis of steady turning motions with KCS, simulations with KVLCC2 (Tab. 5.1) conducted in the context of the parameter identification procedure (Chapter 6.2, Tab. 6.1) are presented for discussion. Owing to the nature of steady turning motions and the aforementioned numerical resemblance in open water condition using moving reference frames, sensitivity studies on tank wall influences are obsolete. Consistent with steady turning simulations in deep and open water condition (Chapter 5.2.3) the domain extended uniformly three ship lengths into all horizontal dimensions and the velocity field was prescribed according to the desired turning motion. The investigated range of turning rates r' corresponded to turning diameters between $3.5L$ and $9.5L$, valid for an equivalent forward speed of $U = 7$ kts in full-scale. Fig. 5.35 to Fig. 5.37 present the trends of nondimensional hydrodynamic forces and squat over turning rate. The anticipated increase of all computed quantities with increasing turning rate is observed, albeit in significantly different fashion. As expected the dependency of X' on r' resemblances a quadratic trend, and the dependency of Y' and N' on r' suggests a cubic trend. Midship sinkage showed a moderate increase with turning rate, as the computed value at the maximum turning rate increased only by 37% compared to the straight ahead condition. More striking is the observed weak sensitivity of trim, which remains almost constant over r' with an increase of just 22% at the highest turning rate. These observations differ from the analysis of steady drift motions at the same operational point (Fig. 8.8). Here, an equivalent increase in sinkage and trim is observed already at small drift angles $\beta < 5°$. At low forward speeds and moderate turning rates turning motions are more similar to the straight ahead condition than drift motions, involving weaker cross-flow along the length of the hull. Besides, the numerical setup for steady turning motion did not consider tank walls and associated increased blockage. These observations suggested to assess how double-body simulations compare to simulations taking into account the free surface and squat. The steady turning motion corresponding to a turning diameter of $3.5L$ ($r' = 0.58$) was chosen for this investigation. The double-body simulation gave results in terms of Y' and N', which were in good agreement with aforementioned simulations. However, the prediction of X' differed by 16%.

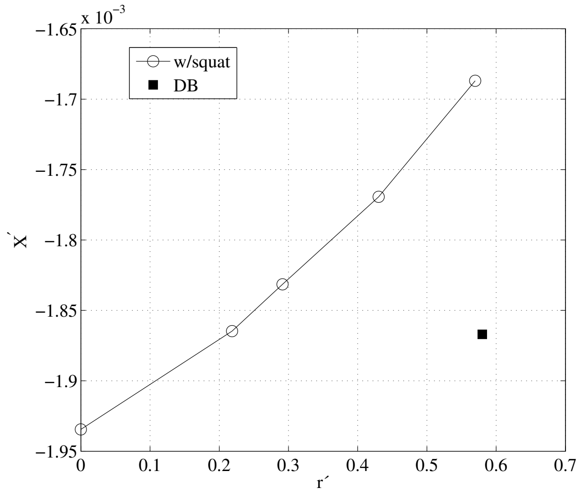

Figure 5.35: Comparison of EFD and CFD predictions of longitudinal forces in yaw motion for KVLCC2 at $h/T = 1.2$, $F_{nh} = 0.23$

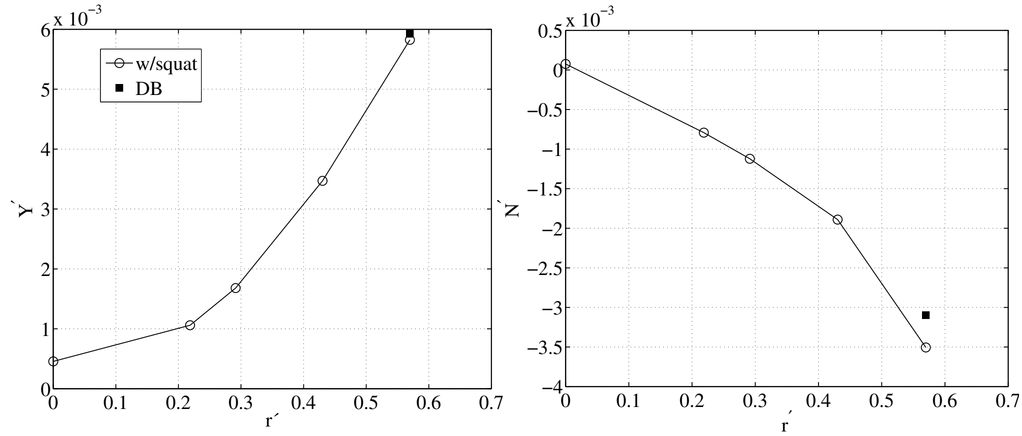

Figure 5.36: Comparison of EFD and CFD predictions of midship lateral force and yaw moments in yaw motion for KVLCC2 at $h/T = 1.2$, $F_{nh} = 0.23$

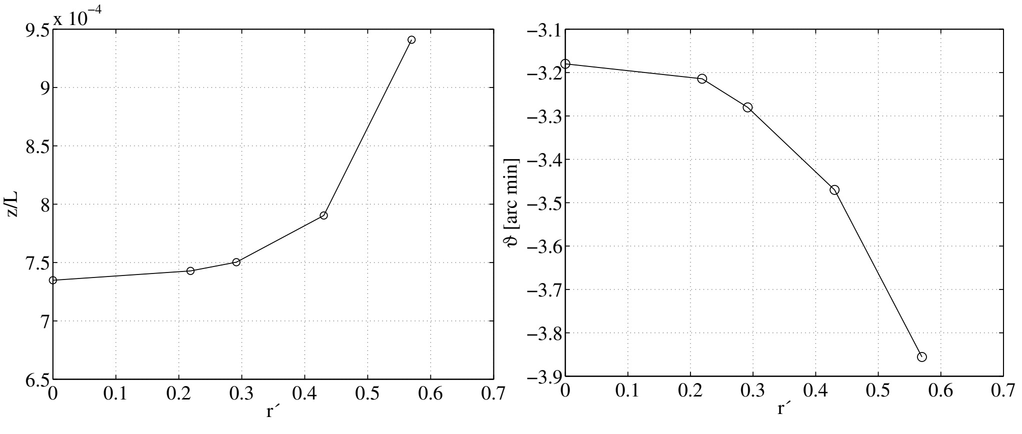

Figure 5.37: Comparison of EFD and CFD predictions of midship sinkage and trim in yaw motion for KVLCC2 at $h/T = 1.2$, $F_{nh} = 0.23$

Captive oscillatory motion tests

Numerical simulations of oscillatory motion tests in shallow water conditions impose increased complexity to the numerical method. Relative motions between ships and the tank prohibit the application of moving reference frames or global motion of the solution domain. Only grid deformation and overset grid methods are able to account for such relative motions. The study of steady drift motion simulations revealed the importance of free surface effects and squat for moderate to high sway velocities. It remains to be determined whether the numerical method is capable of modeling prescribed oscillatory motions in presence of the free surface and small UKC, while trim and sinkage remain unconstrained. Further considerations relate to the overall high number of CVs required for simulations of ship flows in shallow water in conjunction with the temporal resolution of the prescribed oscillatory motion tests. The evaluation of the convergence history of forces, moments, sinkage and trim showed that in shallow water flow regimes the solution takes a longer time to converge than in deep water. Mesh morphing was shown to perform well for squat predictions in straight ahead, and steady drift and yaw motion condition using the method of hydrostatic balancing, but oscillatory motion tests require transient coupling of the flow and rigid body equations of motion. In this context, the main problem of mesh morphing refers to the deformation of CVs in both vertical and horizontal direction, and the stretching in response to trim and yaw motions. Fig. 5.39 illustrates the limitations of the mesh morphing method with regard to the modeling of such motions in shallow water using a spheroid as an academic sample body. Exemplary, a mesh around the spheroid (initial UKC: 20% of ship draft) of dimensions typical to ship geometries was deformed following typical amplitudes in sway and heave. Given a required fine degree of mesh resolution there exists a limit for concurrent stretching of CVs in horizontal and vertical direction. Pure yaw, and combined yaw and sway oscillations with free floating position represent the extreme case, as CVs are required to participate in rigid body motions in the yaw, sway, heave and pitch mode of motions. Numerical experiments confirmed that CVs compressed in response to such motions are prone to attaining zero volume at practically reasonable grid resolution and relevant motion amplitudes. Mesh morphing routines are able to project prescribed motions in lateral direction to the bottom CVs, which could relax above conflict. The method of overlapping grids holds inherent advantages in terms of feasible motion amplitudes in the modeling of relative motions between background and overset meshes. However, application of overset grids requires a certain number of CVs between moving bodies and interface boundaries to enable interpolation between acceptor and donor cells. It is generally desirable to extend the overset region boundaries sufficiently far away from the moving body boundary, where flow gradients are anticipated to be lower. In light of the interpolation between donor and acceptor cells, fine meshes with low aspect ratio are desirable. Such requirements create a conflict for the present problem of ships moving at small UKC, because it was shown that anisotropic refinement in the UKC area is favorable to keep computational costs reasonably low. Moreover, the transient resolution of CV motions becomes the limiting criterion for the time step, rather than the transient resolution of the flow. A rule of thumb is to employ a time step which ensures that the smallest CV involved in the interpolation does not move more than half of its characteristic length in the direction of motion, which for captive oscillatory motion tests results in time steps which can be three

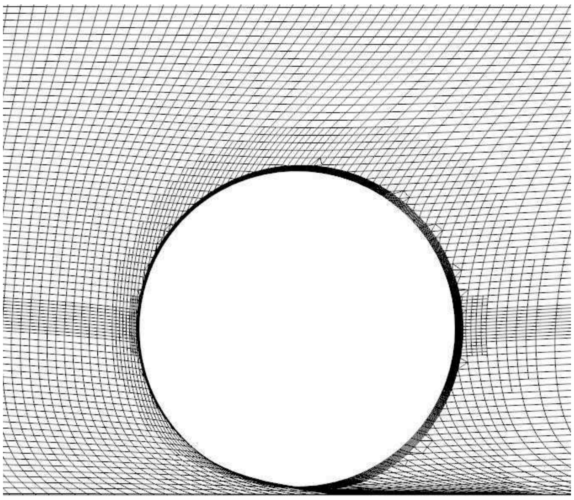

Figure 5.38: Conflict for mesh morphing in captive oscillatory tests.

to four times smaller than required for single domain computations, illustrated in Fig. 5.39. For small UKC a problem emerges from oscillations in heave and pitch, which the overset region participates in and which cause the overset region to intersect with the background domain boundary. Special numerical techniques have been developed to allow such intersections. For example, overset CVs leaving the background mesh can be excluded from the interpolation procedures, CD-adapco (2016). However, the numerical solution is prone to deteriorate in such cases. To circumvent above problems, it appears favorable to combine the overset grid with the mesh morphing technique. Motions in the horizontal plane, which are one or two orders of magnitude greater than displacements in heave and trim, could be modeled using overset grids, while mesh morphing accounts for squat within the overset region. This approach was discussed for pure sway and pure yaw motion tests by Deng et al. (2016). However, numerical stability could only be assured at high computational cost. The solution required initialization in straight ahead condition and employing a pre-deformation of the mesh based on the anticipated mean squat to account for dynamic variations in heave and pitch during captive oscillations in sway and yaw. The resulting wall clock time was ten days for resembling six periods of oscillations. Owing to overall low to moderate motion amplitudes in maneuvering at shallow water, the question arose, whether it was necessary to perform captive oscillatory simulations with free floating condition, or, whether simplifications in terms of modeling squat were admissible. Experimental data for benchmarking of numerical captive oscillatory tests were available for DTC, Eloot et al. (2016). Numerical results were available for comparison from Deng et al. (2016). Pure sway and pure yaw oscillations were performed at $\lambda = 89.11$, $h/T = 1.2$ and $F_{nh} = 0.433$, corresponding to 11 kts in full-scale. Investigated test parameters are summarized in Tab. 5.7. To check for the sensitivity of hydrodynamic forces to squat, circumventing the computational expensive initialization of the flow and motion, the strategy of the simulations was to compare tests with fixed floating position to tests in which dynamic sinkage and trim were prescribed based on the time histories available from experiments. Grid generation and case setup followed the strategy from the validation studies in Chapter 5.3.4. Preliminarily conducted resistance

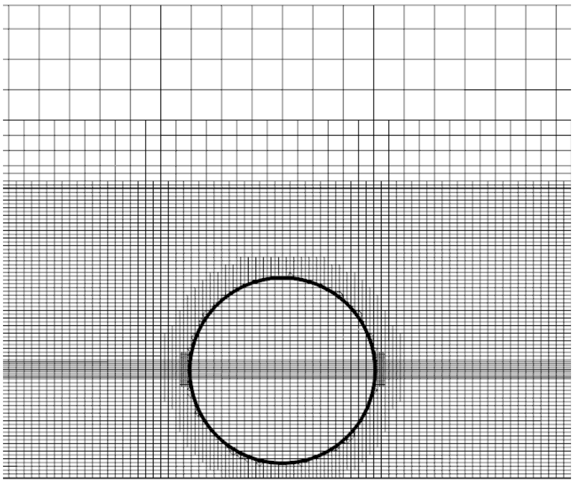

Figure 5.39: Conflict for overset grid application in shallow water condition.

tests yielded good agreement to experiments (Tab. 5.8). Fig. 5.41 compares the time histories of trim and sinkage over one period of oscillation for a pure sway and a pure yaw oscillation, Eloot et al. (2016). While in pure yaw, trim and sinkage only slightly vary around their mean values of the straight ahead condition, variations for pure sway are significant. Fig. 5.42 compares the time histories over one period of oscillation of the lateral force and yaw moment for the discussed sensitivity. The neglection of squat in simulations yielded amplitudes between 30 to 50 % less than if squat was modeled. A phase shift in N can be observed, too. In this case Y' and N' are in good agreement with experimental values. The wall time of the simulation of three periods of oscillation with prescribed squat was 23 hours, which was 10 hours more than the simulation without considering squat.

Table 5.7: Captive maneuvering test cases under scrutiny for DTC, $h/T = 1.2$.

Oscillatory test	U_c [m/s]	y_A [m]	ψ_A [deg]	T [s]	ω' [-]
Pure sway	0.599	0.2	0	20	2.1
Pure yaw	0.599	0	15	25	1.68

Table 5.8: Resistance computation for DTC at straight ahead condition, $U = 0.599$ m/s, $h/T = 1.2$.

$n_{CV}/10^6$	X [N]	z [mm]	θ [arcmin]
7.33	3.55	5.25	-0.41
Experiment	3.43	5.00	-0.42
E%	-3.50	-5.00	2.40

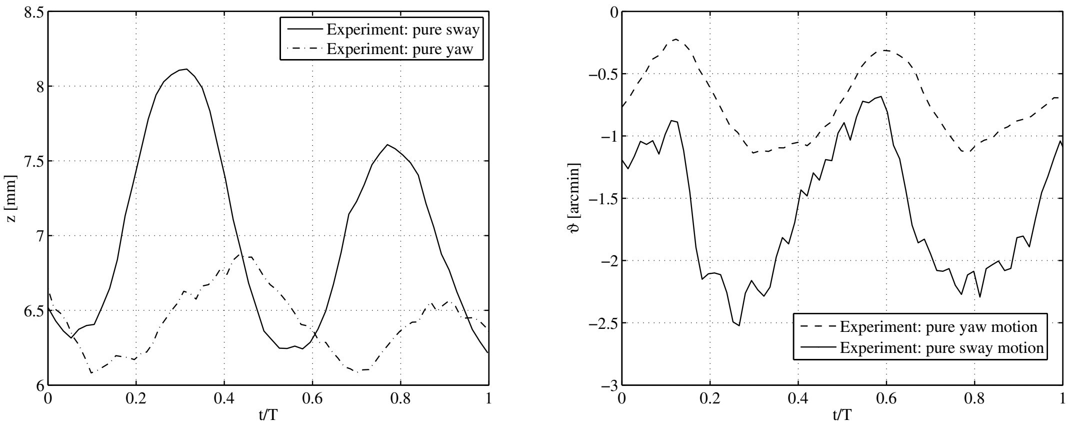

Figure 5.40: Comparison of time histories of squat during captive pure sway (solid line) and pure yaw (dashed line) oscillation experiments in shallow water, Eloot et al. (2016).

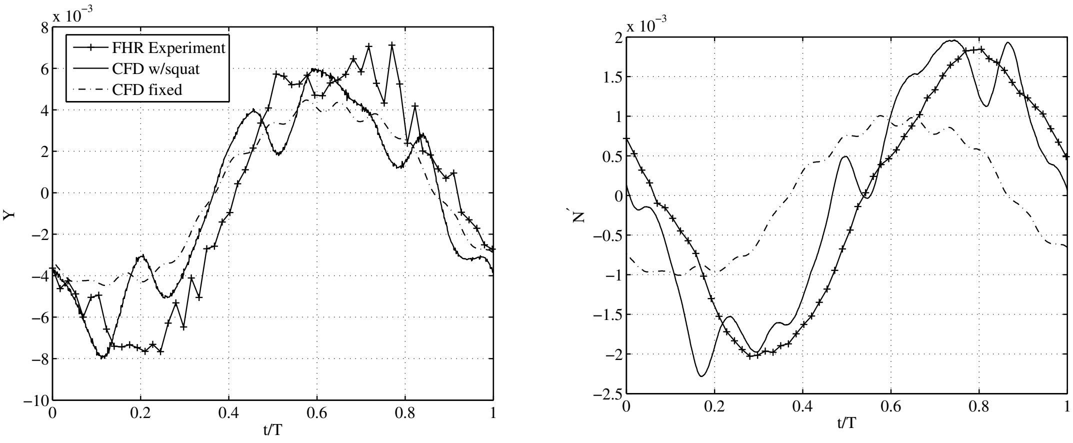

Figure 5.41: Comparison of computed sway force and yaw moment on DTC during captive pure sway oscillation tests in shallow water. Experimental results refer to Eloot et al. (2016).

5.4 Concluding remarks

The investigation of idealized flows around models of KVLCC2 and KCS in deep and shallow water condition included verification and validation of a numerical method based on the solution of the RANS equations. Resembling captive maneuvering tests on idealized trajectories in deep water condition was shown to be in good agreement with experiments. Taking advantage of appropriate simplifications in terms of neglecting the modeling of the free water surface, employing wall functions in the near-wall treatment of the flow around the hull and substituting the expensive transient modeling of the rotating propeller by a body force propeller reduced both number of CVs and time to convergence of the solution. In absence of flow restrictions, global motion of the solution domain or moving reference frames could be used to avoid expensive mesh morphing or overset grids. Hydrodynamic forces were predicted with deviations of 1% to 15% to to experimental results, without taking into account elaborate uncertainty analysis of EFD. All

Table 5.9: Wall clock times of RANS-based captive maneuvering tests using different setups.

Test	Deep water		Shallow water	
	Wall time	CVs	Wall time	CVs
Static tests (DB)	15 min	$1.3 \cdot 10^6$	23min	$3 \cdot 10^6$
Static tests (w/squat)	25min	$2 \cdot 10^6$	8h	$7.5 \cdot 10^6$
Dynamic tests (DB)	30min	$1.3 \cdot 10^6$	1h	$3 \cdot 10^6$
Dynamic tests (w/squat)	1h	$2 \cdot 10^6$	4d	$7.5 \cdot 10^6$

in all, the presented simulation framework represents a fast and reliable procedure as an alternative to experiments, which complies with the recently established state of the art in ship hydrodynamics, ITTC (2014), Cura-Hochbaum (2006). The extension of the procedure to shallow water conditions required the assessment of the capabilities and reliability of CFD to model such flow regimes. It was found that powerful hydrodynamic interactions between ship models and flow restriction are present, affecting the computation of hydrodynamic forces. The importance of ship-induced free surface dynamics and squat was confirmed. Simplified turbulence modeling and near-wall treatment was disqualified for the accurate prediction of resistance in presence of small UKC. Overall differences in the prediction of hydrodynamic forces between experimental and computational results increased compared to the analysis in deep water condition, in part taking values of up to 40%, while in absence of uncertainty analysis of results quantification of the reliability of EFD remains undetermined. The complexity and challenges of EFD for the present problem were addressed, too. The coupling of the flow to rigid body equations was shown to introduce increased complexity and computational cost, especially for captive oscillatory tests. In light of wall times in the order of days for just one test, numerical replication of captive oscillatory tests carries significant disadvantages compared to experiments. Once a model is set up in the towing tank variational runs can be performed much faster. Tab. 5.9 summarizes the performance evaluation of numerical captive maneuvering tests in deep and shallow water condition in terms of wall time. An efficient way to circumvent the expensive conduction of captive oscillatory tests was seen in the application of three-dimensional panel methods for the computation of the hydrodynamic added mass tensor for various water depths, which can be used to approximate hydrodynamic coefficients acting on rigid body accelerations. This procedure was demonstrated within the scope of the present investigation for KVLCC2 and addressed in Chapter 2.5.1. Coefficients associated with damping could then exclusively be identified on the basis of steady drift and yaw, and combined steady drift and yaw tests, which makes captive oscillatory motion simulations obsolete.

6. Maneuvering Simulations

This chapter concludes the investigation of simulation-based ship maneuvering predictions of standard rudder maneuvers in deep and shallow water. Comparison is drawn to experiments with a free-running model of the KVLCC2 tanker, Quadvlieg and Brouwer (2011), Tonelli and Quadvlieg (2015) and Eloot et al. (2015), all of which were conceived for the SIMMAN (2008, 2014) workshops. Available experimental analyses comprise repeatability studies and uncertainty analyses, which is of particular value for validation exercises of mathematical models for maneuvering simulations. Comparing investigations entail predictions of turning and zig-zag maneuvers.

6.1 Experimental setups

Quadvlieg and Brouwer (2011) present experimental analyses of maneuvering in deep water for KVLCC2. A scale models of KVLCC2 ($\lambda = 45.741$, Tab. 5.1) was tested in the basin of MARIN. The procedures for turning and zig-zag maneuvers essentially followed descriptions given in Chapter 2.2. The model was accelerated to the desired approach speed, and then manually released. The position of the free-sailing model with respect to the carriage was recorded by means of an optical measurement system. The carriage position itself was measured with rulers. Rigid body velocities followed from processing of position signals, the rudder angle was measured using potentiometers and rate of turn was measured with a yaw velocity sensor. Results were scaled to the dimensions of the ship using Froude similarity. The approach speed corresponded to 15.5 kts in full scale. Propeller rate of revolution was kept constant throughout the tests. Repeatability studies concerned the -10°/10° zig-zag and -35° turning maneuvers, for which four realizations were run. Uncertainty analysis leaned on the ISO Guide for Uncertainty in Measurement (GUM) procedures, e.g. Coleman and Steele (2009) and ITTC (2008). It sought to obtain a quantification of uncertainty for a given measured quantity taking into account measurement uncertainty, repeatability studies and uncertainty propagation analysis. Measurement uncertainty concerns random and systematic errors involved in application of sensors or any measurement equipment. Repeatability studies provide scatter in results from a number of test runs and stochastic uncertainties. Uncertainty propagation analyses deal with the quantification of how uncertainty in input variables translates to uncertainty in output variables. Confidence levels are used to generate confidence intervals. A conventional level is the 95% confidence level (U95). In Quadvlieg and Brouwer (2011), the total U95 uncertainty for a measurement variable is given by

$$U95 = \sqrt{U95_m^2 + U95_r^2 + U95_p^2} \tag{6.1}$$

where $U95_m$ is measurement uncertainty, $U95_r$ is repeatability uncertainty and $U95_p$ is propagation uncertainty. Uncertainties were applied to the remaining maneuvers of the experimental programme, for which only one realization was run. The investigation of Tonelli and Quadvlieg (2015) represents an extension of above outlined experimental analyses to maneuvering in shallow water. When conducting such free-running tests in shallow water towing tanks several issues arise in terms of the anticipated altered maneuvering behavior of the models on one hand, and measurement techniques and uncertainty analyses on other hand. Experiments at MARIN were carried out in the shallow water tank, which is 220 m long, 15.8 m wide and adjustable to a maximum water depth of 1.15 m. The model of KVLCC2 was tested at a scale factor $\lambda = 75$ and an approach speed of 7 kts corresponding to the speed of the ship (Tab. 5.1). The water depth under investigation corresponded to $h/T = 1.2$. Waviness of the concrete tank bottom was shown to be less than 10% of UKC, as required by ITTC (2014). Due to the increased space required for turning maneuvers at the given approach speed and shallow water condition in conjunction with finite basin dimensions, turning maneuvers could only be run partially. Eloot et al. (2015) report on free-running model tests with the same model of KVLCC2 at FHR. There the model was accelerated by the carriage and released upon meeting of prescribed initial conditions. The tank at FHR is 68 m long, 7m wide and adjustable to a maximum water depth of 0.5 m. Zigz-zag maneuver parameters were chosen to 10°/5° and 20°/5°. The 35° turning maneuver was terminated upon change of heading of 90° at MARIN and 40° at FHR compared to the initial heading. Results from repeatability studies at FHR were translated into mean values and standard deviations. Quantification of uncertainties following Eq. (6.1) was not done.

6.2 Maneuvering simulations

The parameter identification procedure outlined in Chapter 2.7 is synchronized with results of RANS-based captive maneuvering tests of Chapter 5 to give hydrodynamic maneuvering coefficients for KVLCC2 in deep water and at an approach speed of 15.5 kts, Tab. 6.1. Comparison to free-running maneuvering tests involves hard-rudder turning maneuvers ($\delta = \pm 35°$) and ±20/20 zig-zag maneuvers. The same captive maneuvering test programme was conducted for KVLCC2 at shallow water condition $h/T = 1.2$ on the basis of the validation study of Chapter 5.3. Results of these tests are summarized in 8.4. In light of the addressed computational costs of simulations of captive oscillatory tests, coefficients related to the functional $F'(v', r')$ were determined from steady drift and yaw tests. Coefficients acting on rigid body accelerations ($Y_{\dot{v}'}$, $Y_{\dot{r}}$, $N_{\dot{v}}$ and $N_{\dot{r}}$) were obtained from available experimental pure sway and pure yaw motion tests at FHR (SIMMAN, 2014).

Table 6.1: nondimensional hydrodynamic coefficients of KVLCC2 found from CFD analysis. Values to be multiplied by 10^{-3}.

h/T	∞	1.2		∞	1.2		∞	1.2
U [kn]	15.5	7		15.5	7		15.5	7
$X'_{\dot{u}}$	-0.06m'	-0.08m'	$Y'_{\dot{v}}$	-20.14	-40.3621	$N'_{\dot{v}}$	-3.0473	-2.876
X'_{u}	-1.97	-0.066	$Y'_{\dot{r}}$	-1.734	-2.869	$N'_{\dot{r}}$	-0.5316	-1.684
X'_{uu}	0.99	-1.30	Y'_{0}	-0.15	0.3326	N'_{0}	0.0661	0.1662
X'_{vv}	-5.00	-144.70	Y'_{v}	-24.90	-92.70	N'_{v}	-8.8	-33.90
X'_{rr}	0.48	0.35	Y'_{vvv}	-30.20	-2011.7	N'_{vvv}	8.00	-33.90
$X'_{\delta\delta}$	-1.82	-2.40	Y'_{r}	4.758	4.2239	N'_{r}	-3.2498	-3.1014
X'_{vr}	7.54	2.30	Y'_{rrr}	-1.224	19.985	N'_{rrr}	-0.920	-9.5820
			Y'_{vrr}	-40.30	-129.30	N'_{vrr}	80.80	-13.30
			Y'_{rvv}	-9.90	81.80	N'_{rvv}	-3.37	13.60
			Y'_{δ}	-3.768	-6.359	N'_{δ}	1.788	2.20
			$Y'_{\delta\delta\delta}$	3.326	1.90	$N'_{\delta\delta\delta}$	-1.6227	-0.774
			$Y'_{\delta u}$	4.562	0.1159	$N'_{\delta u}$	-2.3209	-1.20

6.2.1 Maneuvers in deep water

Fig. 6.1 shows the trajectories of the turning maneuvers in the earth-fixed reference frame. Solid lines refer to one experimental realization and dashed lines represent simulation results. Coordinates of advance and transfer are indicated with a square, and those of tactical diameter with a circle. Tab. 6.2 and 6.3 summarize the comparison of simulations and mean values of turning maneuver quantities from the four experimental realizations. The initial maneuver phase was predicted in close agreement between simulations and experiments, quantified in terms of the deviations in advance, transfer and time to advance T_{90}, Tab. 6.2. These observations are valid for both the starboard and portside turn. The asymmetric turning behavior of the single-screw tanker was reflected in both simulations and experiments. Simulation results lay within the uncertainty of experiments. In the remainder of the maneuver the trajectories of simulations deviate from the given single realization experimental trajectory, becoming evident in the over-prediction of tactical diameters. The steady turning to starboard diameter differs by 8.1% with an experimental U95 of 4.5%. The turning to port diameter differs by 8.4% with an experimental U95 of 7.1%. More insight into the comparison of simulations and experiments is gained through the evaluation of time histories of rigid body velocities. Fig. 6.2 shows the comparisons of the temporal evolution of longitudinal and transverse velocities and yaw rate for both starboard and portside turn. Fig. 6.3 adds the temporal evolution of forward speed loss and drift angle to the comparison. The steady state predictions of u, v, r, U/U_0 and β are in good agreement with experiments, Tab. 6.2 and 6.3. Deviations in the overshoot of v in the initial turning phase are observed in the turn to port side.

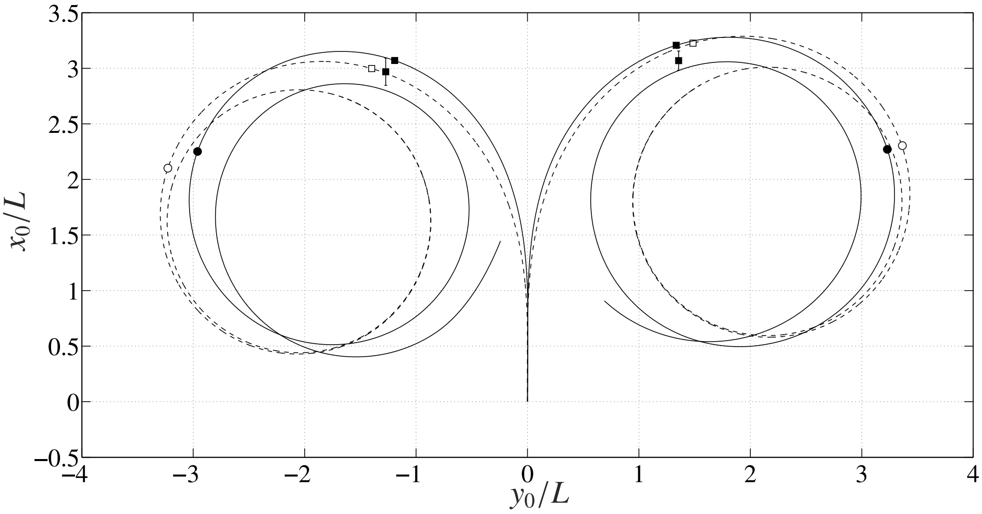

Figure 6.1: Comparison of simulated (dashed lines) and measured (solid lines) turning maneuvers of KVLCC2 to port side and starboard. Squares (□): coordinates of advance and transfer. Circles (○): coordinates of tactical diameter. Filled markers (■, ●): experimental results.

Table 6.2: Comparison of simulated and measured turning maneuver facts (absolute values) of KVLCC2 to starboard.

	Experimental average	U95	Simulation	$E\%$
Advance [m]	982	26	1032	-11.2
Transfer [m]	434	18	475	-9.5
Tactical diameter [m]	1049	23	1077	-2.7
Turning diameter [m]	801	36	736	8.1
T_{90} [s]	174	5	178	-2.3
T_{180} [s]	367	8	348	5.2
T_{360} [s]	796	16	758	4.8
U_{st} [m/s]	5.6	0.2	5.5	1.8
r_{st} $[^\circ/s]$	0.41	0.02	0.42	-2.4
β_{st} $[^\circ]$	18.6	0.7	18.7	0.5

Table 6.3: Comparison of simulated and measured turning maneuver facts (absolute values) of KVLCC2 to port side.

	Experimental average	U95	Simulation	$E\%$
Advance [m]	950	37	959	0.9
Transfer [m]	407	32	447	9.8
Tactical diameter [m]	989	35	1032	-4.3
Turning diameter [m]	786	56	720	8.4
T_{90} [s]	165	6	166	0.6
T_{180} [s]	345	13	333	3.5
T_{360} [s]	757	26	740	2.2
U_{st} [m/s]	5.6	0.3	5.4	3.6
r_{st} $[^\circ/s]$	0.41	0.02	0.42	2.4
β_{st} $[^\circ]$	20.2	1.1	19.2	4.6

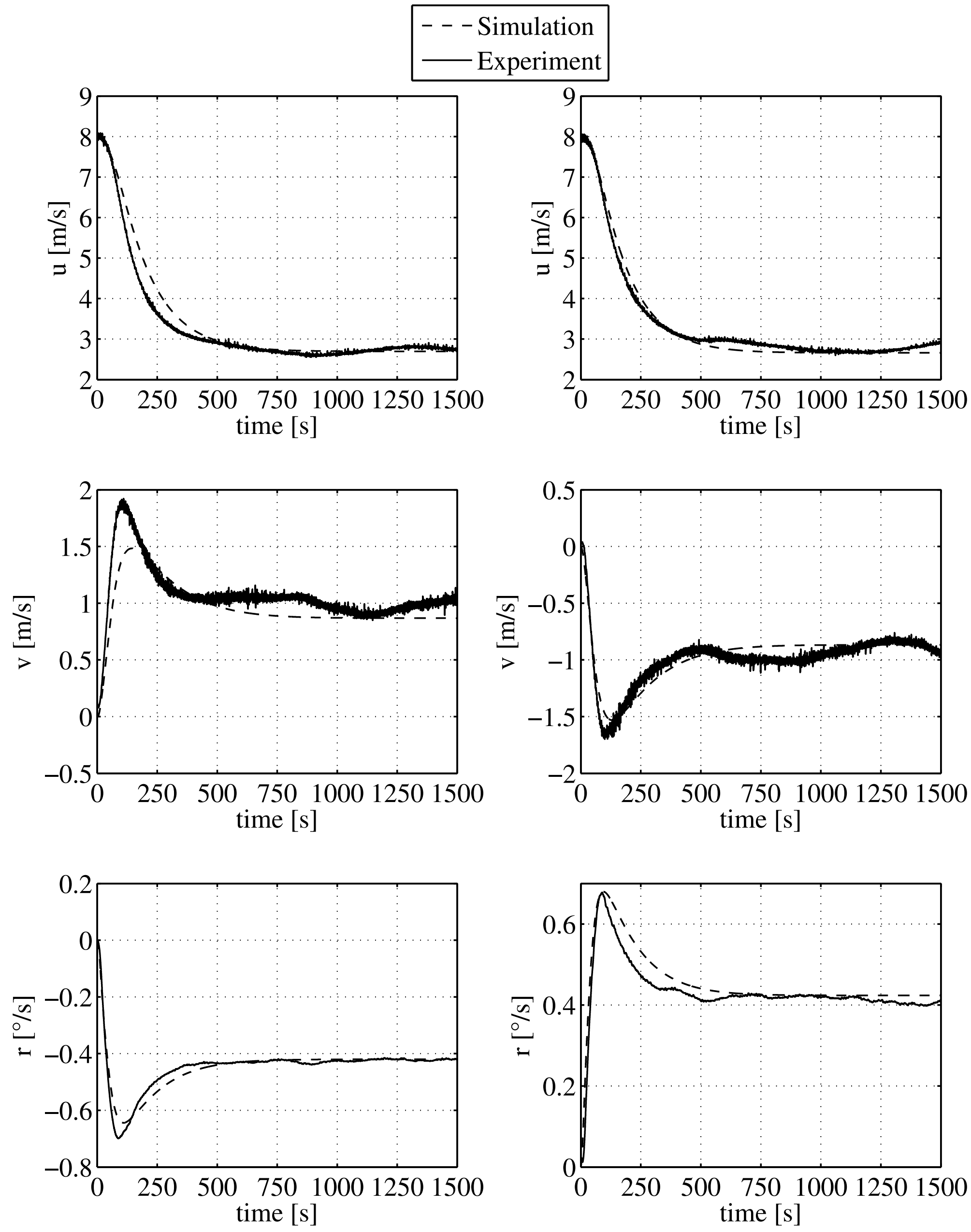

Figure 6.2: Time histories of state variables of turning maneuvers of KVLCC2 to port side (l.h.s.) and starboard (r.h.s.).

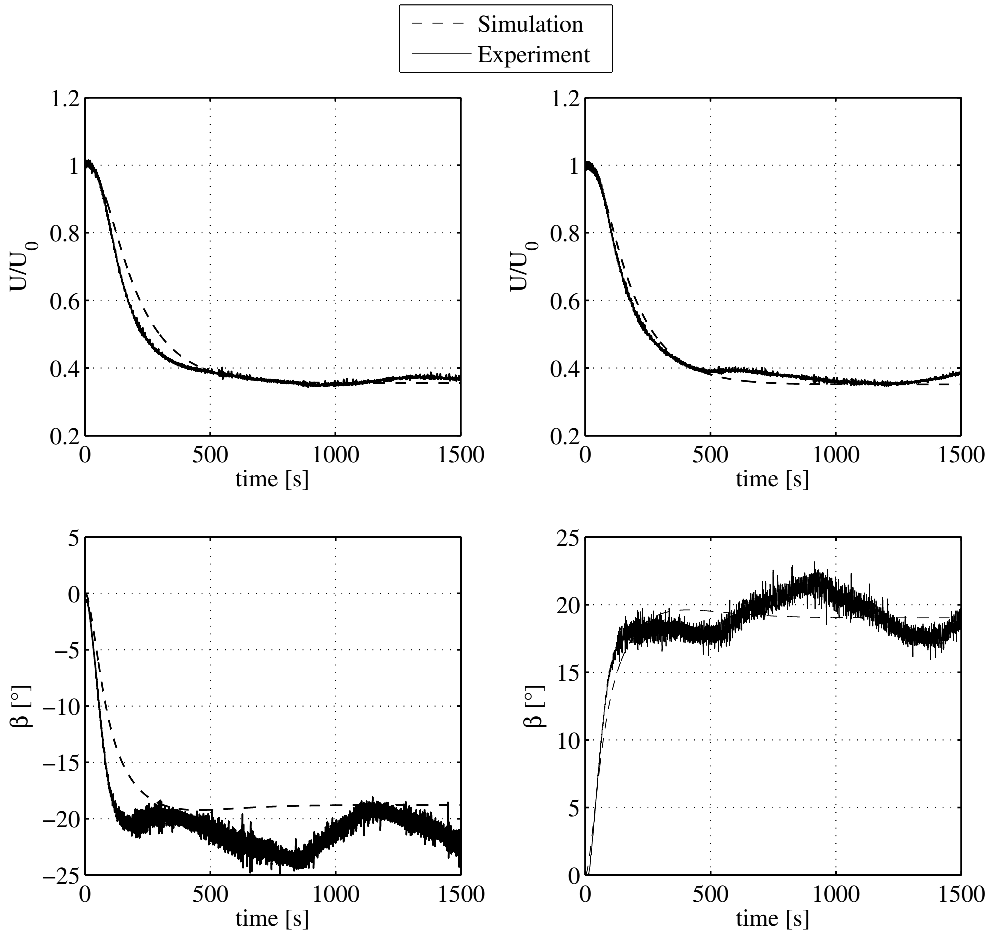

Figure 6.3: Time histories of state variables of turning maneuvers of KVLCC2 to port side (l.h.s.) and starboard (r.h.s.).

The comparison of simulated and experimental zig-zag maneuvers starting to both port and starboard is added to the validation study. Contrary to the study of turning maneuvers, the dynamic variation of the rudder angle in zig-zag maneuvers reveals the capabilities of generating and reducing turning rate, which addresses from the mathematical modeling point of view both damping and inertial characteristics. Fig. 6.4 shows the time histories of heading and rudder angle of ±20/20 maneuvers. Both simulations and experiments predict a different behavior between the port and starboard initiations, while the maneuver initiated to port shows overall higher overshoot angles. The turning maneuvers showed that there were slight differences in the overshoot of the dynamic response in v and r between simulations and experiments, while the steady state responses agreed well. In zig-zag maneuvers rudder is applied based on the transient evolution of heading angle. Small differences in rudder execution times are thus carried through the entire maneuver and propagate initial deviations in heading angle, becoming evident in the trajectory plots. The initial conditions of the plotted single realization of the experiment were unknown and, recalling the model acceleration strategy which seeks to keep the model on straight course, v and r might have been non-zero upon initiation of the maneuver. In the context of the characteristic of the zig-zag maneuver, simulations resemble the maneuvering behavior observed in the experiment with satisfactory agreement. Differences are quantified in Tab. 6.4 and 6.5. Comparison error $E_\Psi\%$ considers absolute heading angle.

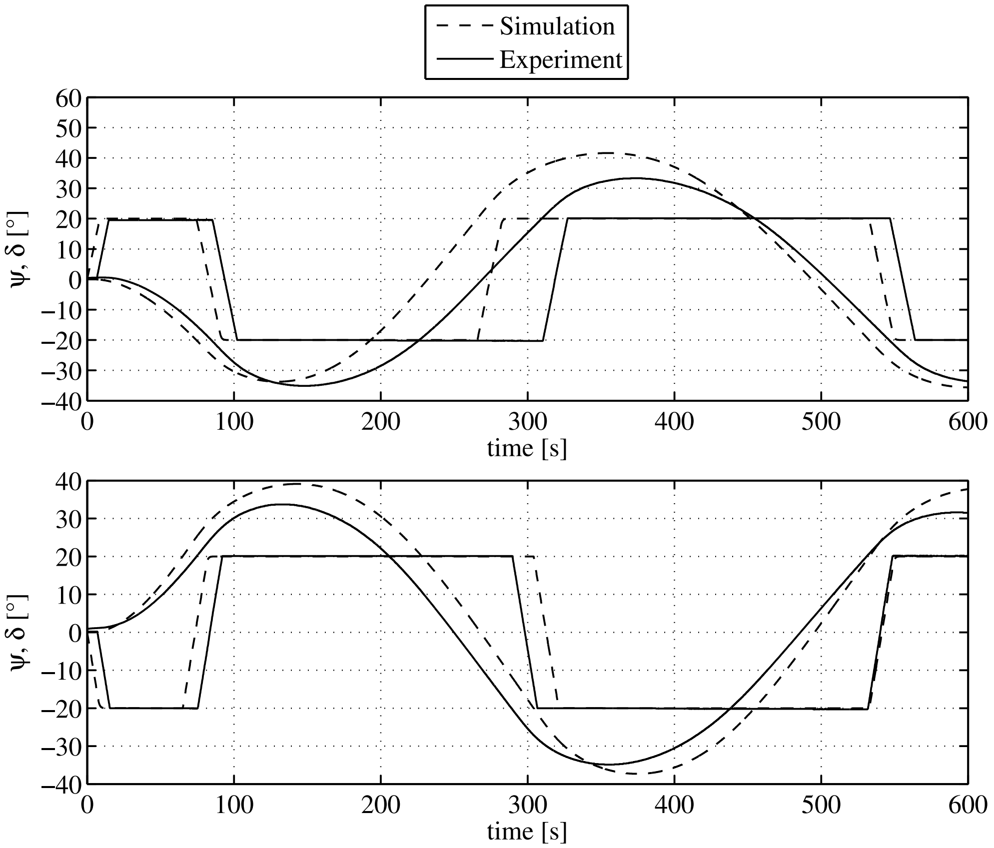

Figure 6.4: Comparison of simulated and measured 20/20 zig-zag maneuvers of KVLCC2 to port side (l.h.s.) and starboard (r.h.s.).

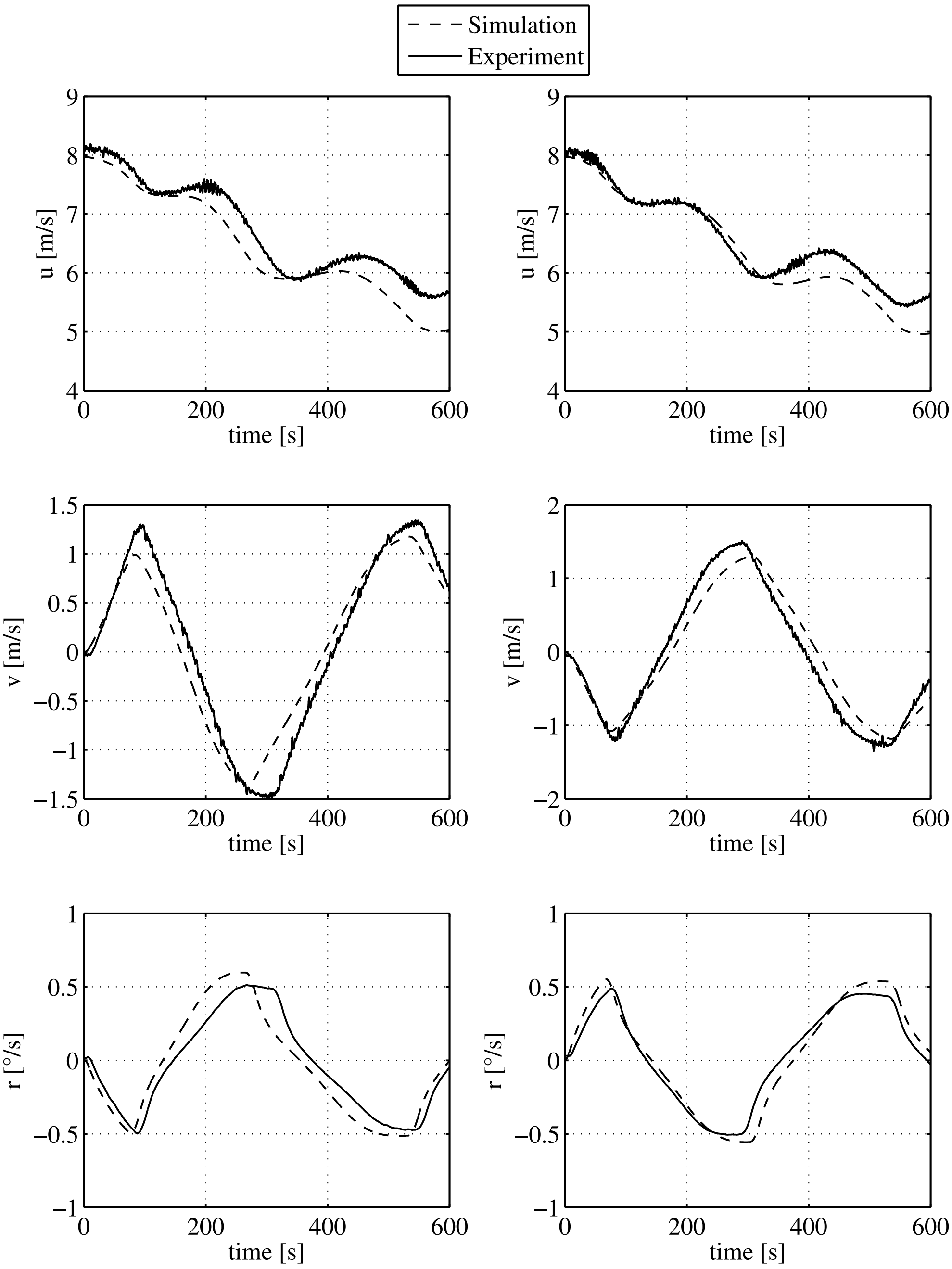

Figure 6.5: Time histories of state variables of zig-zag maneuvers of KVLCC2 to port side (l.h.s.) and starboard (r.h.s.).

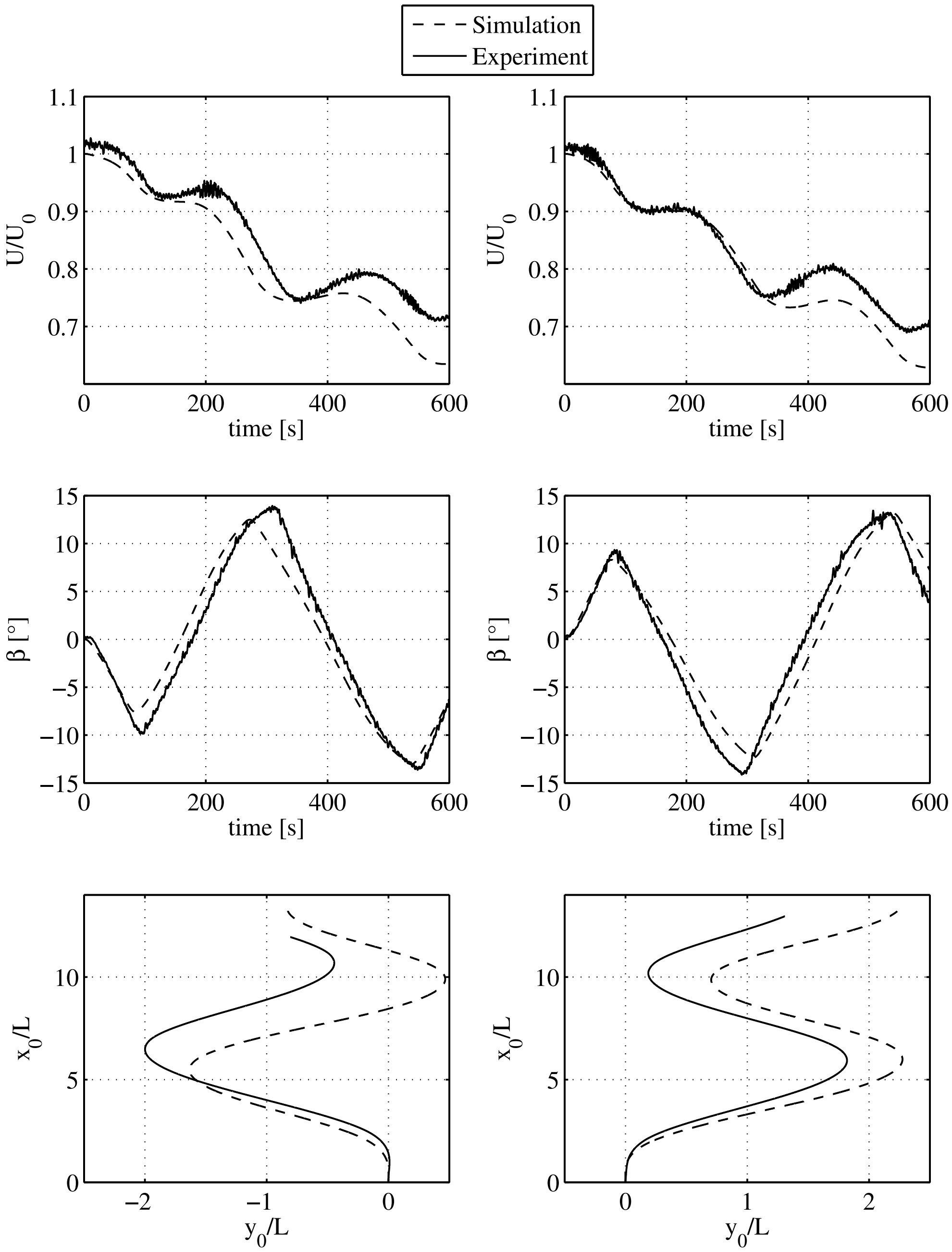

Figure 6.6: Time histories of state variables of zig-zag maneuvers of KVLCC2 to port side (l.h.s.) and starboard (r.h.s.).

Table 6.4: Comparison of simulated and measured 20/20 zig-zag maneuver facts (absolute values) of KVLCC2, initiated to starboard.

	Experimental average	U95	Simulation	$E\%$	$E_\Psi\%$
1^{st} overshoot [°]	13.3	1.6	13.7	-3.0	-2.19
2^{nd} overshoot [°]	14.5	1.6	21.6	-48.9	-31.28
3^{rd} overshoot [°]	11.3	1.6	15.6	-37.1	-26.38
2^{nd} execute [s]	69	6	74	-7.24	-
3^{rd} execute [s]	283	22	266	6	-
4^{th} execute [s]	526	35	533	-1.3	-

Table 6.5: Comparison of simulated and measured 20/20 zig-zag maneuver facts (absolute values) of KVLCC2, initiated to port side.

	Experimental average	U95	Simulation	$E\%$	$E_\Psi\%$
1^{st} overshoot [°]	14.7	1.6	19.1	-29.9	-22.23
2^{nd} overshoot [°]	12.9	1.6	17.3	-34.1	-24.58
3^{rd} overshoot [°]	13.6	1.6	18.1	-33.1	-24.19
2^{nd} execute [s]	79	6	65	15.4	-
3^{rd} execute [s]	305	22	304	0.3	-
4^{th} execute [s]	542	35	532	1.8	-

6.2.2 Maneuvers in shallow water

Experimental campaigns of free-running maneuvering tests with KVLCC2 in shallow water condition ($h/T = 1.2$) revealed increased complexity and scatter of results compared to equivalent tests in deep water condition. In general, the requirement for lower yaw checking angles in zig-zag maneuvers introduced larger relative errors, confirmed by results of 10°/2.5° zig-zag maneuvers, Tonelli and Quadvlieg (2015). Fig. 6.7 illustrates the trajectory within the towing tank of FHR. The influence of the tank walls on measurements could not be quantified, but remains a potential source for deviations compared to simulations, which do not consider transient interactions with lateral restrictions. For comparison of time histories the realization discussed in Eloot et al. (2015) was used. Comparison of simulations to statistical analysis of experiments is drawn in Tab. 6.6 to 6.8. No time histories of partial turning maneuvers were available.

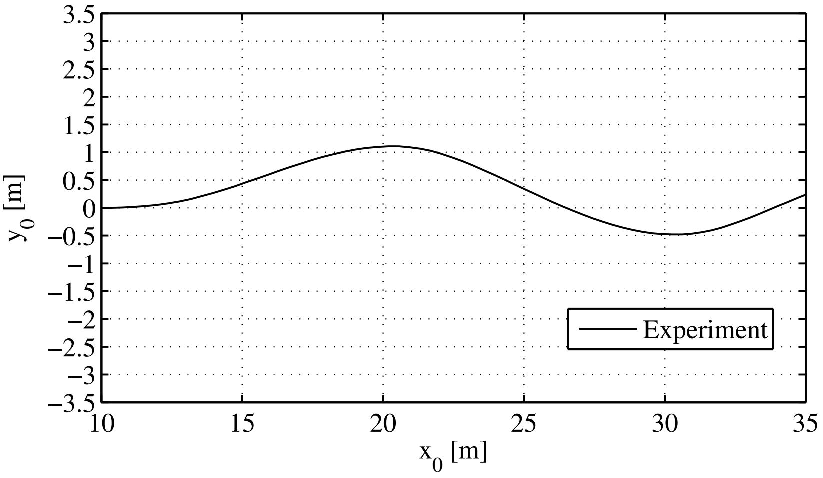

Figure 6.7: 20/5 zig-zag maneuver trajectory of the KVLCC2 model in the shallow water tank of FHR, Eloot et al. (2015).

Fig. 6.8 presents measured trim and sinkage during one realization of a 20°/5° zig-zag maneuver. Both quantities decrease in the course of the maneuver owing to the decrease in forward speed. The magnitude of the decrease is approximately 20% for midship sinkage and 30% for trim, while both quantities are generally small. Midship sinkage is around 30 cm in full scale. Fig. 6.9 compares the measured heading angle to the prediction of the simulation. The simulation generally over-predicted overshoot angles, while deviations to the experiment are greatest for the first overshoot angle and yaw checking time. Time histories of rigid body velocities show significant differences in sway velocity and maximum values of yaw rate, Fig. 6.10. The measured time history of the experiment shows a non-zero yaw rate upon initiation of the maneuver. The temporal evolution of sway velocity in the initial maneuver phase is different in experiments as well. Fig. 6.11 and Fig. 6.12 present the ±35° turning maneuver predictions by simulations. The comparison to advance and turning diameter from the partial experimental turning maneuvers yields better agreement than observed in zig-zag maneuvers. In Eloot et al. (2015) the drift angle from experimental runs at the end of the partial maneuver to port side was between 2° and 3° and the yaw rate around $0.25°/s$. The simulation predicts a steady state drift angle of 3.5° and yaw rate of $0.185°/s$. In terms of the underlying mathematical model the observed deviations in the zig-zag maneuver are attributable to the important damping terms. Numerical experiments showed that perturbation of N_r and Y_r by +10% results in a decrease of overshoot angles by 12% and better agreement of the yaw rate to experiments. The mathematical model includes only implicitly the effect of trim and sinkage on hydrodynamic forces based on the conditions of the source tests for parameter identification, which represents a potential source of error compared to experiments. Sources of simulations errors, other than introduced through the notion of the mathematical model itself, are referred to the following aspects. The parameter identification for KVLCC2 at $h/T = 1.2$ based on the replication of captive maneuvering tests in a numerical towing tank with greater dimensions than the tanks in which the free-running tests were performed. While scale effects in maneuvering were estimated to be low to moderate in deep water conditions, el Moctar et al. (2014), no quantification of introduced scale effects in shallow water maneuvering predictions were available and remain a further potential source of error, since the parameter identification based on CFD was performed with a different scale factor (λ = 45.741) than maneuvering experiments (λ = 75). The sensitivity of the prediction of longitudinal forces with the employed CFD-method, which lead to a systematic under-prediction, was addressed in Chapter 5. Additionally, no experimental data was available for validation of RANS-based rudder tests to check on the reliability of the body force propeller in shallow water condition. Due to the previously discussed low sensitivity of rudder forces to UKC, these effects were considered insignificant. All in all, deviations in the comparison of simulated and measured zig-zag and turning maneuvers are greater at shallow water of $h/T = 1.2$ than in deep water condition.

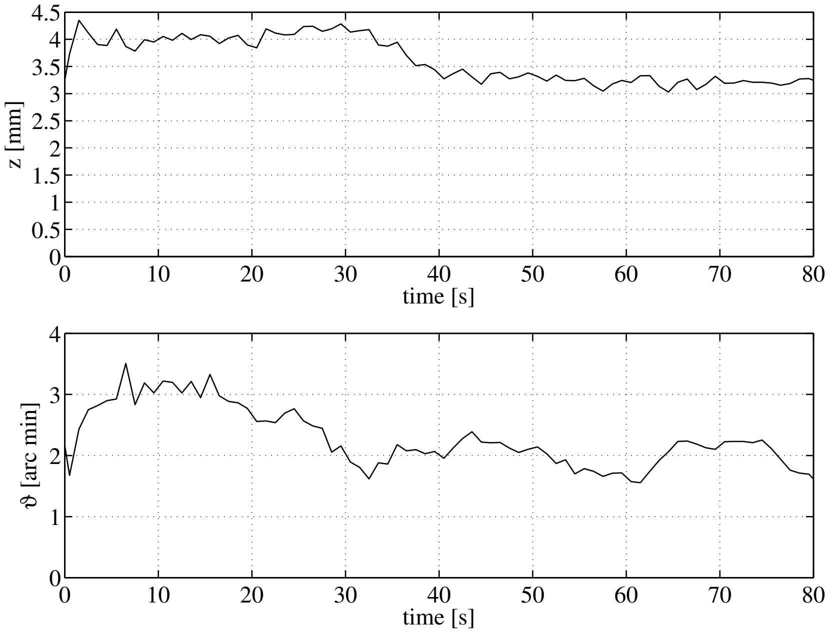

Figure 6.8: Measured bow-down trim and midhsip sinkage of the KVLCC2 model during 20/5 zig-zag maneuver at FHR, Eloot et al. (2015).

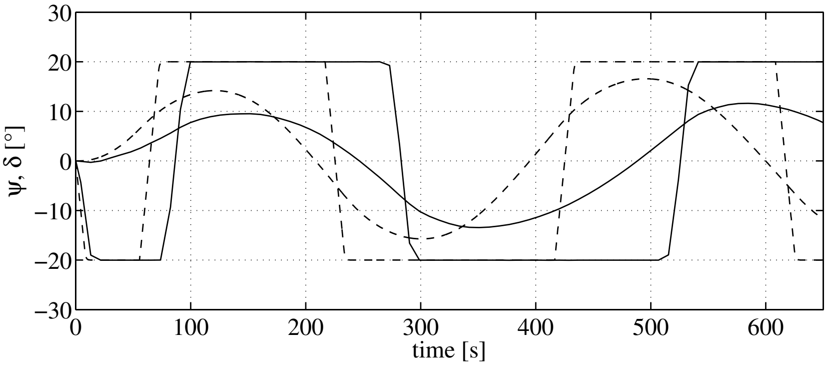

Figure 6.9: Comparison of simulated and measured 20/5 zig-zag maneuver of KVLCC2, extrapolated to full-scale, $h/T = 1.2$.

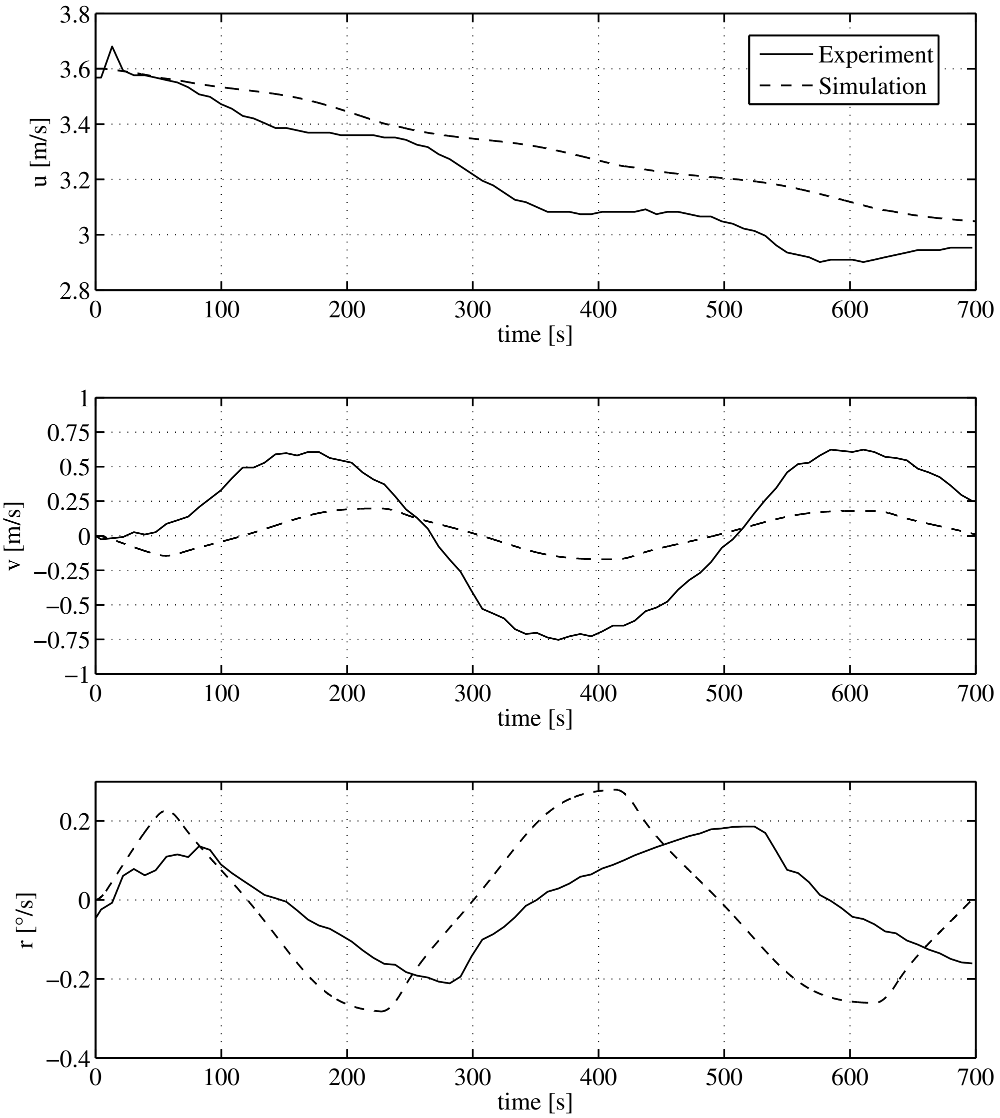

Figure 6.10: Comparison of simulated and measured state variables of 20/5 zig-zag maneuver of KVLCC2, extrapolated to full-scale, $h/T = 1.2$.

Table 6.6: Comparison of simulated and measured 20/20 zig-zag maneuver facts (absolute values) of KVLCC2, initiated to starboard, $h/T = 1.2$.

	FHR		MARIN		Simulation
	Average	Std. deviation	Average	Std. deviation/U95	
1^{st} overshoot [°]	4.73	0.16	3.6	0.1/0.2	8.5
2^{nd} overshoot [°]	8.19	0.26	6.0	1.0/2.8	11.2
2^{nd} execute [s]	8.92	0.24	n.A.	n.A.	6.0

Table 6.7: Comparison of simulated and measured 20/20 zig-zag maneuver facts of KVLCC2, initiated to port side, $h/T = 1.2$.

	FHR		MARIN		Simulation
	Average	Std. deviation	Average	Std. deviation/U95	
1^{st} overshoot [°]	3.73	0.23	3.5	0.8/2.7	8.45
2^{nd} overshoot [°]	7.94	0.49	5.5	1.3/4.2	11.2
2^{nd} execute [s]	9.79	0.31	n.A.	n.A.	6.0

Table 6.8: Comparison of simulated and measured turning maneuver facts facts of KVLCC2 to port side, $h/T = 1.2$.

Test	MARIN		Simulation	$E\%$
	Average	Std. deviation/U95		
Advance [m]	863	36.7/94	761	11.81
Turning diameter [m]	1430	41.6/n.A.	1172	18.04

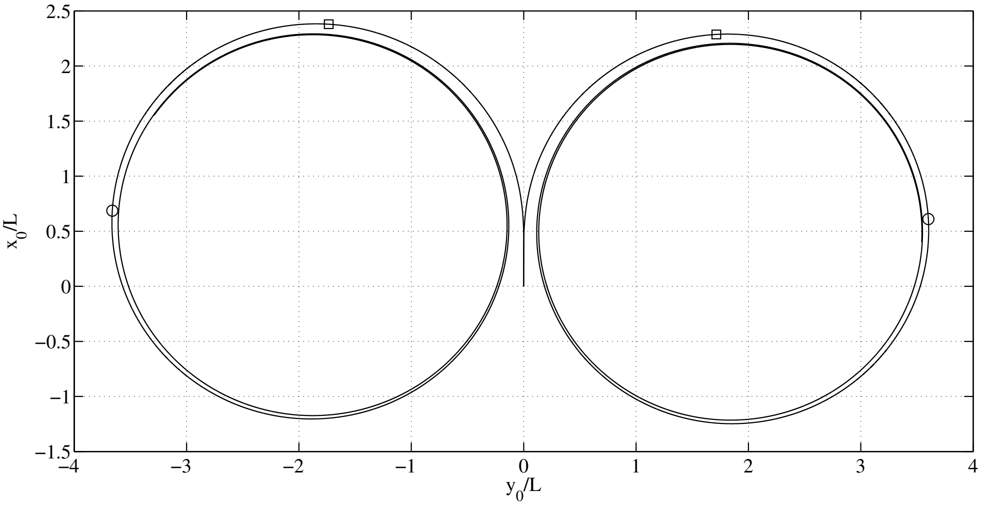

Figure 6.11: Simulated 35° turning maneuvers to port side and starboard. Squares mark the location of advance and transfer, circles the location relevant for the tactical diameter, $h/T = 1.2$.

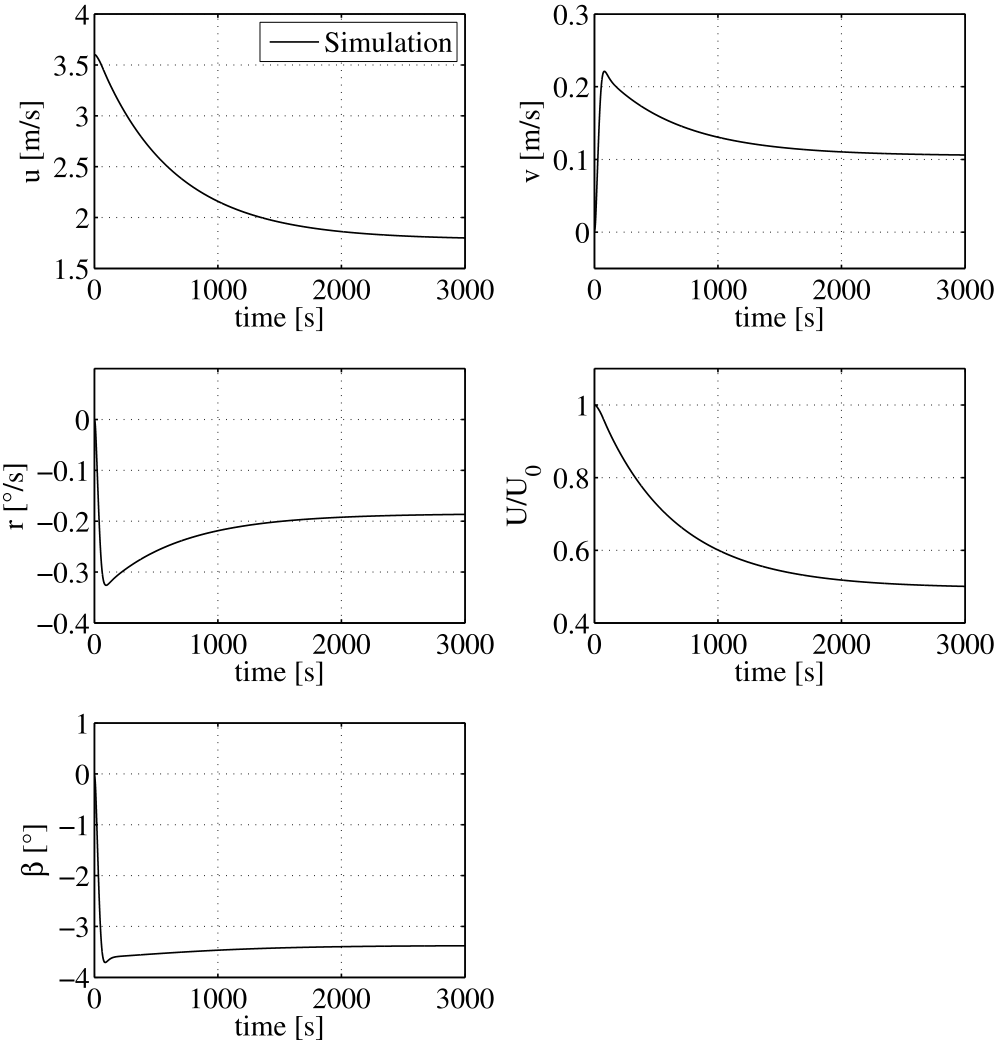

Figure 6.12: Time histories of state variables of simulated 35° turning maneuvers to port side, $h/T = 1.2$.

7. Summary

Investigations into a simulation-based framework of the prediction of ship maneuvering in deep and shallow water were presented. The increasing need for ship motion predictions in response to growing ship dimensions and requirements for energy-efficiency calls for the assessment of the reliability of computational methods, because sea trials and model experiments are not always feasible, e.g. in the early stages of ship design.

Different approaches to the mathematical modeling of hydrodynamic forces in the maneuvering equations of motion were reviewed and analyzed. A mathematical model for maneuvering was derived, represented by a set of coupled nonlinear differential equations in the framework of Newtonian mechanics. Hydrodynamic forces are therein seen to be functions of rigid body kinematics, control inputs and water depth. Multivariat polynomials stemming from Taylor-series expansions express these forces in terms of ship-specific hydrodynamic inertial and damping coefficients of different order. Based on physical notion, mathematical properties and sensitivity studies a model structure for arbitrary rudder maneuvers in three degrees of freedom at a given operational point was established. The physics of ship flows in shallow water were discussed, related to the mathematical modeling of maneuvering, and helped to identify how strong different contributions to the balance of forces are affected by shallow water effects. Approaches to incorporate the effect of shallow water were suggested. Parameter identification procedures for such models, which have been developed in the hydrodynamic community since the introduction of captive maneuvering experiments, were reviewed and synchronized with the mathematical model. Contrary to sea trials captive maneuvering tests offer the analysis of hydrodynamic forces on ships in idealized flow condition in terms of rigid body kinematics, control inputs and water depth. The theory of experimental design was addressed to explore associated optimization prospects with regard to parameter identification effort.

Captive maneuvering tests were performed for a tanker in deep water condition using CFD and the results were compared to experimental data. Tying in with the state of the art favorable agreement for both captive tests for parameter identification and maneuverability analyses involving the prediction of turning and zig-zag maneuvers was observed, turning the computational method into a competitive alternative to experiments. Moreover, taking advantage of admissible simplifications of CFD simulations in deep water, the computational effort was shown to be acceptably low. The simulation-based framework gave a set of maneuvering coefficients for arbitrary rudder maneuvers within short time using moderate computational resources.

A straightforward extension of simulations to shallow water was impaired by fundamental questions on the reliability of CFD for flows around ships in shallow water. In presence of pressure variations on and around the ship hull in flows with low UKC crucial aspects in the setup of simulations refer to the modeling of dynamic responses of the free water surface and motions of the ship. Besides, the analysis of hydrodynamic interactions between the hull and the vertical restriction revealed the sensitivity of viscosity-dominated longitudinal forces to near-wall treatment of the hull and tank bottom. The requirement for smaller scale flow models than dictated by the RANS equations to account for the unsteadiness of the flow and recirculation in the aft ship was addressed.

The numerical prediction of squat was shown to be favorable in comparison to experiments up to Froude depth numbers of 0.5. Hydrodynamic analysis stemming from potential flow theory represent an efficient and accurate tool compared to expensive CFD simulations, but were shown to yield increasing deviations in higher Froude depth number regimes. The investigation of lifting flows with CFD confirmed the anticipated dependency of hydrodynamic forces and squat on forward speed, drift angle, yaw rate and UKC. The squat effect on forces was shown to be driven by trim. Besides, the blockage induced by lateral restrictions in towing tanks were shown to affect hydrodynamic forces on ship models in large amplitude drift motion, raising questions on tank effects in captive experimental maneuvering tests. For low to moderate drift angles and yaw rates the squat effect on forces was shown to be moderate.

Resembling prescribed oscillatory motion tests in shallow water with CFD bears essential challenges for the numerical handling of rigid body motions relative to flow restrictions, raising the computational effort to an extent which makes the method less competitive to experimental analysis. In the context of entirely simulation-based parameter identification procedures, an alternative is seen in the application of BEM for the computation of the added mass tensor and its relation to maneuvering hydrodynamic coefficients, which act on rigid body accelerations. The identification of damping coefficients then leans entirely on steady drift and yaw motion tests. All in all, the validation study of numerical captive maneuvering tests confirmed the potential for ship flow investigations in shallow water and parameter identification for various mathematical models for maneuvering. When applied to ship handling simulation models, special attention is referred to the four quadrants of ship operation, the modeling of which involves a wide range of motion parameters. In this context, a particular advantage of CFD-based analysis is the capability of ensuring open water conditions, contrary to model experiments.

While the capabilities of multivariat polynomial models to predict the altered maneuvering behavior in shallow water was demonstrated before, the present application provides a quantification of the reliability through comparison with experimental benchmark. The presented simulation-based maneuvering framework yielded good agreement with experiments in deep water condition. Larger deviations were observed in shallow water maneuvering predictions, albeit these also stand in the context of the complexity and challenges involved in conducting free-running maneuvering experiments. Experiments themselves showed increased sensitivity and uncertainty compared to deep water conditions. Given the complexity of the physics and the simplicity of the mathematical model, the performance of the method is altogether considered favorable.

The general objective of developing CFD for the application to ship hydrodynamics is driven by the idea of obtaining a generic numerical method, which would enable abandoning the established segmented approach, in which specific fields are tackled with specific flow models. Sparing a discussion on the rationale behind this approach, the present investigation contributed to the conclusion that the modeling of complex flows around ships, as encountered in maneuvering in shallow water, still imposes challenges to simulation engineering and computational resources, which impair the routine application to parametric investigations and the ultimate transformation from a tool for academic investigations to a tool for industrial use. The academic treatise of CFD applications for ship flows still almost exclusively focuses on investigations at model scale, to maintain a common basis for benchmarking with experiments. However, once applied to full scale ship flows, the presented method takes a unique selling point, as captive maneuvering tests for parameter identification are only feasible virtually.

Concerted future research efforts in CFD will most likely be directed towards the development of hybrid flow models which seek to provide a small-scale resolution of the flow in the near-field and simplified forms of the Navier-Stokes equations in appropriate regions of the solution domain. The extension of investigations involving direct simulation of maneuvering with rotating propellers and moving rudders on the basis of the Navier-Stokes equations to shallow water is expected to draw increasing attention, too.

8. Appendix

8.1 Parameter identification for captive oscillatory maneuvering tests

The prescribed motion in pure sway for given U_c is

$$v = -y_A \omega \cos \omega t; \qquad r = 0 \tag{8.1}$$

with mathematical model

$$X(t) \approx X_0 + X_{vv} v^2 \tag{8.2}$$

and

$$F(t) \approx F_0 + F_{\dot{v}} + F_v v + F_{vvv} v^3 \tag{8.3}$$

which in harmonic form is

$$X(t) \approx X_0 + X_{a2} cos 2\omega t \tag{8.4}$$

and

$$F(t) \approx F_{a0} + F_{b1} sin \omega t + F_{a1} cos \omega t + F_{a3} cos 3\omega t \tag{8.5}$$

and coefficients are

$$F_0 = F_{a0} \tag{8.6}$$

$$F_{\dot{v}} = -\frac{F_{b1}}{v_A \omega} \tag{8.7}$$

$$F_v = -\frac{(F_{a1} - 3F_{a3})}{v_A} \tag{8.8}$$

$$X_{vv} = -\frac{2F_{a2}}{v_A^2} \tag{8.9}$$

$$F_{vvv} = -\frac{4F_{a3}}{v_A^3} \tag{8.10}$$

Prescribed motion in pure yaw for given U_c is

$$v = 0; \qquad r = \psi_A \omega \sin \omega t \tag{8.11}$$

with mathematical model

$$X(t) \approx X_0 + X_{rr} r^2 \tag{8.12}$$

and

$$F(t) \approx F_{a0} + F_{\dot{r}} + F_r r + F_{rrr} r^3 \tag{8.13}$$

which in harmonic form is

$$X(t) \approx X_{a0} + X_{a2} cos2\omega t \tag{8.14}$$

and

$$F(t) \approx F_{a0} + F_{a1} cos\omega t + F_{b1} sin\omega t + F_{b3} sin3\omega t \tag{8.15}$$

and coefficients are

$$F_0 = F_{a0} \tag{8.16}$$

$$F_{\dot{r}} = -\frac{F_{a1}}{r_A \omega} \tag{8.17}$$

$$F_r = -\frac{(F_{b1} - 3F_{b3})}{r_A} \tag{8.18}$$

$$X_{rr} = -\frac{2F_{b2}}{r_A^2} \tag{8.19}$$

$$F_{rrr} = -\frac{4F_{b3}}{r_A^3} \tag{8.20}$$

Prescribed motion in sway-yaw for given U_c is

$$r = \psi_A \omega \sin \omega t; \qquad v = -u_0 \sin\beta \tag{8.21}$$

with mathematical model

$$X(t) \approx X_0 + X_{vv} v^2 + X_{rr} r^2 + X_{vr} r^2 \tag{8.22}$$

and

$$F(t) \approx F_0 + F_v v + F_{vvv} v^3 + F_r r + F_{rrr} r^3 + F_{vrr} v r^2 + F_{rvv} r v^2 \tag{8.23}$$

which in harmonic form is

$$X(t) \approx X_0 + X_{b1} sin\omega t + X_{a2} cos(2\omega t) \tag{8.24}$$

and

$$F(t) \approx F_0 + F_{a1} cos\omega t + F_{b1} sin\omega t + F_{a2} cos2\omega t + F_{b3} sin3\omega t \tag{8.25}$$

and coefficients are

$$F_0 = F_{a0} \tag{8.26}$$

$$X_{vr} = -\frac{F_{b1}}{v r_A} \tag{8.27}$$

$$X_{rr} = -\frac{2F_{a2}}{r_A^2} \tag{8.28}$$

$$X_{vv} = -\frac{2F_{a2}}{v_A^2} \tag{8.29}$$

$$F_{vrr} = -\frac{(2F_{a2})}{vr_A^2} \tag{8.30}$$

$$F_{rvv} = -\frac{\left(F_{b1} - F_r r_A - \frac{3}{4} F_{rrr} r_A^3\right)}{v^2 r_A} \tag{8.31}$$

8.2 Tables of hydrodynamic coefficients

Table 8.1: Non-dimensional hydrodynamic coefficients of the sample ships from Wolff (1981) for the deep water study. Values to be multiplied by 10^{-6}.

	Tanker	Mariner	Ferry		Tanker	Mariner	Ferry
$X'_{\dot{u}}$	-1077.4	-214.4	0	$Y'_{\dot{v}}$	-11420	-7488.7	-7395.6
$X'_{\dot{u}uu}$	-5283.9	0	0	$Y'_{\dot{v}vv}$	-21559.7	-41070.3	0
X'_{u}	-2217.1	-2760.8	-4335.8	$Y'_{\dot{r}}$	-713.7	-143.7	-599.8
X'_{uu}	1509.6	0	-2354.6	$Y'_{\dot{r}rr}$	-467.5	-1303.6	0
X'_{uuu}	0	-2210.3	-2593.9	Y'_{0}	-243.5	-20.3	0
X'_{vv}	-888.5	-4657.7	-3278.9	Y'_{u}	262.6	-208.1	57.4
X'_{rr}	236.8	-432.7	-570.6	Y'_{v}	-15337.7	-11592.7	-12095.2
$X'_{\delta\delta}$	-1598.1	-1420.4	-2878.8	Y'_{vvv}	-36831.5	-95040.1	-137301.5
X'_{vvu}	0	0	-2558.7	Y'_{vrr}	-19039.6	-22143.2	-44364.8
$X'_{\delta\delta u}$	2000.8	1944.4	3424.8	$Y'_{v\delta\delta}$	0	1490.1	2198.8
X'_{vr}	9477.5	2304.9	4626.7	Y'_{r}	4842.0	3529.0	1900.9
$X'_{v\delta}$	1016.7	1013.7	876.7	Y'_{rrr}	1988.8	744.1	-1361.0
$X'_{r\delta}$	-482.1	-485.1	-350.7	Y'_{ru}	0	-1405.7	-1297.1
X'_{vu}	744.8	2052.6	0	Y'_{rvv}	22878.0	0	-36490.1
X'_{ru}	0	-388.9	0	$Y'_{r\delta\delta}$	1492.3	0	-2751.9
X'_{r}	48.6	279.7	-19.2	Y'_{δ}	3167.5	2640.4	3587.4
X'_{δ}	165.8	54.2	0	$Y'_{\delta\delta}$	0	675.4	97.9
$X'_{\delta uu}$	0	2296.4	0	$Y'_{\delta\delta\delta}$	3620.9	-6868.9	0
$X'_{vv\delta}$	-4716.7	0	0	$Y'_{\delta\delta\delta\delta}$	1551.5	-1317.7	0
$X'_{rr\delta}$	-364.9	0	0	$Y'_{\delta\delta\delta\delta\delta}$	-5526.3	4105.7	-6262.1
X'_{vvv}	1163.8	0	0	$Y'_{\delta rr}$	1637.4	0	0
X'_{rrr}	-118.4	-191.6	0	$Y'_{\delta u}$	-4562.2	-3711.2	-5095.6
$X'_{\delta\delta\delta u}$	-278.4	1408.1	0	$Y'_{\delta\delta\delta u}$	2639.9	5871.7	3192.4
$X'_{\delta\delta\delta\delta}$	0	957.6	2185.1	$Y'_{v\|v\|}$	-11512.8	0	0
X'_{vvvu}	0	-22765.0	0	$Y'_{r\|r\|}$	-351.2	1789.6	0
$X'_{\|v\|r}$	0	-674.9	0	$Y'_{v\|r\|}$	0	-6183.2	0
$X'_{v\|\delta\|}$	0	-158.3	0	$Y'_{r\|v\|}$	0	6443.5	0
X'_{v}	0	-220.4	0	$Y'_{\delta\|v\|}$	0	2065.8	0
X'_{rru}	0	0	-734.4	$Y'_{\delta\|r\|}$	0	845.5	0
m'	14622.1	7973.6	6765.4	Y'_{vvu}	0	-3614.4	0
x'_G	$365.2/m'$	$-176.2/m'$	$-115.8/m'$	$Y'_{r\|\delta\|}$	0	-1031.0	0
I'_z	765.6	428.0	318.8	$Y'_{v\delta}$	0	559.1	0
				$Y'_{\delta\|\delta\|}$	-888.9	1984.3	0
				Y'_{vvvr}	12397.6	8131.5	0
				Y'_{rrru}	0	1806.2	0

	Tanker	Mariner	Ferry		Tanker	Mariner	Ferry
$N'_{\dot{v}}$	-522.7	78.2	425.9	N'_{rrr}	-864.7	-1134.0	-2253.2
$N'_{\dot{v}vv}$	2311.2	849.4	10048.7	N'_{ru}	0	-135.7	0
$N'_{\dot{r}}$	-575.8	-444.3	-230.9	N'_{ruu}	912.8	0	0
$N'_{\dot{r}rr}$	-129.9	210.9	0	N'_{rvv}	-16196.0	0	-60109.9
N'_{0}	66.8	8.1	0	$N'_{r\delta\delta}$	-323.8	1300.4	236.5
N'_{u}	-144.1	64.8	-35.9	N'_{δ}	-1402.3	-1282.4	-1620.8
N'_{v}	-5544.4	-3466.7	-3919.4	$N'_{\delta\delta}$	0	-236.1	-72.6
N'_{vv}	-131.7	0	0	$N'_{\delta\delta\delta}$	-1640.9	3401.2	0
N'_{vvv}	-2718.1	0	-33856.6	$N'_{\delta\delta\delta\delta}$	-536.2	441.1	0
N'_{vu}	0	0	-3665.9	$N'_{\delta\delta\delta\delta\delta}$	2220.4	-2014.5	2886.3
N'_{vrr}	3448.1	3870.5	0	$N'_{\delta vv}$	0	0	-2949.5
$N'_{v\delta\delta}$	2316.9	0	570.3	$N'_{\delta rr}$	-854.9	0	-328.7
N'_{r}	-3073.6	-2083.3	-2578.6	$N'_{\delta u}$	2320.9	1997.9	2258.6
$N'_{\delta uu}$	0	408.6	0	$N'_{\delta\delta u}$	316.4	361.9	0
$N'_{\delta\delta\delta u}$	-1538.3	-2737.3	-1381.6	$N'_{v\|v\|}$	0	1687.3	0
$N'_{r\|r\|}$	0	-485.0	0	N'_{vr}	-394.4	0	0
$N'_{\delta\|\delta\|}$	383.7	-100.8	0	N'_{vvvu}	-27133.4	-35494.9	0
N'_{rrru}	0	0	-1322.0	N'_{rru}	0	152.1	0
$N'_{r\|v\|}$	0	-7199.6	0	$N'_{\delta\|v\|}$	0	-1066.4	0
$N'_{\delta\|r\|}$	0	-471.3	0	$N'_{v\|\delta\|}$	0	349.9	0
$N'_{r\|\delta\|}$	0	-381.3	0	$N'_{v\delta}$	0	-296.1	0

Table 8.2: Non-dimensional maneuvering coefficients of KCS. Values to be multiplied by 10^{-3}.

h/T	1.2	1.3	1.4	1.6	2
X_u	-2.8763	-2.7195	-2.5263	-2.1858	-1.4413
X_{uu}	1.5101	1.4444	1.3638	1.2188	0.89878
X_{vv}	10.093	6.0415	8.0420	6.0061	0.38104
$X_{\delta\delta}$	-0.93044	-0.88410	-0.82560	-0.72792	-0.51498
$X_{\delta uu}$	-0.067465	-0.064358	-0.060566	-0.053695	-0.038635
$X_{\delta\delta u}$	6.0744	5.7971	5.4490	4.8487	3.5042
$X_{\dot{u}}$	-1.0467	0	-1.2634	0	0
X_{rr}	0.51661	0.50173	0.40776	0.35773	0.40737
X_{vr}	13.254	9.6549	8.7065	6.5632	3.5147
Y_v	-38.948	-16.977	-12.556	-9.5320	-8.0070
$Y_{v\|v\|}$	-236.29	-173.26	-122.27	-68.676	-41.052
Y_δ	1.4308	1.3595	1.2696	1.1194	0.79191
$Y_{\delta\delta\delta}$	-0.42923	-0.40787	-0.38088	-0.33581	-0.23758
$Y_{v\delta\delta}$	82.675	20.750	6.1790	-10.639	-2.0046
$Y_{vv\delta}$	-2.0504	-1.9500	-1.8107	-1.6143	-1.151
$Y_{\delta u}$	-2.9539	-2.8102	-2.6368	-2.3166	-1.6169
$Y_{\delta uu}$	1.6490	1.5755	1.4844	1.3235	0.96731
$Y_{\dot{v}}$	-23.889	-16.788	-10.188	-6.5168	-5.9969
$Y_{\dot{r}}$	-1.0510	-0.19676	0.21962	0.30642	0.041380
Y_r	2.0031	1.0234	0.52114	0.75466	0.80934
Y_{rrr}	-2.0492	-1.1222	-0.91520	-0.93576	-0.95175
Y_{rvv}	89.915	21.368	-0.49963	-20.942	-7.0536
Y_{vrr}	-98.663	-39.494	-26.189	-16.349	-15.534
N_v	-14.287	-11.191	-9.0121	-7.2345	-5.1803
$N_{v\|v\|}$	-27.789	-14.122	-9.2613	-4.0362	-2.3034
N_δ	-0.71540	-0.67977	-0.63479	-0.55968	-0.39596
$N_{\delta\delta\delta}$	0.21462	0.20393	0.19044	0.16791	0.11879
$N_{v\delta\delta}$	12.347	-0.83939	-0.68857	-3.3918	-0.73935
$N_{vv\delta}$	1.0253	0.97498	0.90532	0.80716	0.57574
$N_{\delta u}$	1.4769	1.4051	1.3184	1.1583	0.80844
$N_{\delta uu}$	-0.82449	-0.78773	-0.74219	-0.66173	-0.48365
$N_{\dot{v}}$	1.1531	0.85074	0.42639	0.18231	0.076276
$N_{\dot{r}}$	-0.50717	-0.39913	-0.35506	-0.31846	-0.31983
N_r	-4.2276	-3.2106	-2.6167	-2.1506	-1.4945
N_{rrr}	-1.5048	-1.3922	-1.2800	-1.1685	-1.3287
N_{rvv}	-51.158	-30.695	-22.063	-17.505	-13.058
N_{vrr}	-10.386	-3.2701	-0.98996	0.30630	-0.91760

8.3 Additions to numerical studies on resistance and squat prediction

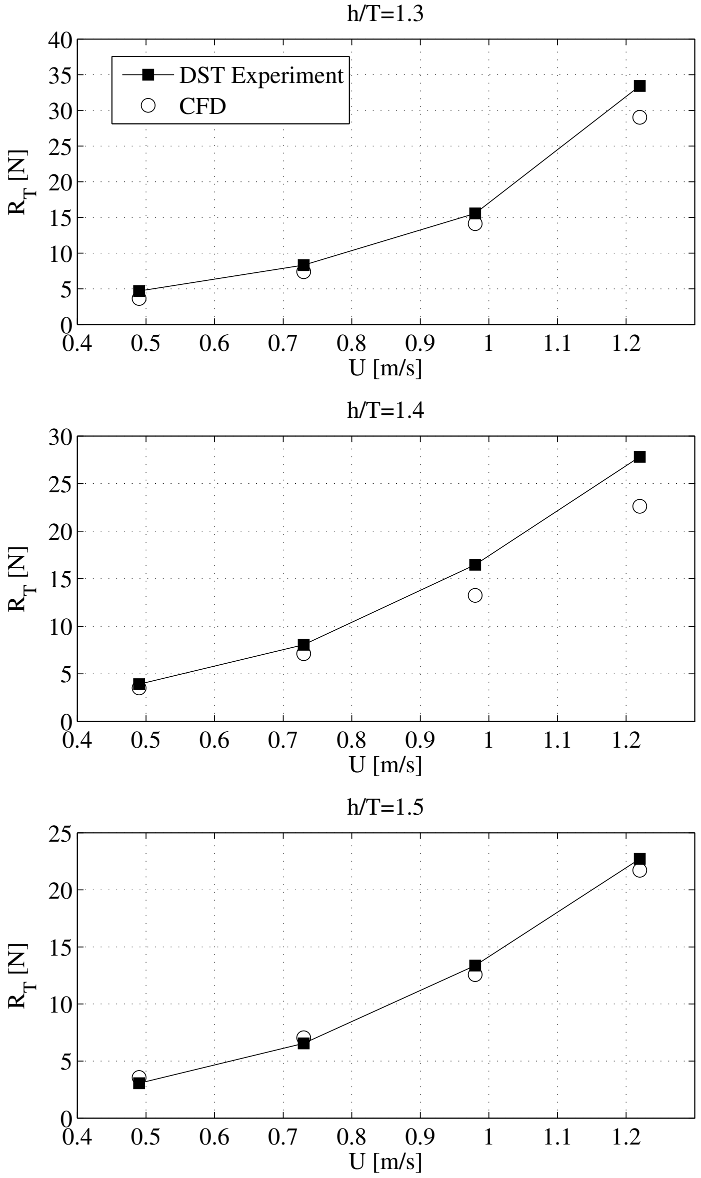

Figure 8.1: Comparison between EFD and CFD resistance predictions for KCS in various shallow water conditions, $0.26 < F_{nh} < 0.68$.

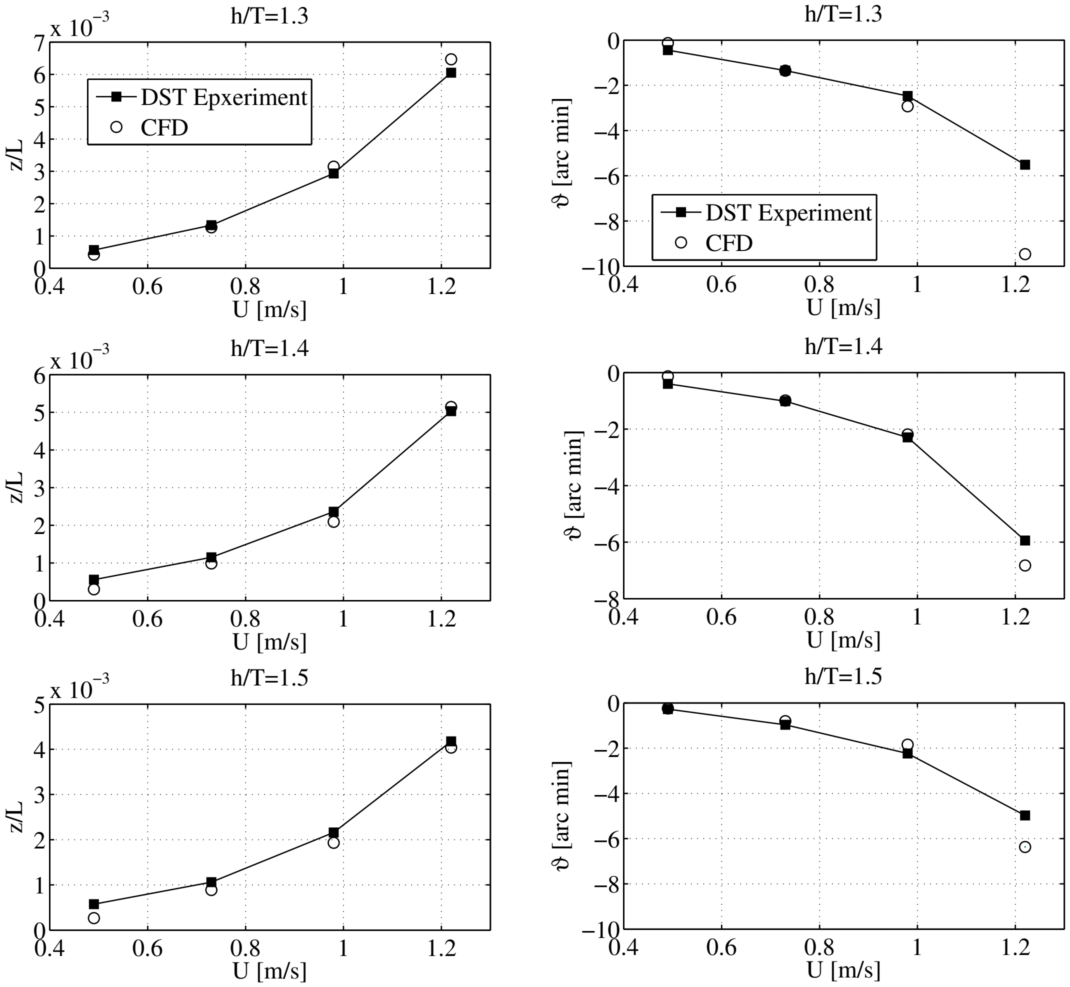

Figure 8.2: Comparison between EFD and CFD squat predictions for KCS in various shallow water conditions, 0.26< F_{nh} <0.68.

8.4 Numerical captive maneuvering test results for KVLCC2 in shallow water

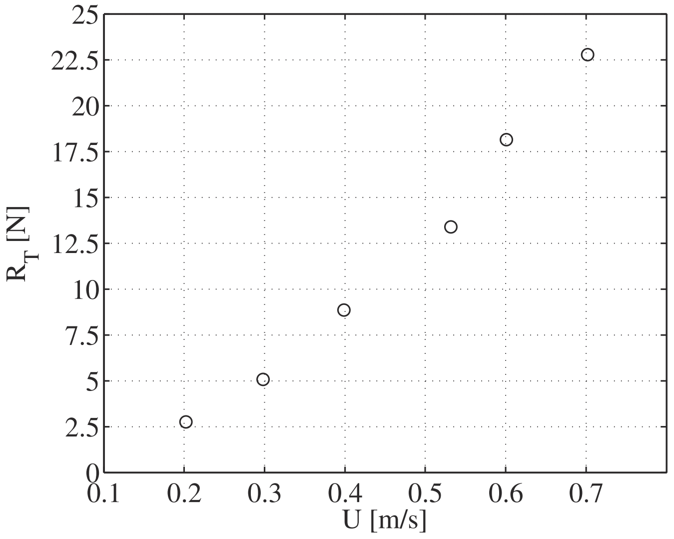

Figure 8.3: CFD prediction of resistance, $h/T = 1.2$.

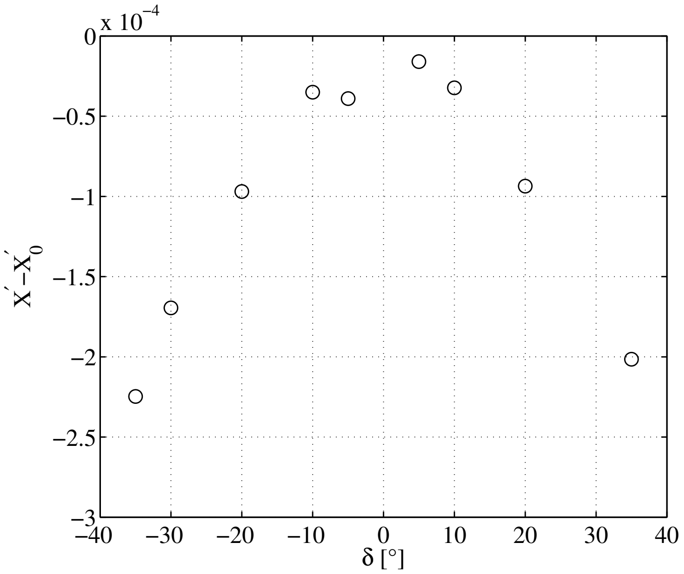

Figure 8.4: CFD predictions of longitudinal forces in rudder tests at h/T=1.2, F_{nh} = 0.23.

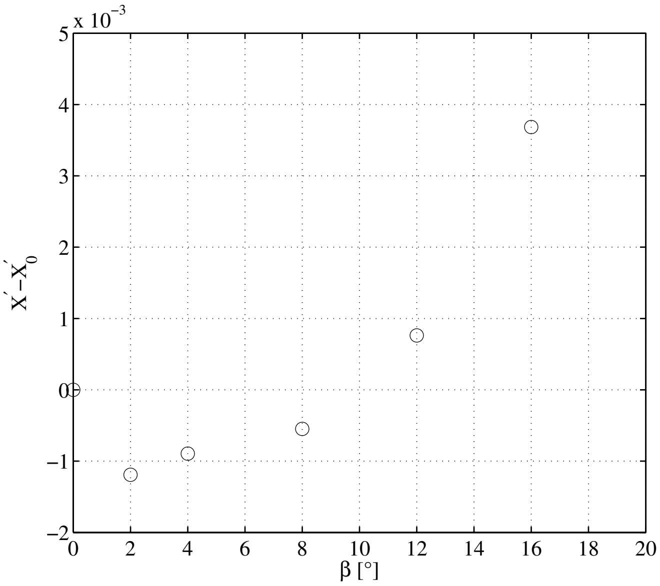

Figure 8.5: CFD predictions of longitudinal forces in drift motion at $h/T = 1.2$, $F_{nh} = 0.23$.

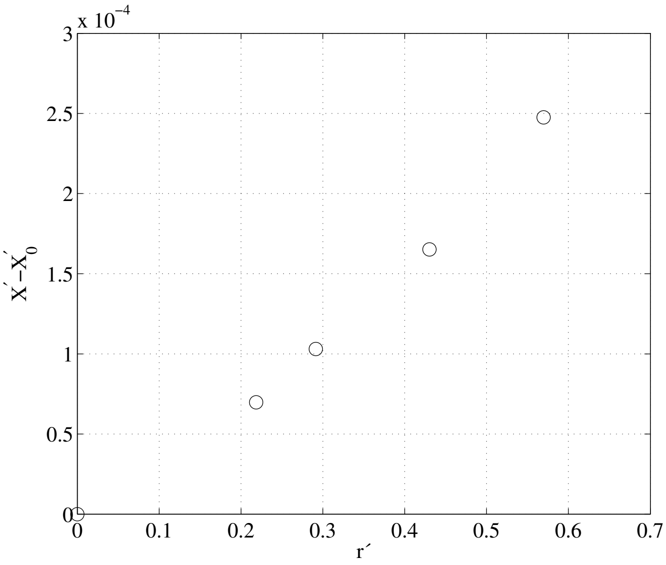

Figure 8.6: CFD predictions of longitudinal forces in yaw motion at $h/T = 1.2$, $F_{nh} = 0.23$.

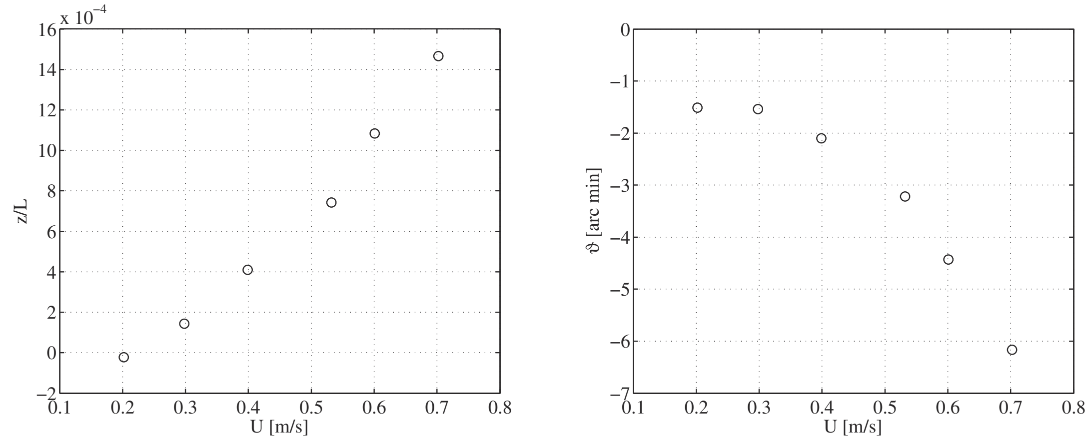

Figure 8.7: CFD predictions of squat in resistance tests, $h/T = 1.2$.

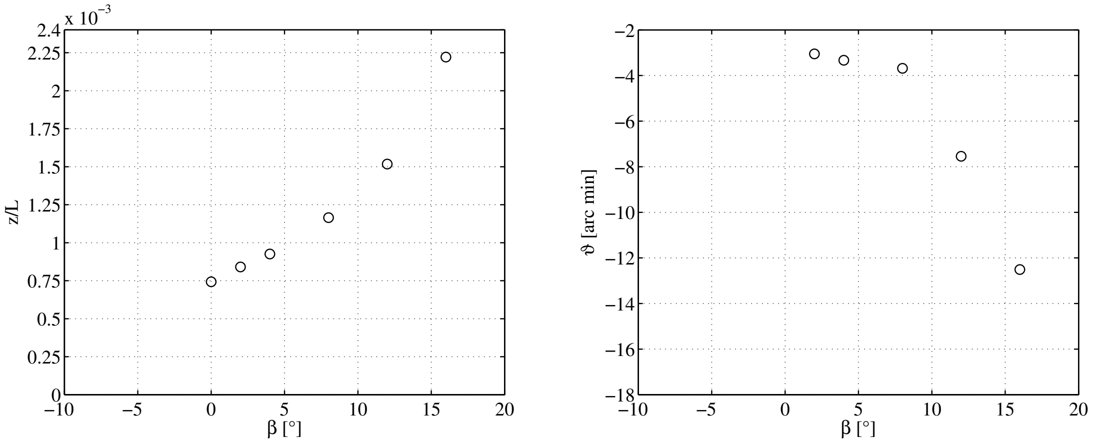

Figure 8.8: CFD prediction of squat in drift motion h/T=1.2, F_{nh}=0.23.

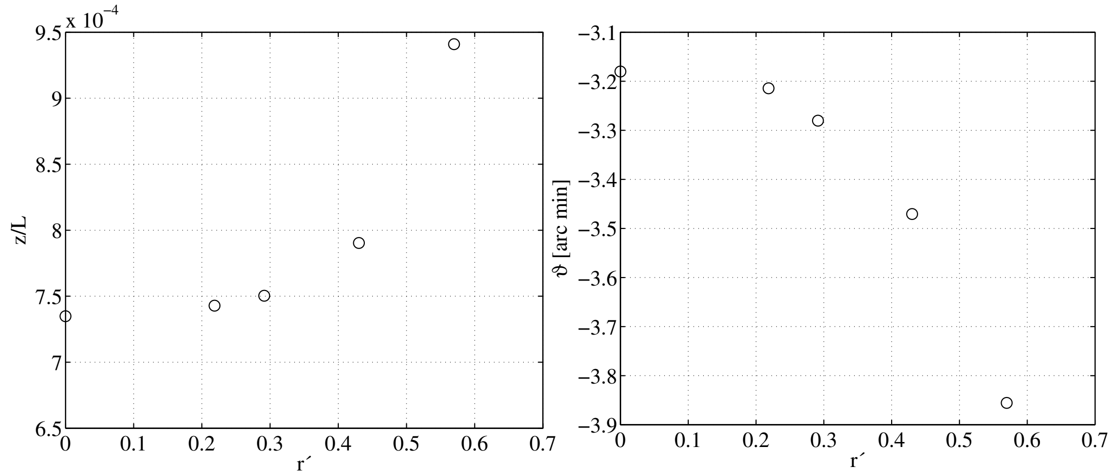

Figure 8.9: CFD prediction of squat in yaw motion at $h/T = 1.2$, $F_{nh} = 0.1378$.

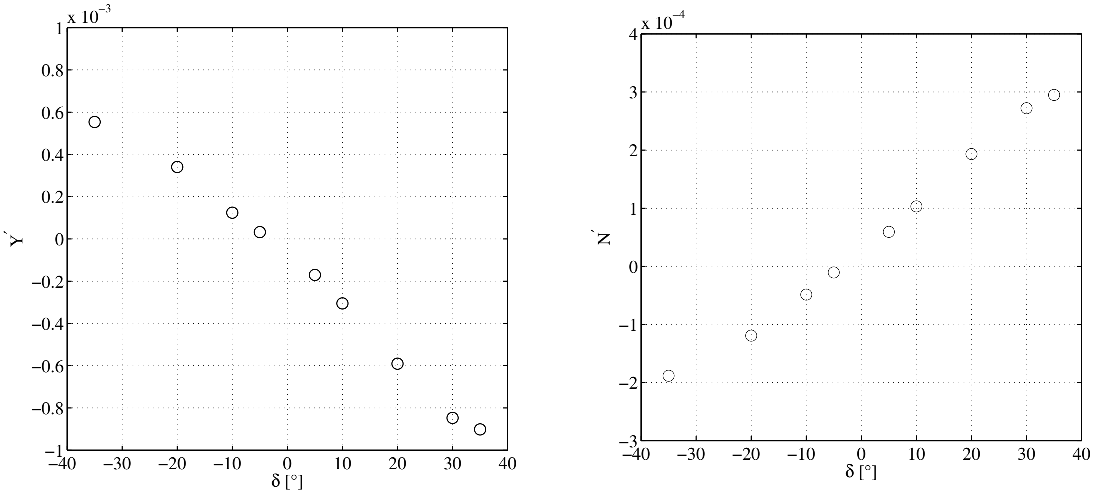

Figure 8.10: CFD prediction of lateral forces and yaw moments in rudder tests at h/T=1.2, F_{nh} = 0.23.

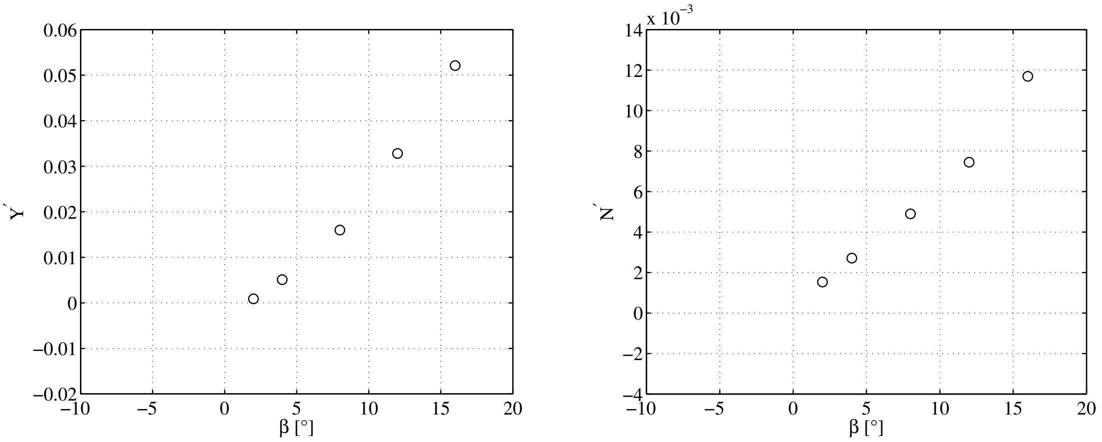

Figure 8.11: CFD prediction of lateral forces and yaw moments in drift motion at h/T=1.2, F_{nh} = 0.23.

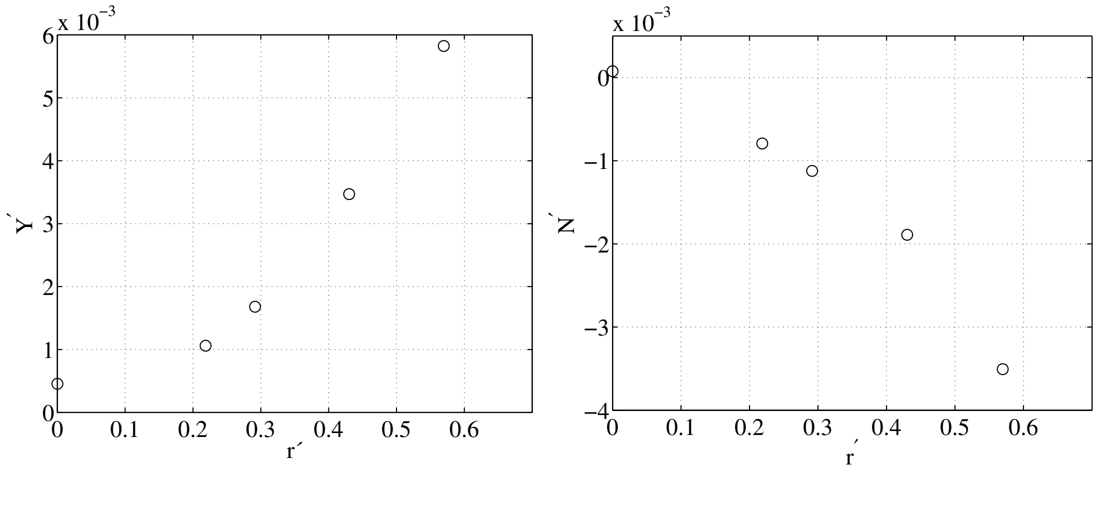

Figure 8.12: CFD prediction of lateral forces and yaw moments in yaw motion at h/T=1.2, F_{nh} = 0.23.

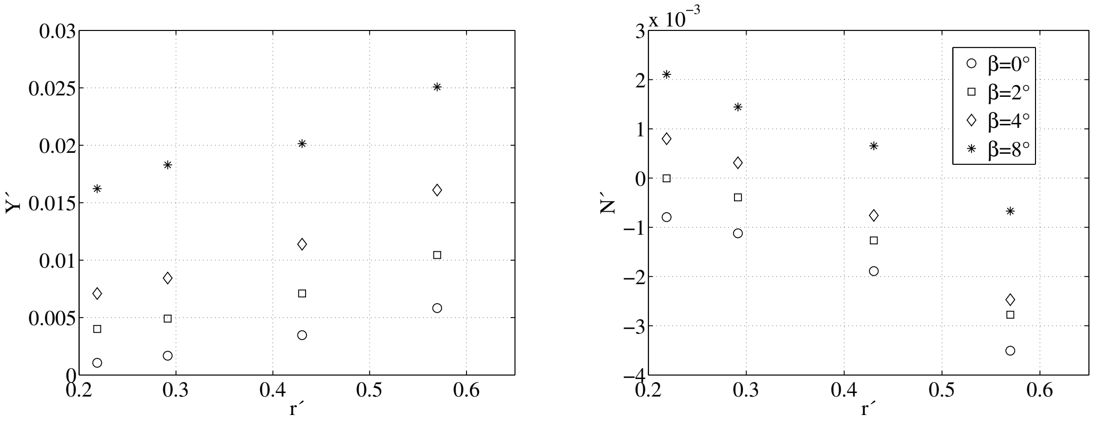

Figure 8.13: CFD prediction of lateral forces and yaw moments in drift and yaw motion at h/T=1.2, $F_{nh} = 0.23$.

References

Abbott, I., Doenhoff, A., 1959, *A theory of wing sections*, Dover

Abkowitz, M.A., 1964, *Lectures on Ship Hydrodynamics - Steering and Maneuverability*, Hydro- og Aeordynamisk Laboratorium, Lyngby, Report No. Hy-5

Alam M.R., Mei, C.C., 2008, *Transcritical ship waves in a randomly uneven channel*, Journal of Fluid Mechanics, 616:397-417

Atta, E. H., 1981, *Component adaptive grid interfacing*, 19th Aerospace Sciences Meeting, Aerospace Sciences Meetings, AIAA Paper 810382

Beatson, R.K., Powell, M.J.D. and Tan, A.M, 2006, *Fast evaluation of polyharmonic splines in three dimensions*, Transactions of Mathematics and its Applications, IMAJ, 27(3):427-450

Beck, R.F., Newman, J.N., Tuck, E.O., 1975, *Hydrodynamic Forces on Ships in Dredged Channels*, Journal of Ship Research, 19:166-171

Beck, R.F., 1977, *Forces and moments on a ship moving in a canal*, Journal of Ship Research, 21(2):107-119

Benek, J. A., Steger, J. L., Dougherty, F. C., 1983, *A flexible grid embedding technique with application to the Euler equations*, AIAA Paper 831944

Bollay, W., 1936, *A New Theory For Wings Of Small Aspect Ratio*, PhD Thesis, California Institute of Technology

Brard, R., 1951, *Maneuvering of ships in deep water, in shallow water, and in canals*, Trans. Soc. Nav. Arch. Mar. Eng. 59:229-57

Breslin, J.P., 1972, *Theory for the first-order gravitational effects on ship forces and moments in shallow water*, Journal of Hydronautics, 6:110-111

Brix, J., 1993, *Manoeuvring Technical Manual*, Seehafen Verlag

Brunswig, J., El Moctar, O., 2004, *Prediction of Ship Motions in Waves Using RANSE*, Proc. of the 7th Numerical Towing Tank Symposium

Caretto, L.S., Gosman, A.D., Patankar, S.V., and Spalding, D.B., 1972, *Two calculation procedures for steady, three-dimensional flows with recirculation*, Proc. of the 3rd International Conference on Numerical Methods Fluid Dynamics

Carrica, P., Ismail, F., Hyman, M., Bhushan, S., Stern, F., 2013, *Turn and zigzag maneuvers of a surface combatant using URANS approach with dynamic overset grids*, Journal of Marine Science and Technology, 18(2):166-181

CD-adapco, 2016, *STARCCM+-User-Guide 11.02.012*

Chen, X.N., Sharma, S.D., 1995, *A slender ship moving at a near-critical speed in a shallow channel*, Journal of Fluid Mechanics, 291:263-285

Chen, X.-N., 1999, *Hydrodynamics of Wave-Making in Shallow Water*, PhD-Thesis, University of Stuttgart, Shaker Verlag

Chesshire, G., Heshaw, W. D., 1990, *Composite overlapping meshes for the solution of partial differential equations*, Journal of Computational Physics 90:1-64.

Chesshire, G., Heshaw, W. D., 1994, *A scheme for conservative interpolation on overlapping grids*, SIAM Journal on Scientific Computation 15:819-845.

Chorin, A.J., 1967, *A Numerical Method for Solving Incompressible Viscous Flow Problems*, Journal of Computational Physics, 135:118-125

Clarke, D., Gedling, P., Hine, G., 1983, *The Application of Manoeuvring Criteria in Hull Desgin Using Linear Theory*, Trans. of RINA 125

Coleman, H.W., Steele, W.G., 2009, *Experimentation, Validation and Uncertainty Analysis for Engineers*, Wiley

Cummins, W.E., 1962, *The Impulse Response Function And Ship Motions*, David Taylor Model Basin, Hydrodynamics Laboratory Research and Development Report 1661

Crane, C.L., Eda, H. and Landsburg, A.C., 1989, *Controllability*, E. V. Lewis (Ed.), Principles of Naval Architecture, 3:191-422, SNAME

Cura-Hochbaum, A., 2006, *Virtual PMM Tests for Manoeuvring Prediction*, Proc. of the 26th ONR Symposium on Naval Hydrodynamics

Davidson, K.S.M., Schiff, L.I., 1946, *Turning and Course Keeping Qualities*, Trans. of SNAME

Deng, G.B., Visonneau, M., 1999, *Comparison of explicit algebraic stress models and second-order turbulence closures for steady flows around ships*, Proc. of the 7th International Conference on Numerical Ship Hydrodynamics

Deng, G.B., Visonneau, M., 2005, *Three-dimensional Flow Computation with Reynolds Stress and Algebraic Stress Models*, Engineering Turbulence Modelling and Experiments 6:389-398.

Deng, G.B., Guilmineau, E., Leroyer, A., Queutey, P., Visonneau, M. and Wackers, J., 2014, *Simulation of container ship in shallow water at model scale and full scale*, Proc. of the 3rd National CFD Workshop for Ship and Offshore Engineering

Dougherty, F. C., 1985, *Development of Chimera Grid Scheme with Applications to Unsteady Problems*, PhD thesis, Stanford University

Draper, N.R., Smith, H., 1998, *Applied Regression Analysis*, Wiley

El Moctar, O., Bertram, V., 2000, *RANS Simulation of Propeller in Oblique Flow*, Proc. of the 3rd Numerical Towing Tank Symposium

El Moctar, O., 2001a, *Numerische Berechnung von Strömungskräften beim Manövrieren von Schiffen*, PhD-Thesis, Technical University of Hamburg-Harburg (in German)

El Moctar, O., 2001b, *Numerical Computations of Flow Forces in Ship Manoeuvring*, Ship Technology Research: Schiffstechnik, 9:98-123

El Moctar, O., Cura-Hochbaum, A., 2005, *Hydrodynamische Belastungen von Schiffsrudern beim Manövrieren von Schiffen*, Jahrbuch der Schiffbautechnischen

Gesellschaft (in German)

El Moctar, O.,Shigunov, V., Zorn, T., 2012, *Duisburg Test Case: Post-Panamax Container Ship for Benchmarking*, Ship Technology Research: Schiffstechnik, 59(3):51-64

El Moctar, O., Lantermann, U., Mucha, P., Höpken, J., Schellin, T.E., 2014, *RANS-Based Simulated Ship Maneuvering Accounting for Hull-Propulsor-Engine Interaction*, Proc. of the 30th ONR Symposium of Naval Hydrodynamics

Eloot, K., Vantorre, M., 2009, *Proceedings of the First International Conference on Ship Manoeuvring in Shallow and Confined Water: Bank Effects*, RINA, Ghent University

Eloot, K., Delefortrie, G., Vantorre, M., Quadvlieg, F., 2015, *Validation of Ship Manoeuvring in Shallow Water Through Free-Running Tests*, Proceedings of the 34th ASME International Conference on Ocean, Offshore and Arctic Engineering, OMAE2015-41912

Fairweather, G., Karageorghis, A., 1998, *The method of fundamental solutions for elliptic boundary value problems*, Advances in Computational Mathematics, 9:65-95

Faul, A.C., Goodsell, G. and Powell, M.J.D., 2005, *A Krylov subspace algorithm for multiquadric interpolation in many dimensions*, IMA Journal of Numerical Analysis, 25:1-24.

Fedajevsky, K.K., Sobolev, G.V., 1964, *Control and Stability in Ship Design*, State Union Shipbuilding, Leningrad (St. Petersburg)

Ferziger, J., Perić, M., 2002, *Computational Methods for Fluid Dynamics*, Springer

Fossen, T.I., 2011, *Marine Craft Hydroynamics and Motion Control*, Wiley

Fox, R.W., Pritchard, P.J, McDonald, A.T., 2010, *Introduction to Fluid Mechanics*, Wiley 7th Edition

Fujino, M., 1968, *Experimental Studies on Ship Maneuverability in Restricted Waters*, International Shipbulding Progress, 15:279-301

Fujino, M., 1972, *New Experimental Results of Forced Yaw Tests in Shallow Water*, Naut. Report No. 5001:1-29, Department of Naval Architecture University of Tokyo

Fujino, M., Ishiguro, T., 1984, *A Study of the Mathematical Model Describing Manoeuvering Motions in Shallow Water - Shallow Water Effects on Rudder-Effectiveness Parameters*, Journal of the Society of Naval Naval Architects of Japan, 156:180-192

Gatski, T.B., Speziale, C.G., 1993 *On explicit algebraic stress models for complex turbulent flows*. Journal of Fluid Mechaniccs, 254:59-78

Gertler. M., 1959, *The DTMB Planar-Motion-Mechanism system*, Symposium on Towing Tank Facilities, Zagreb

Goldstein, S., 1929, *On the vertex theory of screw propellers*, PhD-Thesis, University of Göettingen

Goodman, A., 1966, *Experimental techniques and methods of analysis used in submerged body research*, Proc. of the 3rd Symposium on Naval Hydrodynamics

Gourlay, T.P., 2000, *Mathematical and computational techniques for predicting the squat of ships*, PhD-Thesis, University of Adelaide

Gourlay, T.P., Tuck, E.O., 2001, *The Maximum Sinkage of a Ship*, Journal of Ship Research, 45:50-58

Gourlay, T.P., 2006, *Flow beneath a ship at small underkeel clearance*, Journal of Ship Research, 50(3):250-258

Gourlay, T.P., 2008, *Slender-body methods for prediction ship squat*, Ocean Engineering, 35(2):191-200

Gourlay, T.P., 2011, *A brief history of mathematical ship-squat prediction, focussing on the contributions of E.O. Tuck*, Journal of Engineering Mathematics, 70(1-3):5-16

Gourlay, T.P., 2014, *ShallowFlow: A Program to Model Ship Hydrodynamics in Shallow Water* Proc. of the ASME 33rd International Conference on Ocean, Offshore and Arctic Engineering, OMAE2014-23291.

Gourlay, T., Jeong, H.H., Mucha, P., Uliczka, K., 2015, *Sinkage and Trim of Modern Container Ships in Shallow Water*, Proc. of the Australasian Coasts and Ports Conference

Graff, W., Kracht, A., Weinblum, G., 1964, *Some extensions of D.W. Taylor's standard series*, Transactions of SNAME 72:375-401

Grim, 0., Oltmann, P., Sharma, S.D., Wolff, K., 1976, *CPMC - A Novel Facility for Planar Motion Testing of Ship Models*, Proc. of the 11th Symp. on Naval Hydrodynamics

Gronarz, A., 1993, *A Mathematical Model for Manoeuvring Simulation on Shallow Water*, Proc. of MARSIM 1993

Gronarz, A., 1997, *Rechnerische Simulation der Schiffsbewegung beim Manövrieren unter besonderer Berücksichtigung der Abhängigkeit von der Wassertiefe*, PhD-Thesis, Unversity of Duisburg (in German)

Gronarz, A., Broß, H., Mueller-Sampaio, C., Jiang, T., Thill, C., 2009, *SIMUBIN - Modellierung und Simulation der realitaetsnahen Schiffsbewegungen auf Binnenwasserstraßen*, (in German). Report 1939 B. Development Centre for Ship Technology and Transport Systems (DST).

Gumerov, N.A. and Duraiswami, R., 2007, *Fast radial basis function interpolation via preconditioned Krylov iteration*, SIAM Journal on Scientific Computing, 29:1876-1899.

Gutsche, F., 1955, *Die Induktion der axialen Strahlzusatzgeschwindigkeit in der Umgebung der Schraubenebene*, Schiffstechnik, 12(13) (in German)

Hadžić, I., Xing, Y., Perić, M., 2002, *Simulation turbulenter Strömung und strömungsbedinger Bewegung schwimmender Körper*, Schriftenreihe 618, Technical University of Hamburg-Harburg (in German)

Hadžić, H., 2005, *Development and Application of a Finite Volume Method for the Computation of Flows Around Moving BOdies on Unstructured, Overlapping Grids*, Ph.D. Thesis, Technical University of Hamburg-Harburg

Hahn, G. J., 1984, *Experimental design in the complex world*, Technometrics, 26:19-31.

Hardy, R. L., 1990, *Theory and applications of the multiquadric-biharmonic method*, Computers Math. Applications, 19:163-208.

Havelock, T.H., 1939, *Note on the sinkage of a ship at low speeds*, Zeitschrift für Angewandte Mathematik und Mechanik 19:458

Heshaw, W. D., 1985, *Part II: Composite Overlapping Grid Techniques*, PhD thesis, California Institute of Technology

Hooft, J.P., 1994, *The Cross-Flow Drag on A Manoeuvring Ship*, Ocean Engineering, 210(3):329-432

Imlay, F.H., 1961, *The Complete Expressions for "Added Mass" of a Rigid Body Moving in an Ideal Fluid*, David Taylor Model Basin, Washington D.C., Report No. 1528

Inoue, S., Murayama, K., 1969, *Calculation ofTurning Ship Derivatives in Shallow Water*. Trans. of the West-Japan Society of N.A.

Inoue, S., Hirano, M., Kijima, K. and Takashina, J., 1981, *A practical calculation method of ship maneuvering motion*, International Shipbuilding Progress X 28(325):207-222.

Isay, W.H., 1962, *Der Schraubenpropeller nahe der freien Wasseroberfläche und in Flachwasser*, Ingenieur-Archiv, XXXI. Band (in German)

Jensen, G., Söding, H., Mi, Z.-X., 1986, *Rankine soruce methods for numerical solutions of the steady wave resistance problem*, Proc. of the 16th Symposium on Naval Hydrodynamics

Jiang, T., 2003, *Ship Waves in Shallow Water*, Fortschritt-Berichte VDI, 13(466)

Kirchhoff, G., 1869, *Über die Bewegung eines Rotationskörpers in einer Flüssigkeit*, Crelle's Journal, 71:237-273 (in German)

Kose, K., 1982, *On a new mathematical model of manoeuvring motions of a ship and its applications*, International Shipbuilding Progress 29(336):205-220.

Kreitner, J., 1934, *Ueber den Schiffswiderstand auf beschraenktem Wasser*, Werft, Reederei, Hafen, 15 (in German)

Kudva, P., Narendra, K.S., 1974, *An Identification Procedure for Discrete Mulitvariable Systems*, IEEE Transactions on Automatic Control, 19(5):549-552

Lantermann, U., Höpken, J., el Moctar, O., 2015, *Maßstabseffekte und Umwelteinflüsse bei der Vorhersage des Manövrierverhaltens seegehender Schiffe -PREMAN*, Bericht zum Teilvorhaben MANÖ-DYN, BMWI FK 03SSX324B (in German)

Larsson, L., Stern, F., Bertram, V., 2003 *Benchmarking of Computational Fluid Dynamics for Ship Flows: The Gothenburg 2000 Workshop*, Journal of Ship Research, 47(1):63-81

Larsson, L., Stern, F. and Visonneau, M., 2013, *Numerical Ship Hydrodynamics*, Springer

Lataire, E., Vantorre, M., 2008, *Ship-Bank Interaction Induced by Irregular Bank Geometries*, Proc. of the 27th Symposium in Naval Hydrodynamics, Seoul, Korea

Launder, B.E., Reece, G.J., Rodi, W., 1975, *Progress in the Development of Reynolds-Stress Turbulent Closures*, Journal of Fluid Mechanics, 68(3):537-566

Li, Y., Sclavounos, P.D., 2002, *Three-dimensional nonlinear solitary waves in shallow water generated by an advancing disturbance*, Journal of Fluid Mechanics, 470:338-410

Mandel, P., 1965, *Ship maneuvering and control*, In J.P. Comstock (Ed.), Principles of Naval Architecture, pp. 463-606, SNAME

Menter, F.R., 1994, *Two-Equation Eddy-Viscosity Turbulence Models for Engineering Applications*, AIAA Journal, 32(8):1598-1605

Millward, A., 1992, *A comparison of the theoretical and empirical prediction of squat in shallow water*, International Shipbuilding Progress, 417:69-78

Mitchell , T. J., 1974, *An algorithm for the constructions of D-optimal experimental designs*, Technometrics, 16:203-210.

Mofidi, A., Carrica, P., 2014, *Simulation of zigzgag maneuvers for a containership with direct moving rudder and propeller*, Computers & Fluids, 96:191-203

Morse, R.V., Price, D., 1961, *Maneuvering Characteristics of the Mariner Type Ship (USS Compass Island) in Calm Seas*, Sperry Gyroscope Co., Syasset N.Y., Publ. No. GJ-2232-1019

Mucha, P., el Moctar, O., 2011, *Numerical analysis of propeller loads for a drifting container vessel using RANSE*, Proc. of the 14th Numerical Towing Tank Symposium

Mucha, P., el Moctar, O., 2013 *Identification of Hydrodynamic Derivatives for Ship Maneuvering Prediction in Restricted Waters*, Proceedings of the 16th Numerical Towing Tank Symposium, Mülheim (GER)

Mucha, P., el Moctar, O., Böttner, C.U., 2014, *Technical note: PreSquat - Workshop on Numerical Prediction of Ship Squat in Restricted Waters*, Ship Technology Research - Schiffstechnik. 61(3)162-165

Mucha, P., el Moctar, O., 2014, *Numerical Prediction of Resistance and Squat for a Containership in Shallow Water*, Proc. of the 17th Numerical Towing Tank Symposium

Mucha, P., el Moctar, O., 2015, *Revisiting mathematical models for maneuvering prediction based on modified Taylor-series expansions*, Ship Technology Research: Schiffstechnik, 62(2):81-96

Mucha, P., Deng, G., Gourlay, T., el Moctar, O., 2016, *Validation Studies on Numerical Prediction of Ship Squat and Resistance in Shallow Water*, Proc. of the 4th International Conference on Ship Manoeuvring in Shallow and Confined Water with Special Focus on Ship Bottom Interaction

Munk, M. M., 1924, *The aerodynamic forces on air-ship hulls*, Technical Report 184, NACA

Muzaferija, S., Peric, M., 1999, *Computation of free-surface flows using interface-tracking and interface-capturing methods*, Chapter 2 in O. Mahrenholtz and M. Markiewicz (Ed.), Nonlinear Water Wave Interaction, Computational Mechanics Publications, WIT Press, Southamption

Newman, J.N., 1966, *Some Hydrodynamic Aspects of Ship Maneuverability*, Proc. of the 6th Symposium on Naval Hydrodynamics

Newman, J.N., 1969, *Lateral Motion of a Slender Body between Two Parallel Walls*, Journal of Fluid Mechanics, 39(1):97-115

Newman, J.N., 1978, *Marine Hydrodynamics*, MIT Press

Nomoto, K., Taguchi, T., Honda, K., Hirano, S, 1957, *On the steering qualities of ships*, International Shipbuilding Progress 4(35)354-370.

Norrbin, N., 1960, *A study of course keeping and maneuvering performance*, Publ. Swedish State Shipbuilding Experinemntal Tank, No. 45, Reprinted in Proc. 1st Symposium on Ship Maneuverability, David Taylor Model Basin, 1960, DTMB Report No. 1461

Norrbin, N.H., 1971, *Theory and Observations on the Use of a Mathematical Model for Ship Manoeuvring in Deep and Confined Waters*, Statens Skeppsprovninganstalt, Gothenburg, Publ. No. 68

Oberhagemann, J., 2016, *On Prediction of Wave-Induced Loads and Vibration of Ship Structures with Finite Volume Fluid Dynamic Methods*, PhD-Thesis, University of Duisburg-Essen

Ogawa, A., 1971, *Calculations on the steered motion of a ship under the action of extrnal forces*, Selected Papers from J.S.N.A. Japan, 7:124-137

Ogawa A., Koyama T., Kijima K., 1977, *MMG report-I, on the mathematical model of ship manoeuvring*, Bull. Soc. Naval Archit. Jpn 575:22-28 (in Japanese)

Ogilvie, T.F., 1964, *Recent progress toward the understanding and prediction of ship motions*, Proc. of The Fifth Symposium on Naval Hydrodynamics

Oltmann, P., 1978, *Bestimmung der Manövriereigenschaften aus den Bahnkurven freimanövrierender Schiffsmodelle*, Institut für Schiffbau, Hamburg, Bericht Nr. 364 (in German)

Oltmann, P., Wolff., K., 1979, *Vergleichende Untersuchung über das Manövrierverhalten des MARINER-Standardschiffes*, Institut für Schiffbau, Hamburg, Report Nr. 385 (in German)

Oltmann, P., Sharma, S.D., 1984, *Simulation of Combined Engine and Rudder Maneuvers*, Institut für Schiffbau, Hamburg, Bericht Nr. 385

Pope, S., 2000, *Turbulent flows*, Cambridge University Press

Prandtl L., Tietjens, O.G., 1957, *Applied Hydro- and Aeromechanics*, Dover Publications Inc., NY, reprint of 1934 Ed.

Quadvlieg, F., Brouwers, J., 2011, *KVLCC2 Benchmark Data Including Uncertainty Analysis To Support Manoeuvring Predictions*, International Conference on Computational Methods in Marine Engineering, MARINE 2011

Queutey, P. and Visonneau, M., 2007, *An interface capturing method for free-surface hydrodynamic flows*, Computers & Fluids, 36(9):1481-1510

Raven, H., 1996, *A Solution Method for the Nonlinear Ship Wave Resistance Problem*, PhD-Thesis, Technical University of Delft

Renilson, M.R., 1986, *A Note on the Fluid Memory Effects and Non-linearities Involved in Oscillatory Ship Model Manoeuvring Experiments*, Proc. of the 9th Australian Fluid Mechanics Conference

Roache, P.S, 1998, *Verification and Validation in Computational Science and Engineering*, Hermosa Publ.

Rodi, W., 1976, *A new algebraic relation for calculating the Reynolds stresses*, ZAMM, 56:219-221, 1976.

Sato, T., Izumi, K., Miyata, H., 1998, *umerical simulation of maneuvering motion*, Proc. of the 22nd Symposium on Naval Hydrodynamics

Schuster, S., 1952, *Untersuchung über Strömungs- und Widerstandsverhältnisse bei der Fahrt von Schiffen auf beschränktem Wasser*, Jahrbuch der STG (in German)

Sharma, S.D., Chen, X.N., 2000, *Interaction of ship waves with river banks and uneven bottom*, Proc. of 4th International Conference on Hydrodynamics, Yokohoma, 157

Sharma, S.D., 1982, *Kräfte am Unter- und Überwasserschiff*, 18. Fortbildungskurs, Institut für Schiffbau, Universität Hamburg (in German)

Silverstein, B. L., 1957, *Linearized Theory of the Interaction of Ships*, PhD Thesis, University of California, Berkeley

SIMMAN, 2014, *Workshop on Workshop on Verification and Validation of Ship Maneuvering Simulation Methods*, http//simman2014.dk, called 03/12/2014

Smitt, L.W., Chislett, M.S., 1974, *Large Amplitude PMM Tests and Manoeuvring Predictions for a MARINER Class Vessel*, Proc. of the 10th Symposium on Naval Hydrodynamics

Stern, F., Agdrup, K., Kim, S.Y., Hochbaum, A.C., Rhee, K.P., Quadvlieg, F., Perdon, P., Hino, T., Broglia, R., Gorski, J., 2011, *Experience from SIMMAN 2008: The First Workshop on Verification and Validation of Ship Maneuvering Simulation Methods*, Journal of Ship Research, 55(2):135-147

Strøm-Tejsen, J., Chislett, M.S., 1966, *A Model Testing Technique and Method of Analysis for the Prediction of Steering and Manoeuvring Qualities of Surface Vessels*, Proc. 6th Symp. on Naval Hydrodynamics

Söding, H., 1982a, *Ruderkräfte*, 18. Fortbildungskurs, Institut für Schiffbau, Universität Hamburg (in German)

Söding, H., 1982b, *Prediction of steering capabilities*, Schiffstechnik, 3

Söding, H., 1982c, *Manövrieren von Schiffen*, Lecture Notes, Institut für Schiffbau, Universität Hamburg (in German)

Söding, H., 1993, *A method for accurate force calculation in potential flow*, Ship Technology Research/Schiffstechnik, 40:176-186

Söding, H., 2005, *Analysis of Overtaking Manouvres in a Narrow Waterway*, Ship Technology Research, 52(4):189-193

Söding, H., von Gräefe, A., el Moctar, O., Shigunov, V., 2012, *Rankine source method for seakeeping predictions*, Proceedings of the 31st Interantional Conference on Ocean, Offshore and Arctic Engineering, OMAE2012-83450

Steinberg, D. M., Hunter ,W. G., 1984, *Experimental design: review and comment*, Technometrics, 26:19-31.

Sutulo, S., Kim, S.Y., 1998, *Systematic Approach to PMM/Rotating Arm Experiment Planning, Parameter Estimation, and Uncertainty Analysis*, International Symposium and Workshop on Forces Acting on a Maneuvering Vessel

Sutulo, S., Guedes Soares, C., 2002, *An Algorithm for Optimized Design of Maneuvering Experiments*, Journal of Ship Research, 46(3):214-227

Sutulo, S., Guedes Soares, C., 2011, *Mathematical models for simulation of manoeuvring performance of ships*, Marine Technology and Engineering, Taylor and Francis Group

The International Maritime Organization (IMO), 1987, *Provision and Display of Manoeuvring Information on Board Ships*, Resolution A.601(15)

The International Maritime Organization (IMO), 2002, *Standards for Ship Manoeuvrability*, Resolution MSC.137(76)

The International Towing Tank Conference, 1975, *Maneuvering Trial Code*, Proc. of 14th ITTC

The International Towing Tank Conference - Recommended Procedures and Guidelines, 1999, *1978 ITTC Performance Prediction Method*, 7.5-02-03-01.4, http://ittc.info

The International Towing Tank Conference - Recommended Procedures and Guidelines, 2002, *CFD General Uncertainty Analysis in CFD Verification and Validation Methodology and Procedures* , 7.5-03-01-01, http://ittc.info

The International Towing Tank Conference, 2002, *Recommended Procedures Full Scale Measurements Manoeuvrability Full Scale Manoeuvring Trials Procedure ITTC Recommended Procedures*, 7.5-04-02-01

The International Towing Tank Conference Recommended Procedures and Guidelines, 2008, *Testing and Extrapolation Methods - Manoeuvrability Free Running Model Tests*, 7.5-02-06-01, http://ittc.info

The International Towing Tank Conference, 2011, *The Manoeuvring Committee - Final report and recommendations to the 26th ITTC* Proc. of 26th ITTC, Volume I

The International Towing Tank Conference - Recommended Procedures and Guidelines, 2014, *Captive Model Test Procedures*, 7.5-02-06-02, http://ittc.info

The International Towing Tank Conference Recommended Procedures and Guidelines, 2011, *Validation of Manoeuvring Simulation Models*, 7.5-02-06-03, http://ittc.info

The International Towing Tank Conference - Recommended Procedures and Guidelines, 2011, *Recommended Procedures and Guidelines on Use of RANS Tools for Manoeuvring Prediction*, 7.5-03-04-01, http://ittc.info

The International Towing Tank Conference, 2014, *Final Report and Recommendations of the Manoeuvring Committee to the 27th ITTC*, Proc. of 27th ITTC

The World Association of Waterborne Transport Infrastructure (PIANC), 1992, *Capabilities of ship manoeuvring simulations models for approach channels in fairways and harbours*, Report of working group no. 20 of permanent technical committee II, supplement to PIANC bulletin no. 77

Thews, J.G., Landweber, L., 1935, *The influence of shallow water on the resistance of a cruiser model*, United States Experimental Model Basin report 408

Thieme, H., 1962, *Zur Formgebung von Schiffsrudern*, Jahrbuch der Schiffbautechnische Gesellschaft, Springer (in German)

Thomas, B. S., Sclavounos, P. D., 2006. *Optimal Control Theory Applied to Ship Maneuvering in Restricted Waters*, Readings in Marine Hydrodynamics, Volume to be Published in Honor of Professor J. Nicholas Newman

Tonelli, R., Quadvlieg, F., 2015, *New Benchmark Data For Manoeuvring In Shallow Water Based on Free Running Manouevring Tests Including Uncertainty of The Results* Proceedings of the ASME... OMAE Paper No. 42254

Tuck, E.O., 1963, *The steady Motion of a Slender Ship*, PhD-Thesis, University of Cambridge

Tuck, E.O., 1966, *Shallow-water Flows Past Slender Bodies*, Journal of Fluid Mechanics, 26:81-95

Tuck, E.O., 1967, *Sinkage and Trim in Shallow Water of Finite Width*, Schiffstechnik, 14:92-94

Tuck, E.O., Taylor, P.J., 1970, *Shallow Water Problems in Ship Hydrodynamics*, Proc. of 8th Symposium on Naval Hydrodynamics

Tuck, E.O., Newman, J.N., 1978, *Hydrodynamic Interactions Between Ships*, Proc. of the 12th Symposium on Naval Hydrodynamics

Tuck, E.O., 1978, *Hydrodynamic Problems of Ships in Restricted Waters*, Ann. Rev. Fluid Mechanics, 10:33-46

Uliczka, K. Böttner, C.U., Kastens, M., Eloot, K., Delefortrie, G., Vantorre, M., Candries, M., Lataire, E., 2016, *Proceedings of the 4th International Conference on Ship Manoeuvring in Shallow and Confined Water with Special Focus on Ship Bottom Interaction*, Hamburg

Vantorre, M., Verzhbitskaya, E., Laforce, E., 2002, *Model Test Based Formulations of Ship-Ship Interaction*, Schiffstechnik, 49:124-141

Viallon, M., Sutulo, S., Guedes Soares, C., 2012, *On the Order of Polynomial Regression Models for Manoeuvring Forces*, Manoeuvring and Control of Marine Craft, IFAC, 9(1):13-18

Visonneau, M., Guilmineau, E., Quetuey, P., Wackers, J., Deng, G.B., 2014, *Assessment of Statistic and Hybrid LES Turbulence Closures for Complex Free-Surface Flow Simulation with Combined Grid Refinement Criteria*, Proc. of the 30th Symposium on Naval Hydrodynamics

Von Graefe, A., 2014, *Rankine-source method for ship-ship interaction and shallow water flows*, PhD-Thesis, University of Duisburg-Essen

Wagner-Smith, L., 1971, *Steering and Manoeuvring of Ships Full Scale and Model Tests*, European Shipbuilding, 20(1)

Weinblum, G., 1934, *Theoretische Untersuchung der Strämungsbeeinflussung zweier Schiffe aufeinander beim gegenseitigen Begegnen und Überholen auf tiefem und beschränktem Wasser*, Schiffbau (in German)

Welch, W. J., 1984, *Computer-aided design of experiments for response estimation*. Technometrics, 26:217-224.

Whicker, L.F., Fehlner, L.F., 1958, *Free-stream characteristics of a family of low aspect ratio control surfaces for application to ship design*, DTMB Report 933, David Taylor Model Basin, Washington D.C.

Wilcox, D.C.,1988, *Re-assessment of the scale-determining equation for advanced turbulence models*, AIAA Journal, 26(11):1299-1310.

Wolff, K., 1981, *Ermittlung der Manövriereigenschaften fünf repräsentativer Schiffstypen mit Hilfe von CPMC-Modellversuchen*, Institut für Schiffbau, Hamburg, Bericht Nr. 412 (in German)

Yahfoufi, N., Deng, 2013, *Resistance prediction of the DTC container ship model in shallow water*, Submission to the PreSquat Workshop, Mülheim, Germany

Yasukawa, H., 1988, *A Theoretical Study of Hydrodynamic Derivatives on Ship Maneuvering in Restricted Water*, Proc. of the Spring Meeting of The Society of Naval Architects of Japan

Yasukawa, H., Yoshimura, Y., 2014, *Roll-Coupling Effect on Ship Maneuverability*, Ship Technology Research: Schiffstechnik, 61(1):16-32

Yasukawa, H., Yoshimura, Y., 2015, *Introduction of MMG standard method for ship maneuvering predictions*, Journal of Maritime Science and Technology, 20(1):37-52

Yeung, R.W., 1978, *On the interactions of slender ships in shallow water*, Journal of

Fluid Mechanics, 85(1):143-159

Yuan, J., Wonham, W., 1977, *Probing Signals for Model Reference Identification*, IEEE Transactions on Automatic Control, 22(4):530-538

Zhao, Y.X., 1986, *Hydroynamische Kräfte an manövrierenden Schiffen auf flachem Wasser*, Institut für Schiffbau der Universität Hamburg, Bericht Nr. 466 (in German)